

University
of Cyprus

DEPARTMENT OF ELECTRICAL AND
COMPUTER ENGINEERING

**DESIGN OF NOVEL METAL
NANOSTRUCTURES FOR BIOLOGICAL
AND BIOMEDICAL APPLICATIONS**

MYRIA ANGELIDOU

A Dissertation Submitted to the University of Cyprus in Partial
Fulfillment of the Requirements for the Degree of *Doctor of Philosophy*

May 2014

MYRIA ANGELIDOU

© Myria Angelidou, 2014

VALIDATION PAGE

Doctoral Candidate: Myria Angelidou

Doctoral Dissertation Title: Design of Novel Metal Nanostructures for Biological and Biomedical Applications

*The present Doctoral Dissertation was submitted in partial fulfillment of the requirements for the Degree of Doctor of Philosophy at the **Department of Electrical and Computer Engineering** and was approved on the **12 May** by the members of the **Examination Committee**.*

Examination Committee:

Research Supervisor: _____
(Name, position and signature)

Committee Member: _____
(Name, position and signature)

Committee Member: _____
(Name, position and signature)

Committee Member: _____
(Name, position and signature)

Committee Member: _____
(Name, position and signature)

DECLARATION OF DOCTORAL CANDIDATE

The present doctoral dissertation was submitted in partial fulfillment of the requirements for the degree of Doctor of Philosophy of the University of Cyprus. It is a product of original work of my own, unless otherwise mentioned through references, notes, or any other statements.

.....

.....

MYRIA ANGELIDOU

ΠΕΡΙΛΗΨΗ

Τα μεταλλικά νανοσωματίδια (NPs) βρίσκονται στο επίκεντρο έντονου ερευνητικού ενδιαφέροντος λόγω των μοναδικών οπτικών ιδιοτήτων τους. Μέχρι τώρα, διάφορα δημοσιεύματα έχουν καλύψει τη σύνθεση, τροποποίηση, και εφαρμογές των νανοσωματιδίων, και πιθανές βιοϊατρικές τους χρήσεις ως αισθητήρες ή παράγοντες αντίθεσης. Οι οπτικές τους ιδιότητες καθορίζονται κυρίως από το φαινόμενο του επιφανειακού πλασμονικού συντονισμού (SPR), το οποίο δεν παρατηρείται στα αντίστοιχες δομές μεγαλύτερων διαστάσεων. Ο επιφανειακός πλασμονικός συντονισμός εξαρτάται από το υλικό, το μέγεθος και τη δομή των μεταλλικών νανοσωματιδίων, τις διηλεκτρικές ιδιότητες του γύρω περιβάλλοντος, καθώς και από τις αλληλεπιδράσεις σύζευξης μεταξύ νανοσωματιδίων. Γι'αυτό το λόγο έχει τη μοναδική ικανότητα να συντονίζεται σε μήκη κύματος που κυμαίνονται από υπεριώδες-ορατό (UV-vis) μέχρι και στο εγγύς υπέρυθρο (NIR). Οι οπτικές ιδιότητες, όπως αυτές μεταβάλλονται από τον SPR μπορούν να υπολογιστούν με τη χρήση αριθμητικών μεθόδων όπως με τη διακριτή προσέγγιση διπόλου (DDA).

Σε αυτή την διατριβή, παρουσιάζονται ο σχεδιασμός και η μελέτη νέων τύπων μεταλλικών νανοδομών: μονοστρωματικά/δίπλοστρωματικά συναθροιστηκά κελύφη (mono-/bi-layer shell aggregates) και πολύ-λειτουργικές (dual-mode) νανοδομές. Αυτές οι νέες μεταλλικές νανοδομές προσφέρουν σαφή πλεονεκτήματα, όσον αφορά στις οπτικές τους ιδιότητες για βιοϊατρικές εφαρμογές σε σχέση με άλλα νανοσωματίδια. Το συναθροιστηκό κέλυφος είναι προσαρμοσμένο για ενδοκυτταρική χρήση της επιφανειακά ενισχυμένης φασματοσκοπίας Raman (SERS), ενώ η πολύ-λειτουργική νανοδομή ως διαγνωστικός (theranostic) παράγοντας, αφού θα συνδυάζει δυνατότητα ταυτόχρονης απεικόνισης και θεραπείας.

Αρχικά, γίνεται με μία διεξοδική θεωρητική διερεύνηση των παραμέτρων που διέπουν τα χαρακτηριστικά των συναθροιστηκών κελυφών. Τα συναθροιστηκά κελύφη αποτελούνται από μικρές χρυσές νανοσφαίρες οι οποίες συναθροίζονται, δημιουργώντας μια ή δύο στρώσεις γύρω από ένα διηλεκτρικό πυρήνα. Οι διερευνόμενες παράμετροι περιλαμβάνουν το μέγεθος και την απόσταση μεταξύ των μικρών νανοσφαιρών, το συνολικό μέγεθος της νανοδομής και τέλος το υλικό των νανοσφαιρών και του πυρήνα. Έγινε επίσης σύγκριση των οπτικών ιδιοτήτων των συναθροιστηκών κελυφών με άλλα νανοσωματίδια και νανοδομές. Από τα αποτελέσματα, φάνηκε ότι η απόσταση μεταξύ των μικρών νανοσφαιρών παίζει ένα πολύ σημαντικό ρόλο στη ρύθμιση του επιφανειακού πλασμονικού συντονισμού του συναθροιστηκού κελύφους.

Η πολύ-λειτουργική νανοδομή είναι σχεδιασμένη ώστε να διαθέτει φάσματα απορρόφησης και σκέδασης με κορυφές σε ξεχωριστά μήκη κύματος. Αρχικά, διερευνήθηκαν οι συντελεστές αποδοτικότητας (efficiency factors) διαφόρων νανοδομών. Μετά, πιο πολύπλοκες νανοδομές σχηματίστηκαν για περαιτέρω μελέτη. Παράμετροι, όπως η συνολική δομή, και ο αριθμός, το μέγεθος και η διάταξη των μικρότερων νανοδομικών στοιχείων, εξετάστηκαν. Ο συνδυασμός ενός χρυσού νανοκύβου (120nm μήκος των ακμών) με 16 (30nm διάμετρο) μικρές αργυρές νανοσφαίρες, αποδείχθηκε ότι παρέχει τα καλύτερα αποτελέσματα.

Η διατριβή ολοκληρώθηκε με πειραματική επαλήθευση της σύνθεσης του μονοστρωματικού συναθροιστηκού κελύφους. Μία απλή μέθοδος χρησιμοποιήθηκε, όπου μικρές χρυσές νανοσφαίρες μορφοποιούνται άμεσα επάνω σε πολυστυρένιες (PS) σφαίρες, με τη βοήθεια κιτρικού διαλύματος. Τα φάσματα απορροφητικότητας συσχετίστηκαν με τις θεωρητικές τιμές εξάλειψης (extinction) των συναθροιστηκών κελυφών και των νανοκελυφών ώστε να εξαχθούν πληροφορίες σχετικά με τη δομή των σύνθετων χρυσών νανοδομών. Μία σειρά από πειράματα διαλεύκαναν τις πειραματικές παραμέτρους που διέπουν την σύνθεση μονοστρωματικών συναθροιστηκών κελυφών.

Αυτού του νέου τύπου μεταλλικές νανοδομές παρέχουν πλασματικό συντονισμό στο εγγύς υπέρυθρο φάσμα και διακριτές πλασματικές ζώνες (plasmon bands) απορρόφησης και σκέδασης. Αυτές οι δύο ιδιότητες είναι πολύ σημαντικές σε κάποιες βιολογικές και βιοϊατρικές εφαρμογές. Τέτοιες μεταλλικές νανοδομές μπορεί να είναι ανεκτίμητα εργαλεία στην ανίχνευση, το χαρακτηρισμό και τη θεραπεία διαφόρων ασθενειών, όπως ο καρκίνος.

ABSTRACT

Metal nanoparticles (NPs) are in the centre of intense research interest due to their unique optical properties. A wide variety of publications has so far covered various aspects including nanoparticle (NP) synthesis, functionalization, applications in biological systems and their potential biomedical uses as sensors or contrast agents. Their optical properties of metal NPs are mainly determined by the phenomenon of surface plasmon resonance (SPR), which is not seen in their bulk counterparts, and can be calculated using numerical methods, such as the discrete dipole approximation (DDA). The SPR depends on the material, size, and structure of the metal NP, the dielectric properties of the surrounding medium and coupling interactions between adjacent NPs. This allows a unique tunability of the SPR, varying from the ultraviolet-visible (UV-vis) to the near-infrared (NIR) wavelength range. In this dissertation, the design and study of new types of metal nanostructures (NSs): the monolayer/bilayer shell aggregates, and the dual-mode nanostructure (NS) is presented. These new metal NSs offer significant advantages in their optical properties, for biomedical applications compared to other NPs. The shell aggregate is tailored for uses in intracellular surface-enhanced Raman spectroscopy (SERS), while the dual-mode NS as a theranostic (diagnostic plus therapeutic) agent, since it can combine simultaneous imaging and therapy capabilities.

Initially, a thorough theoretical investigation of the parameters that govern the monolayer/bilayer shell aggregate characteristics was performed. The shell aggregate is comprised of small gold nanospheres that aggregate around a dielectric core, creating a monolayer or bilayer shell. Important parameters include the size, and distance between small nanospheres, the overall shell aggregate size, and finally the nanospheres/core materials. The optical properties of shell aggregates were also compared with that of classical gold NPs. From the results, it was found that the distance between nanospheres plays a major role in the tuning of the shell aggregate's SPR.

The dual-mode NS is designed to exhibit distinct and separated absorption and scattering plasmon bands. Initially, the efficiency factors of various simple NSs were investigated. Then, more complex NSs were considered for further study. Parameters, such as the overall structure and the number, size, and arrangement of small nanospheres, were examined. It was that the combination of a gold nanocube (120nm edge length) with 16 (30nm diameter) small silver nanospheres provides the best results.

The dissertation concludes with the experimental verification of the synthesis of monolayer shell aggregates. A simple method was used to synthesize composite gold NSs, where small gold nanospheres were directly formed onto a polystyrene (PS) core, with the help of citrate. The absorbance spectra were compared to the theoretical extinction values of shell aggregates and nanoshells to extract information regarding the structure of the synthesized composite gold NSs. A series of experiments were performed to elucidate the parameters which control the synthesis of monolayer shell aggregates.

These new type metal NSs can provide with NIR plasmon resonances and distinct and separated absorption and scattering plasmon bands, both significant for biological and biomedical applications. Such novel metal NSs can be invaluable tools in detection, characterization and therapy of various diseases, such as cancer.

ACKNOWLEDGEMENTS

First, I would like to express my sincere gratitude to my supervisor Dr. Constantinos Pitris, for his valuable guidance and many encouragements during this project.

A special thanks to my colleagues at the University of Cyprus for their useful discussions and encouragements during my graduate studies, and group meeting sessions..

Many special thanks to the University of Nicosia for letting me use their laboratory facilities (instruments and supplies).

I would personally thank Dr. Evdokia Kastanos for guiding and assisting me during my experimental essays.

Also, I thank Dr. Maria Kokkonou for assisting me in obtaining the SEM images.

I am very grateful to the KIOS Research Center for Intelligent Systems and Networks (a University of Cyprus research center), the Cyprus Research Promotion Foundation, and the European Regional Development Fund of the EU, for their financial support.

Finally, I would like to thank my family, and Kyriakos Parides for their love and support all the time.

To my family

MYRIA ANGELIDOU

Table of Contents

List of Figures	xiii
List of Tables.....	xix
List of Symbols and Abbreviations.....	xxi
1. Introduction.....	1
1.1 Metal Nanoparticles	1
1.1.1 A historical overview.....	1
1.1.2 Nanoparticles and applications	3
1.2 Research Motivation.....	4
1.3 Dissertation Objectives.....	5
1.4 Dissertation Organization.....	6
1.5 List of Publications out of Dissertation.....	8
2. Theory	9
2.1 Surface Plasmon Resonance (SPR).....	9
2.2 Dielectric Function or Refractive Index.....	13
2.2.1 Refractive index – Tabulated data sets.....	13
2.2.2 Drude “free” electron model.....	15
2.2.3 Interband transitions.....	16
2.2.4 Size-dependent dielectric function	18
2.3 Summary	21
3. Methodology	22
3.1 Discrete Dipole Approximation (DDA).....	22
3.1.1 DDA method.....	23
3.1.2 Applicability of DDA.....	25
3.2 Implementation: DDSCAT Software	27
3.2.1 Solution Methodology	28
3.2.2 Other parameters	29
3.2.3 Target material.....	31
3.2.4 Target generation: shape files	32
3.2.4.1 Spherical – Monolayer/bilayer shell aggregates.....	33
3.2.4.2 Complex/combined nanostructures	34
3.2.5 Target Orientation	35
4. Investigation of Novel Monolayer/Bilayer Shell Aggregates – Comparison with Classical Gold Nanoparticles	37

4.1 Introduction	37
4.2 Classical Gold Nanoparticles	40
4.2.1 Single nanospheres.....	40
4.2.2 Uniform spherical aggregates.....	41
4.2.3 Nanoshells.....	43
4.3 Monolayer/Bilayer Shell Aggregates.....	45
4.3.1 Monolayer shell aggregate: the effect of small nanosphere radius (r).....	48
4.3.2 Monolayer shell aggregate: the effect of various nanosphere edge-to-edge distance (d_s).....	51
4.3.3 Monolayer shell aggregate: the effect of the outer radius (R).....	54
4.3.4 The effect of interdipole separation (d) on the calculations	56
4.3.5 Comparison with classical nanoparticles	56
4.3.6 Bilayer shell aggregates.....	58
4.4 Model of a Pair of Small Gold Nanospheres.....	59
4.4.1 Extinction efficiency spectra of the pair of nanospheres as a function of the edge-to-edge distance (d_s)	60
4.4.2 Polarization dependence of the pair of nanospheres	62
4.4.3 Universal plasmon ruler	63
4.5 Absorption and Scattering of Monolayer Shell Aggregates.....	64
4.6 Monolayer Shell Aggregates with Various Core/Sphere Materials	65
4.6.1 Monolayer shell aggregates with various internal core/external media.....	66
4.6.2 Monolayer shell aggregates with various metallic cores.....	66
4.6.3 Comparison between monolayer shell aggregates with various cores	67
4.6.4 Effect of using different refractive index tabulated data sets.....	69
4.6.5 Comparison between monolayer shell aggregates with gold/silver nanospheres.....	69
4.7 Summary	70
5. Theoretical Investigation of a Dual-Mode Nanostructure	72
5.1 Introduction	72
5.2 Simple Metal Nanostructures	75
5.2.1 Nanostructures of various materials and shapes	76
5.2.2 Effect of size (edge length, b) on the nanocube properties	82
5.2.3 Discussion	83
5.3 Small Nanospheres as Absorption Building Blocks.....	83
5.4 Complex Metal Nanostructures.....	84
5.4.1 Gold nanocube combined with various numbers (sizes) of small gold and silver nanospheres	85
5.4.2 Comparison spectra between individual and combined nanostructures.....	88

5.4.3	<i>Effect of the overall size and other nanosphere arrangements</i>	90
5.4.3.1	Overall complex nanostructure size variation	90
5.4.3.2	Small nanosphere arrangement on nanocube	91
5.4.3.3	Addition of a second layer of small nanosphere to the complex nanostructure	93
5.4.4	<i>Nanocube covered by small nanospheres</i>	94
5.5	Cubical Nanoshells	95
5.5.1	<i>Cubical nanoshells consisting of a silica core and various metal shells</i>	96
5.5.2	<i>Comparison with spherical nanoshells</i>	97
5.5.3	<i>Cubical nanoshells with metal cores</i>	98
5.6	Summary	99
6.	Synthesis and Experimental Verification of Monolayer Shell Aggregates	101
6.1	Introduction	101
6.2	Materials – Equipment	102
6.3	Experimental Procedures	103
6.3.1	<i>Basic protocol for AuNP-coated PS synthesis</i>	103
6.3.2	<i>Experimental considerations</i>	104
6.3.2.1	Aqueous solutions preparation	104
6.3.2.2	Estimation of the amount of PS to be used	105
6.3.2.3	Centrifugation of the final solutions	105
6.3.2.4	UV-vis spectrophotometry	106
6.3.2.5	SEM imaging	106
6.3.3	<i>Experiments</i>	106
6.3.3.1	Experiment 1	107
6.3.3.2	Experiment 2	108
6.3.3.3	Experiment 3	108
6.4	Analysis	109
6.4.1	<i>Step 1: Water subtraction</i>	109
6.4.2	<i>Step 2: Data interpolation</i>	110
6.4.3	<i>Step 3: Data normalization</i>	111
6.4.4	<i>Step 4: Data fitting and comparison</i>	112
6.4.5	<i>Step 5: Fitting constant normalization</i>	113
6.5	Results	113
6.5.1	<i>Synthesis of composite Au@PS NSs – Color variations</i>	113
6.5.2	<i>Composite Au@PS NSs characterization – SEM imaging</i>	115
6.5.3	<i>Measurements – Calculations</i>	116
6.5.4	<i>Fitting results</i>	117
6.6	Discussion	123
6.6.1	<i>Effect of cooling the final solution</i>	125

6.6.2 Effect of the total amount of $HAuCl_4$	125
6.6.3 Experimental repeatability.....	127
6.7 Summary	128
7. Conclusions and Future Work	130
7.1 Conclusions	130
7.2 Future Work	133
Bibliography.....	134
Appendix A – General Information.....	149
A.1 Equations of Energy, E, Versus Wavelength, λ	149
A.2 Electron Configurations of Various Metals.....	149
A.3 Mathematical Equations for Various Objects.....	149
A.4 Chemical Formulas.....	150
A.5 Centrifuge Parameters	150
A.6 UV-vis Spectrophotometer	151
A.7 Scanning Electron Microscope (SEM).....	151
Appendix B – Parameter Files for DDSCAT Software	152
B.1 Parameter File for DDSCAT6.1	152
B.2 Parameter File for DDSCAT7.0	153
Appendix C – Bilayer Shell Aggregate Results (J&C).....	154
Appendix D – Efficiency Factors of Various Classical Nanoparticles (J&C).....	157
D.1 Nanoshells	157
D.2 Spherical Aggregates.....	157
D.3 Monolayer Shell Aggregates of Various Cores/Spheres	158
Appendix E – Efficiency Factors of Various Simple Nanostructures (Palik).....	159
Appendix F – Shapes of Various Complex Nanostructures (Gold Nanocube Combined with Various Small Nanospheres)	171
Appendix G – Other Results of Complex Nanostructures (Gold Nanocube Combined with Small Gold (Au) Nanospheres) (Palik)	173
Appendix H – Efficiency Factors of Nanoshells Comprised of a Constant Polystyrene Core and Various Gold Shell Thicknesses.....	175
Appendix I – Fitting Constants and Rayleigh Coefficient for Calculated New Absorbances A_{fit}	176

List of Figures

Figure 1.1: Photographs of the famous Lycurgus Cup which displays a different color depending on whether it is illuminated (A) externally, or (B) internally. For details, consult website of the British Museum [14], and Freestone et al. [15].	2
Figure 2.1: (A) Schematic representation of a dipole plasmon oscillation for metal nanospheres, showing the displacement of the electron cloud relative to the nuclei [2], (B) Dipole, quadrupole, and octupole modes in a sphere [82].	10
Figure 2.2: SPR dependence on (A) size (silver, nanocube (edge length, b)), (B) shape (gold, $r_{\text{eff}} = 74.4\text{nm}$), (C) material (nanocube, $b = 120\text{nm}$), and (D) external medium (silver, nanosphere, $r = 50\text{nm}$). Material properties obtained from the tabulated data of Palik [91]. (A)–(C) assumed water as the external medium.	11
Figure 2.3: SPR refractive index data set dependence examples. (A) Gold nanosphere ($r = 50\text{nm}$), (B) gold nanocube ($r_{\text{eff}} = 74.4\text{nm}$), (C) small ($r = 30\text{nm}$), and (D) large ($r = 70\text{nm}$) silver nanospheres. The external medium was assumed to be water.	15
Figure 2.4: Interband contribution on the SPR of noble metals. Spectra examples of (A) small ($r = 15\text{nm}$), and (B) large ($r = 50\text{nm}$) nanospheres in water. (Optical constants obtained from J&C [98].)	17
Figure 2.5: Size-dependent dielectric functions to include the surface damping modification. Example spectra of (A) small ($r = 5\text{nm}$), and (B) large ($r = 50\text{nm}$) silver nanospheres in vacuum. (J&C [98].)	20
Figure 3.1: Nanosphere approximated by four discrete dipole arrays with $N = 136, 304, 1064,$ and 2320 [126].	26
Figure 3.2: Interdipole separation, d , dependence for gold nanosphere with (A) $r = 5\text{nm}$, and (B) $r = 50\text{nm}$ in water. (J&C [98].)	26
Figure 3.3: Comparison between the two DDSCAT versions, for a gold nanosphere with (A) $r = 30\text{nm}$, and (B) $r = 70\text{nm}$ in water. (J&C [98].)	28
Figure 3.4: (A) Error tolerance (TOL), and (B) ETASCA parameters dependence on extinction for a small gold nanosphere ($r = 15\text{nm}$, $d = 0.55\text{nm}$) in water. (J&C [98].)	30
Figure 3.5: Comparison between worst and best case scenarios for the tolerance and ETASCA parameters for a small gold nanosphere ($r = 15\text{nm}$) approximated with (A) 4224, and (B) 82712 dipoles in water. (J&C [98].)	30
Figure 3.6: Images of (A) sphere triangulation, and (B) the corresponding monolayer shell aggregate. (Core in red, and spheres (shell) in blue.)	34
Figure 3.7: Image of a complex NS, where 16 spheres arranged on the front face of the cube, as viewed from the (A) side (x - y plane), and (B) front (y - z plane). (Cube in black, and spheres in orange.)	34

Figure 3.8: Vectors and polar angles for target orientation [136].	36
Figure 3.9: Setup of a target NS (monolayer shell aggregate) for DDSCAT simulations.	36
Figure 4.1: Images of (A) a monolayer and (B) a bilayer shell aggregates (Spheres (shell) are in blue, core is in red and layer between nanospheres in green.) A quarter of the shape was removed in each case to better visualize the NSs.	40
Figure 4.2: Extinction efficiency spectra of (A) small and (B) large gold nanospheres having various radii, r .	41
Figure 4.3: (A) Section (x - y plane) of a uniform spherical aggregate having $R \approx 50\text{nm}$, $r = 8\text{nm}$, and (B) a 3-dimensional image of the same aggregate. (Spheres are in blue.)	42
Figure 4.4: Extinction efficiency spectra of uniform spherical aggregates having (A) a constant $R \approx 50\text{nm}$, and various small nanosphere radius, r , and (B) a constant $r \approx 5\text{nm}$, and various outer radii, R .	43
Figure 4.5: (A) Section (x - y plane) of an $R_c/R = 0.6$ nanoshell, and (B) a 3-dimensional image of the same nanoshell. (Metal shell is in blue and dielectric core in red.)	44
Figure 4.6: Extinction efficiency spectra of silica/gold – core/shell NPs having (A) a constant outer radius, $R = 50\text{nm}$, and various ratios, R_c/R , and (B) a constant ratio of $R_c/R = 0.5$, and various outer radii, R .	45
Figure 4.7: (A)-(B) Section (x - y plane) of a monolayer, and a bilayer shell aggregate, having shape parameters of $R \approx 70\text{nm}$, $r \approx 10\text{nm}$. (C)-(D) 3-dimensional images of the same shell aggregates.	46
Figure 4.8: Effect of the different value of r (input, and real) used in size-dependent, l_{eff} , modification for the monolayer shell aggregates having (A) $R \approx 30\text{nm}$, $d = 1\text{nm}$, and (B) $R \approx 50\text{nm}$, $d_s = 0\text{nm}$.	48
Figure 4.9: Normalized extinction efficiency spectra of monolayer shell aggregates having $R \approx 30\text{nm}$, for various nanosphere radii, r , and interdipole separations, d , of (A) $d = 1\text{nm}$, and (B) $d = 0.5\text{nm}$.	49
Figure 4.10: Normalized extinction efficiency spectra of monolayer shell aggregates having (A) $R \approx 50\text{nm}$, (B) $R \approx 70\text{nm}$, for various small nanosphere radii, r .	50
Figure 4.11: Normalized extinction efficiency spectra of densely-packed monolayer shell aggregates having (A) $R \approx 50\text{nm}$, (B) $R \approx 70\text{nm}$, and various small nanosphere radii, r .	51
Figure 4.12: Normalized extinction efficiency spectra of monolayer shell aggregates having $R \approx 30\text{nm}$, and various distances, d_s , for interdipole separation, d , of (A) $d = 1\text{nm}$, and (B) $d = 0.5\text{nm}$.	53
Figure 4.13: Normalized extinction efficiency spectra of monolayer shell aggregates having (A) $R \approx 50\text{nm}$, (B) densely-packed, $R \approx 70\text{nm}$, and various distances, d_s .	54
Figure 4.14: Comparison between outer radii, R , for monolayer shell aggregates having (A) $d_s = 0\text{nm}$, and (B) $d_s = 1\text{nm}$.	55

Figure 4.15: Comparison between different interdipole separations, d , for a monolayer shell aggregate having $R \approx 30\text{nm}$, and (A) $r = 8\text{nm}$, (B) $d_s = 0\text{nm}$	56
Figure 4.16: Comparison between normalized extinction efficiency spectra of monolayer shell aggregate with that of the corresponding classical NPs. The structures have dimensions of (A) $R \approx 30\text{nm}$ ($r = 8\text{nm}$, shell = 15nm ($R_c/R = 0.5$)), (B) $R \approx 50\text{nm}$ ($r = 12.5\text{nm}$, shell = 25nm ($R_c/R = 0.5$)), and (C) $R \approx 70\text{nm}$ ($r = 12.5\text{nm}$, shell = 25nm ($R_c/R \approx 0.64$)).....	57
Figure 4.17: Comparison spectra between monolayer and bilayer shell aggregates having dimensions of (A) $R \approx 30\text{nm}$, $r \approx 5\text{nm}$, $d = 1\text{nm}$, (B) $R \approx 30\text{nm}$, $r \approx 5\text{nm}$, $d = 0.5\text{nm}$, (C) $R \approx 50\text{nm}$, $r \approx 5\text{nm}$, (D) $R \approx 50\text{nm}$, $r \approx 8\text{nm}$, (E) $R \approx 70\text{nm}$, $d_s = 0\text{nm}$, and (F) $R \approx 70\text{nm}$, $d_s = 1\text{nm}$	59
Figure 4.18: Two orientations of the model of the pair of small gold nanospheres The small nanospheres were arranged (A) along, and (B) perpendicular to the propagation, x , axis.....	60
Figure 4.19: Extinction efficiency spectra of a single and a pair of gold nanospheres arranged along x axis, having various distances, d_s , between them	61
Figure 4.20: Extinction efficiency spectra of a pair of gold nanospheres arranged along y axis having, various distances, d_s , and interdipole separations, d , of (A) 1nm , and (B) 0.5nm	61
Figure 4.21: Polarization dependence of pair of nanospheres arranged along y axis having $d = 1\text{nm}$, and $d_s = 1\text{nm}$. Comparison with the normalized extinction efficiency spectrum of the monolayer shell aggregate (T6H)	63
Figure 4.22: Normalized efficiency spectra of various monolayer shell aggregates having (A) $R \approx 30\text{nm}$, $r = 8\text{nm}$, (T2C), (B) $R \approx 30\text{nm}$, $d_s = 0\text{nm}$, (T2B), (C) $R \approx 50\text{nm}$, $r = 13.4\text{nm}$, (T3E), (D) $R \approx 50\text{nm}$, $d_s = 1\text{nm}$, (T6A), (E) $R \approx 70\text{nm}$, $r = 8\text{nm}$, (T4B), and (F) $R \approx 70\text{nm}$, $d_s = 1\text{nm}$, (T6E).....	65
Figure 4.23: Normalized extinction efficiency spectra of monolayer shell aggregate ($R \approx 50\text{nm}$, $r \approx 5\text{nm}$, T3A) consisting of various (A) dielectric cores, and (B) core/external medium combinations. (J&C [98].)	66
Figure 4.24: Extinction efficiency spectra of monolayer shell aggregates having $R \approx 50\text{nm}$, $r \approx 5\text{nm}$ (T3A), and various metallic cores. (Palik [91].)	67
Figure 4.25: Comparison between extinction efficiency spectra for various core materials for the monolayer shell aggregates having (A) $R \approx 50\text{nm}$, $r \approx 5\text{nm}$, varied d_s , (B) $R \approx 50\text{nm}$, $d_s = 0\text{nm}$, and (C) $R \approx 50\text{nm}$, $d_s = 1\text{nm}$. (D) Extinction efficiency spectra of single nanospheres having $r = 50\text{nm}$. (J&C [98].).....	68
Figure 4.26: Refractive index dependence of monolayer shell aggregates having $R \approx 50\text{nm}$, $r \approx 5\text{nm}$ (T3A), and consisting of (A) gold, or (B) silver metal cores.....	69

Figure 4.27: Comparison spectra for gold and silver nanospheres for the monolayer shell aggregates having (A) $R \approx 50\text{nm}$, $r \approx 5\text{nm}$, varied ds , (B) $R \approx 50\text{nm}$, $ds = 0\text{nm}$, and (C) $R \approx 50\text{nm}$, $ds = 1\text{nm}$. The internal core was assumed to be water. (J&C [98].)	70
Figure 5.1: Dual-mode spectral characteristics, exhibiting distinct and separated absorption and scattering plasmon bands, located at red and NIR wavelengths, respectively.	73
Figure 5.2: Efficiency factors of (A) nanoshell with $R = 70\text{nm}$ and shell thickness 10nm ($R_c/R \approx 0.86$), and (B) nanorod with $r_{\text{eff}} = 21.86\text{nm}$ and aspect ratio (length/width) of 3.9. (J&C [98].)	74
Figure 5.3: Shapes and corresponding size parameters for simple NSs.	76
Figure 5.4: Efficiency factors of a gold nanocube with various edge lengths, b , of (A) 50nm , (B) 70nm , and (C) 100nm	82
Figure 5.5: Examples of three complex NSs. First the small spheres were arranged on the front face of cube, as viewed from the (A) side (x - y plane), and (B) front (z - y plane). Then the nanospheres were (C) arranged on the side (viewed from the front), and, finally (D) covering the nanocube (viewed from the front). (Cube in black, spheres in orange.) The incident wave propagation direction is along the x axis, while the polarization is along the y axis.	85
Figure 5.6: Efficiency factors of an Au nanocube combined with 16 Ag nanospheres having dimensions of (A) $b = 100\text{nm}$, $d_m = 25\text{nm}$, and (B) $b = 140\text{nm}$, $d_m = 35\text{nm}$	91
Figure 5.7: Efficiency factors of an Au nanocube combined with 16 Ag nanospheres arranged (A) on the back, and (B) on the side of the nanocube. (C) Extinction efficiency spectra showing the polarization dependence when the 16 Ag nanospheres were arranged on the side, perpendicular to the z axis.	93
Figure 5.8: Efficiency factors of an Au nanocube combined with 2 layers of 16 Ag nanospheres arranged (A) on the front and back, and (B) on opposite sides of the nanocube. (C) Extinction efficiency spectra showing the polarization dependence when the 16 Ag nanospheres were arranged on opposite sides, perpendicular to the z axis.	94
Figure 5.9: Efficiency factors of a nanocube combined with (A) 96 (30nm), and (B) 384 (15nm) Ag nanospheres. The small nanospheres cover all 6 nanocube facets.	95
Figure 5.10: Sections of two cubical nanoshell, which have a constant edge length, $b = 140\text{nm}$, and ratios, b_{core}/b , of (A) 0.57 , and (B) 0.86nm . (Core is in orange, and shell in black.) ...	96
Figure 5.11: Comparison between extinction efficiency spectra of spherical and cubical nanoshells of silica core and (A) gold, or (B) silver shell.	98
Figure 5.12: Comparison between extinction efficiency spectra of simple gold and silver nanocubes ($b = 140\text{nm}$) with cubical nanoshells, having (A) Au/Ag, and (B) Ag/Au, core/shell materials.	99

Figure 6.1: Image of a whole monolayer shell aggregate. (B) A quarter of the shell aggregate was removed for better visualization. (Gold nanospheres (shell) are in blue, and core material in red.).....	101
Figure 6.2: Charts showing the time scale and gold drops for each experimental procedure.	107
Figure 6.3: (A) Average water spectrum, (B) Measured absorbance, A , of a redispersed solution, and (C) Measured absorbance, A' with water spectrum subtracted.....	110
Figure 6.4: Comparison between measured and interpolated data for (A) the average water spectrum and (B) a redispersed solution spectrum.	111
Figure 6.5: (A) Absorbance of a redispersed solution, A'_{new} , and the corresponding (B) normalized spectrum, A'_{norm}	111
Figure 6.6: Comparison between the measured, A'_{norm} , with the fitted, A_{fit} , absorbances.	113
Figure 6.7: Step-by-step images of the experimental procedure for the formation of composite Au@PS NSs. (A) Initial solution, where PS and Na ₃ Citrate are added. (B) Bluish final solution, where gold is added. (C) Color changes as the synthesis was progressing with the addition of gold drops. (D) Different final solution colors after cooling at room temperature or on ice.	114
Figure 6.8: SEM image of a redispersed solution prepared using experiment 3.	115
Figure 6.9: Example of a (A) good fit (B3), and (B) a sub-optimal fit (F3) for experiment 3.	123
Figure 6.10: Nanoparticle–Nanostructure (NP–NS) contributions to each synthesized composite Au@PS NSs resulting from (A)–(B) experiment 1(a), (C)–(D) experiment 1(b), (E)–(F) experiment 2, and (G)–(H) experiment 3.	124
Figure 6.11: Composite Au@PS NSs synthesized in experiment 1, and cooled down at two different temperatures. The normalized fitting constants are given for the redispersed solutions of (A) day 2, (B) day 8, and (C) day 2 measured on day 8.....	126
Figure 6.12: Composite Au@PS NSs synthesized using two different total amounts of gold solution. The normalized fitting constants are given for the redispersed solutions of (A) day 2, (B) day 8, and (C) day 2 measured on day 8.	126
Figure 6.13: Composite Au@PS NSs synthesized in experiment 2. Two redispersed solutions were produced from the same final solution, with the same centrifugation parameters on the same day. The normalized fitting constants are given for the two redispersed solutions of (A) day 2, (B) day 8, and (C) day 2 measured on day 8.	128
Figure C.1: (A) Normalized extinction spectra of densely-packed bilayer shell aggregates having $R \approx 30\text{nm}$, $r \approx 5\text{nm}$, and various interdipole separations, d . (B) Normalized efficiency factors of bilayer shell aggregate with $R \approx 30\text{nm}$, $r \approx 5\text{nm}$, and $d = 1\text{nm}$ (C1A).	155
Figure C.2: (A) Normalized extinction spectra of densely-packed bilayer shell aggregates having $R \approx 50\text{nm}$, $d = 1\text{nm}$, and various radii, r . (B) Normalized efficiency factors of bilayer shell aggregate with $R \approx 50\text{nm}$ and $r = 8.2\text{nm}$ (C1E).	155

Figure C.3: Normalized extinction spectra of densely-packed bilayer shell aggregates having $R \approx 70\text{nm}$, $d = 1\text{nm}$, and various (A) radii, r , and (B) distances, ds .	156
Figure C.4: Normalized efficiency factors of bilayer shell aggregates having $R \approx 70\text{nm}$, (A) $r = 8.5\text{nm}$ (C3B), and (B) $r \approx 15\text{nm}$, $ds = 1\text{nm}$, and $dl = 0\text{nm}$ (C3D).	156
Figure D.1: Efficiency factors of nanoshells having (A) $R = 30\text{nm}$, shell = 15nm , ($R_c/R = 0.5$), (B) $R = 50\text{nm}$, shell = 30nm , ($R_c/R = 0.40$), (C) $R = 50\text{nm}$, shell = 10nm , ($R_c/R = 0.8$), and (D) $R = 70\text{nm}$, shell = 25nm , ($R_c/R \approx 0.64$).	157
Figure D.2: Efficiency factors of spherical aggregates having (A) $R \approx 30\text{nm}$, $r = 5\text{nm}$, (T1A), (B) $R \approx 50\text{nm}$, $r = 5\text{nm}$, (T1C), (C) $R \approx 50\text{nm}$, $r = 15\text{nm}$, (T1G), and (D) $R \approx 70\text{nm}$, $r = 12.5\text{nm}$, (T1I).	158
Figure D.3: Efficiency factors of monolayer shell aggregate ($R \approx 50\text{nm}$, $r = 12.5\text{nm}$ and $ds = 1\text{nm}$) of (A) gold/gold, (B) silver/gold, and (C) water/silver – core/spheres.	158
Figure F.1: Various other arrangements of small, 30nm , nanospheres. (A) 16 single nanospheres (no cube), arranged perpendicular to x axis, (B) 16 nanospheres arranged behind cube, (C) 16 nanospheres arranged on the side, and (D) 2 layers of 16 nanospheres arranged on opposite sides. All viewed from the front (y - z plane). Incident light propagation is along x axis, and polarization is along y or z axis. (Cube in black, spheres in orange.)	172
Figure F.2: Complex shapes of a nanocube covered with (A) 96 (30nm), and (B) 384 (15nm) small nanospheres. Both viewed from the front (y - z plane). Incident light propagation is along x axis, and polarization is along y or z axis. (Cube in black, spheres in orange.)	172
Figure G.1: Efficiency factors of a nanocube combined with 16 Au nanospheres having dimensions of (A) $b = 100\text{nm}$, $dm = 25\text{nm}$, and (B) $b = 140\text{nm}$, $dm = 35\text{nm}$.	173
Figure G.2: Efficiency factors of a nanocube combined with 16 Au nanospheres arranged (A) on the back, and (B) on the side of the nanocube. (C) Extinction efficiency spectra showing the polarization dependence when the 16 Au nanospheres were arranged on the side, perpendicular to the z axis.	173
Figure G.3: Efficiency factors of an Au nanocube combined with 2 layers of 16 Au nanospheres arranged (A) on the front and back, and (B) on opposite sides of the nanocube. (C) Extinction efficiency spectra showing the polarization dependence when the 16 Au nanospheres were arranged on opposite sides, perpendicular to the z axis.	174
Figure G.4: Efficiency factors of a nanocube combined with (A) 96 (30nm), and (B) 384 (15nm) Au nanospheres. The nanospheres cover all 6 nanocube facets.	174

List of Tables

Table 2.1: Values of the various parameters for surface damping modification.....	20
Table 4.1: Spherical aggregates having various R , r , and d_s dimensions.....	42
Table 4.2: Monolayer shell aggregates having $R \approx 30\text{nm}$, and variable r , and d	48
Table 4.3: Monolayer shell aggregates having $R \approx 50\text{nm}$, and variable r	49
Table 4.4: Monolayer shell aggregates having $R \approx 70\text{nm}$, and variable r	50
Table 4.5: Monolayer shell aggregates having $R \approx 30\text{nm}$, $r \approx 7.5\text{nm}$, and variable d , and d_s	52
Table 4.6: Monolayer shell aggregates having (i) $R \approx 50\text{nm}$, $r \approx 15\text{nm}$, (ii) densely-packed, $R \approx 70\text{nm}$, $r \approx 12.5\text{nm}$, and various d_s	53
Table 4.7: Wavelength specific extinction values for various monolayer shell aggregates	55
Table 5.1: Optical constants, n and k , for the four metals, at three wavelengths, in water	76
Table 5.2: Efficiency factors of various simple metal NSs having a constant size parameter of 120nm	79
Table 5.3: Ratios of absorption to scattering efficiencies (and vice versa) for various metal nanocubes having $b = 120\text{nm}$, for the two wavelengths of interest	81
Table 5.4: Ratios of absorption to scattering efficiencies (and vice versa) for the three gold nanostructures having a size parameter of 120nm, for the two wavelengths of interest	81
Table 5.5: Ratios of absorption to scattering efficiencies (and vice versa) for a gold nanocube having various edge lengths, b , for the two wavelengths of interest	83
Table 5.6: Efficiency factors of small nanospheres having various diameters, d_m	84
Table 5.7: Efficiency factors of complex NSs having various numbers (sizes) of small gold and silver nanospheres	87
Table 5.8: Ratios of absorption to scattering efficiencies (and vice versa) for the two wavelengths of interest for the various complex NSs.....	88
Table 5.9: Comparison spectra between individual and combined NSs	89
Table 5.10: Efficiency factors of cubical nanoshells with silica, SiO_2 , core and metal shell, for two ratios, b_{core}/b	97
Table 5.11: Efficiency factors of cubical nanoshells with metal core for two ratios, b_{core}/b	99
Table 6.1: Experiment 1(a): Gold-polystyrene solution (8.25mL HAuCl_4 + 0.35mL PS) cooled at room temp (25°C), then stored at 4°C	118
Table 6.2: Experiment 1(b): Gold-polystyrene solution (8.25mL HAuCl_4 + 0.35mL PS), cooled on ice (0°C), then stored at 4°C	119
Table 6.3: Experiment 2: Gold-polystyrene solution (8.5mL HAuCl_4 + 0.35mL PS) cooled on ice (0°C), then stored at 4°C	120

Table 6.4: Experiment 3: Gold-polystyrene solution (10mL H _{Au} Cl ₄ + 0.35mL PS) cooled on ice (0°C), then stored at 4°C	121
Table 6.5: Normalized fitting constants, a'_f , for the various fitted absorbances	122
Table C.1: Shape parameters of bilayer shell aggregates ($R \approx 30, 50\text{nm}$) with various small nanosphere radii, r , edge-to-edge distances, d_s , and $d_l = 0\text{nm}$ ($R_{\text{inner}} = R_{\text{real}} - 2r_{\text{inner}} - d_l$)	154
Table C.2: Extinction peak characteristics and number of dipoles for bilayer shell aggregates with $R \approx 30\text{nm}$, and $R \approx 50\text{nm}$	154
Table C.3: Shape parameters of bilayer shell aggregates ($R \approx 70\text{nm}$) with various small nanosphere radii, r , and edge-to-edge distances, d_s ($R_{\text{inner}} = R_{\text{real}} - 2r_{\text{inner}} - d_l$)	155
Table C.4: Extinction peak characteristics and number of dipoles for bilayer shell aggregates with $R \approx 70\text{nm}$	156
Table E.1: Gold (Au) Nanostructures.....	159
Table E.2: Silver (Ag) Nanostructures	161
Table E.3: Aluminum (Al) Nanostructures	164
Table E.4: Nickel (Ni) Nanostructures	166
Table E.5: Comparison between extinction efficiency spectra for various nanostructure sizes, shapes, and materials	169
Table I.1: Rayleigh coefficients and other constants for fitting equation.....	176
Table I.2: Unnormalized fitting constants, a_f , for calculating new absorbances, A_{fit}	177

List of Symbols and Abbreviations

(In Alphabetic Order)

Symbols

a_f	fitting constants, for comparison
A_{ij}	dipole-dipole interaction matrix
A	absorbance
A, B, C	fitting constants, for universal ruler
b	edge length of a nanocube
b_{core}	edge length of core material in cubical nanoshells
c	speed of light in vacuum
C	dimensionless parameter, for size-dependent effects
$C_{\text{ext, abs, sca}}$	extinction, absorption, and scattering cross sections
d	interdipole separation, or lattice spacing
dl	space between two nanosphere layers
dm	nanosphere diameter
ds	edge-to-edge distance between nanospheres
e	electron charge
E	energy
E_0	amplitude of incident electric field
E_{inc}	incident electric field
E_F	Fermi energy
g	earth gravitational acceleration
h	Planck constant
\hbar	reduced Planck constant
i	i^{th} dipole
I	intensity
I_0	initial intensity
\mathbf{k}	wave vector
k	wavenumber
k	imaginary part of refractive index
l_∞	electron mean free path in bulk material
l_{eff}	effective electron mean free path
L	characteristic size of nanoparticle, for universal plasmon ruler
L	optical path length
m	atomic mass
m	complex refractive index
m_{eff}	electron effective mass
M	molarity
MM	molar mass

n	amount of atoms in moles
n	real part of refractive index
n_e	free electron density
n_{sph}	number (#) of spheres
N	number of dipoles
N	number of particles per unit volume
N_x, N_y, N_z	number of dipoles in x , y , or z axis
N_{sph}	number of nanosphere dipoles
P	polarization
$Q_{\text{avg}(y,z)}$	averaged efficiency over (y,z) polarizations (same value as Q_{ext})
$Q_{\text{ext, abs, sca}}$	extinction, absorption, and scattering efficiency factors
Q_{max}	efficiency at plasmon maximum
$Q_{\text{polar.}(y \text{ or } z)}$	efficiency at polarization y , or z
r	nanosphere radius
r_{eff}	effective radius
r_{real}	real value of radius
R	outer radius
R_c	core radius
$R_{c1, c2}$	radius of the outer, and inner layer
R_{real}	real value of outer radius
s	tetrahedron side length
S	particle surface area
T	transmittance
V	volume of a particle or mixture
$W_{\text{abs,sca}}$	rate at which intensity is absorbed or scattered by the particle
w/v	weight per volume
x	size parameter for DDA
y	absorbance or extinction values, for data manipulation

Greek Alphabet Symbols

α, β	Rayleigh coefficients
α_i	polarizability of i^{th} dipole
Γ	damping factor
Γ_∞	damping constant
$\Delta\lambda$	shift of the plasmon wavelength maximum
ε_0	dielectric permittivity in vacuum
$\varepsilon, \varepsilon_1, \varepsilon_2$	dielectric function, real, and imaginary part
θ_s	scattering angle
λ	wavelength of incident light
λ_0	single-nanosphere plasmon wavelength maximum
λ_{max}	wavelength maximum
τ	electron relaxation time
v_F	Fermi velocity
ω	angular frequency
ω_p	plasmon frequency

Symbols of Materials

Ag	silver
Al	aluminum
Au	gold
Cu	copper
HAuCl ₄	chloroauric acid
Na ₃ Citrate	trisodium citrate
Ni	nickel
PS	polystyrene sphere
SiO ₂	silicon dioxide or silica

Units and Numbers

eV	electronvolt, a unit of energy
g	gram
i	complex number, $i = (-1)^{1/2}$
J	joule
mg	milligram
min	minute
μm	micrometer ($\times 10^{-6}$ m)
nm	nanometer ($\times 10^{-9}$ m)
π	the number pi = 3.1416
s	second

Abbreviations

A.U.	absorbance units
Abs	absorption
ABS	absolute value of a number
cube	cubical
DDA	discrete dipole approximation
Ext	extinction
FDTD	finite-difference time-domain
FFT	fast Fourier transform
IR	infrared
J&C	Johnson and Christy
MAX (or max)	maximum
MIN (or min)	minimum
NIR	near-infrared
NP(s)	nanoparticle(s)
NS(s)	nanostructure(s)
OCT	optical coherence tomography
PAI	photoacoustic imaging
rcf	relative centrifugal force
rpm	revolutions per minute
Sca	Scattering
SEM	scanning electron microscope
SERS	surface-enhanced Raman spectroscopy
sph	spherical
SPR(s)	surface plasmon resonance(s)
temp	temperature
UV	ultraviolet
vis	visible

1. Introduction

1.1 Metal Nanoparticles

Metal nanoparticles (NPs) are in the centre of an intense research interest, due to their unique optical properties. Their nanoscale dimensions result markedly in different physical and chemical properties compared to their bulk counterparts. A wide number of new phenomena arise, including discrete spectra of the electronic states, coherent motion of conducting electrons, and higher surface to volume ratios. The optical properties of metal NPs are mainly determined by this coherent electron motion, called the surface plasmon resonance (SPR).

When an electromagnetic wave, incident on the metal nanoparticle (NP) surface, interacts with its conducting electrons induces excitations and oscillations of these electrons. When the frequency of the incident light wave coincides with an oscillation frequency of the electrons, a collective, coherent, oscillation is observed which is called surface plasmon resonance (SPR). The SPR depends on the material, the size, and shape of the metal NP, the dielectric properties of the surrounding medium and coupling interactions between adjacent NPs. The various combinations of these parameters allow for a broad tunability of the NPs optical properties [1-4]. By varying the parameters, the SPR can be tuned from the ultraviolet-visible (UV-vis) to the near-infrared (NIR) wavelength range. The plasmon excitations produce strong effects in both the near- and far-field responses of metal NPs. The far-field effect relates to the absorption and scattering effects and the near-field effect relates to the local field enhancement generated around the NP surface [5, 6].

1.1.1 A historical overview

NPs of noble metals, such as gold and silver, exhibit strong absorption in the visible region of the wavelength spectrum with rich colors varying from yellowish for silver [7, 8] to red for gold spherical NPs [9, 10]. The bright colors of noble metal NPs have historically attracted considerable interest as decorative pigments in stained glasses and artworks [3, 11]. A most famous example is the Lycurgus cup (4th century A.D.) illustrated in Fig. 1.1(A,B). This extraordinary cup, which has silver and gold NPs embedded in its glass, is an example of a very special type of glass, known as dichroic glass, that changes color when held up to the light. In the 16th century, the darkening of silver compounds by light

was already known. Industrial manufacturing of stained glass with colloidal particles was established in the 17th century. Of course, the glass stainers had no idea, at the time, that they were producing gold NPs, or that plasmon resonances were responsible for the red colors produced. In the mid-19th century, silver halide photochemistry for photography was successfully applied. An outline of the historic background of NPs use can be found in the literature [12, 13].



Figure 1.1: Photographs of the famous Lycurgus Cup which displays a different color depending on whether it is illuminated (A) externally, or (B) internally. For details, consult website of the British Museum [14], and Freestone et al. [15].

The history of biomedical NP use is dated back to ancient times. Soluble gold appeared around the 5th or 4th century B.C. in Egypt and China. In antiquity, materials were used for both aesthetic and curative purposes. The first book on the colloidal gold was published by the philosopher and medical doctor Francisci Antonii in 1618. It includes information on the formation of colloidal gold sols and their medical uses. In 1676, the German chemist Johann Kunckels published another book, whose chapter 7 considered “drinkable gold that contains that exert curative properties for several diseases”. Later, there were various attempts to explain the “drinkable” gold properties [11, 13].

In 1857, in a well-known publication, Michael Faraday [10] postulated that the color of ruby glass, as well as the aqueous solutions of gold, is due to finely divided gold particles. However, Faraday did not offer a rigorous theoretical basis; he based his postulate on an intuitive understanding of highly reflective metals and the scattering process. Around the same time, James Clerk Maxwell developed the theory of light as an electromagnetic wave. In 1904, Maxwell-Garnett attempted a quantitative theoretical description of the colors of nanoscopic metal particles. However, the issue of particle size was not addressed in the theory. In 1908, Gustav Mie [16] presented the first rigorous theoretical treatment of the optical properties of spherical metal NPs. His solutions to

Maxwell's equations showed resonant structures in the scattering spectra, which now are referred to as plasmon resonances. However, the term "plasmon" was coined in the 1950s by David Pines to describe high frequency collective oscillations in metals. The discovery of the surface-enhanced Raman scattering effect (SERS) sparked a renewed interest in metal NP optics and physics. It was soon recognized that the SERS effect is due to strongly enhanced local electromagnetic fields produced by excitation of plasmon resonances in rough metal films [12, 17].

New experimental and theoretical numerical toolboxes have been developed since. Simulation techniques for modeling the optical response of complex nanostructures (NSs) have been greatly expanded, providing a detailed, quantitative understanding of these systems. Also, lithographic and chemical methods allow the routine production of a wide variety of complex NPs and assemblies. Finally, characterization methods have advanced greatly in the last two decades, so that the optical and physical properties of metal NPs can be effectively probed [12].

1.1.2 Nanoparticles and applications

Nowadays, a wide variety of publications covers metal NP synthesis and applications. The rapid development of technologies for metal NP synthesis and evaluation has provided wide possibilities for researchers, developing colloidal NPs [18-20], aggregates [21-23], nanoshells [24-26], nanorods [27-29], nanocubes [30, 31], and tetrahedra [32, 33], and finally more exotic structures such as nanocages [34, 35], nanostars [36, 37], nanorice [38, 39], nanodumbbells [40, 41], and nanopyramids [42, 43]. NPs exhibiting hollow interiors such as nanoshells [44-46], nanoboxes [47, 48], and nanoframes [49, 50] were also reported.

The fascinating optical properties of metal NPs led to important biomedical applications in a number of areas including sensing, spectroscopy, imaging, and therapy [3, 51-53]. Metal NPs have great potential as chemical and biological sensors, due to their sensitive optical response (absorption and scattering) to changes in the refractive index of the surrounding environment [54-57]. Metal NPs especially gold and silver, can serve as spectroscopic probes, for example in surface-enhanced Raman spectroscopy (SERS) [58-60], due to their intense local electric fields resulting from the SPR, which can lead to strong enhancement of the spectroscopic signal from molecules in the vicinity of the NPs.

In addition, metal NPs, due to their strong absorption and scattering optical responses, have the potential to be used as contrast agents in imaging and therapy applications, including optical coherence tomography (OCT) [61-63], photoacoustic or

optoacoustic tomography [64-66], and photothermal therapy [67-69]. In the new field of theranostics, whose name is derived from the combination of therapeutics and diagnostics, the use of metal NPs for combined imaging and therapy applications is being explored [70-72].

1.2 Research Motivation

In this dissertation, we will investigate two novel metal NSs, the so-called “shell aggregate”, and “dual-mode” nanostructure (NS). These novel NSs will provide NIR plasmon resonances, and distinct and separated absorption and scattering plasmon bands, both significant in spectroscopy, imaging, therapy and even theranostic applications.

Optical imaging and spectroscopic applications can significantly benefit from using NIR light. Biomolecules, such as hemoglobin, and water, absorb visible and far infrared light, respectively, while they have the lowest absorption coefficients in the NIR region around 650-900nm. This “optical window” is optimal for imaging since it offers maximal light penetration into the sample under examination [73-75]. In contrast, for therapy applications, a rapid and high photothermal conversion of the absorbed light radiation is required, for the selective heating and destruction of malignant cells [3, 51]. In surface-enhanced Raman spectroscopy (SERS) applications, the usually weak Raman signal is intensely amplified with the aid of metal NPs, and the spectroscopic process becomes more efficient and sensitive. Noble metals, especially gold, are commonly used in SERS [76, 77]. Due to their chemical properties and nontoxicity, gold NPs have been extensively explored for biomedical applications as well.

Several types were investigated so far, such as nanoshells [78] and nanorods [79], each of them with its advantages and limitations. Even though these two NPs exhibit good tunability of their SPR wavelength ranging from the visible to the NIR, the nanoshells are rather large NPs for NIR excitation, and when entering the cell they remain localized into vesicles, thus limiting their sensing capabilities. On the other, nanorods have the disadvantage of their shape, which limits their probability of entering the cells and also due to their fabrication method they need to be modified to avoid cell toxicity.

A novel gold NS, the “shell aggregate”, which consist of small gold nanospheres aggregated around a dielectric core creating a monolayer or a bilayer shell, should exhibit (i) a shift of the plasmon resonance peak towards the more biologically desirable NIR range, and (ii) enhanced intersphere coupling interactions due to close distance between neighboring nanospheres. In addition, the “shell aggregate” addressed another important biological challenge, that of intracellular imaging and spectroscopy. In theory, the small

nanospheres could more easily enter the cell, distribute into the cytoplasm, and then aggregate around a vesicle to create a larger overall NS which would provide an efficient SERS signal as well as NIR plasmon resonances.

Another novel metal NS, the “dual-mode” NS, it is design to exhibit distinct and separated absorption and scattering plasmon bands both ranging in the biologically desirable NIR wavelengths. Ideally, the absorption plasmon band should be located at $\lambda \approx 635\text{nm}$, while the scattering plasmon band at $\lambda \approx 785\text{nm}$. This new metal NS has the potential for combined imaging and therapy, or more specific in theranostics. The various metal NSs reported so far, have either absorption, or scattering or overlapping plasmon bands, since absorption and scattering are competing process. None of them have distinct and separated absorption and scattering plasmon bands. Therefore, when used in imaging there will be loses due to absorption, and when used in therapy there will be loses due to scattering. The “dual-mode” NS would exhibit the most intense scattering with minimal absorption, in the NIR for imaging and the opposite in the red, for therapy. This could be beneficial for theranostics since the laser wavelengths used for each application can be at distinct wavelengths for increased efficacy and safety.

These novel metal NSs aim to be powerful tools in imaging (e.g., photoacoustic imaging (PAI) and optical coherence tomography (OCT)), in spectroscopy (e.g., surface-enhanced Raman spectroscopy (SERS)), and therapy applications (e.g., photothermal therapy), since they offer combined properties and additional advantages compare to various known metal NPs. Each of the new metal NPs can have a different and significant role in the field of sensing, spectroscopy, imaging, and therapy, and even theranostics. The novel shell aggregate can provide an early stage prognosis of a disease, such as cancer, and the dual-mode NS can both image and control the therapy of a potential treatment.

1.3 Dissertation Objectives

The main research objectives of this work are summarized as follows:

- Explore the theory of SPR and its dependence on the various parameters such as size, shape, and material of NPs, and the surrounding medium.
- Study the Drude “free” electron model and the surface damping modification of the size-dependent dielectric function.
- Explore the discrete dipole approximation (DDA) method used for the simulations.
- Investigate the optical properties and potential SERS and PAI applications of the novel monolayer/bilayer shell aggregates

- Study the dependence on the small nanosphere radius (r), the outer radius (R), the edge to edge distance between small nanospheres (d_s), and finally the material of small nanospheres, core, and surrounding medium.
- Compare the monolayer shell aggregates with classical gold NPs, such as nanospheres, aggregates, and nanoshells.
- Compare the monolayer with the bilayer shell aggregates.
- Design of a dual-mode NS for combined imaging and therapy applications
 - Explore the optical properties of simple metal NSs, by varying the shape, size and material.
 - Investigate more complex metal NSs, such as by combining a scattering NS with absorption NPs.
 - Study the cubical nanoshells, which have a cubical shape and consist of a dielectric or metal core and a gold or silver shell, and its potential applications in OCT and SERS.
- Synthesize and experimentally verify the monolayer shell aggregates
 - Find simple methods for small nanosphere formation on a dielectric core.
 - Explore the experimental procedure. Perform the experiments to study various parameters dependence, such as the time of reaction, cooling temperature, total amount of gold, and reproducibility.
 - Image the synthesized monolayer shell aggregates.
 - Verify monolayer shell aggregates through comparison between measurements and curve-fitting results.

1.4 Dissertation Organization

The dissertation is divided and organized into seven chapters.

Chapter 1 is the introduction chapter, which includes a general description and a historical overview of metal NPs. It also introduces the motivation, and objectives of this dissertation.

Chapter 2 presents the metal NP theory. It begins with a description of the surface plasmon resonance (SPR) phenomenon and its dependence on the NP size, shape, material, and surrounding medium. Then the dielectric properties characterizing the metal NPs are described. The most common tabulated data sets for the optical constants used for the various simulations are explored. The Drude “free” electron model, contribution of

interband transitions, and size dependent dielectric function, modified to include the surface damping effects are described as well.

Chapter 3 explains the discrete dipole approximation (DDA) method used to calculate the optical responses of the novel metal NPs. The DDA applicability is explored, as well as the criteria that must be satisfied. A detailed description of the DDSCAT software implementation follows, where the various techniques and parameters are described.

Chapter 4 describes the extensive study of the novel gold monolayer and bilayer shell aggregates by using simulations. The optical properties were explored by varying the parameters of overall size (R), the small gold nanosphere radius (r) and the edge-to-edge distance between the nanospheres (ds). Also, this chapter explains the potential use of these NSs as photoacoustic imaging (PAI) agents and as surface-enhanced Raman spectroscopy (SERS) probes. The optical properties of classical gold NPs, such as single, pair, and aggregate nanospheres, and nanoshells, are given as well for comparison.

Chapter 5 initially presents the optical properties of various simple metal NSs. Nanospheres, nanocubes and tetrahedra of various sizes, made of gold, silver, aluminum and nickel NPs are investigated and discussed. Then, more complex metal NSs are presented. The complex NSs are examined in order to obtain the characteristic property of distinct and separated absorption and scattering plasmon bands. Variations in parameters such as number (diameter), material and positioning of small nanospheres are explored. Cubical nanoshells are investigated as well and compared with the simple nanocubes and classical nanoshells.

Chapter 6 describes the synthesis method and procedures used for the experimental design gold monolayer shell aggregates. Images of the color variation of the solution and synthesized structures are given as well. Data analysis and comparison between the measured and calculated absorbances, in order to extract information regarding the structure of the synthesized gold NPs, are also included.

Finally, **Chapter 7** presents some concluding remarks and potential future work.

1.5 List of Publications out of Dissertation

Journal Articles

- M. Angelidou and C. Pitris, “Investigation of shell aggregate gold nanostructures,” *International Journal of Nanotechnology*, vol. 8, nos. 6/7, pp. 507-522, 2011.
- M. Angelidou and C. Pitris, “Investigation of nanostructures with distinctly separated absorption and scattering spectra for theranostic applications” (to be submitted).
- M. Anelidou and C. Pitris, “ Monolayer shell aggregates: design, synthesis and experimental verification” (to be submitted).

Conference Proceedings

- M. Angelidou and C. Pitris, “Plasmon resonances of novel monolayer and bilayer shell aggregate gold nanostructures,” *SPIE Conference Proceedings*, vol. 8089, pp. 8089071-8089077, 2011.
- M. Angelidou and C. Pitris, “Novel monolayer and bilayer shell aggregate gold nanostructures,” *SPIE Conference Proceedings*, vol. 7911, pp. 7911141-7911146, 2011.
- M. Angelidou and C. Pitris, “Investigation of nanostructure scattering and absorption for combined diagnostic and therapeutic applications,” *SPIE Conference Proceedings*, vol. 8231, 8231081-8231087, 2012.
- M. Angelidou and C. Pitris, “Design of a new nanostructure for theranostic applications,” in *BioInformatics and BioEngineering (BIBE), 2012 IEEE 12th International Conference on*, pp. 240-244, 2012.

2. Theory

Nanotechnology refers to structures of a nanometer scale, ranging from 1 to 100nm, incorporating a collection of atoms, whose properties are neither those of individual atoms nor those of the bulk [9]. Metal nanoparticles (NPs) can be thought as an aggregate composed of a number of atoms, starting with clusters consisting of a few atoms to large particles with more than 10^5 atoms. Therefore, metal NPs can be considered as mesoscopic objects which scale between the microscopic and macroscopic worlds. At this scale new phenomena occur including discrete spectra of the electronic states and coherent oscillation of electrons as far as electron can propagate through the whole system without experiencing inelastic or phase-breaking (dephasing) scattering [1]. The optical properties of metal NPs are mainly determined by this coherent electron oscillation, called surface plasmon resonance (SPR), which is not seen in bulk materials. In this chapter, the SPR and dielectric properties of noble metals, such as gold and silver, are mostly considered.

2.1 Surface Plasmon Resonance (SPR)

The phenomenon of surface plasmon resonance (SPR) arises from the interaction of the metal nanoparticle (NP) “free” electrons with an incident electromagnetic radiation. However, an exact and general description of the SPR, and its dependence on various parameters, has not yet been formulated. The SPR theory mostly arises from theoretical analysis and experimental observations of the optical response of various metal NPs.

Briefly, an electromagnetic light wave, incident on a metal NP surface, interacts with the conducting, free, electrons of the metal NP. The electric field of the wave excites and displaces the cloud of conducting electrons from its equilibrium position, thus creating induced surface polarization charges that act as a restoring force (Fig. 2.1(A)). When the frequency of the incident light wave coincides with an oscillation frequency of the conducting, free, electrons, it induces a collective, coherent oscillation of the electronic cloud, giving rise to different surface charge distributions also called surface plasmon resonances (SPRs). These collective excitations of the conducting electrons are called “plasmons”. Depending on the size of the NP, and the surface charge distribution, various modes, such as dipole and quadrupole, can be observed at the NP surface. The dipole-like mode, with negative charge accumulating on one side of the particle and positive charge accumulating on the opposite side, as also shown in Fig. 2.1(B). The quadrupole and

octupole charge distributions are shown as well. The higher multipole modes are always located at shorter wavelengths with respect to the dipolar ones [1, 4, 53, 80, 81]. For NPs, these surface modes are localized and have to “fit” on the circumference of the nanospheres or more general of the nanostructures (NSs) [57, 82].

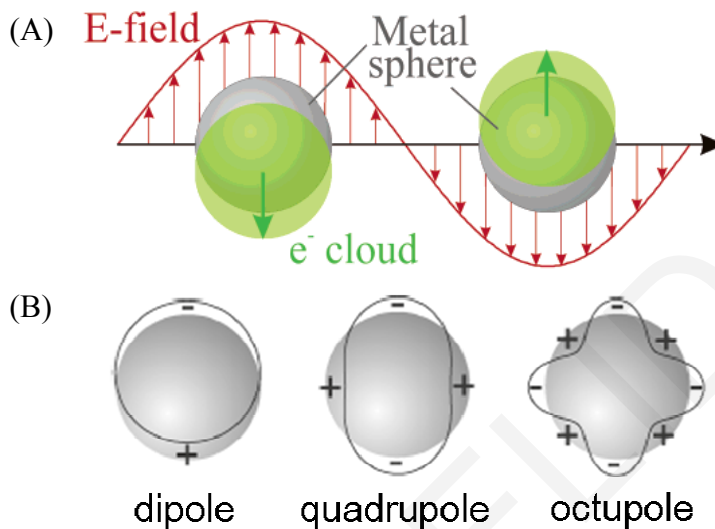


Figure 2.1: (A) Schematic representation of a dipole plasmon oscillation for metal nanospheres, showing the displacement of the electron cloud relative to the nuclei [2], (B) Dipole, quadrupole, and octupole modes in a sphere [82].

The SPR oscillation is exposed to a number of processes that damp the collective, coherent motion of the conducting electrons. This results in “dephasing” of the oscillation that ultimately decays the plasmon resonance. Damping can occur either through radiative or nonradiative processes. The surface charges generated by the incident wave and metal NP interaction, can convert part of the electromagnetic energy into thermal energy (an absorption process) and/or reradiate the energy at any direction, due to electron acceleration (a scattering process). The sum of both effects is called the light extinction, with the extinction peak occurring at the resonant wavelength of the plasmon. [79, 80, 83]. Absorption and scattering are far-field optical effects [5, 6, 84]. Nonradiative damping occurs when the plasmon excites intraband or interband electronic transitions, or through electron scattering at the surface of the NS [83, 85].

At the boundary of the dielectric surrounding medium and the particle surface, a strong local electric field enhancement occurs, due to the surface plasmon oscillations. The enhancement is confined at the particle surface and decays exponentially over a distance comparable to the NP size. The strong field enhancement appears at high curvatures and between dimers of various NPs. This near-field property of metal NPs affects the

surroundings of the particle within a distance smaller than or of the order of the light wavelength. Thus, exists only between particles placed in close proximity (such as densely-packed arrays) or between NPs and immediately adjacent molecules, which is useful in sensing applications [5, 6, 86, 87].

The SPRs (number, frequency or wavelength maximum, intensity, and width) depend on the material, size and shape of the NP, the dielectric properties of the surrounding medium [2, 85, 88, 89], and on interparticle (or particle-particle) coupling interactions [23, 86, 90]. Varying these parameters allows for a very broad tunability of the NP optical properties. For noble metals, such as silver and gold, the SPRs are in the visible wavelength range [3]. Figures 2.2(A)–(D) illustrate some of the effects of size, shape, material and surrounding or external medium on the SPRs. They show the extinction spectra which reflect the plasmon resonances, since the attenuation of the incident electromagnetic wave is a result of SPR-induced absorption and scattering.

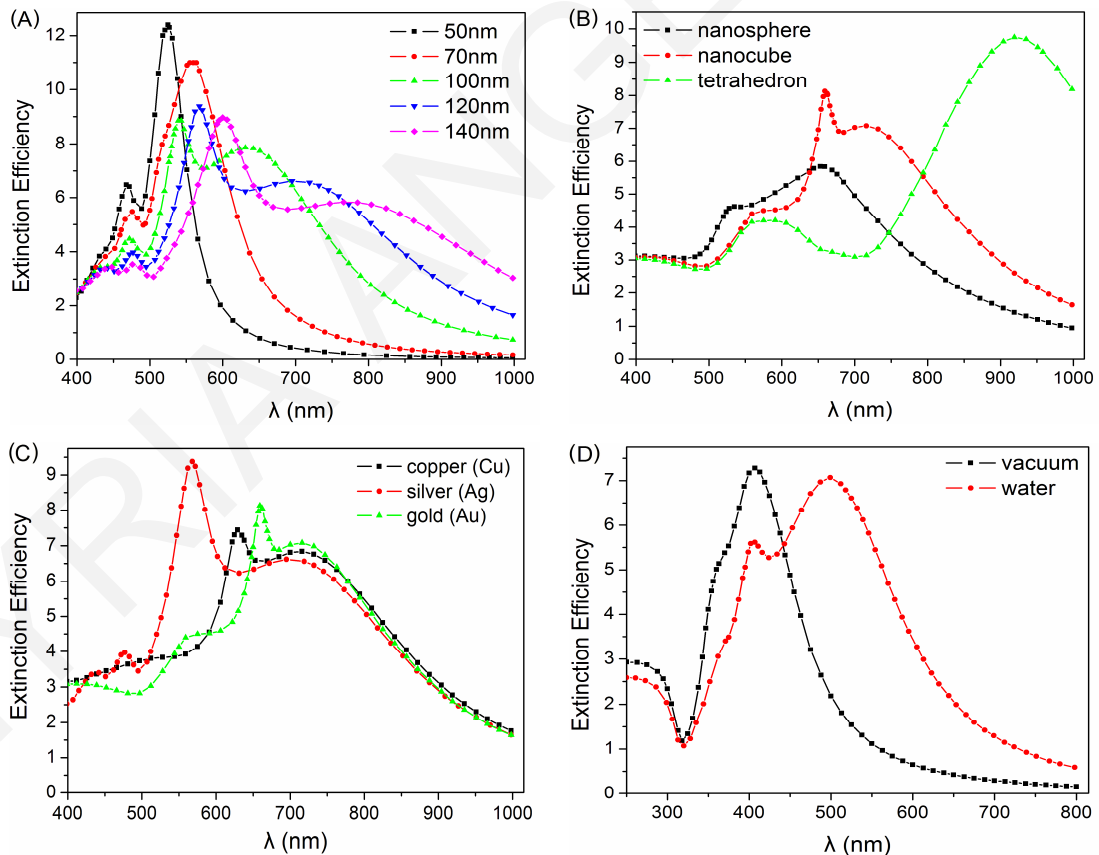


Figure 2.2: SPR dependence on (A) size (silver, nanocube (edge length, b)), (B) shape (gold, $r_{\text{eff}} = 74.4$ nm), (C) material (nanocube, $b = 120$ nm), and (D) external medium (silver, nanosphere, $r = 50$ nm). Material properties obtained from the tabulated data of Palik [91]. (A)–(C) assumed water as the external medium.

Figure 2.2(A) shows the spectra of silver nanocubes of various sizes. For a small nanocube (50nm), more than one peak exist in the spectrum, which correspond to dipole modes. Fuchs [92] demonstrated that a nanocube can exhibit six significant strong dipole modes, because the cubical shape has several distinct symmetries for dipole plasmon resonance compared with only one for the nanosphere [7, 93]. As the size of the nanocube increased, the first, long-wavelength peak, at $\lambda = 525\text{nm}$, shifted to longer wavelengths, with the width broadened, and decreased amplitude due to phase retardation effects. The second, short-wavelength, dipole mode, at $\lambda = 469\text{nm}$, remains at the same wavelength, with slightly decreased amplitude. This behavior of dipole mode broadening with decreasing amplitude, applies to larger NPs in general, and is referred to as an extrinsic size-effect [85]. Another observation is that a third peak, emerges between the two long- and short-wavelength dipoles, which corresponds to the quadrupole mode, and as the size is increased even more, the quadrupole slightly red-shifts and becomes more intense compared to the long-wavelength dipole mode. Similar findings were also reported, and explained by other researchers [94].

Figure 2.2(B) shows the spectra of three simple gold NSs (sphere, cube, and tetrahedron) which all have equal volumes for comparison. By changing the spherical shape of the particle to a nonspherical structure, the dipole resonance peak increased and shifted to longer wavelengths, with the simultaneous emergence of a quadrupole peak. The more non-spherical is the nanostructure (NS), the larger is the red-shifting. For NPs having sharp corners and tips, the distribution of the induced surface charges is strongly inhomogeneous, hence the strongest field enhancements are generated at the corners and tips [95]. The dissociation of the surface charges into corners increases the charge separation, thereby reduces the restoring force on the electron oscillation. The weak restoring force manifests itself in a red-shift of the plasmon resonance. The weaker the force, the more red-shifting is observed [7].

Figure 2.2(C) shows the spectra of nanocubes of same size made of different materials (copper, silver, and gold). At the visible wavelength range, the three noble metals have a different optical response to the incident light, with silver exhibiting the most intense and blue-shifted quadrupole plasmon peak, while gold has the most red-shifted. At wavelengths above 700nm, the position (and intensity) of the dipole peak is almost identical, due to similar dielectric functions of the noble metals at wavelengths above 700nm, giving rise to nearly identical optical responses [82].

Figure 2.2(D) shows the spectra of a silver nanosphere embedded in two different nonabsorbing, homogeneous media (vacuum/air, $m_{\text{med}} = 1.00 + i0$, and water, $m_{\text{med}} = 1.33 +$

i0). The plasmon resonance peaks are shifted when the dielectric properties of the surrounding media are altered. The plasmon resonance peaks in a medium with refractive index $n_{\text{med}} > 1$ are red-shifted with respect to those in vacuum. Furthermore, this shift depends on the proper mode itself, that is the larger the wavelength, the greater the red-shifting, and the more spread out of the peaks [53, 80].

2.2 Dielectric Function or Refractive Index

The linear optical response of a metal NP to an applied electric field is characterized by a dielectric function, $\varepsilon = \varepsilon_1 + i\varepsilon_2$, or a refractive index, $m = n + ik$. Both are complex functions, which depend strongly on the angular frequency, ω , or wavelength, λ , of the incident light wave. The dielectric constants, ε_1 and ε_2 , are related to the optical constants, n and k , by

$$\varepsilon_1 = n^2 - k^2, \quad \varepsilon_2 = 2nk. \quad (2.1)$$

The real part of the dielectric function, ε_1 , determines the degree to which the material polarizes in response to an electromagnetic field, while the imaginary part, ε_2 , controls the relative phase of this response with respect to the applied field. Intrinsic loss mechanisms of a material, such as absorption, are all condensed into ε_2 [5, 81, 96].

The real and imaginary parts of refractive index functions can be extracted from the dielectric constants by using the following equations

$$n = \sqrt{\frac{\varepsilon_1 + \sqrt{\varepsilon_1^2 + \varepsilon_2^2}}{2}}, \quad k = \sqrt{\frac{-\varepsilon_1 + \sqrt{\varepsilon_1^2 + \varepsilon_2^2}}{2}}. \quad (2.2)$$

The functions n and k are often referred to as optical constants. The real part, n , determines the phase velocity of the electromagnetic wave in the medium, and the imaginary part, k , determines the attenuation of the wave as it propagates through the medium. [81, 84] For any material, increased real part, n , leads to enhanced scattering, while increased imaginary part, k , leads to enhanced absorption [97].

2.2.1 Refractive index – Tabulated data sets

There are various data sets for the complex refractive indices. The most commonly used are those of Palik [91], Johnson and Christy [98, 99], and Hugemann et al. [100]. The Handbook of Optical Constants, edited by Palik [91], provides tables and figures for the values of n and k for various materials ranging from the X-ray to the millimeter-wave region of the light spectrum. These values were experimentally measured by various

authors and chosen by expert optical scientists. On the other hand, Johnson and Christy (J&C) performed their own experiments and published their results on the measured optical constants, n and k , of noble [98], and transition [99] metals. They have tabulated the measured values, for the photon energies ranging from 0.5 to 6.5eV. These photon energies correspond to the wavelength range from the ultraviolet (UV, 190nm) to the infrared (IR, 2.5 μ m). Hugemann et al. [100] measured the optical constants of various materials, using 13 to 150eV photon energy (i.e., from 8 to 95nm wavelength range), and used calculations to extend the values from the far infrared to the X-ray region. Their results are shown in figures.

Figure 2.3 show how the different values of n and k affect the plasmon resonances. It is observed that the spectra are mostly affected in the wavelength region of the peak, while it seems that they are unaffected in the region of 400–500 nm (Fig. 2.3(A,B)) for gold, and 300–380nm (Fig. 2.3(C,D)) for silver. Also for wavelengths 700nm and above, for a nanosphere (Fig. 2.3(A,C)) the spectra are similar. The variations in the spectra are a result of the fact that the values from Palik [91] resulted from a combination of various experimental measurements, where small fluctuations on the value of k could occur, while Johnson and Christy [98] performed their own experiments, and exhibit consistency between the various values.

The values of the optical constants, n and k , are given relative to the photon energy E (eV). The equation and universal constants to calculate the wavelength, λ , of the electromagnetic wave, are given in Appendix A.1. For Chapter 4, the Johnson and Christy (J&C) [98] tabulated data set was used since a consistency is observed between the values. For Chapter 5, the Palik [91] tabulated data sets were used, since the J&C lack of the optical constants for the metal aluminum, while Palik provides with the optical constants for a variety of materials, and for the comparison between the spectra is better to use the same optical constants tabulated data set. Though, a comparison between the different refractive index tabulated data sets was also investigated in both chapters.

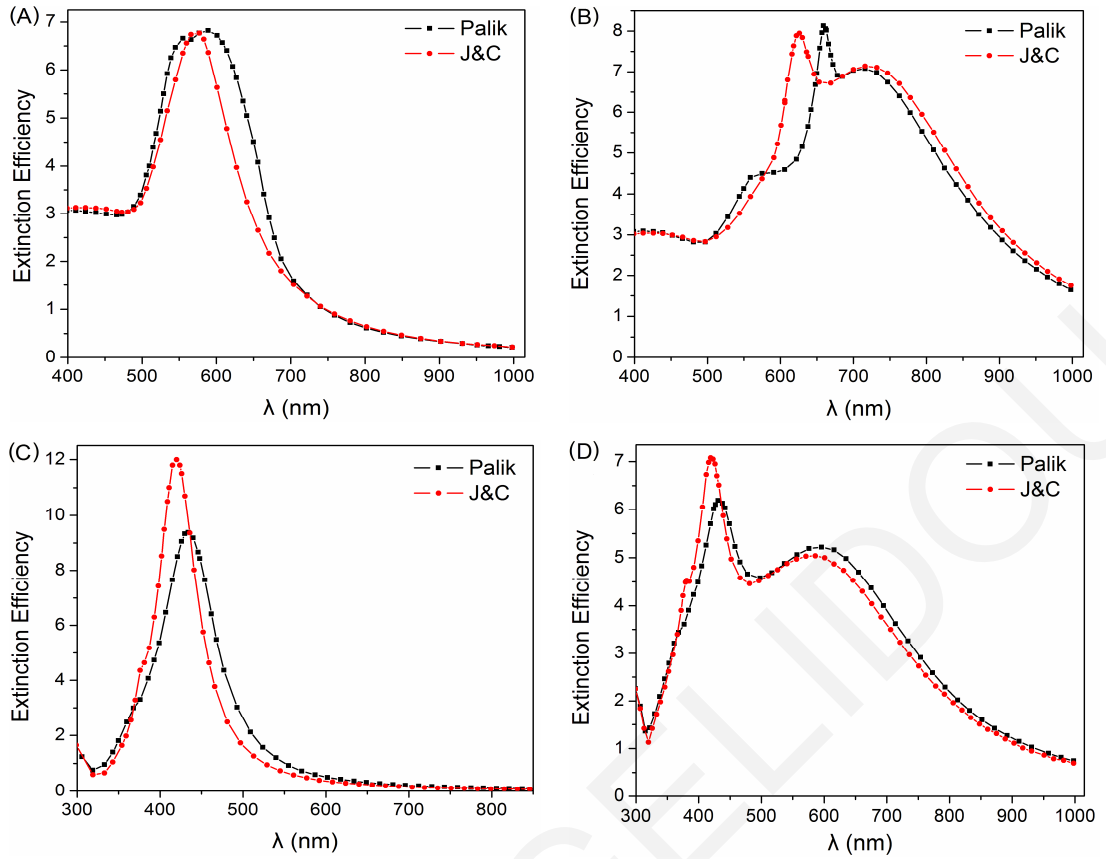


Figure 2.3: SPR refractive index data set dependence examples. (A) Gold nanosphere ($r = 50\text{nm}$), (B) gold nanocube ($r_{\text{eff}} = 74.4\text{nm}$), (C) small ($r = 30\text{nm}$), and (D) large ($r = 70\text{nm}$) silver nanospheres. The external medium was assumed to be water.

2.2.2 Drude “free” electron model

The electronic transitions in bulk material are directly related to the complex dielectric function, $\varepsilon(\omega)$ [98]. The complex dielectric function, $\varepsilon_{\text{bulk}}(\omega)$, for metals, depends on the material and the wavelength, λ , or frequency, ω , of the incident radiation and is described by

$$\varepsilon_{\text{bulk}}(\omega) = \varepsilon_{\text{bound}}(\omega) + \varepsilon_{\text{free,D}}(\omega), \quad (2.3)$$

where $\varepsilon_{\text{bound}}$, is the contribution of the bound electrons (i.e., interband transitions) and $\varepsilon_{\text{free}}$ is the contribution of conducting, free electrons (i.e., intraband transitions).

Interband transitions are due to electron transitions from occupied and completely filled bands to empty bulk bands, separated by an energy gap. The electrons are bound by a restoring force given by the energy difference between ground and excited electronic states in metals. For noble metals, this energy transition occurs from d (valence) bands to sp (conducting) bands. Intraband contributions come from electron transitions at the Fermi level in incompletely filled bands, or when a filled band overlaps in energy with an empty band. Noble metals, such as gold and silver, have incomplete conducting bands. Electrons

at the top of the energy distribution (near the Fermi level) can be excited into other higher, vacant electron states in the same energy band, by photons of very small energies, hence, they are essentially “free” electrons [80, 84, 101]. The Fermi energy, E_F , is the highest possible energy of electrons, at absolute zero temperatures. All electrons occupy energy bands below the threshold energy E_F , while energy bands above E_F are empty. The Fermi level is characterized by a spherical surface, where the occupied electron states are inside that surface [102, 103].

The conducting electron contribution of the dielectric function is described by the Drude model

$$\varepsilon_{\text{free,D}}(\omega) = 1 - \frac{\omega_p^2}{\omega^2 + i\Gamma_\infty\omega}. \quad (2.4)$$

By multiplying and dividing with the complex conjugate, eq. (2.4) can be rewritten as

$$\varepsilon_{\text{free,D}}(\omega) = 1 - \frac{\omega_p^2}{\omega^2 + \Gamma_\infty^2} + i \frac{\omega_p^2 \Gamma_\infty}{\omega(\omega^2 + \Gamma_\infty^2)}. \quad (2.5)$$

The quantity ω_p , which is called the plasmon frequency, is defined as $\omega_p^2 = n_e e^2 / \varepsilon_0 m_{\text{eff}}$, where the constant ε_0 is the dielectric permittivity in vacuum, n_e , e , and m_{eff} are the free electron density, electron charge, and electron effective mass, respectively. The term Γ_∞ is the damping constant, which sometimes is given as the inverse of the relaxation time ($1/\tau$) for conducting electrons. The damping constant, Γ_∞ , describes the intrinsic width of plasmon resonances, and is characterized by the scattering of electrons by phonons, electrons, lattice defects or impurities. Γ_∞ is described by the relationship $\Gamma_\infty = v_F / l_\infty$, where l_∞ is the mean free path of the conducting electrons, and v_F is the maximum velocity that the electron can assume at the Fermi level [80, 104-106].

The electron mean free path, l_∞ , is the distance which a random electron, picked at a random moment, will travel, on average before its next collision. At room temperature this distance is of the order of a few nanometers [80].

2.2.3 Interband transitions

The bound electron contribution, $\varepsilon_{\text{bound}}$, does not participate in the collective motion of the electron cloud, thus SPRs are independent of the interband contributions to the dielectric function. However, interband transitions offer additional decay paths for the excited free electrons, and hence either prohibit or damp the excitation of SPRs. Figure 2.4 shows

spectra of small and large, gold and silver nanospheres, where the interband contribution is present in the case of gold nanospheres.

Figure 2.4(A) shows the spectra of small gold and silver nanospheres having a radius, r , of 15nm. The SPR wavelength maximum lies around 520nm for gold and at 380nm for silver. Also the intensity and spectral width are different for the two materials, with the silver plasmon peak being more intense and narrow compared to gold. Similar results have been reported in the literature [55, 86]. Figure 2.4(B) shows the spectra for larger gold and silver nanospheres ($r = 50$ nm). The SPR maxima are red-shifted, and higher-order modes appear (for silver) and the spectral widths are again different. Even though the spectral intensity of the gold nanosphere spectrum is increased significantly, it has an asymmetric peak due to the presence of interband transitions.

Despite the fact that gold and silver have similar electronic configuration (full d bands, and one free s electron, see Appendix A.2), the threshold energy for interband transitions ($d \rightarrow sp$ bands) is different for the two metals, resulting in their different SPR peaks and intensities [55, 86]. The energy threshold for interband transitions, for gold, is approximately 2.42eV (i.e., 515nm), while for silver is at considerably higher energy, at approximately 3.87eV (i.e., 320nm) [81]. Interband transitions in gold lead to damping of the resonance maxima, while in silver, since the energy threshold is at considerably higher energies (shorter wavelengths), there is much less interference with the behavior of the free electrons involved in the plasmon resonances [82].

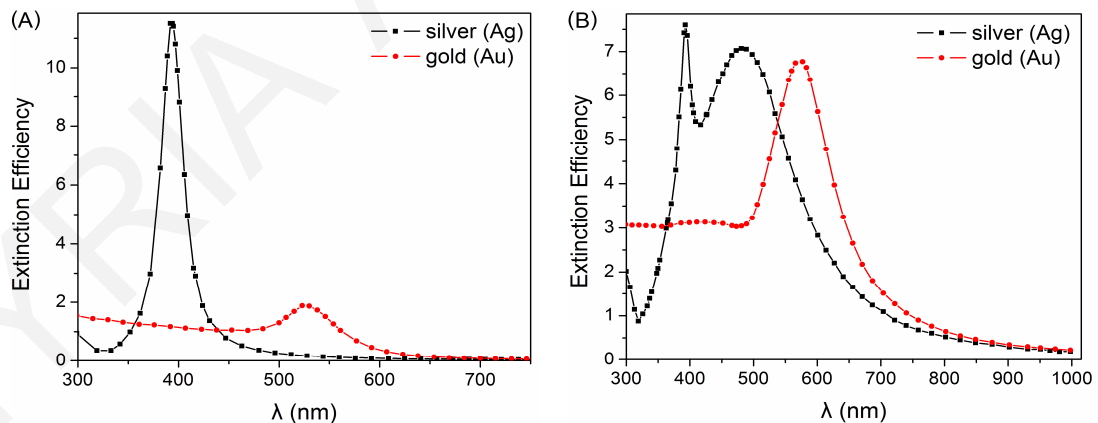


Figure 2.4: Interband contribution on the SPR of noble metals. Spectra examples of (A) small ($r = 15$ nm), and (B) large ($r = 50$ nm) nanospheres in water. (Optical constants obtained from J&C [98].)

The interband contribution is independent of shape of the NP [80], as it is also observed in Fig. 2.2(B,D). The bound electrons absorb energy from the incident radiation

for interband transitions, yet they do not contribute to the SPRs, only slightly affect them. They act by changing the environment of the free electrons, as described previously [80].

2.2.4 Size-dependent dielectric function

Small nanospheres and nanoshells can have dimensions comparable to or smaller than the conduction electron mean free path (l_∞) of bulk material. In such cases, when $2R \leq l_\infty$ for a nanosphere, the dielectric function must be modified to include intrinsic size-dependent effects. In the case of gold (Au), $l_\infty = 42\text{nm}$, and for silver (Ag), $l_\infty = 52\text{nm}$, at room temperatures [81]. For NPs with sizes comparable to or smaller than l_∞ , the interaction of the conduction electrons with the particle surface becomes important and is added as an additional collision process. This results in a reduced effective mean free path (l_{eff}) and in an increased damping factor, Γ , which now depends on the NP size

$$\Gamma(l_{\text{eff}}) = \Gamma_\infty + C v_F / l_{\text{eff}} = v_F / l_\infty + C v_F / l_{\text{eff}}, \quad (2.6)$$

where C is a dimensionless parameter, usually close to unity, and is determined by the details of the scattering process. Classical theory gives C the value of 1 for isotropic scattering, $3/4$ for diffusive scattering, and 0 for elastic scattering. The term $\Gamma(l_{\text{eff}})$ describes the surface damping effect. It alters the magnitude of both the real and imaginary parts of the dielectric function, which also becomes size dependent [81, 104, 107].

The size-dependence of the dielectric function affects the free electron contribution more. This is included in the modified dielectric function which is now given by

$$\varepsilon(\omega, l_{\text{eff}}) = \varepsilon_{\text{bound}}(\omega) + 1 - \frac{\omega_p^2}{\omega^2 + i\omega\Gamma(l_{\text{eff}})}, \quad (2.7)$$

which it can also be expressed as

$$\varepsilon(\omega, l_{\text{eff}}) = \varepsilon_{\text{bulk}}(\omega) + \frac{\omega_p^2}{\omega^2 + i\omega\Gamma_\infty} - \frac{\omega_p^2}{\omega^2 + i\omega\left(\Gamma_\infty + C \frac{v_F}{l_{\text{eff}}}\right)}. \quad (2.8)$$

By multiplying and dividing with the complex conjugates, it can be rewritten as

$$\varepsilon(\omega, l_{\text{eff}}) = \varepsilon_{\text{bulk}}(\omega) + \omega_p^2 \left(\frac{1}{\omega^2 + \Gamma_\infty^2} - \frac{1}{\omega^2 + \Gamma^2(l_{\text{eff}})} \right) + i \frac{\omega_p^2}{\omega} \left(\frac{\Gamma(l_{\text{eff}})}{\omega^2 + \Gamma^2(l_{\text{eff}})} - \frac{\Gamma_\infty}{\omega^2 + \Gamma_\infty^2} \right), \quad (2.9)$$

where $\varepsilon_{\text{bulk}}(\omega)$ incorporates both size-independent free electron processes and interband transitions. The smaller the NP, the more important is the surface damping effect [80, 81, 83, 105].

The plasmon frequency, ω_p , is assumed to be independent of size, since the electron density, n_e , remains constant for different sizes. Also, the bound electron contribution remains unchanged. Scaffardi et al. [96, 108] explored the size-dependent modification of ϵ_{bound} , and they demonstrated that, for particles with radius larger than 1nm, the variance above the bound electron contributions is negligible.

The electron effective mean free path, l_{eff} , depends on the size for small NPs, but also on their shape or structure. For example, in a nanosphere the effective mean free path is considered to be equal to the radius, $l_{\text{eff}} = r$. For NPs with a dielectric core and a metal shell, such as nanoshells, Granqvist and Hunderi [109] proposed the expression

$$l_{\text{eff}} = \left[(R_{\text{out}} - R_{\text{in}}) (R_{\text{out}}^2 - R_{\text{in}}^2) \right]^{1/3} / 2, \quad (2.10)$$

where R_{out} and R_{in} are the shell outer and inner radius, respectively. Equation (2.10) was also supported by Schelm and Smith [110]. Others have used even more complex expressions [4, 111] while other researchers have simply set the value of l_{eff} to be equal to the shell thickness, $l_{\text{eff}} = (R_{\text{out}} - R_{\text{in}})$ [112, 113].

For a nonspherical NP, the modified effective mean path can be calculated by $l_{\text{eff}} = 4V/S$ where V and S are the NP volume, and surface area, respectively. This expression shows that the effective mean free path depends only on the geometrical properties of the object. For a nanosphere, the above expression predicts a value of $l_{\text{eff}} = 4/3r$, which is similar to the constant C obtained for diffusive scattering. Therefore, it can be considered as a general expression which can be applied to any NP structure [4, 105].

Figure 2.5 show the results of the surface damping effect on the extinction efficiency of two silver nanospheres. For a small nanosphere, the effective mean path has a value of 5nm ($l_{\text{eff}} = r$), which resulted in an increased damping factor since Γ is inversely proportional to the effective mean path. As a consequence, plasmon resonance peak was decreased and broadened (Fig. 2.5(A)). For a large nanosphere, whose radius is larger than l_{∞} , the damping factor, Γ , does not change significantly and resulting in almost identical spectra (Fig. 2.5(B)). While for large NPs there is no need to modify their dielectric function, for small NPs it is imperative to include the surface damping effect. It should be noted that the surface damping effect does not change the wavelength of the peaks of the proper modes but it only affects the intensity and width of the peaks. The surface damping

effect was also explored and discussed in detail in the literature [83] and is in good agreement with our findings.

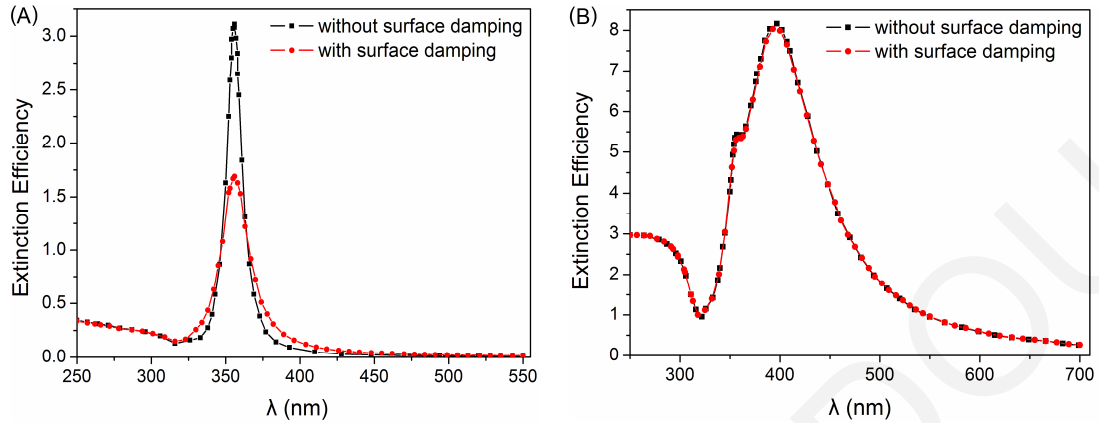


Figure 2.5: Size-dependent dielectric functions to include the surface damping modification. Example spectra of (A) small ($r = 5\text{nm}$), and (B) large ($r = 50\text{nm}$) silver nanospheres in vacuum. (J&C [98].)

The modified dielectric function was used for small nanospheres and nanoshells, with radii and shell thicknesses ranging from 5nm to even 30nm. For larger size nanospheres ($r > 30\text{nm}$), bulk material values were applied. For the purposes of this dissertation, isotropic scattering ($C = 1$) was considered in all cases. The effective mean free path, for a nanosphere, was taken to be equal to the radius (r), while for a nanoshell it was taken to be equal to the shell thickness. The constant values of bulk plasmon frequency, ω_p , damping constant, Γ_∞ , and Fermi velocity, v_F were obtained from the literature for gold [114], and silver [115, 116]. These values are shown in Table 2.1. Small nanosphere simulations were performed only for the noble metals. For the case of the other metals, such as aluminum ($l_\infty = 16\text{nm}$) [81], and nickel ($l_\infty \approx 7.7\text{nm}$) [117], considered in Chapter 5, the larger sizes of the NPs used (compared to their mean free path), meant that no surface damping modification of their dielectric functions, was necessary.

Table 2.1: Values of the various parameters for surface damping modification

	$\hbar\omega_p$ (eV)	$\hbar\Gamma_\infty$ (eV)	v_F (m/s)
Gold (Au)	8.55	0.108	1.41×10^6
Silver (Ag)	9.6	0.021	1.4×10^6

2.3 Summary

- Surface plasmon resonances (SPRs) result from the collective, coherent oscillations of the conducting “free” electrons. These collective oscillations are also called “plasmons”.
- SPRs (number, frequency or wavelength maximum, intensity, and width) depend strongly on size, shape, material, and surrounding medium.
- Plasmon resonances can be tuned from the visible to the near-infrared (NIR) wavelength regions. Noble metals (silver and gold) have SPRs in the visible wavelength range.
- The optical response of NPs is characterized by complex, wavelength dependent, dielectric functions or refractive indices. The Drude model characterizes the response of the free conducting electrons.
- At short wavelengths, below 320nm and 515nm for silver and gold respectively, interband transitions mostly affect the SPR spectra. At longer wavelengths, the free electron contributions dominate the SPR spectra.
- If the NP size is smaller or equal to the electron mean free path, surface scattering becomes important and must be included into the dielectric function. This phenomenon is called the “intrinsic size-effect”.
- For small nanosphere radii, and shell thicknesses, ranging from 5 to 30nm, modified optical constants must be used. For larger nanospheres ($r > 30\text{nm}$) and other NSs, bulk values can be applied.
- The surface damping effect does not change the wavelength of the SPRs but makes the spectrum wider and less intense.

3. Methodology

The metal nanoparticles (NPs) of interest in biomedical applications are typically large in size, so that classical electromagnetic theory can accurately describe their interaction with light but small enough so that they exhibited different optical properties which are a function of their size, shape, material, and surrounding medium [118]. The optical response of a metal nanoparticle (NP), characterized by a given dielectric function, is obtained by solving the Maxwell's equations in a medium. Mie theory provides the exact analytical solution of Maxwell's equations for a sphere of arbitrary size immersed in a homogeneous medium, and subjected to a plane monochromatic wave [16, 119]. However, rigorous solutions of Maxwell's equations for nonspherical NPs are not straight-forward. Thus, the optical properties of NPs with arbitrary shapes can be found only by approximation [80].

Numerical methods, such as the Discrete Dipole Approximation (DDA) [118, 120], the Finite-Difference Time-Domain (FDTD) [121, 122], and the T-Matrix [123, 124], have been reported and explored by various authors. The main advantage of the DDA over the other methods, is that it has a broad range of applicability and is limited only by available computational power [120]. The DDA method is a flexible and powerful technique for computing scattering and absorption of arbitrary geometry [6] and for this reason it was chosen as the method for calculating the optical properties of various simple and complex metal NPs in this dissertation.

3.1 Discrete Dipole Approximation (DDA)

The DDA is a frequency-domain, numerical method first introduced by Purcell and Pennypacker [125] and further developed by Draine and co-workers [126-132]. It approximates a continuous target NP by a finite array of polarizable points. The points acquire dipole moments in response to the local electric field and also interact with each other via their electric fields. There is no restriction regarding the localization of the polarizable point dipoles so the DDA method can solve for any NP of arbitrary geometry, orientation and composition as long as the appropriate dielectric function is given, and the validity criteria are satisfied.

Although DDA is not an exact method, comparisons of DDA results with other methods such as Mie theory indicate that errors in the extinction spectra are often less than

10% [122, 133]. A disadvantage of DDA is that it requires a lot of computational effort for its matrix complex elements to be calculated.

3.1.1 DDA method

The target NP is geometrically approximated by a cubic lattice of N polarizable point dipoles, localized at \mathbf{r}_i , with each characterized by a polarizability α_i , where $i = 1, 2, \dots, N$. Purcell and Pennypacker [125] used the Clausius-Mossotti polarizability expression

$$\alpha_i^{\text{CM}} = \frac{3d^3}{4\pi} \frac{\varepsilon_i - 1}{\varepsilon_i + 2}, \quad (3.1)$$

where ε_i is the dielectric function of the target material at location \mathbf{r}_i , and d represents the interdipole separation or lattice spacing. Draine and Goodman [128] introduced the following corrected polarizabilities using the lattice dispersion relation (LDR)

$$\alpha_i^{\text{LDR}} \approx \frac{\alpha_i^{\text{CM}}}{1 + \left(\alpha_i^{\text{CM}}/d^3\right) \left[\left(b_1 + m^2 b_2 + m^2 b_3 S \right) (kd)^2 - (2/3) i (kd)^3 \right]}, \quad (3.2)$$

$$b_1 = -1.891531, \quad b_2 = 0.1648469, \quad b_3 = -1.7700004, \quad S = \sum_{i=1}^3 (\hat{\alpha}_i \hat{\varepsilon}_i)^2$$

where S is a function of the propagation direction and polarization of the incident wave, $\hat{\varepsilon}_i$ and $\hat{\alpha}_i$ are the unit propagation and polarization vectors, with the directions $i = 1, 2, 3$, correspond to the axes of the dipole lattice [130], $m = \varepsilon^{1/2}$, is the complex refractive index, and $k = \omega/c$, represents the wavenumber.

The induced polarization \mathbf{P}_i for each dipole element is determined by

$$\mathbf{P}_i = \alpha_i \cdot \mathbf{E}_{\text{loc},i}, \quad (3.3)$$

where α_i is the polarizability of the i^{th} dipole and $\mathbf{E}_{\text{loc},i}$ is the local electric field experienced by the i^{th} dipole. The local electric field, for an isolated, individual NP, is given by

$$\mathbf{E}_{\text{loc},i} = \mathbf{E}_{\text{inc},i} - \sum_{j \neq i} \mathbf{A}_{ij} \cdot \mathbf{P}_j. \quad (3.4)$$

$\mathbf{E}_{\text{inc},i}$ is the electric field at position \mathbf{r}_i due to the incident plane wave,

$$\mathbf{E}_{\text{inc},i}(\mathbf{r}_i) = \mathbf{E}_0 \exp(i\mathbf{k} \cdot \mathbf{r}_i - i\omega t), \quad (3.5)$$

where \mathbf{E}_0 and \mathbf{k} are the amplitude and wave vector of the incident field, respectively.

The \mathbf{P}_j , in eq. (3.4) is the dipole polarization of the j^{th} dipole, while \mathbf{A} is an interaction matrix. The second term, $-\mathbf{A}_{ij} \cdot \mathbf{P}_j$, is the contribution to the electric field at position \mathbf{r}_i due to the dipole at position \mathbf{r}_j and has the following form

$$\mathbf{A}_{ij} \cdot \mathbf{P}_j = \frac{\exp(ikr_{ij})}{r_{ij}^3} \left\{ k^2 \mathbf{r}_{ij} \times (\mathbf{r}_{ij} \times \mathbf{P}_j) + \frac{(1 - ikr_{ij})}{r_{ij}^2} \times [\mathbf{r}_{ij}^2 \mathbf{P}_j - 3\mathbf{r}_{ij}(\mathbf{r}_{ij} \cdot \mathbf{P}_j)] \right\} \quad (i \neq j), \quad (3.6)$$

where $\mathbf{r}_{ij} = \mathbf{r}_i - \mathbf{r}_j$ and $r_{ij} = |\mathbf{r}_i - \mathbf{r}_j|$, are the vector and magnitude of the displacement between i^{th} and j^{th} dipoles. Equation (3.6) characterizes the dipole-dipole interactions, and it serves to define the matrices for $i \neq j$. Also, by defining $A_{ii} \equiv \alpha_i^{-1}$, which means that the diagonal elements ($i = j$) of the matrix \mathbf{A} are equal to the inverse polarizability of the i^{th} dipole, the scattering problem is reduced and can be formulated as a set of inhomogeneous linear complex vector equations

$$\mathbf{E}_{\text{inc},i} = \sum_{j=1}^N \mathbf{A}_{ij} \cdot \mathbf{P}_j \quad (i = 1, \dots, N). \quad (3.7)$$

For a system with a total number of N dipoles, \mathbf{E} , and \mathbf{P} are $3N$ -dimensional vectors, and \mathbf{A}_{ij} is a $3N \times 3N$ symmetric matrix. By solving these $3N$ -coupled complex linear equations, using iterative methods, the polarizations (\mathbf{P}_j) can be determined [126, 129, 132].

If the nanostructure (NS) of interest consisted of many metal NPs, an additional contribution is included to the local electric field, the $\mathbf{E}_{\text{others},i}$, which is due to the fields from dipoles on other NPs (the interaction between particles) [134].

$$\mathbf{E}_{\text{others},i} = -\sum_{j'} \mathbf{A}_{ij'} \cdot \mathbf{P}_{j'} \quad (i \neq j'). \quad (3.8)$$

The absorption, scattering and extinction cross sections, C_{abs} , C_{sca} , and C_{ext} , are then evaluated from the resultant polarization, [126, 129]

$$C_{\text{abs}} = \frac{4\pi k}{|\mathbf{E}_0|^2} \sum_{i=1}^N \left\{ \text{Im} \left[\mathbf{P}_i \cdot (\alpha_i^{-1})^* \mathbf{P}_i \right] - \frac{2}{3} k^3 |\mathbf{P}_i|^2 \right\}, \quad (3.9)$$

$$C_{\text{ext}} = \frac{4\pi k}{|\mathbf{E}_0|^2} \sum_{i=1}^N \text{Im}(\mathbf{E}_{\text{inc},i}^* \cdot \mathbf{P}_i), \quad (3.10)$$

$$C_{\text{sca}} \equiv C_{\text{ext}} - C_{\text{abs}}. \quad (3.11)$$

Consider W_{sca} to be the rate at which energy is scattered across the surface A , W_{abs} to be the rate at which energy is absorbed by the particle and W_{ext} to be the sum of the energy absorption rate and the energy scattering rate, $W_{\text{ext}} = W_{\text{abs}} + W_{\text{sca}}$. The ratio of W_{ext} to the incident radiation, I_{inc} , is a quantity with dimensions of area and is called extinction cross section, $C_{\text{ext}} = W_{\text{ext}}/I_{\text{inc}}$. The same stands for absorption and scattering [84, 123].

The extinction, absorption and scattering efficiency factors, Q_{ext} , Q_{abs} , and Q_{sca} , are dimensionless cross sections which were used to explore and compare the optical properties of the various metal NPs. The efficiency factors or efficiencies, Q , are defined as the ratios of the corresponding cross sections, C , over the effective particle cross-sectional area (the “effective sphere”) projected onto a plane perpendicular to the incident beam, as shown in the following relationships

$$Q_{\text{abs/sca}} = C_{\text{abs/sca}} / \pi r_{\text{eff}}^2, \quad Q_{\text{ext}} = Q_{\text{abs}} + Q_{\text{sca}}, \quad (3.12)$$

where r_{eff} is the effective radius, which characterizes the size of the NP, and is given by

$$r_{\text{eff}} \equiv (3V_{\text{NP}}/4\pi)^{1/3}. \quad (3.13)$$

The effective radius is defined as the radius of a sphere having a volume equal to that of the NP of arbitrary shape [82, 84]. In the case of a spherical NP, the effective radius (r_{eff}) is equal to the sphere radius (r). The volume equations for simple shapes can be found in Appendix A.3. When composite shapes of NPs are considered, V_{NP} , is taken to be the overall volume structure, V_{str} , where individual volumes are added. For example, when considering a cube combined with a number of small spheres, n_{sph} , the total complex NS volume is $V_{\text{str}} = V_{\text{cube}} + n_{\text{sph}} V_{\text{sph}}$.

3.1.2 Applicability of DDA

The principal advantage of the DDA method is that it is completely flexible with regards to the geometry of the target NP, limited only by the need to use an interdipole separation, d , small compared to (i) any structural lengths in the target, and (ii) the wavelength, λ , of the incident light [129, 132]. According to the first criterion (i), a sufficient number of dipoles (N) must be used to approximate the target NP. Figure 3.1 displays an example of a single nanosphere approximated by four different numbers, N , of dipoles. As N increases, the shape better converges to that of a sphere.

The number of dipoles, N , is related to the interdipole separation, d , and the effective radius, r_{eff} , via the equation

$$r_{\text{eff}} = (3N/4\pi)^{1/3} d, \quad (3.14)$$

where the NP volume, V_{NP} , from eq. (3.13) was set to be equal to N multiplied by the lattice size, d^3 . Therefore, for the same target NP, when the number of dipoles, N , is increased, the corresponding interdipole separation, d , is decreased.

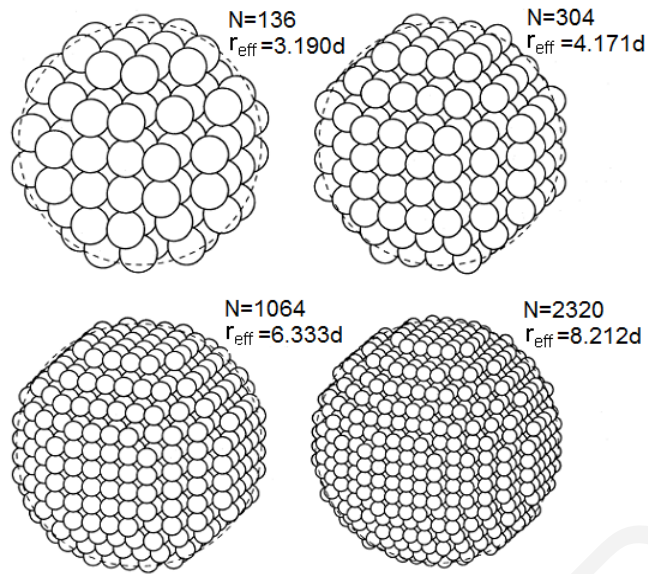


Figure 3.1: Nanosphere approximated by four discrete dipole arrays with $N = 136, 304, 1064,$ and 2320 [126].

Figure 3.2(A) shows the extinction spectra of a small sphere calculated for various d . Even though by reducing d , the sphere is better approximated and the results converge towards the exact solution, even for relatively large separation, for example $d = 2\text{nm}$, the extinction spectra are only slightly red-shifted with a small increase in the extinction value. Figure 3.2(B) shows the results for a larger nanosphere. In this case, there are no significant differences and the spectra are almost identical even for $d = 3\text{nm}$. This is very important since further reducing the lattice size ($\sim d^3$), is often not feasible, for either small or large spheres, due to computational limitations (mainly increased memory requirements).

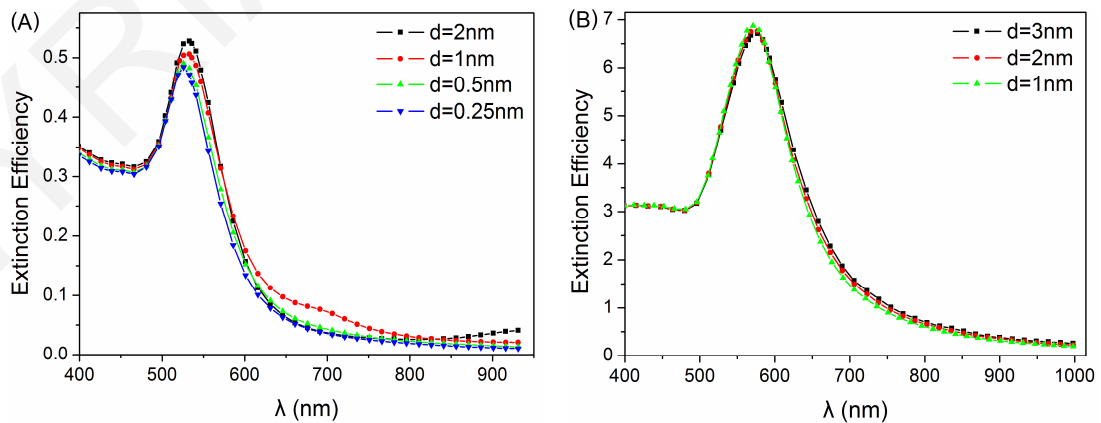


Figure 3.2: Interdipole separation, d , dependence for gold nanosphere with (A) $r = 5\text{nm}$, and (B) $r = 50\text{nm}$ in water. (J&C [98].)

To better approximate a nanosphere, the ratio of surface to bulk dipoles must be small, which would suggest taking a very large number of dipoles, N (or small size of the interdipole separation, d) [89, 126]. However, there are two major limitations. First, the maximum number of dipoles used in each axis (N_x , N_y , and N_z) is limited due to computational resources and second, the time required to obtain a solution is approximately to N^3 [129], therewith imposing an upper limit to the number of dipoles used.

The second criterion (ii) is adequately satisfied if

$$|m|kd < 1, \quad (3.15)$$

where m is the complex refractive index, and $k = 2\pi/\lambda$, is the wavenumber where λ is the wavelength in vacuum. This criterion is valid provided that $|m| \leq 2$ or $|m-1| \leq 3$ [129, 132].

Equation (3.15) can be further expanded to provide more insight on to the second criterion. Let V be the volume of the target NP. If the target is represented by an array of N dipoles, located on a cubic lattice with interdipole separation, d , then $V = Nd^3$. The size of the target is characterized by the effective radius, r_{eff} . A given scattering problem is then characterized by a dimensionless “size parameter”, $x \equiv k r_{\text{eff}}$. The second criterion is equivalent to

$$(4\pi/3)|m|^3 (k r_{\text{eff}})^3 < N, \quad (3.16)$$

which relates the number of dipoles, N , the complex refractive index, m , and the size parameter, x . Thus targets with large values of $|m|$ or scattering problems with large values $k r_{\text{eff}}$ will require a larger number of dipoles to represent the targets [129].

3.2 Implementation: DDSCAT Software

Draine and Flatau have developed a portable Fortran DDA implementation, the DDSCAT software, which is freely available online. For the purpose of this dissertation, two versions (DDSCAT6.1 (plain), and DDSCAT7.0) were adapted and used [135, 136]. There are few changes between the two versions; the main difference is that DDSCAT6.1 is fortran77, while DDSCAT7.0 is fortran90 implementation. At the beginning of this dissertation, only the 6.1 version was available, and later a new version was published and subsequently used. The differences between the two versions can be found in their user guides [135, 136]. It is important to note that both adaptations give the same results, as shown in Fig. 3.3(A,B).

DDSCAT can solve the system of $3N$ -coupled complex linear equations (eq. (3.7)) by using fast Fourier transforms (FFT) and complex-conjugate gradient (CCG) methods. It can effectively deal with the problem of scattering and absorption by a finite target, represented by an array of polarizable point dipoles, interacting with a monochromatic plane wave incident from infinity. The software has the capability of automatically generating the dipole array representation for various target geometries and can also accept dipole arrays supplied by the user. Target NPs may be both inhomogeneous and anisotropic. The incident plane wave can have arbitrary elliptical polarization and the target can be arbitrarily oriented to the incident radiation. By solving the problem, DDSCAT provides various efficiency factors, such as extinction and absorption, and also the 4×4 Mueller scattering intensity matrix S_{ij} values.

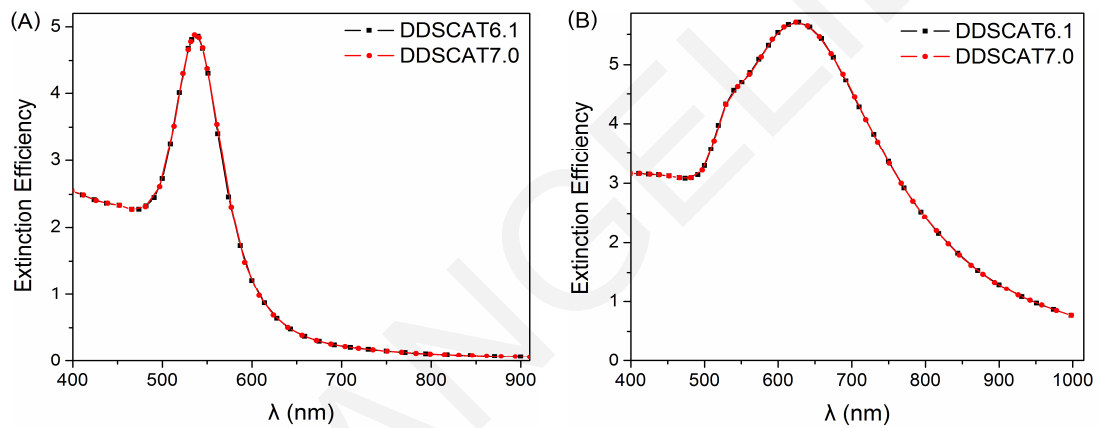


Figure 3.3: Comparison between the two DDSCAT versions, for a gold nanosphere with (A) $r = 30$ nm, and (B) $r = 70$ nm in water. (J&C [98].)

3.2.1 Solution Methodology

The polarization, \mathbf{P} , is a $3N$ -dimensional complex vector of the unknown dipole polarizations. Direct methods for solving a system of $3N$ eq. (3.7) for the unknown vector \mathbf{P} are impractical and hence iterative methods are used. Complex-conjugate gradient (CCG) techniques have proven effective and efficient in DDA applications. CCG methods are guaranteed to converge in $3N$ iterations but, generally, may yield an excellent approximation to the exact solution in far less iterations. Since this is an iterative technique, it requires an initial guess for \mathbf{P} . The simplest choice is $\mathbf{P}_j = 0$ [129]. The iteration starts with the initial guess and continues to improve the estimate of \mathbf{P} until the error criterion is met. The error tolerance (err_tol) is specified as [132]

$$\frac{|\mathbf{A} \cdot \mathbf{P} - \mathbf{E}_{\text{inc}}|}{|\mathbf{E}_{\text{inc}}|} < \text{err_tol}. \quad (3.17)$$

For a given incident wave the scattering problem is solved by CCG iteration until a specified level of accuracy is achieved. The error tolerance is typically set at 10^{-5} in order to satisfy eq. (3.7) to high accuracy.

The CCG methods do not require the actual components of \mathbf{A} , but only matrix-vector products of the form $\mathbf{A} \cdot \mathbf{X}$ and $\mathbf{A}^\dagger \cdot \mathbf{X}$, where \dagger signifies the Hermitian conjugate. Note that since matrix \mathbf{A} is symmetric, the product $\mathbf{A}^\dagger \cdot \mathbf{X} = (\mathbf{A} \cdot \mathbf{X}^*)^*$. The fast-Fourier transforms (FFT) can be used to evaluate these products (eq. (3.6)). The FFT can greatly accelerate the required computations, but only if the dipoles are located on a periodic, cubic lattice. The number $N_L \equiv N_x N_y N_z$, is the number of lattice sites in a rectangular volume containing all the N occupied sites [127, 129]. For a rectangular target, $N_L = N$, but for other targets N_L is larger than N . For spherical and tetrahedral targets, $N_L \approx (6/\pi)N$ and $N_L \approx 6N$, respectively [132]. If N_x , N_y , and N_z are highly factorizable, the Fourier transforms require $O(N_L \ln N_L)$ operations rather than $O(N^2)$ required for general matrix-vector multiplications [127, 129].

3.2.2 Other parameters

In order to solve a scattering problem, the wavelength (in vacuum or medium), incident polarization, shape, effective radius, and other parameters, such as shape parameters, must be specified. The shape parameters describe the dimensions of the finite target NP, for example, an edge length of a nanocube is characterized by the ratio of x/d , where x , is the dimension in the x axis, and d , the interdipole separation. Therefore, the x/d value assigns the number of dipoles along the x axis. The same applies for the other axes, y and z . Two examples of parameter files are shown in Appendix B.

Another parameter is the ETASCA, which determines the selection of scattering angles used for the computation of certain averages, such as $\langle \cos \theta_s \rangle$ and $\langle \cos^2 \theta_s \rangle$, where θ_s is a scattering angle. Small values of ETASCA result in increased accuracy but also result in increased computation time. If accurate computation on angular averages is not required, then the user can set ETASCA to some large number to minimize unnecessary computations. A third parameter, called GAMMA, determines the interaction cut off parameter for periodic targets. In this dissertation, it was set to zero since isolated, finite, targets were investigated.

Figure 3.4 shows the extinction spectra of a gold nanosphere ($r = 15\text{nm}$) calculated using different error tolerances (TOL) and ETASCA values. Figure 3.4(A) shows results for tolerances of 10^{-3} , 10^{-4} , and 10^{-5} and a constant 0.5 ETASCA value while Fig. 3.4(B) shows the results of two ETASCA values, 0.5 and 10, for a constant tolerance of 10^{-5} . The number of dipoles used to represent the nanosphere was 82712 ($d = 0.55\text{nm}$). Figure 3.4(A) shows the approximations is quite accurate even for a large error tolerance, such as 10^{-3} . Figure 3.4(B) shows that the extinction efficiency results are not affected by a large value of ETASCA.

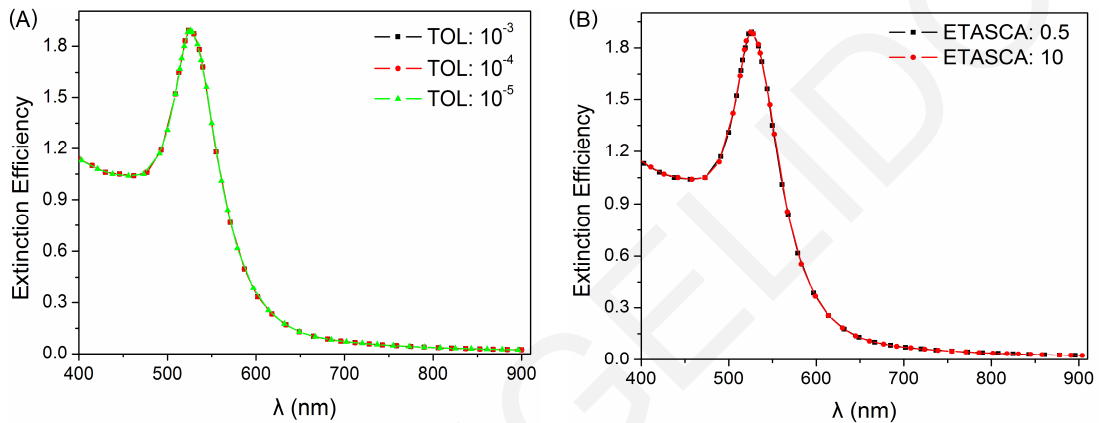


Figure 3.4: (A) Error tolerance (TOL), and (B) ETASCA parameters dependence on extinction for a small gold nanosphere ($r = 15\text{nm}$, $d = 0.55\text{nm}$) in water. (J&C [98].)

Figure 3.5 shows two examples of worst (TOL: 10^{-3} , ETASCA: 10) and best (TOL: 10^{-5} , ETASCA: 0.5) case scenarios of the error tolerances and ETASCA parameters for a gold nanosphere approximated with two different numbers of dipoles. In all four cases, the results are similar.

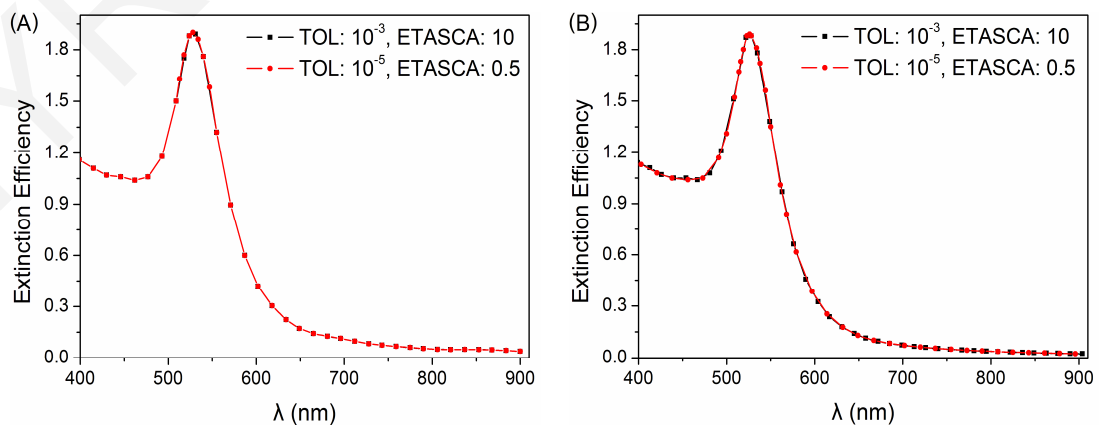


Figure 3.5: Comparison between worst and best case scenarios for the tolerance and ETASCA parameters for a small gold nanosphere ($r = 15\text{nm}$) approximated with (A) 4224, and (B) 82712 dipoles in water. (J&C [98].)

The results of Fig. 3.4 and 3.5 determined the parameters for the simulations in this dissertation. An error tolerance of 10^{-3} and an ETASCA value of 10 were used throughout since they resulted in accurate approximated efficiency results.

3.2.3 Target material

The dielectric function or refractive index values for the target material must be provided as tables by the user. If the target NP is consists of more than one material, then the user must specify the number of different materials used. For the simulations in this dissertation, the complex refractive index values were supplied.

The software can deal with any surrounding or external medium where the target is embedded, as long as the relative refractive index, m , is supplied

$$m(\omega) = \frac{m_{\text{target}}(\omega)}{m_{\text{med}}}, \quad (3.14)$$

where m_{target} and m_{med} are the complex refractive indices of the target metal NP, and the surrounding or external medium, respectively.

The wavelength in the medium, λ_{med} , is supplied as well

$$\lambda_{\text{med}} = \frac{\lambda}{m_{\text{med}}}, \quad (3.15)$$

where λ is the wavelength in vacuum. All the results are given relative to the wavelength in vacuum.

Note that, for the purposes of this dissertation, the refractive index of the surrounding medium, m_{med} , was set not to depend on the wavelength of the light and have only a real part value, n_{med} . This is similar to water with $m_{\text{med}} = 1.33 + i0$, where $n_{\text{med}} = 1.33$, and $k_{\text{med}} = 0$, representing a nonabsorbing, homogeneous medium. An example is given below, with gold (Palik [91]) values of relative complex refractive index as a function of wavelength, and water as the external medium.

m = 1.247 + 1.471i at lambda = 0.300 μm (nmed: 1.33)		
1 2 3 0 0 = columns for wave. Re(n). Im(n). eps1. eps2		
LAMBDA	Re(N)	Im(N)
0.20265	1.20150	1.36992
0.20715	1.23910	1.39248
.	.	.
.	.	.
.	.	.
0.99168	0.31504	6.33083
1.01324	0.32782	6.45865

3.2.4 Target generation: shape files

The software contains routines to generate dipole arrays for finite targets of various geometries including spheres, ellipsoids, rectangular solids, cylinders, tetrahedra, two concentric spheres (nanoshell) and so on. The target type and shape parameters can be specified in the parameter file. However, if the desired target has arbitrary geometry then the number of dipoles, N , and the location and composition of each dipole must be provided by the user in a separate file. The target materials, considered in this dissertation, are isotropic meaning that the refractive index had the same value in all directions.

An example of a shape file is shown below. It is a shape file of a complex NS consisting of a nanocube combined with 16 nanospheres. The interdipole separation, d , was set to be 1.5nm. The first line is just a description of the shape and maximum dipoles used along each axis. Line 2 gives the total number of dipoles representing the complex NS. Lines 3–6 refer to the components for a specific orientation (e.g., Target Frame), where the vectors \hat{a}_1 and \hat{a}_2 are embedded in the target (see section 3.2.5 of target orientation and userguide for more information). The remaining lines provide the position and composition of each dipole. ICOMP takes two different values at different dipole locations. This means that the target is composed of two different materials.

```
1. >TARGET DP_Spheres_Cube; AX,AY,AZ,= 102.00 82.00 82.00
2. 597665 = NAT
3. 1.0000 0.0000 0.0000 = A_1 vector
4. 0.0000 1.0000 0.0000 = A_2 vector
5. 1.0000 1.0000 1.0000 = lattice spacings (d_x,d_y,d_z)/d
6. 1.0000 1.0000 1.0000 = TF coordinates (d_xtf,d_ytf, d_ztf)/d
7. JA IX IY IZ ICOMP(x,y,z)
8. 1 1 1 1 1 1 1
9. 2 2 1 1 1 1 1
. . . . .
. . . . .
. 531440 80 81 81 1 1 1
. 531441 81 81 81 1 1 1
. 531442 -10 7 2 2 2 2
. 531443 -9 7 2 2 2 2
. . . . .
. . . . .
. 597664 -9 75 80 2 2 2
. 597665 -8 75 80 2 2 2
```

There is also a program in DDSCAT software, the CALLTARGET, which allows the user to generate dipole arrays for simple targets. For the purposes of the simulations in this dissertation, shape files of aggregates, shell aggregates, and complex nanostructures (NSs) were created using the MATLAB programming language and the CALLTARGET program.

3.2.4.1 Spherical – Monolayer/bilayer shell aggregates

For the various aggregates shapes, described in Chapter 4, a sphere triangulation algorithm was used to position a number of small nanospheres around a larger spherical core, and create the overall NP [137].

First, the values of outer radius, R , sphere radius, r , edge-to edge distance between spheres, ds , border width around outer radius, b_o , grid spacing, d , are specified in nanometers. These values were then redefined as distances in dipoles, for example R/d . The grid size was determined as $2(R + b_o)/d$.

In order to determine the location of each small sphere around the core, the sphere representing the core was triangulated, i.e. it was approximated by a structure consisting of equilateral triangles and approaching the volume of the core sphere. Each triangle had three equal sides of $2(r + ds/2)$ length. The vertices of the triangles served as the centroids of the small spheres. (The equations can be found in Appendix A.3.) Given that the number of triangles used for the process of triangulation can only take values of 4, 8, or 20 when forming a closed surface (i.e. tetrahedra, octahedra, and icosahedra) the number of spheres around the core are also limited to specific numbers (i.e. 4, 6, and 12). In addition, if a specific edge-to-edge distance between small spheres is required, the sphere size must be adjusted accordingly. Hence, when running certain simulations, not all desired combinations of number of small spheres and small sphere radius were available. For the bilayer aggregates, the triangulation was performed twice: once for a sphere corresponding to the outer shell radius and again, for a second time, for the sphere radius corresponding to the inner shell radius. For the spherical aggregate shape, the triangulation was performed at all layers. The Matlab shape was then converted to a shape file assigning a different index of refraction to each material.

Figure 3.6 shows an example of this process, for the monolayer shell aggregate shape. The core was approximated by an icosahedron (Fig. 3.6 (A)) and subsequently a small sphere (blue) was placed at the coordinates of each of its vertices around a central core (red) as shown in Fig. 3.6 (B).

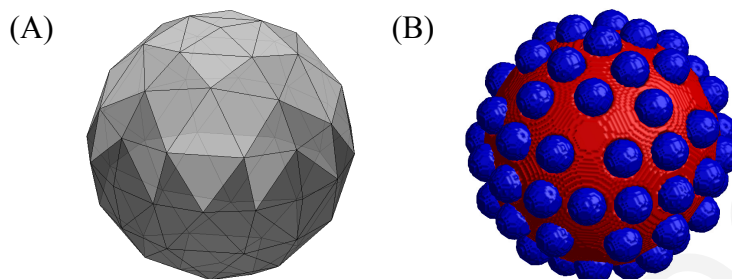


Figure 3.6: Images of (A) sphere triangulation, and (B) the corresponding monolayer shell aggregate. (Core in red, and spheres (shell) in blue.)

3.2.4.2 Complex/combined nanostructures

For the complex NSs in Chapter 5, a nanocube was combined with various numbers of small nanospheres which were arranged as layers either on the front or side face or even covering all its surfaces. The small nanospheres had equal diameters. Figure 3.7(A,B) shows a structure formed by combining 16 nanospheres arranged on the front face (y - z plane) of a nanocube, perpendicular to the x axis. Such shapes were generated using the built-in capabilities of the DDSCAT software.

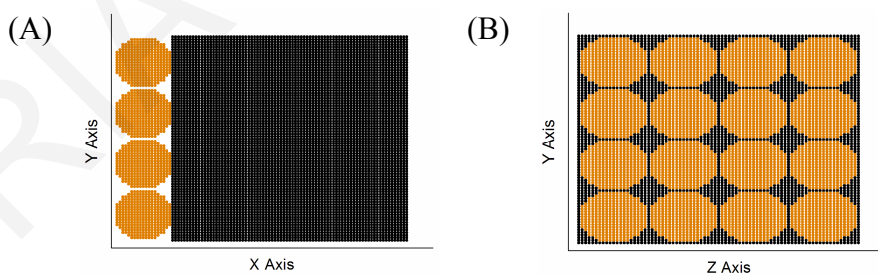


Figure 3.7: Image of a complex NS, where 16 spheres arranged on the front face of the cube, as viewed from the (A) side (x - y plane), and (B) front (y - z plane). (Cube in black, and spheres in orange.)

The dipole representation of a nanocube was obtained using the CALLTARGET program. For the nanospheres, the radius, and relative locations (center coordinates) were defined in an external file, similar to the one shown below. The nanosphere radius is represented in dipoles (radius/ d).

4 (= N number of spheres)			
X	Y	Z	sphere radius
-19	21	21	20
-19	21	61	20
-19	61	21	20
-19	61	61	20

Then, using the CALLTARGET program, the dipole arrangement of the nanospheres was generated. The interdipole separation, d , was set to be equal for both nanocube and small nanospheres. The final shape file was a combination (number of dipoles added) of the two target files. The nanocube dipole array material, and the nanosphere dipole array material were assigned different indices of refractions.

3.2.5 Target Orientation

For the purposes of the simulations in this dissertation, the incident radiation was always assumed to propagate along the positive x direction. The orientation of the target was characterized by the angles theta (θ), phi (φ), and beta (β) relative to the incident direction. The target is assumed to have two vectors \hat{a}_1 and \hat{a}_2 embedded in it, where \hat{a}_2 is perpendicular to \hat{a}_1 . The polar angles, θ and φ specify the direction of \hat{a}_1 relative to the incident direction \hat{x} , while β specifies how the target is to rotated around the axis \hat{a}_1 (Fig. 3.8) [135, 136].

Figure 3.9 shows an example of the setup of the monolayer shell aggregate for the simulations. The incident polarization was set to be along the y axis. An average value was obtained between the two orthogonal polarization states, for all simulations. By considering the average polarization, the optical response of the NSs was approximately that corresponding to unpolarized incident light. For the shapes studied in this dissertation, there was no need to rotate the targets, since most of the NSs had symmetrical shapes and were independent of the direction of polarization. Therefore, the angles θ , φ , and β were set to zero. When polarization dependence was observed, the values of efficiency factors at the two polarization states were independently explored.

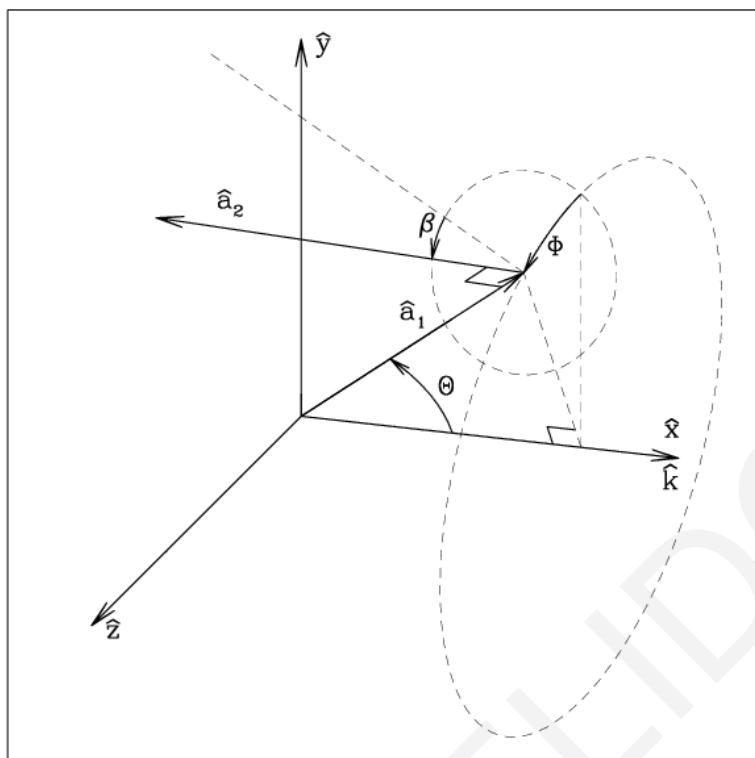


Figure 3.8: Vectors and polar angles for target orientation [136].

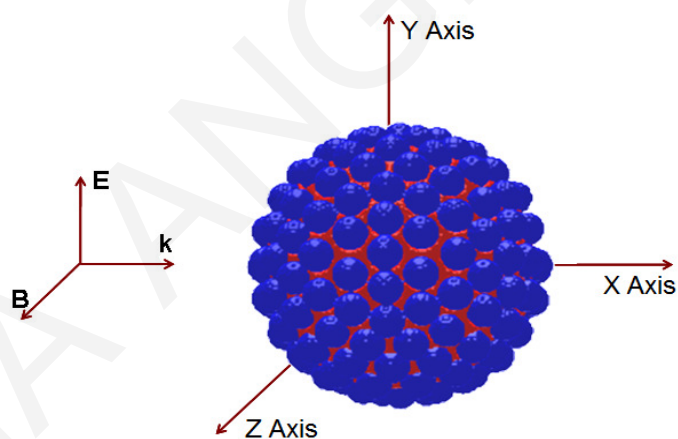


Figure 3.9: Setup of a target NS (monolayer shell aggregate) for DDSCAT simulations.

4. Investigation of Novel Monolayer/Bilayer Shell Aggregates – Comparison with Classical Gold Nanoparticles

4.1 Introduction

Noble metal nanoparticles (NPs), such as gold (Au) and silver (Ag), have been extensively investigated for potential uses in various biological and biomedical applications [51, 138, 139]. This chapter mainly focuses on the optical properties of a new tunable gold nanostructure (NS), the so-called “shell aggregate”, which is composed of small nanospheres aggregated around a dielectric core creating a monolayer or a bilayer shell. Its potential application as an imaging agent and surface-enhanced Raman spectroscopy (SERS) probe are also mentioned.

Raman spectroscopy is known to provide detailed information about the chemical composition of a molecule or a tissue. It is based on the Raman effect, which was discovered by Sir C. V. Raman. Briefly, when light interacts with a molecule, a small fraction of photons is inelastically scattered, thus losing or gaining energy. As a result, the scattered photons have different frequencies than the photons of incident light. Raman scattering can occur due to changes at the vibrational, or rotational, or electronic energy levels of the molecule [140, 141]. In SERS applications, with the aid of metal NPs, the usually weak Raman signal is intensely amplified and the spectroscopy becomes more efficient and sensitive. Local electric field enhancement, resulting from surface plasmon resonances (SPRs), can lead to stronger and richer spectroscopic signals for molecules which are localized adjacent to the metal nanoparticle (NP) [142-144].

Noble metal NPs are commonly used in SERS applications [19, 58, 145]. Molecules absorbed onto these materials exhibit intense SERS signal in the visible region, with intensities dropping, as the wavelength is blue-shifted [116]. Even though silver NPs produce stronger and larger field enhancement than gold NPs [58, 146], their biological applications have been limited due to inadequate stability, as a result of oxidation, and poor biocompatibility [55]. In vitro studies have shown that silver NPs could potentially induce toxicity in cells and microorganisms [147, 148]. New synthetic methods are explored for more stable and “environmental friendly” silver NPs [149] which are, currently, used in bacterial and viral SERS applications [150, 151], and antibacterial studies [152].

In contrast, gold NPs appear to be resistant to photobleaching, biocompatible and noncytotoxic to human cells [153-156]. Let’s note that photobleaching is the process of the

irreversible destruction of a fluorophore in its excited state due to its interactions with molecular oxygen or other surrounding molecules [157]. In addition, NPs composed of gold are easy to synthesize, stabilize and can be conjugated to a variety of biomolecular ligands, antibodies, and other targeting moieties [11, 77, 158-161]. For many years, gold salts were used as treatment for rheumatoid arthritis [162]. Another, therapeutically useful property of gold is that its SPR absorption is followed by rapid conversion of the absorbed light energy into heat [3, 101]. Several types of gold NPs have been reported, with the most commonly used being nanospheres, nanoshells, and nanorods. These gold NPs were extensively explored as potential candidates for SERS [76, 163-166], and photoacoustic imaging (PAI) [167-169] applications, with each of them having specific advantages but also limitations. The SERS enhancement mechanism is mainly due to the enhanced local electric fields generated at the metal NP surface, and thus SERS depends strongly on the size and the morphology of the metal NPs [146, 163].

For biological applications of light, including imaging [74] and SERS [75], it is often preferable to use near-infrared (NIR) wavelengths. Using NIR light, at the so-called "optical window" of the spectrum, that is around 800 nm, offers many unique advantages such as deeper penetration, due to decreased absorption by the biomolecules, and less chance of photobleaching or damage to the tissue, again due to decreased absorption. Therefore, it would be significantly advantageous to have metal NPs with NIR plasmon resonances for biological applications. Another important design factor, especially when attempting to investigate cellular and intracellular changes, is the size of the metal NPs which must be such that they can enter the cells but at the same time are not confined into lysosomes. To date, no metal NP or NS has been reported that which possesses all of the above properties..

Small gold nanospheres, having a size range between 10 and 40nm, exhibit a visible SPR response, located around 520nm [88], which translates into weak field enhancement at NIR wavelengths. Larger size gold nanospheres of 50–60nm demonstrate higher enhancement factors but their peaks are still in the visible [170, 171]. Another disadvantage of nanospheres is that they can easily penetrate the cell membrane and distribute intracellularly but remain confined in vesicles, such as endosomes and lysosomes [172]. The nanospheres require biochemical surface modifications in order to be released from the endosomes into the cytoplasm [56]. Another option, to avoid endosomal entrapment, is to grow gold NPs intracellularly, though this method can not be well controlled [173, 174].

One approach to achieve NIR plasmon resonances and high enhancement factors is to allow small nanospheres to aggregate and create larger nanostructures (NSs). The aggregate SPR wavelength can be red-shifted when the aggregation is carefully controlled. However the shift depends on various parameters such as the number, positioning, and distance between the nanospheres and the overall size of the aggregate [3, 23]. However, aggregate synthesis and, especially, size and shape, are not easy to control, and depend on many experimental parameters, such as the reaction time, temperature, pH, and solvent [90, 175, 176].

Another option to get NIR plasmon resonance is to use nanoshells which are spherical NPs commonly composed of a silica core and a gold shell. Nanoshells can provide good tunability of the SPR wavelength ranging from 600 to 1500nm by varying the ratio of the core radius to the outer radius [1, 88]. The main limitation, for biological uses, is that nanoshells with NIR plasmon resonance are rather large NPs (70nm radius) and when uptaken by the cells, they remain confined in vesicles [164, 177]. Nanorods also provide good tunability of the SPR wavelength, from the visible to the NIR range, by varying their length or aspect ratio (length/width) [1, 88]. However, the non-uniform shape limits the probability of entering the cells and, more importantly, their surface must be modified to avoid cell toxicity, a result of their fabrication method [79, 172, 178].

The discussion of the limitations above suggests that when it comes to investigating the intracellular milieu, with SERS or similar techniques in the NIR, there is no ideal NP that would: (a) easily enter the cell, (b) distribute everywhere in the cytoplasm and nucleus (passing through the pores of the nuclear membrane), and (c) provide adequate signal enhancement in the NIR region. One approach to solve this problem would be to create a more complex NS which would consist of small nanospheres, appropriately modified to avoid vesicle sequestration, which would enter the cell and distribute easily throughout. Subsequently, these nanospheres could aggregate around a vesicle or other endocellular organelle to form a larger NS with NIR plasmon resonance. In this chapter we explore the properties of this novel gold NS, the so-called "shell aggregate." Also, if the shell aggregates mainly absorb light rather than scatter light, they can be considered as potential PAI contrast agents as well.

The shell aggregate model, for the purposes of the simulations, consists of small gold nanospheres which aggregate around a dielectric core and create a monolayer or bilayer shell (Fig. 4.1(A,B)). The bilayer shell was inspired by the bilayer membrane of the cell [179]. These novel gold NSs are expected to produce a combination of the properties of nanoshells and aggregates. Such properties are (i) a shift of the SPR wavelength towards

the more biologically desirable NIR range, and (ii) increased field enhancement as a result of the increased intersphere coupling interactions due to the close distance between neighboring nanospheres.

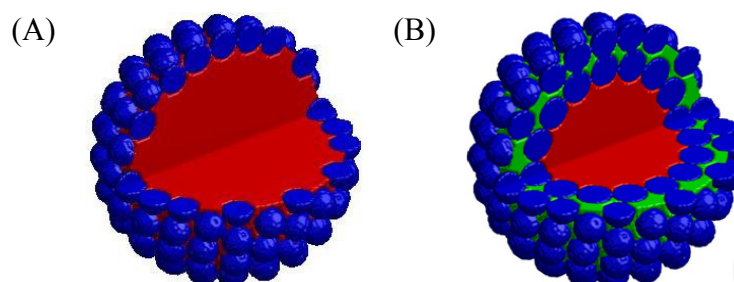


Figure 4.1: Images of (A) a monolayer and (B) a bilayer shell aggregates (Spheres (shell) are in blue, core is in red and layer between nanospheres in green.) A quarter of the shape was removed in each case to better visualize the NSs.

4.2 Classical Gold Nanoparticles

Small and large single nanospheres, aggregates, and nanoshells are the classical (commonly used) gold NPs that have been explored in this chapter. The extinction efficiency factor, Q_{ext} , was calculated, as a function of the wavelength, λ , of an incident electromagnetic wave, ranging from the visible to the NIR. Spectral characteristics, such as amplitude, width, and wavelength maximum, λ_{max} , of the various distinct peaks were determined for each NP. The optical constants for gold were obtained from Johnson and Christy [98]. For small nanosphere radii and shell thicknesses, the optical constants were modified to include the surface damping effect, as described in Chapter 2. Nanorods were not considered for simulations because their properties depend on geometry, orientation, and polarization [29, 180, 181].

4.2.1 Single nanospheres

The extinction efficiency factors of small nanospheres having radius, r , ranging from 5 to 15nm, and larger size nanospheres having a radius of 30, 50, and 70nm were calculated. The interdipole separation, d , was set to be 1nm for all nanosphere radii. Figures 4.2(A) and (B) show the extinction efficiency spectra for the various small and large nanospheres.

For the small nanospheres (Fig. 4.2(A)) only a single peak is observed, which corresponds to the dipole mode, and as the radius of the nanosphere increases the peak is stronger and narrower, while the wavelength maximum, λ_{max} , is slightly blue-shifted, from 529 to 526nm. Since the shifting was rather small, one can assume that the position of the

peak of small nanospheres is independent of the radius and only the width is affected. As the nanosphere radius increases, less surface scattering occurs, which results in smaller damping factors and a narrower spectral width.

The extinction efficiency spectra of larger nanospheres are shown in Fig. 4.2(B). As the nanosphere radius increases, the dipole peak continues to increase in amplitude, to a maximum value of 6.87 ($r = 50\text{nm}$), and then decreases again. Also, the spectral width broadens, due to extrinsic size-effects, while λ_{max} is shifted to longer wavelengths, from 535 to 625nm. At the larger radii a small second peak appears, at $\lambda = 535\text{nm}$, which according to the literature [82] it corresponds to the quadrupole mode. Individually, none of these nanospheres is suitable for NIR imaging. They can, however, be used as building blocks for the shell aggregate.

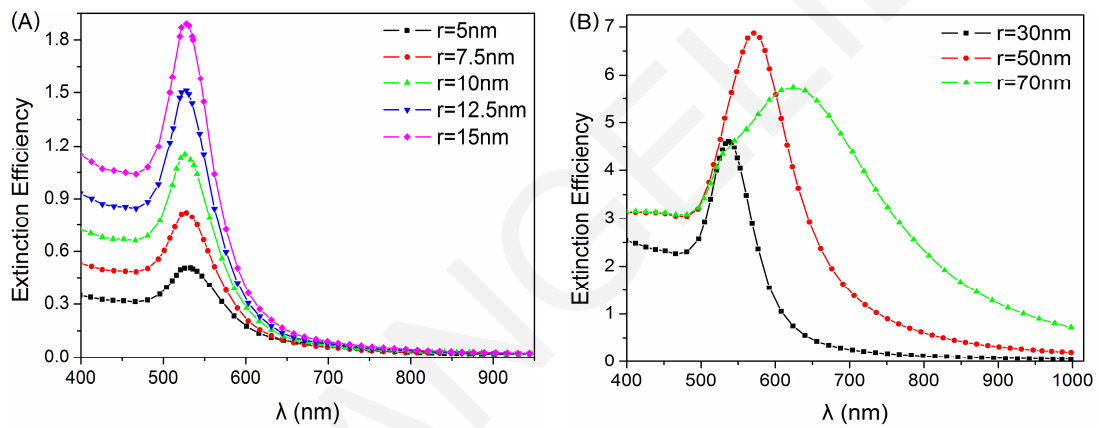


Figure 4.2: Extinction efficiency spectra of (A) small and (B) large gold nanospheres having various radii, r .

4.2.2 Uniform spherical aggregates

Aggregates of small gold nanospheres with an overall spherical structure have been described in Chapter 3. Extinction efficiency factors for the various aggregations were calculated as a function of wavelength, λ , to examine the effect of two variables: (i) the small nanosphere radius, r , and (ii) the outer radius, R , of the spherical aggregate. The interdipole separation, d , was set to be 1nm and the effective radius, r_{eff} , was set to be equal to the value of R . Figure 4.3(A) shows a section (x - y plane) of a spherical aggregate, with the relevant parameters noted, and Fig. 4.3(B) a 3-dimensional image of the same aggregate.

Table 4.1 summarizes the shape parameters and results for the uniform spherical aggregate. The ideal size parameters (R and r) as well as their real values (determined by the geometrical constraints of the shape), the edge-to-edge distance between the

nanospheres, ds , the number of nanospheres, n_{sph} , used to create the aggregate, and the total number of dipoles, N , are given as well. Spectral characteristics of the extinction efficiency, such as the wavelength maximum, λ_{max} , and the corresponding extinction value, Q_{max} , are also provided in Table 4.1.

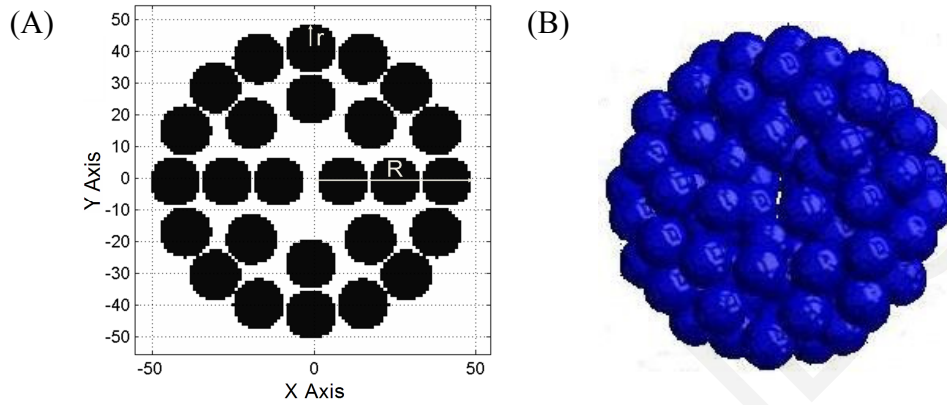


Figure 4.3: (A) Section (x - y plane) of a uniform spherical aggregate having $R \approx 50\text{nm}$, $r = 8\text{nm}$, and (B) a 3-dimensional image of the same aggregate. (Spheres are in blue.)

Table 4.1: Spherical aggregates having various R , r , and ds dimensions

	R (nm)	r (nm)	R_{real} (nm)	r_{real} (nm)	ds (nm)	n_{sph}	N	λ_{max} (nm)	Q_{max}
T1A	30	5	29.09	4.88	0.0–0.82	86	41494	546	3.13
T1B		7.5	29.223	8.00	0.84–6.0	19	40481	543	3.37
T1C	50	5	49.05	4.88	0.0–3.09	314	152350	565	4.89
T1D		7.5	49.13	8.00	0.0–1.76	86	183574	567	5.13
T1E		10	49.02	9.19	0.0–3.47	52	168928	568	5.45
T1F		12.5	49.20	13.0	2.32–11.0	19	174250	595	5.61
T1G	70	15	49.265	15.0	2.18–5.0	11	154830	608	6.52
T1H		5	69.04	4.88	0.0–2.12	830	402202	615.5	6.005
T1I		12.5	69.19	13.0	0.0–5.15	53	486597	660.5	6.56

First simulations were performed for a constant outer radius, $R \approx 50\text{nm}$, and various small nanosphere radii, r , ranging from 5 to 15nm. The edge-to-edge distance, ds , was also varied due to geometrical limitations of the aggregate. Depending on the small nanosphere radius, r , a certain number, n_{sph} , was used to create the aggregate, with different edge-to-edge distances, ds , in order for the nanospheres to fit in the overall structure. Extinction efficiency spectra are shown in Fig. 4.4. No significant NIR plasmon resonance

is observed, since λ_{\max} is only 43nm red-shifted, from 565 to 608nm, with an increase of the peak amplitude and broadening of the width.

Simulations for a constant small nanosphere radius, 5nm and various outer radii of $R \approx 30, 50,$ and 70nm were also performed. Figure 4.4(B) shows the extinction efficiency spectra for this case. The wavelength maximum, λ_{\max} , is red-shifted approximately 70nm, from 546 to 615.5nm, while the peak amplitude is increased and the spectral width broadened. It is important to note that only a single peak is observed in all extinction spectra. Because the distance between the nanospheres was variable, intersphere coupling interactions were not seen in the spectra. The extinction efficiency spectra of the uniform spherical aggregates were used for comparison with the extinction efficiencies of monolayer shell aggregates.

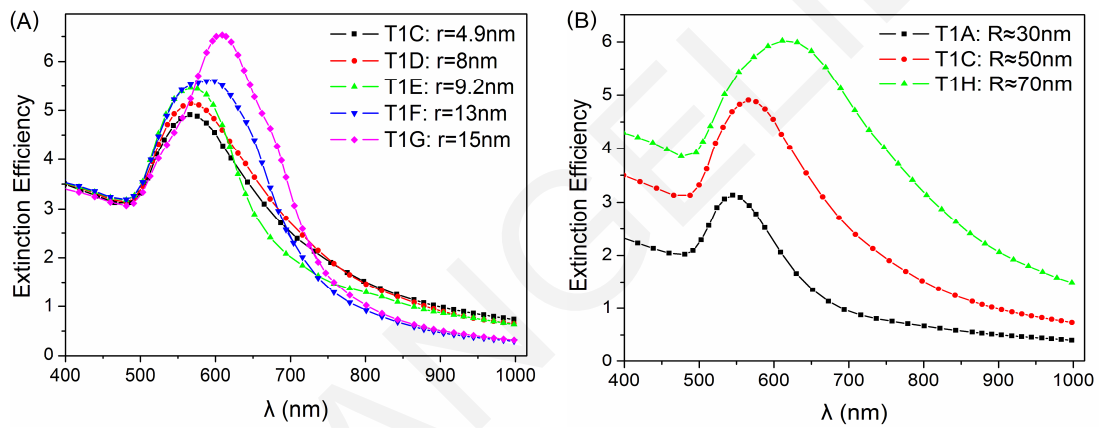


Figure 4.4: Extinction efficiency spectra of uniform spherical aggregates having (A) a constant $R \approx 50$ nm, and various small nanosphere radius, r , and (B) a constant $r \approx 5$ nm, and various outer radii, R .

4.2.3 Nanoshells

Additional simulations were performed to obtain detailed optical properties of nanoshells, which are composed of a dielectric core (silica, SiO_2 , $m_{\text{core}} = 1.44 + i0$, at all wavelengths) and a metal (gold) shell. The extinction efficiency factors, as a function of the wavelength, λ , were examined for two variables: (i) the ratio of the core radius to the outer radius, R_c/R , and (ii) the outer radius, R , of the nanoshell. The shell thickness was defined as $R - R_c$. The interdipole separation, d , was set to be 1nm for the nanoshells of radii of 30, and 50nm. For $R = 70$ nm, d , was set to be 2.5nm to avoid unreasonably large computational memory and time requirements. The effective radius, r_{eff} , was set to be equal to the outer radius, R . Figure 4.5(A) shows a section (x - y plane) of an $R_c/R = 0.6$ ($R = 50$ nm, shell = 20nm) nanoshell, with the relevant parameters noted, and Fig. 4.5(B) a 3-dimensional

image of the same nanoshell, with a quarter removed for better visualization of the core/shell structure.

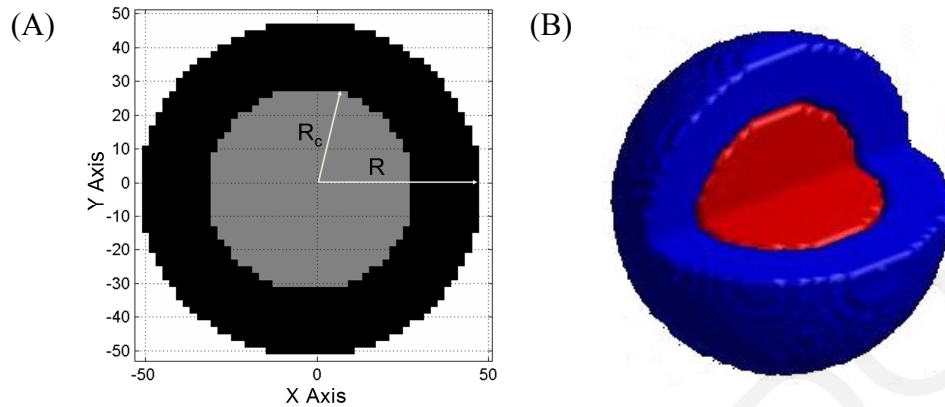


Figure 4.5: (A) Section (x-y plane) of an $R_c/R = 0.6$ nanoshell, and (B) a 3-dimensional image of the same nanoshell. (Metal shell is in blue and dielectric core in red.)

First simulations were performed for a constant outer radius $R = 50\text{nm}$ and various ratios of core to outer radius, R_c/R , ranging from 0.4 to 0.8. These ratios correspond to the shell thicknesses ranging from 30 to 10nm, respectively. From Fig. 4.6(A), only a single peak is observed, the dipole mode, and, as the ratio is increased, the amplitude of the peak is slightly increased and the spectral width is broadened, while λ_{max} is red-shifted 125nm, from 580 to 705nm.

Simulations were also performed for various outer radii R . Figure 4.6(B) shows the extinction efficiency spectra for nanoshells having a constant core-shell ratio, $R_c/R = 0.5$, and various outer radii, R , of 30, 50, and 70nm. For this ratio, the shell thicknesses correspond to half the outer radius of each nanoshell. Again, a single peak is observed and as R is increased, the amplitude increases to a maximum value of 6.95 and then decreases again with a spectral broadening. The wavelength maximum, λ_{max} , is 80nm red-shifted, from 560 to 640nm. For $R = 70\text{nm}$, a second peak starts to emerge, at $\lambda = 535\text{nm}$. The extinction spectra of nanoshells (Fig. 4.6(B)) are similar to the extinction spectra of single gold nanospheres (Fig. 4.2(B)). Again, these results were used for comparison with the monolayer shell aggregates.

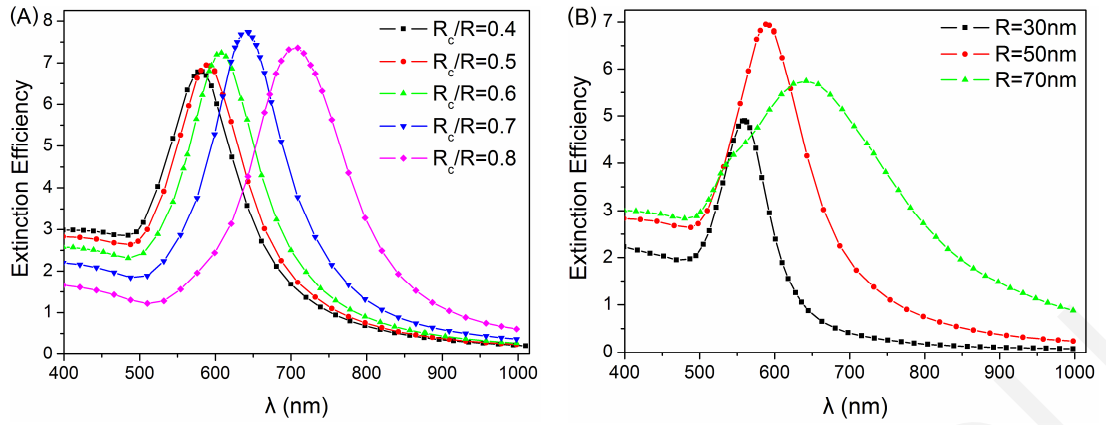


Figure 4.6: Extinction efficiency spectra of silica/gold – core/shell NPs having (A) a constant outer radius, $R = 50\text{nm}$, and various ratios, R_c/R , and (B) a constant ratio of $R_c/R = 0.5$, and various outer radii, R .

4.3 Monolayer/Bilayer Shell Aggregates

In order to provide a thorough understanding of the optical properties of the novel gold shell aggregates, as well as to comprehend the dependence of these properties on the shape parameters, a series of simulations was performed. The varying shape parameters included:

- The small nanosphere radius, r .
- The edge-to-edge distance between the nanospheres, ds .
- The outer radius, R .
- The distance between the nanosphere layers, dl , for the bilayer model.

For the monolayer shell aggregate, the outer radius, R , included the radius of the spherical dielectric core and the radius of small nanospheres, $R = R_c + r$, whereas for the bilayer, the outer radius was equal to $R = R_{c1} + r$, where R_{c1} was the radius of the outer nanosphere layer. The distance between the nanosphere layers was equal to $dl = R_{c1} - R_{c2} - 2r$, where R_{c2} was the radius of the inner nanosphere layer. Figures 4.7(A), and (B) show a section (x - y plane) of a monolayer and bilayer shell aggregate structure, respectively, with the various parameters noted on the figures. Figures 4.7(C), and (D) show the corresponding 3-dimensional images of the shell aggregates, with a quarter removed for better visualization of the core/shell structure.

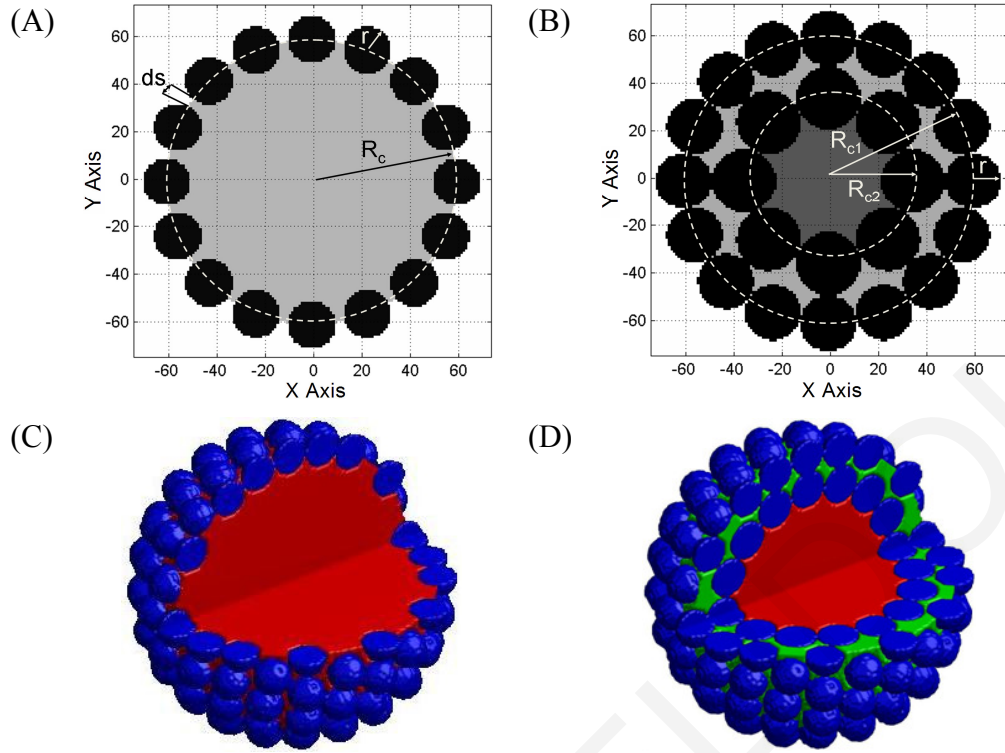


Figure 4.7: (A)-(B) Section (x - y plane) of a monolayer, and a bilayer shell aggregate, having shape parameters of $R \approx 70\text{nm}$, $r \approx 10\text{nm}$. (C)-(D) 3-dimensional images of the same shell aggregates.

The outer radius, R , for both shell aggregates, was set to be approximately 30, 50, and 70nm, whereas the nanosphere radius, r , was varied from 5 to 15nm. The edge-to-edge distance between the nanospheres, ds , was varied from 0 to 5nm. The interdipole separation, d , was set to be 0.5 or 1nm, for $R \approx 30\text{nm}$, and 1nm for $R \approx 50$, and 70nm. The effective radius, r_{eff} , was set to be equal to R . The optical constants for gold were obtained from Johnson and Christy [98]. Since small nanospheres were considered in the design, the optical constants were modified to include the surface damping effect, as described in Chapter 2. For the shell aggregate simulations, the dielectric core was assumed to be water ($m_{\text{core}} = 1.33 + i0$, at all wavelengths). The medium between the two layers of the bilayer assumed to have a refractive index of $m_{\text{lay}} = 1.47 + i0$ [182], equivalent to that of a cell membrane.

It should be noted that the parameters, R , r , and ds , are not independent but are related by the geometrical dimensions of the shell aggregate structure. As a result, when one parameter is varied, other values have to change as well so that the nanospheres will fit on the overall NS surface. Also, all the extinction, absorption, and scattering efficiency factors were normalized, using the ratio of the number of dipoles, N , to the number of the nanosphere dipoles, N_{sph} ,

$$Q'_{\text{ext,abs,sca}} = Q_{\text{ext,abs,sca}} \times \frac{N}{N_{\text{sph}}}. \quad (4.1)$$

The normalization was performed so that the results of the simulations would be comparable. After normalization, the efficiency factors represent the optical response of the gold nanospheres (shell), and not that of the overall NS (nanospheres shell plus water core), reflecting the fact that the small nanospheres interact with each other, while the water core simply shifts their SPRs to longer wavelengths. Also, the normalized efficiency factor remains dimensionless parameter, since it is multiplied and divided with unitless parameters.

The tables (4.2 to 4.6) in the following sections show the shape parameters (R , r , d , d_s , d_l , and d_{dense}) for the various shell aggregates. The real values of outer radius, R , small nanosphere radius, r , the edge-to-edge distance between the nanospheres, d_s , the number of nanospheres, n_{sph} , the total number of dipoles, N , and the number of nanosphere dipoles, N_{sph} , used to create the shell aggregate, are shown too. Spectral characteristics, such as the wavelength maximum, λ_{max} , and the corresponding normalized extinction value, Q'_{max} , are also provided in the tables. The extinction efficiency spectra for each outer radius, R , were investigated relative to the nanosphere radius, r , the edge-to-edge distance, d_s , the interdipole separation, d , and the arrangement of the nanospheres (densely-packed or not).

It should also be noted that the value l_{eff} , used for the size-dependent modification, was set to be equal to the ideal value of the radius, r , for all simulations, except when the real value, r_{real} , differ significantly from the ideal value due to geometrical constrains (e.g., in the case of a monolayer having $R \approx 30\text{nm}$, and $r = 10\text{nm}$, were r_{real} was 7.65nm). Figure 4.8(A) shows the results obtained when different l_{eff} values were used. Only a slightly decrease of the peak intensity is observed. For larger size NSs, the modification with either input or real value of r did not have any significant effect on the spectra (Fig. 4.8(B)).

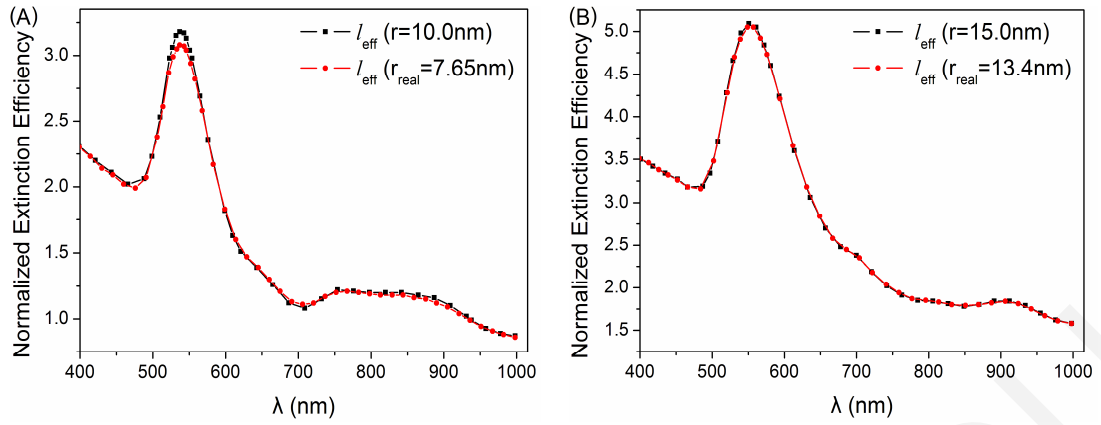


Figure 4.8: Effect of the different value of r (input, and real) used in size-dependent, I_{eff} , modification for the monolayer shell aggregates having (A) $R \approx 30\text{nm}$, $d = 1\text{nm}$, and (B) $R \approx 50\text{nm}$, $d_s = 0\text{nm}$.

4.3.1 Monolayer shell aggregate: the effect of small nanosphere radius (r)

Initially, the effect of the small nanosphere radius, r , on the monolayer shell aggregate optical response, was investigated. For three outer radii, $R \approx 30, 50,$ and 70nm , the extinction efficiency factors were calculated for various small radii, r . Tables 4.2–4.4 show the ideal and real shape parameters and the spectra maxima. Even though the edge-to-edge distance, d_s , was preferred to have been constant, it was not feasible due to the geometrical limitations imposed by the arrangement of the nanospheres around the spherical core. For a given nanosphere radius, r , only a unique number of spheres, n_{sph} , could fit around the core of a shell aggregate, with radius R , with an appropriate intersphere spacing which was different for each combination of r and R .

Table 4.2: Monolayer shell aggregates having $R \approx 30\text{nm}$, and variable r , and d

	d (nm)	r (nm)	R_{real} (nm)	r_{real} (nm)	d_s (nm)	n_{sph}	N	N_{sph}	λ_{max} (nm)	Q'_{max}
T2A	1	5	29.08	4.88	0.0–0.82	128	82259	31914	553	3.10
T2B		10	27.16	7.65	0.00	32	52775	33750	538	3.185
T2C		7.5	29.22	8.00	0.84	32	66171	38378	542	3.25
T2D	0.5	5	29.555	4.88	0.0–0.82	128	660411	256554	548	3.07
T2E		10	27.54	7.65	0.00	32	423191	271218	538	3.05
T2F		7.5	29.62	8.00	0.84	32	530939	307934	539	3.22

Figures 4.9(A), and (B) show the extinction efficiency spectra of a monolayer shell aggregate having an outer radius $R \approx 30\text{nm}$, for various nanosphere radii, $r = 5, 7.65,$ and 8nm , calculated using interdipole separations of $d = 1\text{nm}$ for (A), and 0.5nm for (B). The

wavelength maximum, λ_{\max} , appeared to be largely unaffected by r , since it only fluctuated between 538–553nm. In some cases (T2C, and T2F, $r = 8\text{nm}$), a second peak appeared, at $\lambda = 610\text{nm}$, while in others (T2B, $r = 7.65\text{nm}$), increased extinction efficiency was observed in the NIR. The second peak was the result of the interaction in the gap between the nanospheres since it appeared for small edge-to-edge distances between nanospheres, d_s , (e.g., 0.84nm). The NIR increase may be explained by the fact that, in those particular structures, the nanospheres were exactly adjacent ($d_s = 0\text{nm}$). In both cases, intersphere coupling interactions were observed.

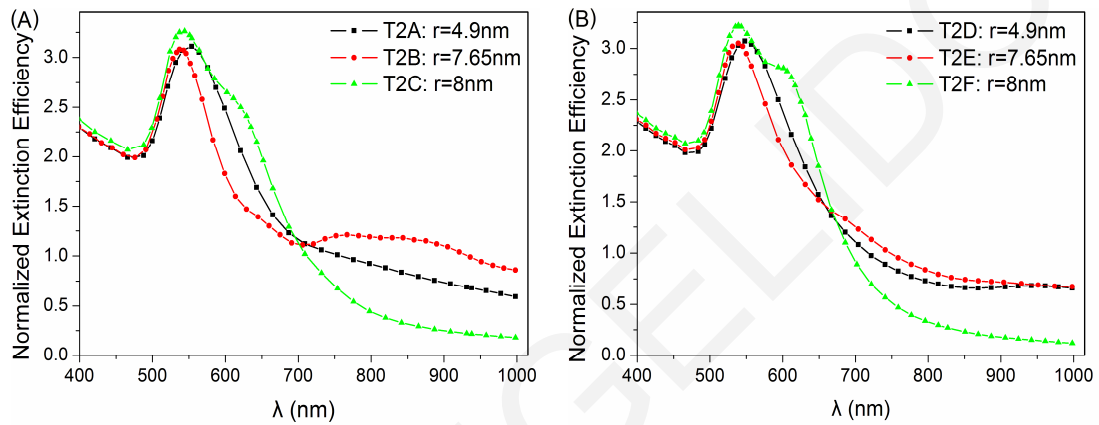


Figure 4.9: Normalized extinction efficiency spectra of monolayer shell aggregates having $R \approx 30\text{nm}$, for various nanosphere radii, r , and interdipole separations, d , of (A) $d = 1\text{nm}$, and (B) $d = 0.5\text{nm}$.

Table 4.3: Monolayer shell aggregates having $R \approx 50\text{nm}$, and variable r

	Dense	r (nm)	R_{real} (nm)	r_{real} (nm)	d_s (nm)	n_{sph}	N	N_{sph}	λ_{\max} (nm)	Q'_{\max}
T3A	0	5	49.08	5.00	2.42–2.85	320	425951	84822	556	5.935
T3B		7.5	49.13	8.00	0.39–1.76	128	385419	140990	558	5.59
T3C		10	49.17	10.0	1.86	80	363891	175526	566.5	6.175
T3D		12.5	49.20	13.0	2.32	32	305452	165157	583	6.04
T3E		15	48.10	13.4	0.00	32	283145	181158	551.5	5.09
T3F	1	5	51.02	6.21	0.0–0.43	320	467079	162474	592	5.84
T3G		7.5	50.02	8.19	0.0–1.375	128	391801	152118	558.5	5.25
T3H		10	50.17	10.93	0.00	80	394253	229506	573	5.82
T3I		15	48.10	13.39	0.00	32	283145	181158	553	5.06
T3J		12.5	51.04	14.16	0.00	32	334435	213702	553	5.04

Figures 4.10(A), and (B) show the normalized extinction efficiency spectra of monolayer shell aggregates of various nanosphere radii, ranging from 5 to 15nm, for the outer radii of $R \approx 50$, and 70 nm, respectively. The wavelength maximum λ_{\max} ranged between 551–583nm, for $R \approx 50$ nm, and 544–598nm, for $R \approx 70$ nm. As seen in Tables 4.3, and 4.4 the edge-to-edge distance, ds , was also varied and that appeared to affect the spectra. Again, a tail in the NIR was observed in the case of $R \approx 50$ nm and $r = 13.4$ nm (T3E) where the spacing between nanospheres was zero and intersphere coupling interactions occurred. The interactions were more pronounced in $R \approx 70$ nm, $r = 8$ nm (T4B) spectrum, where the nanospheres were at a distance close to 1.5nm and a second peak, or a shoulder appeared at $\lambda = 685$ nm. As the radius of the nanosphere varied, there was an apparent inconsistency in the way extinction amplitude and spectral width increased or decreased. This, again, is attributed to the different and variable distances between the small nanospheres imposed by the geometrical limitation of the shell aggregate structure.

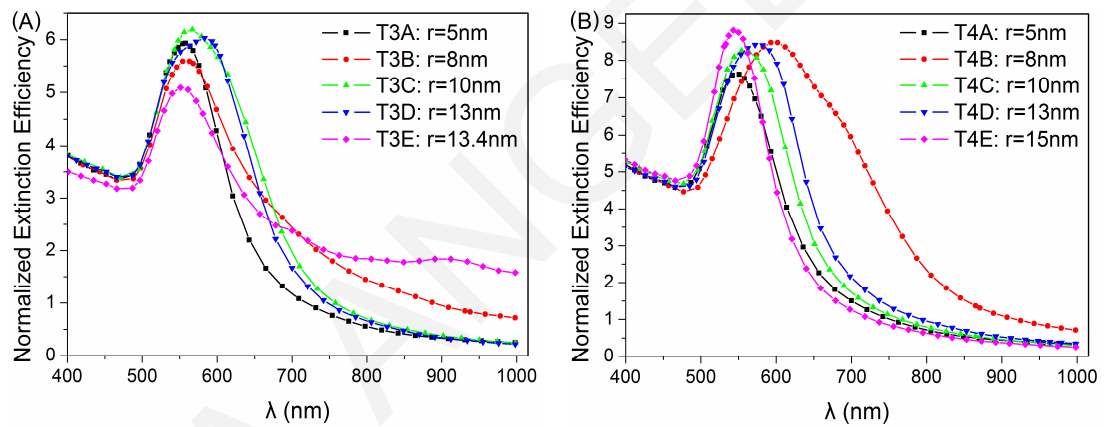


Figure 4.10: Normalized extinction efficiency spectra of monolayer shell aggregates having (A) $R \approx 50$ nm, (B) $R \approx 70$ nm, for various small nanosphere radii, r .

Table 4.4: Monolayer shell aggregates having $R \approx 70$ nm, and variable r

	dense	r (nm)	R_{real} (nm)	r_{real} (nm)	ds (nm)	n_{sph}	N	N_{sph}	λ_{\max} (nm)	Q'_{\max}
T4A	0	5	69.06	5.00	2.74–7.48	512	1218791	134190	546	7.63
T4B		7.5	69.09	8.00	1.10–1.70	320	1179739	346586	598	8.50
T4C		10	69.12	10.0	3.41–5.37	128	1051267	276194	561	8.32
T4D		12.5	69.145	13.0	5.15	80	985022	385977	576	8.425
T4E		15	69.19	15.0	12.095	32	835769	253608	544	8.79
T4F	1	7.5	70.06	8.55	0.0–0.59	320	1221881	425034	596	7.34
T4G		10	71.11	11.705	0.0–1.96	128	1142547	443826	587	6.84
T4H		12.5	72.12	15.58	0.0	80	1142249	664962	583	6.47

To investigate the impact of a small intersphere spacing, on the extinction spectra, densely-packed shell aggregates were further considered. As seen in Tables 4.3, and 4.4, in a densely-packed arrangement, the value of the radius of the small nanospheres was changed so that the nanospheres could be positioned as close as possible. This resulted in a less variable d_s compared to the non-dense shell aggregates. Figures 4.11(A), and (B) show the normalized extinction efficiency spectra of densely-packed monolayer shell aggregates of various r and for outer radii of $R \approx 50$, and 70 nm, respectively. The wavelength maximum, λ_{\max} , ranged between 553 – 592 nm for $R \approx 50$ nm and 583 – 596 nm for $R \approx 70$ nm. The spectral shape appeared to be largely unaffected when the intersphere spacing was either 0 or greater than 1 nm. This is also attributed to the coupling effects, due to the small d_s , that affect the spectrum in the NIR region.

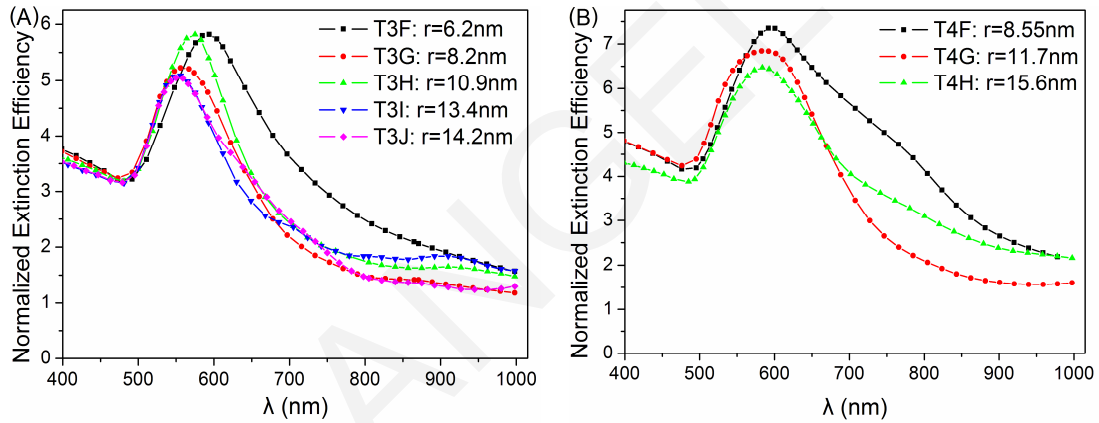


Figure 4.11: Normalized extinction efficiency spectra of densely-packed monolayer shell aggregates having (A) $R \approx 50$ nm, (B) $R \approx 70$ nm, and various small nanosphere radii, r .

It should be noted that, the larger the outer radius, R , the more red-shifting occurs. Also the maximum wavelength does not depend just on the nanosphere radius, but on the combination of r and d_s . The distance between the small nanospheres plays a critical role in the NIR optical response of the monolayer shell aggregates.

4.3.2 Monolayer shell aggregate: the effect of various nanosphere edge-to-edge distance (d_s)

A series of simulations was performed to examine the effect of the intersphere spacing or distance between the small nanospheres. The edge-to-edge distance, d_s , was varied while keeping the radius, r , as constant as allowed by the geometrical limitations. For three outer radii $R \approx 30$, 50 , and 70 nm, the extinction efficiency spectra were calculated for d_s ranging

from 0 to 5nm. The nanospheres radius, r , was slightly varied, for each d_s , in order for the same n_{sph} , to fit around the spherical core. Tables 4.5, and 4.6 show the ideal and real shape parameters and the spectra maxima.

Table 4.5: Monolayer shell aggregates having $R \approx 30\text{nm}$, $r \approx 7.5\text{nm}$, and variable d , and d_s

	d (nm)	r (nm)	d_s (nm)	R_{real} (nm)	r_{real} (nm)	n_{sph}	N	N_{sph}	λ_{max} (nm)	Q'_{max}
T5A	1	10	1.0	27.03	7.15	32	49367	27570	543	3.305
T5B			2.0	26.15	6.65		46133	22458	543	3.50
T5C			3.0	26.02	6.15		43085	17394	539	3.49
T5D	0.5	10	0.5	27.09	7.40	32	407237	244746	538	3.15
T5E			1.0	27.04	7.15		393293	220470	543	3.33
T5F			1.5	26.59	6.90		380039	198714	543	3.50
T5G			2.0	26.54	6.65		367931	177558	543	3.53

Figures 4.12(A) and (B) show the normalized extinction efficiency spectra of a monolayer shell aggregate having an outer radius $R \approx 30\text{nm}$ and various edge-to-edge distances between nanospheres, d_s . For an interdipole separation, d , of 1nm, d_s was varied from 0 to 3nm in 1nm steps (Fig. 4.12 (A)). For d of 0.5nm, d_s was varied with a 0.5nm step (Fig. 4.12(B)). For $d_s = 0\text{nm}$, a NIR tail appeared in the extinction efficiency spectra. Unfortunately, the low amplitude of the extinction efficiency along that tail makes it less useful as a potential broad NIR plasmon excitation band. For $d_s = 0.5\text{nm}$ (Fig. 4.12(B), T5D) a second peak appeared at $\lambda = 645\text{nm}$, and as the d_s increased, the second peak blue-shifted and merged with the first peak, thus explaining the broadening observed in the $d_s = 1\text{nm}$ spectrum. As the d_s is increased even further only a single narrower peak was observed. Even though the radius, r was slightly different for different simulations that did not affected the spectra.

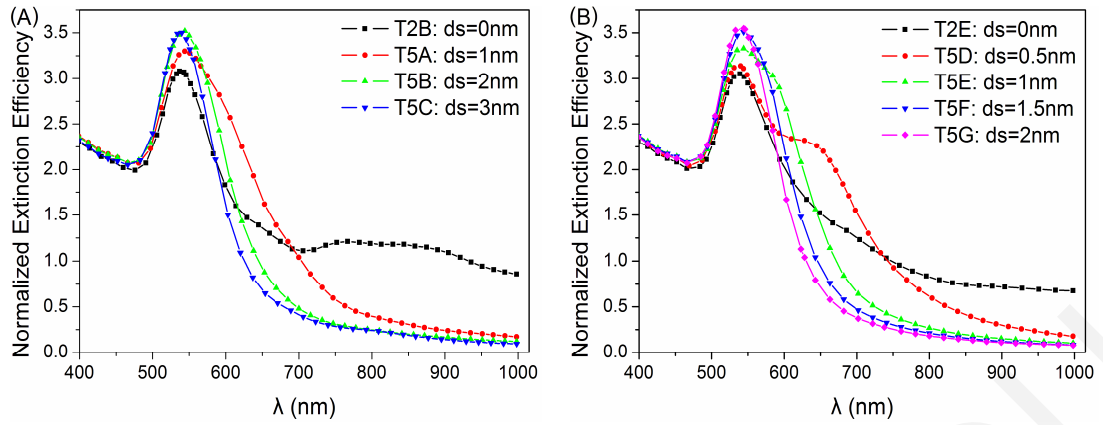


Figure 4.12: Normalized extinction efficiency spectra of monolayer shell aggregates having $R \approx 30\text{nm}$, and various distances, ds , for interdipole separation, d , of (A) $d = 1\text{nm}$, and (B) $d = 0.5\text{nm}$.

Table 4.6: Monolayer shell aggregates having (i) $R \approx 50\text{nm}$, $r \approx 15\text{nm}$, (ii) densely-packed, $R \approx 70\text{nm}$, $r \approx 12.5\text{nm}$, and various ds

	dense	R (nm)	r (nm)	ds (nm)	R_{real} (nm)	r_{real} (nm)	n_{sph}	N	N_{sph}	λ_{max} (nm)	Q'_{max}
T6A	0	50	15	1.0	47.21	12.89	32	271583	161886	548, 644	5.13, 5.24
T6B				2.0	47.10	12.39		261119	142742	593	5.92
T6C				3.0	46.22	11.89		251057	126774	567	6.31
T6D				5.0	45.19	10.89		233903	97746	547	6.52
T6E	1	70	12.5	1.0	72.01	15.08	80	1106981	603366	574, 702	6.56, 6.31
T6F				2.0	71.11	14.58		1074587	544962	573, 637	6.935, 7.11
T6G				3.0	71.01	14.08		1044119	491178	603	7.65
T6H				5.0	70.01	13.08		989021	392874	576	8.35

Figure 4.13(A,B) illustrates the dependence of extinction on the distance ds for the larger monolayer shell aggregates. When the nanospheres were touching ($ds = 0\text{nm}$) a NIR tail was observed in both Fig. 4.13(A), and (B). As ds was increased, a second peak emerged at $\lambda = 644\text{nm}$, for $R \approx 50\text{nm}$. By increasing ds even more, the second peak shifted to shorter wavelengths, and merged with the first peak, finally resulting in only a single narrower peak at $\lambda = 547\text{nm}$ (Fig. 4.13(A)). For the larger, $R \approx 70\text{nm}$ monolayer shell aggregate (Fig. 4.13(B)) two distinct peaks and a small shoulder in the NIR were observed for a $ds = 1\text{nm}$. When ds was increased to 2nm , the second peak at $\lambda = 702\text{nm}$ and the shoulder at $\lambda = 830\text{nm}$, both blue-shifted, increased in amplitude and started to merge with

the first peak at $\lambda = 573\text{nm}$. As the distance d_s increased even more, the two red-shifted peaks merged with the first, and finally only a single, blue-shifted peak was observed, at $\lambda = 576\text{nm}$, with a less broad width and an increased intensity compared to the other spectra.

The effect of the distance between nanospheres on the extinction spectra appears to fall into three interesting regimes. First, for adjacent nanospheres, where the edge-to-edge distance is 0nm , an increased extinction, extending into the NIR range in the form of a long tail in the spectrum, was observed for all outer radii. Second, for an edge-to-edge distance between 0.5 and 1nm , the NIR tail disappeared but the extinction efficiency spectrum was significantly broadened by a second and, even, a third red-shifted peak appearing at NIR wavelengths. Third, for distances larger than 1nm , the second and third peaks blue-shifted and merged with the first peak, at green wavelengths, and as the distance was increased even further the spectrum remained almost constant, resembling that of individual single nanospheres.

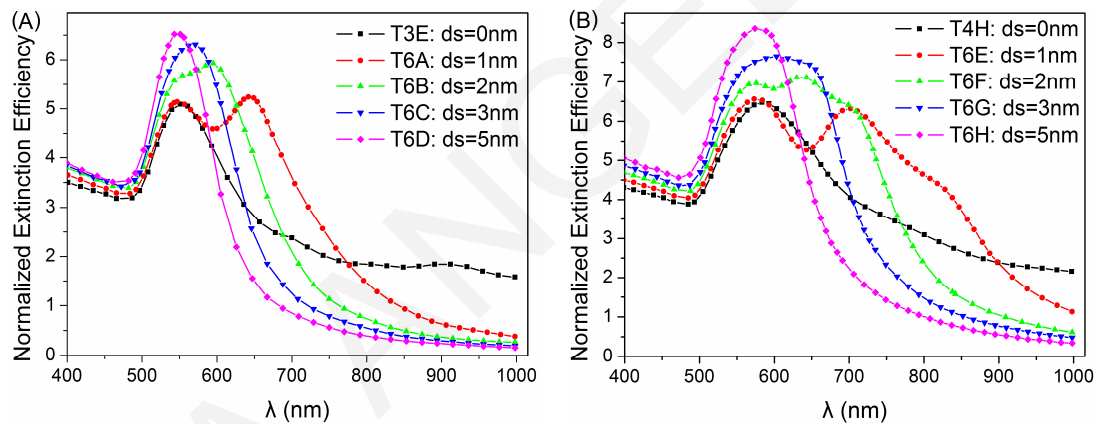


Figure 4.13: Normalized extinction efficiency spectra of monolayer shell aggregates having (A) $R \approx 50\text{nm}$, (B) densely-packed, $R \approx 70\text{nm}$, and various distances, d_s .

4.3.3 Monolayer shell aggregate: the effect of the outer radius (R)

The outer radius, R , also affects the extinction efficiencies of the monolayer shell aggregates. Figures 4.14(A), and (B) display the dependence of the extinction efficiency spectra on R for edge-to-edge distances, d_s of 0nm for (A) and 1nm for (B). As the outer radius increased, the extinction efficiency amplitude increased, broadened and shifted to longer wavelengths by 45nm , while the NIR tail intensified (Fig. 4.14(A)). For a distance, $d_s = 1\text{nm}$, as R increased, a second peak appeared and progressively red-shifted (Fig. 4.14(B)). This second peak is probably the result of intersphere coupling interactions. The nature of these interactions will be further explored in Section 4.4.

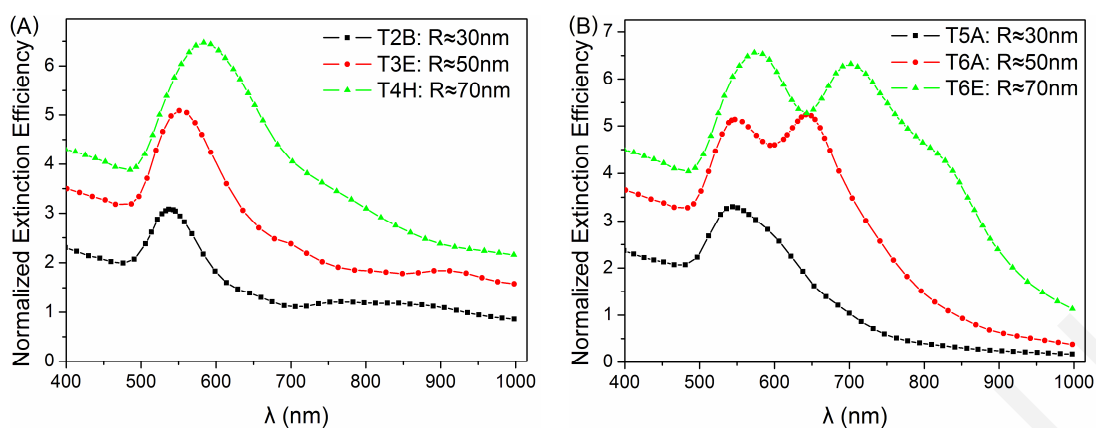


Figure 4.14: Comparison between outer radii, R, for monolayer shell aggregates having (A) $ds = 0\text{nm}$, and (B) $ds = 1\text{nm}$.

Table 4.7 provides the normalized extinction efficiency values for some common SERS excitation wavelengths $\lambda = 635$, and 785nm for various monolayer shell aggregates. Small size monolayer shell aggregates did not provide adequate efficiency values at the wavelengths of interest. Increasing the size of the monolayer shell aggregate, larger extinction values were obtained due to enhanced coupling interactions between the small nanospheres.

Table 4.7: Wavelength specific extinction values for various monolayer shell aggregates

		R (nm)	r_{real} (nm)	ds (nm)	$Q'_{635\text{nm}}$	$Q'_{785\text{nm}}$
1	T2B	30	7.65	0.0	1.43	1.20
2	T2C		8.0	0.0–0.82	2.30	0.49
3	T3E	50	13.4	0.0	3.09	1.84
4	T3F		6.2	0.0–0.43	5.04	2.605
5	T6A		13.0	1.0	5.18	1.68
6	T4B	70	8.0	1.10–1.70	7.80	2.74
7	T4F		8.55	0.0–0.59	6.75	4.43
8	T6E		15.1	1.0	5.33	4.82
9	T6F		14.6	2.0	7.11	2.81
10	T6G		14.1	3.0	7.51	1.67

For an incident wavelength of $\lambda = 635\text{nm}$, the best maximum extinction value obtained was 7.80, provided by a monolayer shell aggregate having dimensions of $R \approx 70\text{nm}$, $r = 8\text{nm}$ and $ds = 1.1$ to 1.7nm . For a NIR incident wavelength of $\lambda = 785\text{nm}$, the extinction value was significantly lower, although still useful, for $R \approx 70\text{nm}$. Again, the best maximum extinction value appeared for the densely-packed monolayer shell aggregate

with $R \approx 70\text{nm}$, $r = 15\text{nm}$, and $d_s = 1\text{nm}$. The extinction efficiencies of these two monolayer shell aggregates have satisfactory values, making them suitable for SERS applications.

4.3.4 The effect of interdipole separation (d) on the calculations

To conclude the analysis of the monolayer shell aggregates, extinction efficiency spectra with different interdipole separations, d , were compared to determine whether the optical properties of monolayer shell aggregates, were accurately calculated. Given the method's computational limitations, calculation of the extinction efficiencies using smaller interdipole separations was only feasible for the smaller monolayer shell aggregate with an outer radius of $R \approx 30\text{nm}$. Figures 4.15(A) and (B) show the extinction spectra for two interdipole separations, 1 and 0.5nm, for two monolayers having small nanosphere radii of $r = 8\text{nm}$ in (A), or a distance $d_s = 0\text{nm}$ in (B). It appears that the interdipole separation, d , becomes a significant limitation when the intersphere spacing, which causes the finer spectral features, is less than the interdipole spacing. In Fig. 4.15 (A) d_s is 0.84nm whereas in Fig. 4.15 (B) is 0nm. Therefore, for accurate representation of the extinction efficiency spectra, care should be taken to use the appropriate simulation parameters. However, this may not always be possible due to computational limitations for the larger grids which are necessary to support the larger outer radii, R .

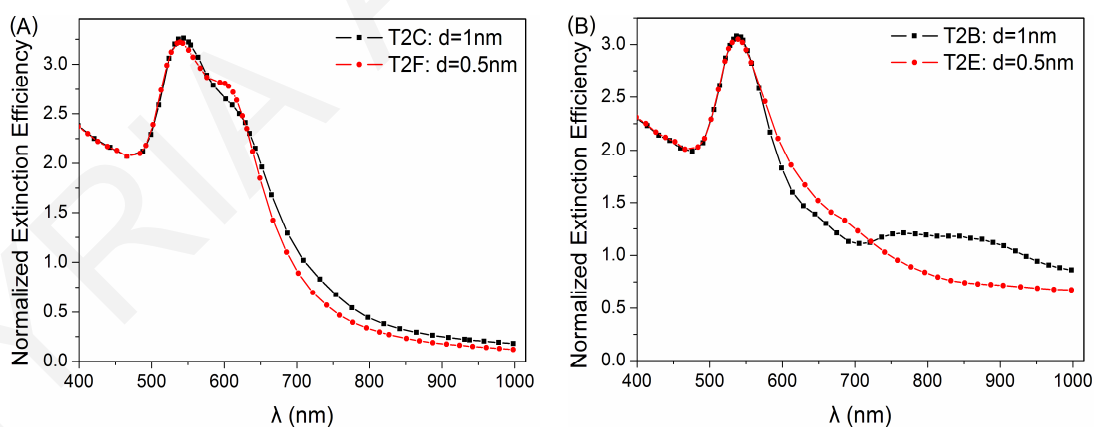


Figure 4.15: Comparison between different interdipole separations, d , for a monolayer shell aggregate having $R \approx 30\text{nm}$, and (A) $r = 8\text{nm}$, (B) $d_s = 0\text{nm}$.

4.3.5 Comparison with classical nanoparticles

Nanospheres and nanoshells are the most commonly used types of gold NPs for biological and biomedical applications. The normalized extinction efficiencies of monolayer shell

aggregates were compared with the extinction efficiencies of classical NPs, and spherical aggregates. Figures 4.16(A)–(C) show the comparison between nanospheres, nanoshells, spherical aggregates and monolayer shell aggregates, all having similar dimensions. The outer radius was equal for all structures as was the small nanosphere radius of the shell aggregate and the shell thickness of the nanoshell.

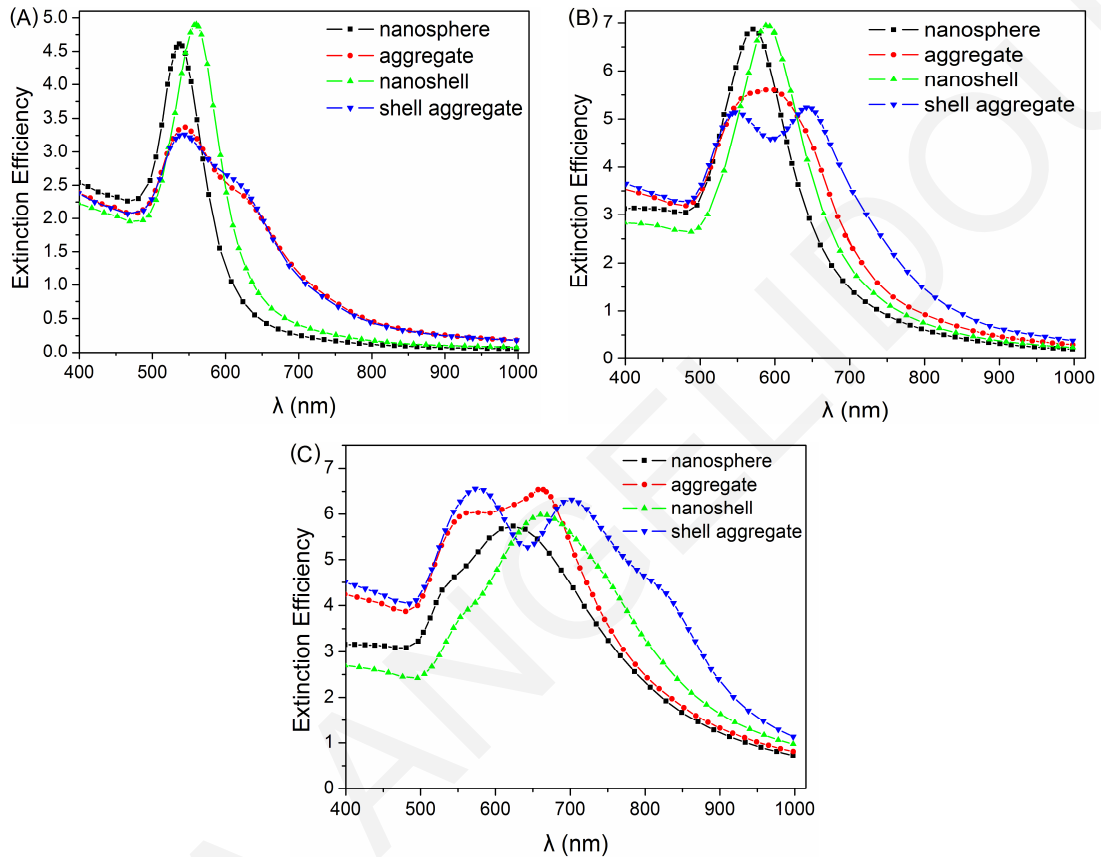


Figure 4.16: Comparison between normalized extinction efficiency spectra of monolayer shell aggregate with that of the corresponding classical NPs. The structures have dimensions of (A) $R \approx 30\text{nm}$ ($r = 8\text{nm}$, shell = 15nm ($R_c/R = 0.5$)), (B) $R \approx 50\text{nm}$ ($r = 12.5\text{nm}$, shell = 25nm ($R_c/R = 0.5$)), and (C) $R \approx 70\text{nm}$ ($r = 12.5\text{nm}$, shell = 25nm ($R_c/R \approx 0.64$)).

For smaller outer radius, R , the nanoshell exhibited a similar, though slightly red-shifted, spectrum to that of a single nanosphere, due to the thick shell thickness. Also, the spherical aggregate displayed a similar extinction spectrum with the monolayer. The monolayer shell aggregate consist of 32 spheres, with $d_s = 0.84\text{nm}$, while the spherical aggregate consist of 19 nanospheres, arranged with varied d_s ranging from 0.84 to 6nm . From this, one can assume that only the nanospheres that interact with each other contribute to the extinction spectrum, and the smaller the distance, the stronger the interaction. For the larger outer radius, R , the extinction efficiency spectra of all structures were broader and red-shifted. However, the monolayer shell aggregates exhibited two and

even three distinct peaks with broader widths and more shifted to the NIR wavelength region, compared to the other gold NPs. This distinct NIR efficiency can be particularly useful for biomedical applications.

4.3.6 Bilayer shell aggregates

Drawing inspiration from the bilayer structure of the cell membrane, an additional series of simulations was performed to answer the question of what happens to the optical properties if a second layer is added to the shell aggregate (Fig. 4.1(B)). A comparison of the normalized extinction efficiency spectra of monolayer and bilayer shell aggregates for various nanosphere radii, are presented in Fig. 4.17(A)–(F). Adding a second layer of nanospheres only caused very minor intensity differences. For the larger bilayer shell aggregates there was some divergence between the spectra. The differences may be attributed to the varying distances, d_s , (i) between the non-densifying and densely-packed shell aggregates and (ii) on the outer layer and the inner layer on the bilayer shell aggregate.

The inner layer did contribute, although at a very small degree, to the bilayer extinction spectrum, especially when the inner layer had different nanosphere radii and edge-to-edge distances d_s from those of the outer layer. However, the optical properties of the bilayer shell aggregate are mainly attributed to the outer layer of the shell aggregate, as can be seen in Fig. 4.17. This can be explained by the fact that the inner layer nanospheres are positioned behind the nanospheres of the outer layer. As demonstrated by Khlebtsov et al. [183], hidden spheres in a cluster do not contribute to the overall extinction spectra, where the interactions of the outer layer dominate. As a result, no major differences are observed between the monolayer and bilayer shell aggregates since the additional, inner, layer did not significantly contribute to the extinction spectrum. Given these results, there was no further investigation of the bilayer NSs. Tables (shape parameters) and figures of the bilayer shell aggregates can be found in Appendix C. This explanation is further explored in the next section.

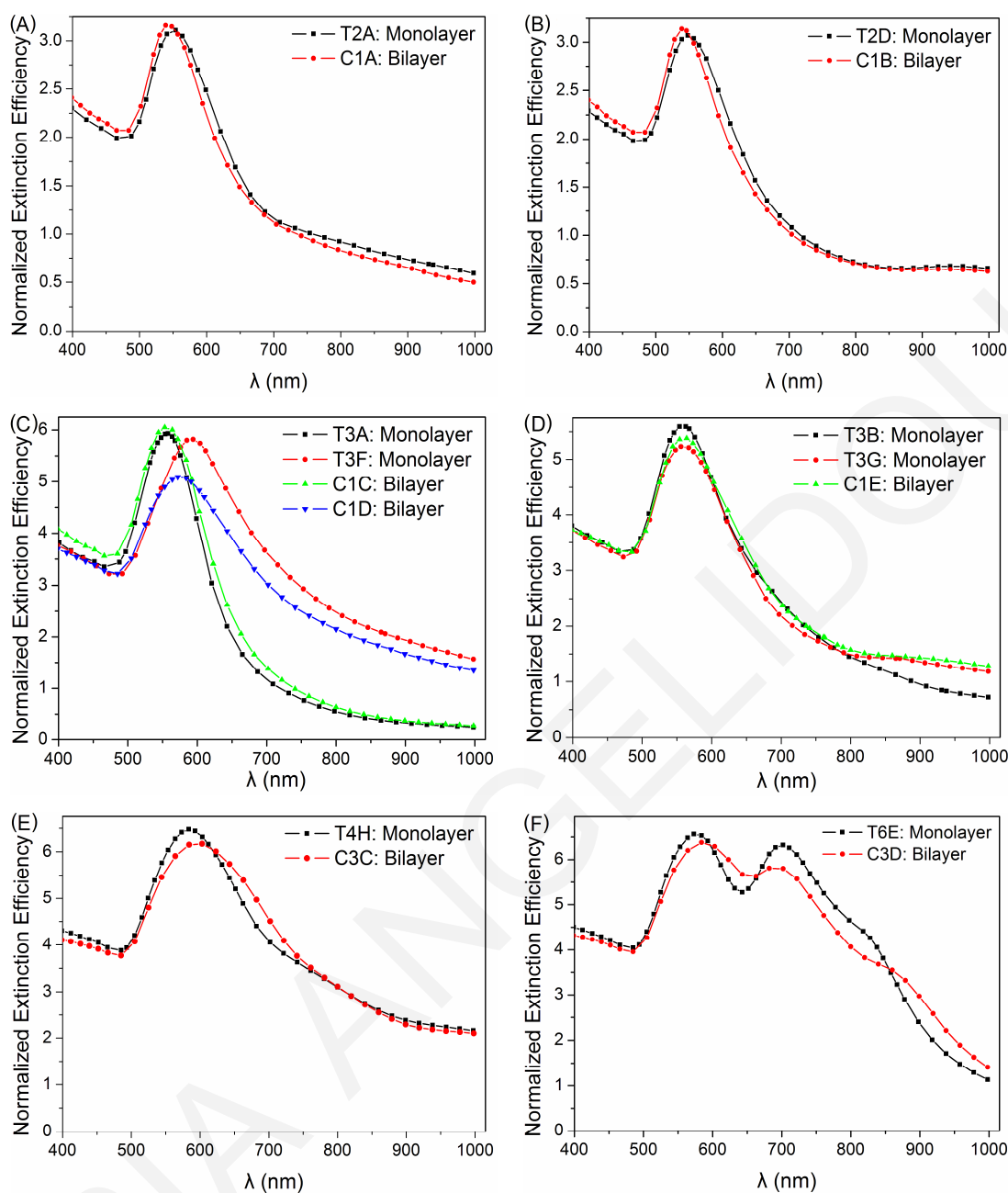


Figure 4.17: Comparison spectra between monolayer and bilayer shell aggregates having dimensions of (A) $R \approx 30\text{nm}$, $r \approx 5\text{nm}$, $d = 1\text{nm}$, (B) $R \approx 30\text{nm}$, $r \approx 5\text{nm}$, $d = 0.5\text{nm}$, (C) $R \approx 50\text{nm}$, $r \approx 5\text{nm}$, (D) $R \approx 50\text{nm}$, $r \approx 8\text{nm}$, (E) $R \approx 70\text{nm}$, $d_s = 0\text{nm}$, and (F) $R \approx 70\text{nm}$, $d_s = 1\text{nm}$.

4.4 Model of a Pair of Small Gold Nanospheres

The variations in the extinction spectrum as a function of the distance between small nanospheres can be explained by the behavior of gold nanospheres in pairs. To illustrate this point, additional simulations were performed both for a single and a pair of nanospheres, having a radius $r = 13.5\text{nm}$. The effect of two parameters was examined: (i) the distance between the nanospheres and (ii) the orientation of the pair model in relation to the incident wave. The edge-to-edge distance, d_s , was varied from 0 to 5nm and the pair

was arranged either along the propagation axis or vertically, parallel to the polarization direction of the incident electromagnetic wave. It should be noted that throughout this dissertation, the average extinction value was obtained by averaging the effect of the two orthogonal polarization states. The effective radius was set to be equal to 27nm. The optical constants for gold were obtained from Johnson and Christy [98]. Figure 4.18 displays the two orientations considered for the simulations with the relevant parameters as indicated. The two nanospheres were arranged either along the propagation (x) axis (Fig. 4.18(A)), or perpendicular to the propagation, along the y axis (Fig. 4.18(B)), which is parallel to one of the polarization states.

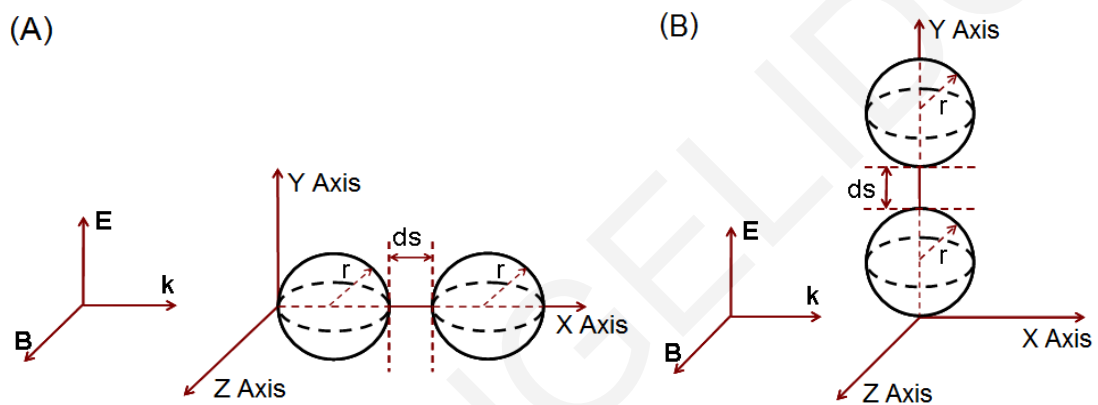


Figure 4.18: Two orientations of the model of the pair of small gold nanospheres The small nanospheres were arranged (A) along, and (B) perpendicular to the propagation, x , axis.

4.4.1 Extinction efficiency spectra of the pair of nanospheres as a function of the edge-to-edge distance (ds)

Figure 4.19 shows the average extinction spectra of a single and a pair of gold nanospheres, arranged along the propagation axis, for various edge-to-edge distances, ds . The interdipole separation, d , was set to be 1nm. Although there is an obvious increase in the extinction efficiency amplitude of the pair compared to the single nanosphere, due to the presence of a second nanosphere, the spectral shape of the two does not differ significantly. This confirms previous finding [23, 183] that nanospheres hidden behind other particles do not exhibit significant coupling interactions ("shadowing").

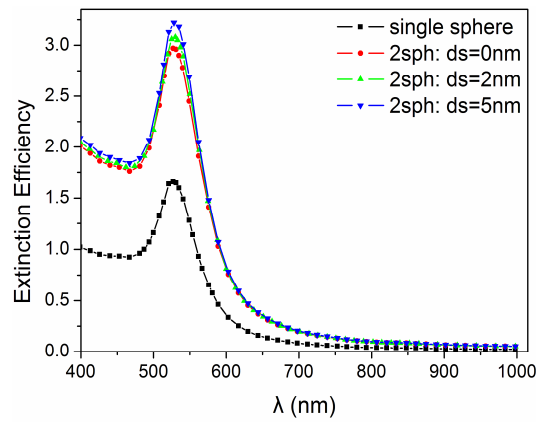


Figure 4.19: Extinction efficiency spectra of a single and a pair of gold nanospheres arranged along x axis, having various distances, ds , between them.

When the pair of nanospheres was arranged either in y or z direction, along one of the polarization states, the results obtained were markedly different. Figures 4.20(A), and (B) show the extinction efficiency spectra, averaged over the two polarization states, calculated using $d = 1$ and 0.5nm , respectively. When the interdipole separation, d , was set to be 1nm , the distance was varied from 0 to 5nm in 1nm steps (Fig. 4.20 (A)) while when set to 0.5nm the distance was varied using a 0.5nm step (Fig. 4.20(B)). As in previous cases, interdipole separation, d , of 1nm is not adequate to accurately estimate the extinction efficiency and, hence, significant differences were observed between the two figures. However, from the shape of Fig. 4.20(B), strong coupling interactions are apparent as evident by the additional, strong, red-shifted peaks. It should be noted that these peaks coincide and explain the spectral characteristics present in the shell aggregate results. Similar findings were reported by Khlebtsov et al. [23, 183].

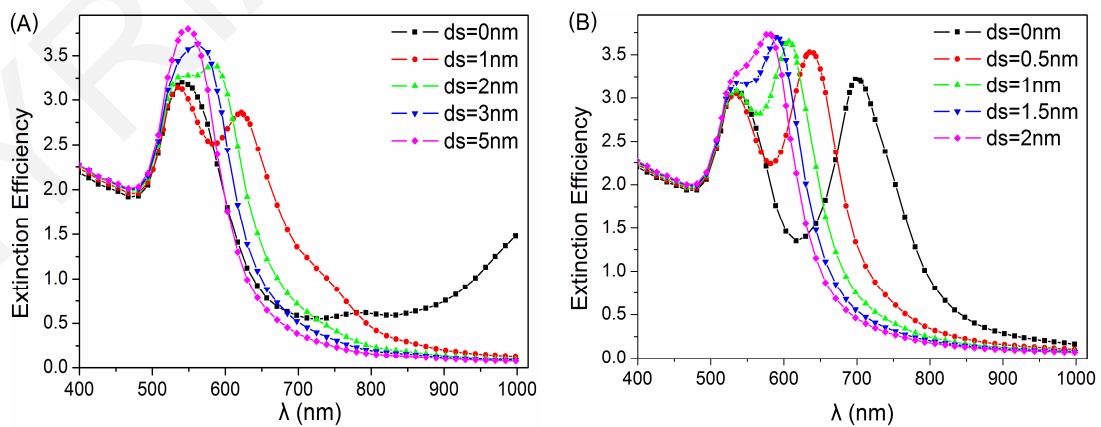


Figure 4.20: Extinction efficiency spectra of a pair of gold nanospheres arranged along y axis having, various distances, ds , and interdipole separations, d , of (A) 1nm , and (B) 0.5nm .

4.4.2 Polarization dependence of the pair of nanospheres

When the pair of nanospheres is arranged along the x axis, the polarization incident on the pair, whether along the y or the z axis, does not affect the calculations since both polarizations are considered and averaged. As a result, there are no significant changes in the extinction efficiency spectrum when the distance between the nanospheres is varied. However, when the pair of nanospheres is arranged along one of the polarization states, different electric magnitudes are incident along the two orthogonal polarization directions. Figure 4.21 shows the effect of polarization on the extinction efficiency spectra of a pair of nanospheres, having $d_s = 1\text{nm}$, and arranged along the y axis. When the polarization is parallel to the pair axis, two peaks are observed. The first peak or shoulder, at $\lambda = 548\text{nm}$, according to the literature for a pair model [90, 184], is attributed to the quadrupole mode, while the second intense peak, located at a longer wavelength is attributed to the dipole mode. The oscillating electrons in one nanosphere feel the electric field due to the oscillations in the second nanosphere which can lead to a collective plasmon oscillation of the pair. Therefore, higher order modes are observed. When the polarization is along the transverse direction (z axis), a single peak is observed which is similar to the optical response of a single nanosphere. The average value of extinction for the two polarization states results in a spectrum having two distinct peaks and broader widths. The results for the pair are in agreement with the literature [90, 158, 183].

The average polarization response of the pair of nanospheres exhibited an extinction profile similar to that of some monolayer shell aggregates (two peaks with the same extinction value, second peak shifted to longer wavelengths). Figure 4.21 suggests that the monolayer shell aggregate acts as the sum of contributions from multiple pairs of nanospheres with various orientations in relation to the incident polarization, with some exhibiting strong, while others weaker, interactions between them, resulting in more than one peaks, and broader widths. Also, the local electric field enhancement, resulting from the SPRs, is confined within a small distance (of nanometer length scales) from the surface of the particles and decays significantly thereafter [87]. Thus, when the distance between the nanospheres is large enough, there is no interaction and the total spectrum of the extinction efficiency is the summation of the individual nanospheres, resulting in intense, narrow, peaks.

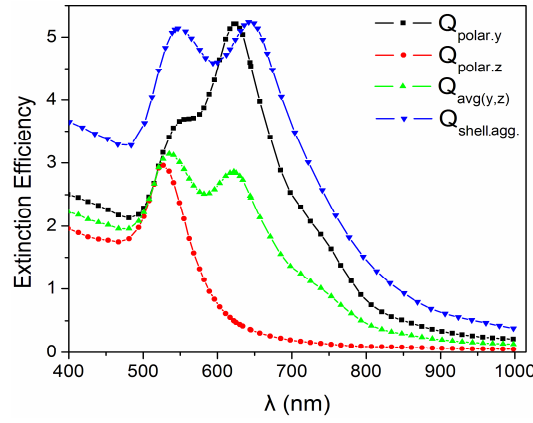


Figure 4.21: Polarization dependence of pair of nanospheres arranged along y axis having $d = 1\text{nm}$, and $d_s = 1\text{nm}$. Comparison with the normalized extinction efficiency spectrum of the monolayer shell aggregate (T6H).

4.4.3 Universal plasmon ruler

Jain and El-Sayed [86], based on experiments and simulations, have derived a relationship which correlates the coupling strength with the size and distance of the NPs

$$\frac{\Delta\lambda}{\lambda_0} \approx B e^{-ds/0.2dm}, \quad (4.2)$$

where ds is the edge-to-edge distance between the nanospheres, dm is the nanosphere diameter, λ_0 is the single-nanosphere plasmon wavelength maximum, $\Delta\lambda = \lambda_{\text{max}} - \lambda_0$, is the shift of the wavelength maximum caused by the nanosphere optical coupling, and B is a fitting constant which depends on the conditions of the nanosphere system.

If $\Delta\lambda/\lambda_0$ represents the near-field coupling strength, then regardless of the nanosphere size, the coupling interaction falls almost exponentially over a distance ~ 0.2 times the nanosphere diameter [185]. Jain and El-Sayed also confirmed the ruler for other NPs, such as nanoshells [186], and elongated nanospheres [187]. The relationship in eq. (4.2) is called “plasmon ruler equation” and is universal, which means that regardless of the type of the material and shape of the NP or the external medium, the near-field coupling depth is always ~ 0.2 times the diameter. In a more general form, eq. (4.2) can be rewritten

$$\Delta\lambda = A \exp[-B(ds/L)] + C, \quad (4.3)$$

where L is the characteristic size (e.g., a nanosphere diameter, or a nanorod length), and A , B , and C are fitting constants [1].

Therefore, for the model of the pair of nanospheres described before, the near-field depth is approximately 5nm. Strong coupling interactions were observed for distances 0.5, and 1nm while for distances larger than 3nm, the coupling between the nanospheres was

poorer and only single peaks were observed. Similar results were obtained for the monolayer shell aggregates. These are in agreement with the universal “plasmon ruler equation”.

4.5 Absorption and Scattering of Monolayer Shell Aggregates

In the previous sections, the extinction efficiency spectra as function of several NS shape parameters were explored. However, the total extinction efficiency is actually the sum of the absorption and scattering efficiencies of the NS. There are various scenarios where the distinction between absorption and scattering is of paramount importance. For example, in spectroscopic diagnostic applications, scattering particles are preferable to avoid sample absorption of the incident power and potential damage. In contrast, therapeutic applications require absorptive particles to transfer the incident power to the sample as heat. A special case, where metal NPs can be quite useful is photoacoustic imaging (PAI).

PAI is a technique that relies on the illumination of tissue by nanosecond pulsed laser light and the subsequent emission of acoustic waves from tissue under thermal stress confinement. Structures of different biological tissues reveal highly varying optical absorption coefficients, and thus, PAI imaging provides a good distinction between malignant and healthy tissues. The signal from the photoacoustic effect is proportional to optical absorption. Gold NPs have been explored as potential PAI contrast agents due to their strong optical absorption properties. The combination of gold NPs and PAI can allow highly sensitive and selective detection of cells [64, 74, 188, 189].

The normalized extinction, absorption, and scattering efficiency spectra of various monolayer shell aggregates are given in Fig. 4.22(A)–(F). Though monolayers have relatively large sizes, they mainly absorb light due to their small nanospheres. As the overall size increases, scattering becomes more pronounced, though it does not overcome the absorption. For the monolayers with $d_s = 1\text{nm}$ (Fig. 4.22(D,F)) two or more distinct absorption peaks are observed, in a wavelength range suitable for NIR applications. These characteristics designate the monolayer shell aggregates as potential PAI contrast agents.

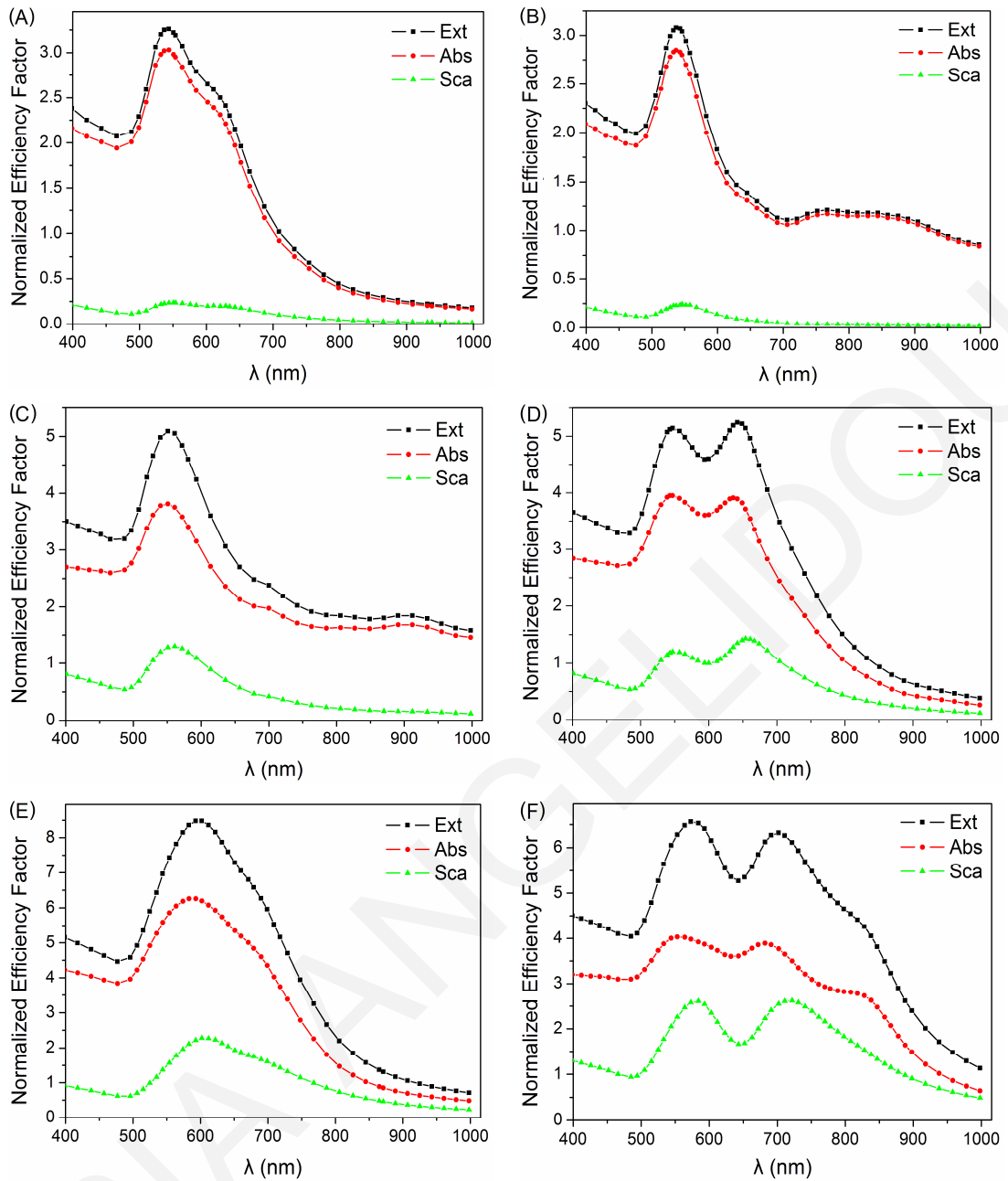


Figure 4.22: Normalized efficiency spectra of various monolayer shell aggregates having (A) $R \approx 30\text{nm}$, $r = 8\text{nm}$, (T2C), (B) $R \approx 30\text{nm}$, $d_s = 0\text{nm}$, (T2B), (C) $R \approx 50\text{nm}$, $r = 13.4\text{nm}$, (T3E), (D) $R \approx 50\text{nm}$, $d_s = 1\text{nm}$, (T6A), (E) $R \approx 70\text{nm}$, $r = 8\text{nm}$, (T4B), and (F) $R \approx 70\text{nm}$, $d_s = 1\text{nm}$, (T6E).

4.6 Monolayer Shell Aggregates with Various Core/Sphere Materials

To conclude the analysis of shell aggregates, the effects of the internal core material, external medium, and other nanosphere material were also examined.

4.6.1 Monolayer shell aggregates with various internal core/external media

First the effect of internal, dielectric core material, n_{core} , was examined. Both k_{core} and k_{med} were set as zero. The results for a monolayer shell aggregate, having dimensions of $R \approx 50\text{nm}$ and $r \approx 5\text{nm}$ (T3A) and consisting of small gold nanospheres and varied internal media are shown in Fig. 4.23(A). The optical constants for gold were obtained from Johnson and Christy [98]. The extinction efficiency spectra were normalized as described in previous sections. The dielectric core, n_{core} , was varied from 1.33 to 1.50, with water as the external medium. This refractive index range is representative of the cellular cytoplasm and membrane [182]. Varying dielectric core did not appear to have any significant effect on the optical response of monolayer shell aggregate (Fig. 4.23(A)).

Three different combinations of dielectric cores and external mediums were further considered. Figure 4.23(B) show the extinction spectra of the same monolayer shell aggregate having (i) air as core, and water as the external medium, (ii) water as core, and air as the external medium, and (iii) water as core and external medium. The effect of having a lower refractive index ($n = 1.0$) is an decrease in the extinction peak amplitude and a slight blue-shift of the wavelength maximum. This effect is more pronounced when the lower refractive index is outside the shell, that is the medium. In a cellular/tissue environment this effect is not expected to be relevant since the refractive index does not vary significantly.

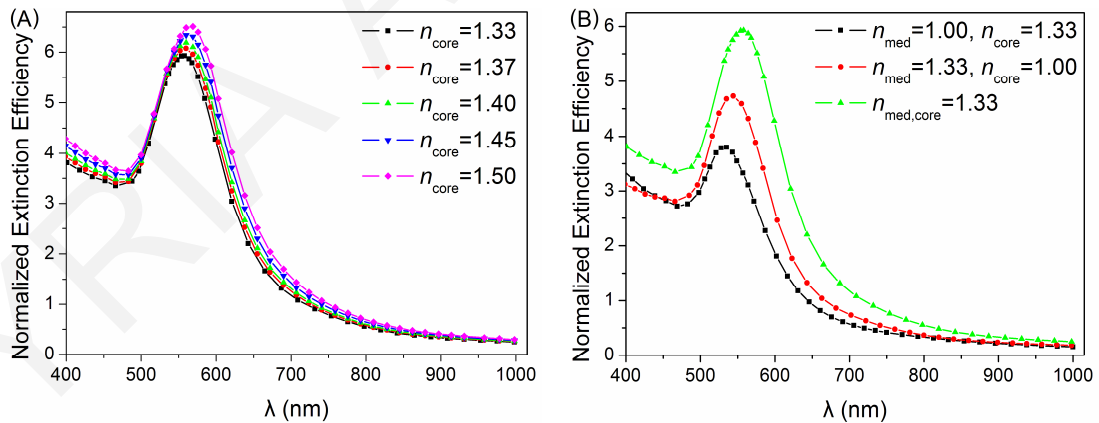


Figure 4.23: Normalized extinction efficiency spectra of monolayer shell aggregate ($R \approx 50\text{nm}$, $r \approx 5\text{nm}$, T3A) consisting of various (A) dielectric cores, and (B) core/external medium combinations. (J&C [98].)

4.6.2 Monolayer shell aggregates with various metallic cores

Next, the material of the core was modified from dielectric to metallic. Figure 4.24 shows the extinction efficiency spectra of monolayer shell aggregates, having dimensions of $R \approx$

50nm, $r \approx 5$ nm (T3A), and various metallic cores, such as gold (Au), silver (Ag), copper (Cu), aluminum (Al), and nickel (Ni). Here, the normalization eq. (4.1) was not applied, since all NSs have identical dipole arrays, and the interaction between the core and shell dipoles is significant. The tabulated data sets from Johnson and Christy [98, 99] do not include the refractive index of aluminum, so the Palik [91] tabulated data sets were employed here. The small nanospheres were set to be gold and the external medium was set to water. Changing the core to metal significantly affects the spectral shape of the extinction efficiency. Silver (Ag) and gold (Au) exhibit the strongest extinction efficiency peaks at 560nm and 630nm respectively. All other metals result in lower extinction efficiencies and a relatively flat and featureless spectral response.

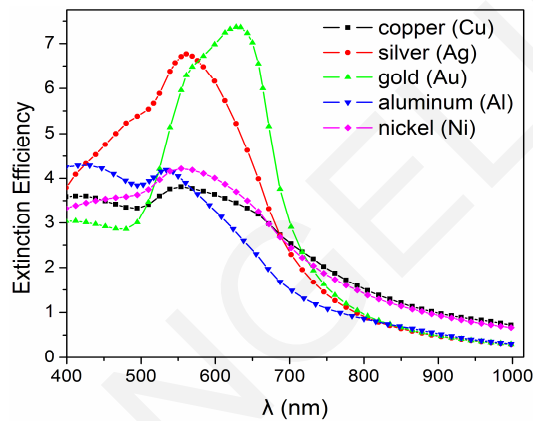


Figure 4.24: Extinction efficiency spectra of monolayer shell aggregates having $R \approx 50$ nm, $r \approx 5$ nm (T3A), and various metallic cores. (Palik [91].)

4.6.3 Comparison between monolayer shell aggregates with various cores

The results of the previous sections show that the optical response of the monolayer shell aggregate depends on the internal (dielectric or metallic) core material. For easy comparison, the extinction efficiency spectra of shell aggregates with different core materials are shown in Fig. 4.25(A)–(C). The monolayer shell aggregates have dimensions of $R \approx 50$ nm, (i) $r \approx 5$ nm (T3A), (ii) $ds = 0$ nm (T3E), and (iii) $ds = 1$ nm (T6A). The core materials, other than water, were the silica (SiO_2 , $m_{\text{core}} = 1.44 + i0$, at all wavelengths), silver, and gold. Normalization was applied only for the water and silica cores, for better comparison. The extinction efficiency spectra of single nanospheres are given as well (Fig. 4.25(D)) for comparison. The optical constants for gold and silver were obtained from Johnson and Christy [98]. The external medium was assumed to be water.

The conclusions from the assessment of the spectra in Fig 4.25(A)–(D) can be summarized as follows:

- Dielectric cores (such as silica) result in shell aggregate extinction efficiency spectra which do not differ significantly from spectra with a water core.
- Metallic cores (such as gold or silver) result in extinction efficiency spectra which are markedly different than those above. They exhibit a single peak, which is red-shifted relative to those of single nanospheres, but the overall spectral shape does not change significantly with nanosphere radius, or edge-to-edge distance.
- The long NIR tail, and two peaks observed in shell aggregates having a dielectric core, due to coupling interactions, are no longer observable, since they were suppressed by the interaction of metal core with the shell gold nanospheres.

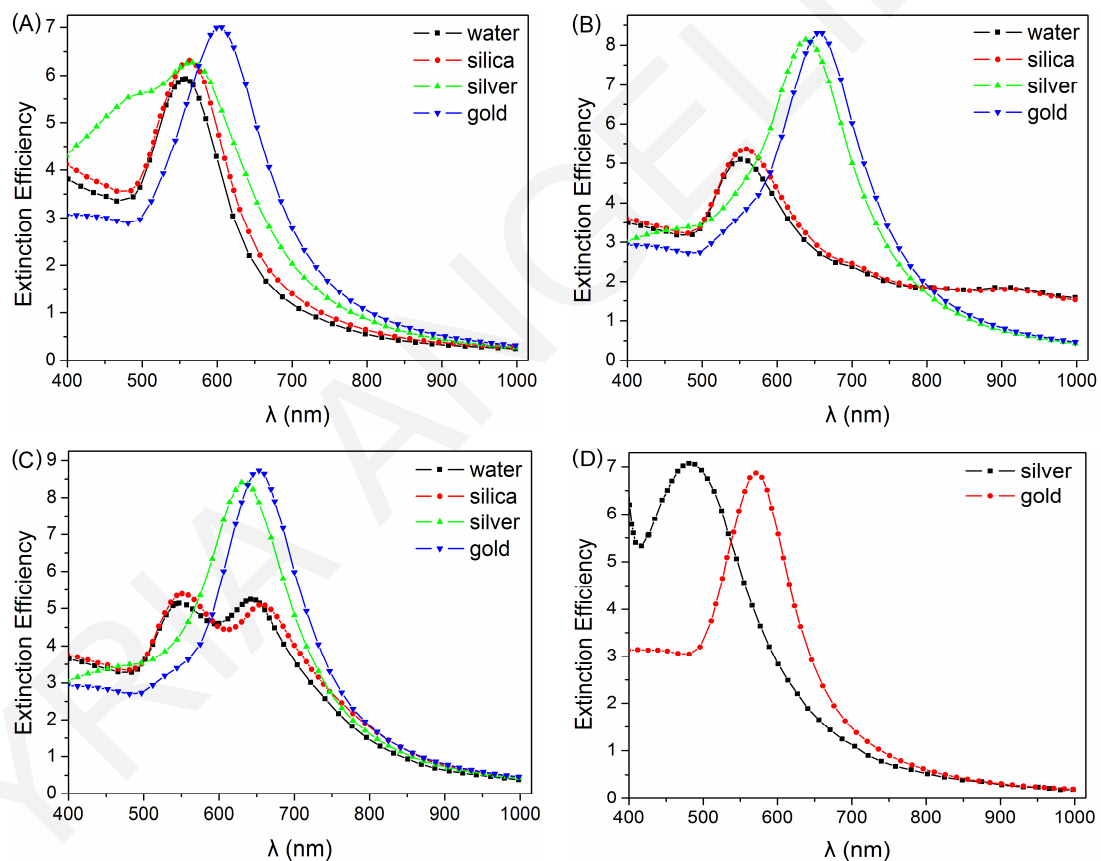


Figure 4.25: Comparison between extinction efficiency spectra for various core materials for the monolayer shell aggregates having (A) $R \approx 50\text{nm}$, $r \approx 5\text{nm}$, varied d_s , (B) $R \approx 50\text{nm}$, $d_s = 0\text{nm}$, and (C) $R \approx 50\text{nm}$, $d_s = 1\text{nm}$. (D) Extinction efficiency spectra of single nanospheres having $r = 50\text{nm}$. (J&C [98].)

4.6.4 Effect of using different refractive index tabulated data sets

As also described in Chapter 2, the optical response of NPs depends on the complex refractive index tabulated data sets used for the simulations. Figure 4.26 compares the extinction efficiency spectra calculated using two different material data sets for the monolayers. No normalization was applied to the extinction spectra. The material data sets were obtained from Johnson and Christy [98], as for most simulations in this chapter, and from Palik [91]. The monolayer shell aggregate has dimensions of $R \approx 50\text{nm}$, $r \approx 5\text{nm}$ (T3A), and consists of gold nanospheres, and a gold (Fig. 4.26(A)), or silver (Fig. 4.26(B)) metal core. The external medium was assumed to be water. The spectra are mostly affected in the wavelength region of the peak, while they seem to be largely unaffected elsewhere. This is due to interband transitions which do not depend on shape. Although significant, these differences are not so large that would preclude the use of either tabulated data set. Similar observations were reported in Chapter 2.

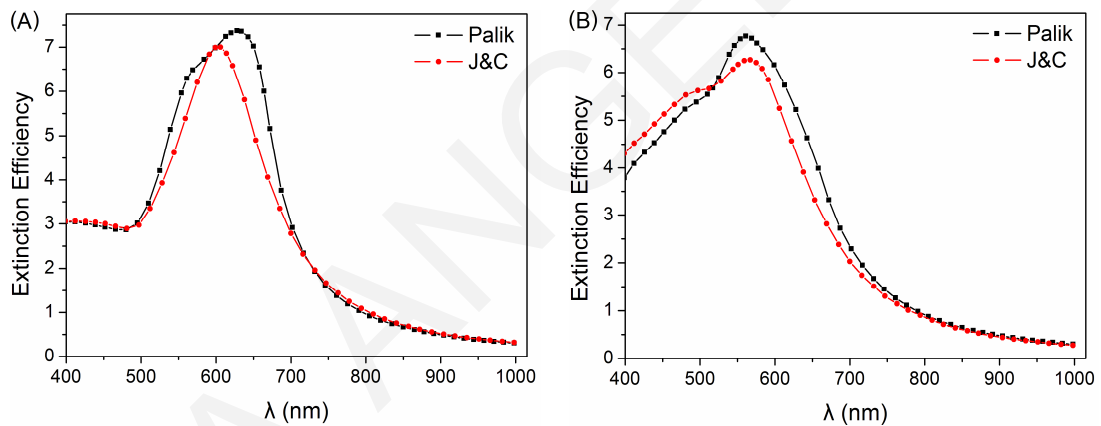


Figure 4.26: Refractive index dependence of monolayer shell aggregates having $R \approx 50\text{nm}$, $r \approx 5\text{nm}$ (T3A), and consisting of (A) gold, or (B) silver metal cores.

4.6.5 Comparison between monolayer shell aggregates with gold/silver nanospheres

Silver nanospheres provide stronger and more enhanced local electric fields than gold ones, when interacting with an incident electromagnetic wave. Additional simulations were performed to study the effect, on the optical properties of shell aggregates, of silver nanospheres instead of gold. Extinction efficiency spectra were calculated for three monolayer shell aggregates, having dimensions of $R \approx 50\text{nm}$, (i) $r \approx 5\text{nm}$ (T3A), (ii) $ds = 0\text{nm}$ (T3E), and (iii) $ds = 1\text{nm}$ (T6A), and consisting of silver nanospheres, and water as the internal core and external medium. The optical constants for silver were obtained from Johnson and Christy [98].

Figures 4.27(A)–(C) show the results for both gold and silver nanospheres for comparison. Extinction efficiency spectra of monolayer shell aggregates with silver nanospheres, have increased amplitude and blue-shifted peaks, relative to those with gold nanospheres. Although the silver nanospheres exhibit improved plasmon resonances for all monolayer shell aggregate sizes, their optical responses are in the violet to blue wavelengths, which is less desirable for imaging and biological applications.

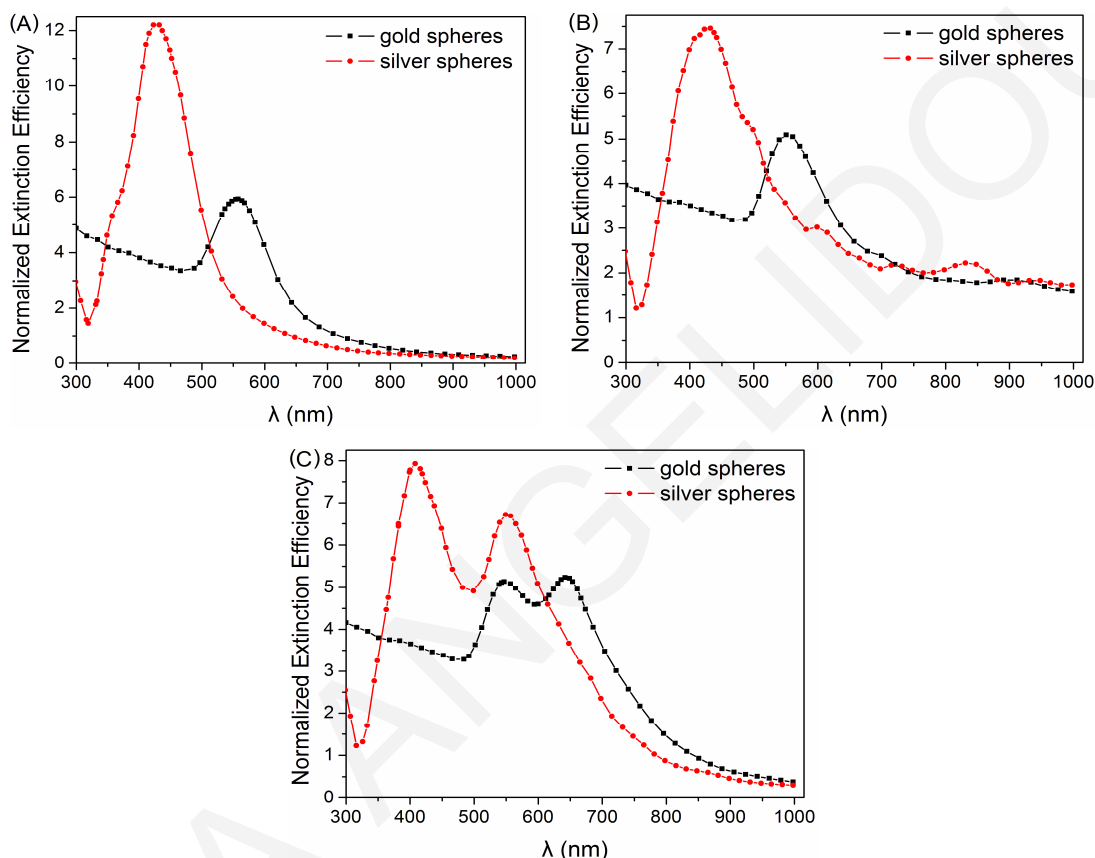


Figure 4.27: Comparison spectra for gold and silver nanospheres for the monolayer shell aggregates having (A) $R \approx 50\text{nm}$, $r \approx 5\text{nm}$, varied d_s , (B) $R \approx 50\text{nm}$, $d_s = 0\text{nm}$, and (C) $R \approx 50\text{nm}$, $d_s = 1\text{nm}$. The internal core was assumed to be water. (J&C [98].)

4.7 Summary

The purpose of this study was to theoretically investigate new NSs, the so-called “shell aggregates”, which consist of small gold nanospheres that aggregate around a core, creating a monolayer or bilayer shell, and their potential application as imaging agents and surface-enhanced Raman spectroscopy (SERS) probes.

First, the optical properties of some commonly used gold NPs, such as nanospheres, aggregates, and nanoshells, were explored. When the outer radius, R , was varied, all three classical gold NPs exhibited a similar red-shifting of the wavelength

maximum, λ_{\max} . Also, the nanoshells were characterized by wide tunability of the SPR when varying the ratio of the core radius to the outer radius of the nanoshell.

Next, the novel monolayer shell aggregates were thoroughly studied. The monolayer shell aggregates consisted of small gold nanospheres, which aggregate to create a shell around a dielectric core. Their optical response depends strongly on the edge-to-edge distance between the nanospheres, d_s , where coupling interactions may occur, and to a less extent to the outer radius, R , whereas the small nanosphere radius, r , did not contribute significantly. By varying the parameters of edge-to-edge distance, d_s , and outer radius, R , the monolayer shell aggregate exhibited tunable optical properties, ranging from visible to NIR wavelengths. The monolayer shell aggregates were also compared with classical NPs, and found to exhibit more elaborate spectra ranging even to NIR wavelengths.

The bilayer shell aggregates exhibited similar and sometimes identical spectra with the monolayers. The addition of a second layer, located behind the first layer, did not contribute significantly to the optical properties of the shell aggregates. This effect was explained using a model of a pair of small nanospheres. The extinction efficiency spectra of the pair were found to be orientation and polarization dependent in relation to the incident light direction, which agreed well with the literature. When the nanospheres were arranged along the propagation axis, there was no shift in their SPR wavelength, while when they were arranged perpendicular, along one of the polarization axis, a second peak was observed at longer wavelengths.

The absorption and scattering efficiency spectra were also investigated. It was shown that the monolayer shell aggregates could be good candidates for PAI applications, since their SPR is mainly due to absorption which is required for PAI imaging.

Finally, the dependence of the extinction efficiency spectra on the core and nanosphere material was explored to conclude the analysis of monolayer shell aggregates. Varying the dielectric core did not have any significant influence. However, changing the core material to metal, markedly different spectra were obtained since coupling interactions between small nanospheres were lost. In addition, monolayer shell aggregates with small silver nanospheres, exhibited blue-shifted and more enhanced SPR spectra, compared to the gold monolayer shell aggregates, though not suitable for NIR applications.

5. Theoretical Investigation of a Dual-Mode Nanostructure

5.1 Introduction

Metal nanoparticles (NPs) demonstrate unique optical properties due to the phenomenon of surface plasmon resonance (SPR). By varying the size, shape, metal type, surrounding medium, and the coupling interactions between adjacent NPs, the SPR wavelengths can be tuned from the visible to near-infrared (NIR) range. Most of the research effort focuses on noble metal NPs, such as silver and gold, since they exhibit strong absorption and scattering plasmon bands which can be exploited in both imaging and therapy applications [1, 3, 51]. The potential uses of metal NPs in a new area called theranostics, are currently being explored. The term “theranostics” comes from the words therapeutics and diagnostics. It describes the combination of diagnosis and therapy into a single agent. In this field of theranostics, and in particular “nano-theranostics”, falls the development of new NPs that may simultaneously image, monitor and treat a disease [70, 97, 190, 191]. Gold NPs, such as nanoshells, nanorods, and nanocages, have been exploited as potential theranostic agents [192-194].

When the frequency of an incident electromagnetic wave coincides with an SPR frequency of the conducting free electrons, it results in collective, coherent plasmon excitations at the nanoparticle (NP) surface. Subsequently, radiative and nonradiative effects occur which restore the free electron motion back into its equilibrium state. First, the oscillating electric field, generated by the electron motion, can radiate electromagnetic energy at the same frequency as that of the surface plasmon oscillation, resulting in elastic scattering by the NP. Alternatively, the plasmon oscillations can decay into electron-hole excitations of either intraband (within the metal conduction band) or of interband (between other bands, for example, d bands and the conducting band) type transitions. This nonradiative pathway of plasmon decay results in absorption of light by the particle. Absorption and scattering together are defined as the optical extinction of the NP [3, 84, 123].

Optical imaging and spectroscopic applications can significantly benefit from using NIR light, which minimizes absorption from water and biomolecules, thus allowing deeper penetration of the incident light into living tissue [3, 73, 74]. For such diagnostic applications, large size NPs are preferred due to plasmon resonance at longer wavelengths and higher scattering efficiencies. Photothermal applications, on the other hand, could

benefit from NPs having strong absorption with limited scattering, for better therapeutic efficacy. Small size NPs, especially gold, offer rapid photothermal conversion, which can create intense localized heating of the medium surrounding the NP, by absorbing light of a frequency strongly overlapping with the NP plasmon resonance. The strongly enhanced absorption of the NPs necessitates much lower laser intensities and results in less unwanted cellular damage [3, 51, 195].

In this chapter, the so-called “dual-mode” nanostructure (NS) is proposed. This novel NS possesses the unique property of distinct and separated absorption and scattering plasmon bands, both ranging in the biological desirable NIR wavelengths. The term “dual-mode” arises from the fact that the proposed NS will have the potential for combined imaging and therapy with absorption and scattering plasmon bands such as those in Fig. 5.1. Ideally, the absorption plasmon band should be located at $\lambda \approx 635\text{nm}$, while the scattering plasmon band at $\lambda \approx 785\text{nm}$, with distinct and non-overlapping bands. Such a NS would exhibit the most intense scattering, with minimal absorption, in the NIR for imaging and the opposite in the red, for therapy. This could be beneficial for combined diagnostics and therapeutics since the laser wavelengths used for each application can be at distinct wavelengths for increased efficacy and safety. It could also allow independent control of imaging and therapy using a single NP.

The excitation wavelengths of ≈ 635 and 785nm were chosen, since they lie in the “optical window” range, and were also used in various biological and biomedical applications [77, 95, 196]. These wavelengths are also widely available.

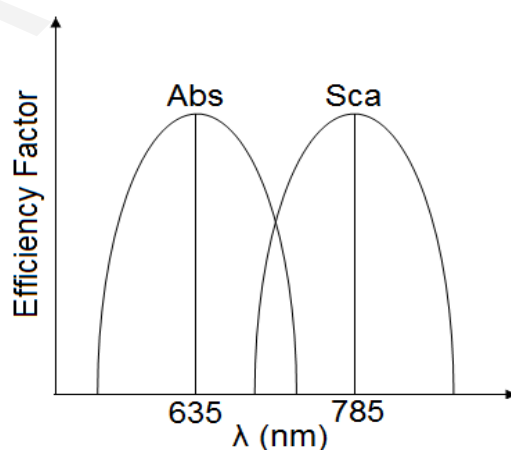


Figure 5.1: Dual-mode spectral characteristics, exhibiting distinct and separated absorption and scattering plasmon bands, located at red and NIR wavelengths, respectively.

Metal NPs can have different optical responses. Their SPRs can be tuned from UV-vis to NIR wavelengths. Noble metal NPs, such as gold and silver, have been extensively

investigated. Their extinction spectra were calculated, using electrodynamic methods, with some results also verified experimentally [2, 53, 82, 115, 197]. There are few reports that explored the absorption and scattering spectra of metal NPs separately, either computationally or experimentally [1, 89, 198, 199]. Absorption and scattering are competing processes which can occur simultaneously and there are some instances where one or the other dominates. Small size NPs exhibit mostly absorption, ranging in UV-vis wavelengths while scattering is negligible. As the size increases, scattering becomes more prominent and for even larger sizes it dominates, with negligible absorption, especially in NIR wavelengths [1, 83, 200].

Silver NPs exhibit both absorption and scattering, depending on the size and shape, but their SPR remains in the visible wavelength range [7]. The optical response of gold NPs can be shifted to longer wavelengths compared to silver although their SPR is still in the visible range [159]. Gold nanoshells, and nanorods, have proved to be good candidates for NIR applications due to the tuning of their plasmon bands as their aspect ratios are varied. However, their extinction is a combination of overlapping absorption and scattering plasmon bands (Fig. 5.2(A,B)) [88, 201]. If used as imaging agents, there will be energy losses due to absorption and, if used as therapy agents, there will be losses due to scattering. Also, the newly explored nanocages have shown tunable SPRs ranging from visible to NIR wavelengths; however their absorption and scattering plasmon bands also overlap [35, 202]. The efficiency factors of the various classical gold NPs explored in Chapter 4, are given in Appendix D. All gold NPs exhibited either absorption, or scattering, or overlapping plasmon bands.

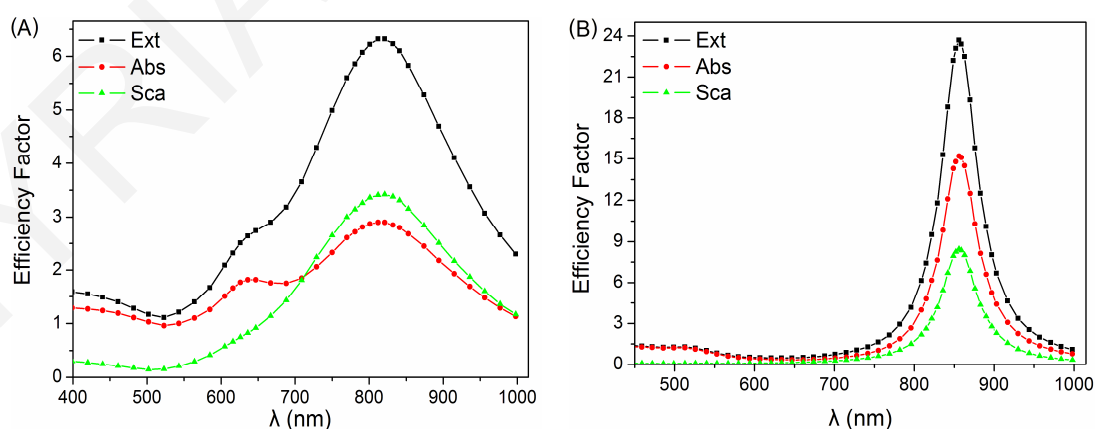


Figure 5.2: Efficiency factors of (A) nanoshell with $R = 70$ nm and shell thickness 10 nm ($R_c/R \approx 0.86$), and (B) nanorod with $r_{\text{eff}} = 21.86$ nm and aspect ratio (length/width) of 3.9. (J&C [98].)

The optical responses of other metals, such as aluminum [203, 204], and nickel [205, 206], were also explored. These metals feature remarkably different optical properties compared to the noble metals. Aluminum is a much cheaper and abundant material, however, it oxidizes very rapidly. Aluminum NPs demonstrate plasmon resonances at much shorter wavelengths, and display broader and less intense plasmon bands compared to the noble metals. Nickel NPs can add magnetic properties to the optical response, thus providing multifunctionality in a single NP. The nickel NPs exhibit stronger damping effects, which result in weaker and broader plasmon bands. There are very few reports on the optical properties of both of these metals and even less computational estimations.

In this chapter, the optical responses (plasmon band characteristics, such as the wavelength, amplitude, and width), of various nanostructures (NSs) of different material, shapes, and sizes are explored .

5.2 Simple Metal Nanostructures

In order to design a dual-mode NS, a series of simulations was first performed for simple metal NSs which could be used as the building blocks for the desired effect. The spectral characteristics of the absorption and scattering plasmon bands were investigated for various parameters. The absorption, scattering, and extinction efficiency factors were calculated relative to the incident wavelength, λ , for various:

- Materials, such as silver (Ag), gold (Au), aluminum (Al), and nickel (Ni).
- Shapes, such as nanosphere, nanocube and tetrahedron.
- Sizes, ranging from 50 to 140nm for
 - nanosphere diameter ($d_m = 2r$),
 - nanocube edge length (b),
 - tetrahedron side length (t).

Figure 5.3 shows the shapes of nanosphere, nanocube and tetrahedron and their corresponding size parameters. The interdipole separation was varied from $d = 0.9$ to 2.8nm depending on the size, and shape for less computational time and memory requirements. The shapes were positioned as assigned by the software, so no orientation was applied, since the NSs are generally symmetric. The refractive index used for the various metals, was taken from Palik [91]. Bulk values of the optical constants were used for all simple NS simulations. Table 5.1 provides the optical constant (n and k) values for the four metals, at three wavelengths. The effective radius, r_{eff} , was calculated as described

in Chapter 3. The characteristic properties of the wavelength maximum, λ_{\max} , amplitude, and width of the efficiency spectra, were recorded. In this chapter, only the most significant of the simulations are presented. All figures, showing the efficiency factors for the various simple NSs, are included in Appendix E.

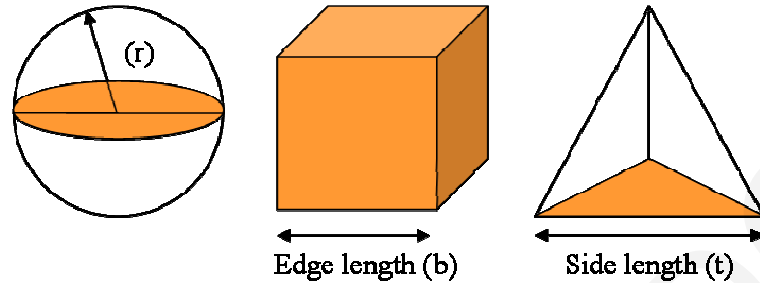


Figure 5.3: Shapes and corresponding size parameters for simple NSs.

Table 5.1: Optical constants, n and k , for the four metals, at three wavelengths, in water

	532nm		635nm		785nm	
	n	k	n	k	n	k
Palik:						
Au	0.1288	3.0554	0.1625	4.1601	0.2182	5.3925
Ag	0.1147	3.4488	0.1085	4.2278	0.1923	5.3214
Al	1.4230	6.3107	1.9713	6.1802	0.9373	7.6240
Ni	1.6849	3.0756	1.9297	3.4029	2.1682	3.8535

5.2.1 Nanostructures of various materials and shapes

By varying the material and shape, absorption and scattering efficiencies can be tuned from UV-vis to NIR wavelength range. Table 5.2 shows the efficiency factors for the various simple NSs of a size parameter of 120nm. Scattering was the prominent effect for nanospheres and nanocubes except for nickel NSs where absorption overlapped with scattering. The tetrahedral shape exhibited intense absorption, except in the case of aluminum where scattering was more pronounced in the UV-vis range. The reason why the tetrahedral shape exhibits mainly absorption effects is due to the fact that its effective radius, r_{eff} , is relative small compared to the other two NSs, where $r_{\text{eff,tetrah}} < r_{\text{eff,sphere}} < r_{\text{eff,cube}}$. For example, for a size parameter of 120nm, r_{eff} of a tetrahedron is equal to 36.5nm, while for a nanocube is equal to 74.4nm, which is relatively larger. This resulted in intense absorption and less or even minimal scattering.

The differences observed between the optical responses of the various metals are a result of the electronic structure and the free conducting electrons of each metal. (Electron

configurations are given in Appendix A.2.) The atoms of silver and gold exhibit one free electron, at $5s^1$, and $6s^1$ subshells, respectively. The “free” s-electron can be easily excited to higher levels in the same energy band. The reason why gold has a more red-shifted spectrum may arise from the fact that its s-electron occupies a higher energy band, compared to the silver s-electron, and the attraction that feels from the positively charged nucleus is smaller. As a result, it requires less energy to be excited to an upper level. Since energy, E , is inversely proportional to wavelength, $E \sim 1/\lambda$, less energy translates to a longer wavelength. The aluminum atom has filled s-bands, and one electron residing in a p-band, ($3s^2p^1$), and since the energy band is even closer to the positively charged nucleus, higher energy is required for electron excitation which results in shorter wavelengths. Finally, the nickel atom has filled energy bands, ($3d^84s^2$), all its electrons are bound, and it is difficult to excite, explaining the broad spectra with no characteristic peaks which are observed.

Gold NSs exhibit the most red-shifted SPR wavelengths, compared to the other three metals. The gold nanosphere ($d_m = 120\text{nm}$) has an intense scattering peak, at $\lambda_{\text{max}} = 625\text{nm}$, and two small absorption peaks at visible wavelengths. The gold nanocube ($b = 120\text{nm}$) has overlapping absorption and scattering spectra in the visible range, while a distinct scattering peak at $\lambda_{\text{max}} = 720\text{nm}$ is observed, with a value of 6.45 and minimal absorption in the NIR range. Finally, the gold tetrahedron ($t = 120\text{nm}$) has an intense absorption peak at $\lambda_{\text{max}} = 745\text{nm}$, and a small scattering peak at $\lambda = 750\text{nm}$. For the gold NSs, absorption is greater in the wavelength range of 400nm to approximately 520nm, which is due to interband transitions.

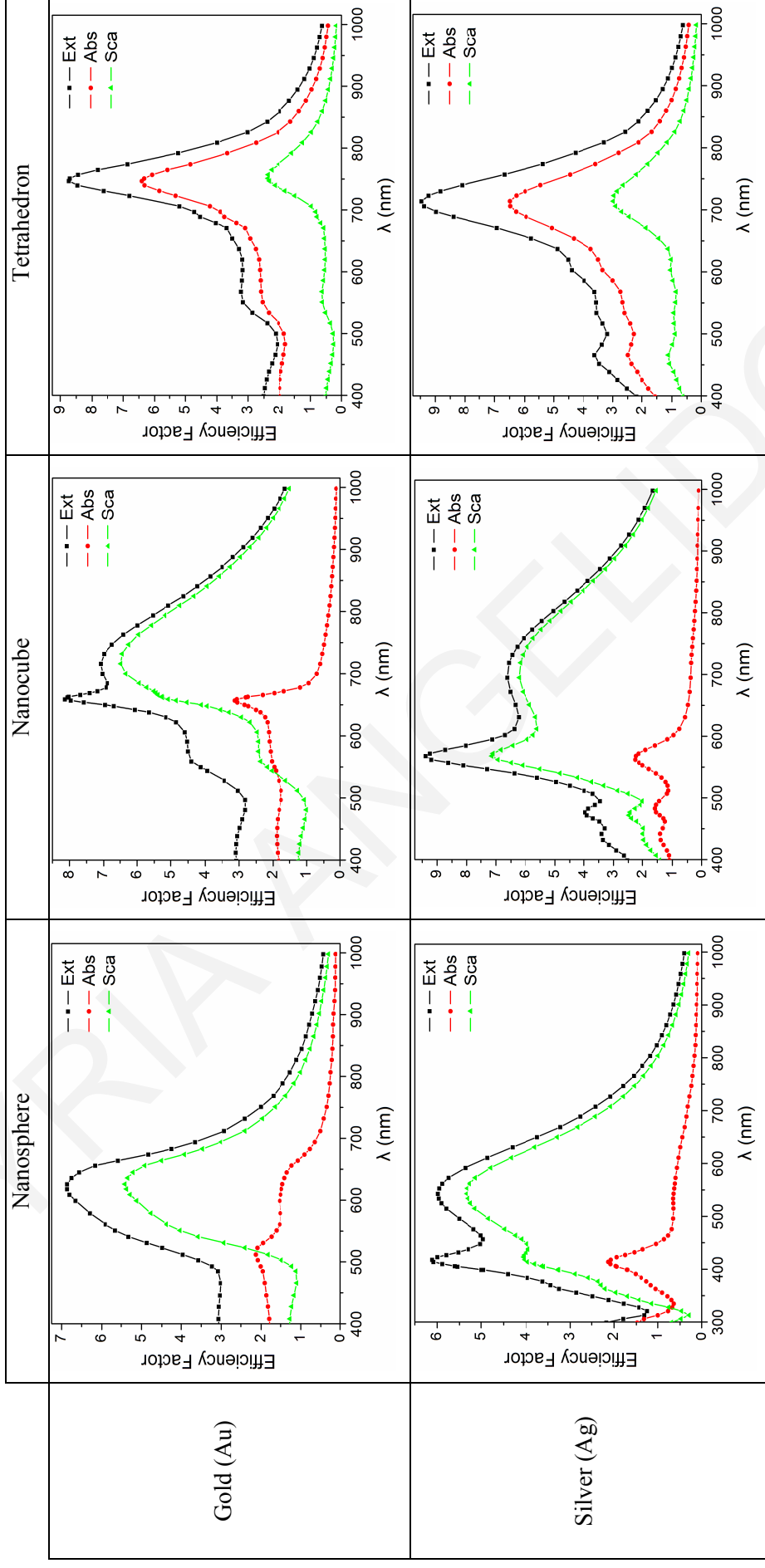
Silver NSs have more intense scattering values. The silver nanosphere has a strong scattering peak at $\lambda_{\text{max}} = 545\text{nm}$, and a smaller blue-shifted peak at $\lambda = 420\text{nm}$. The first peak corresponds to the dipole mode, while the blue-shifted peak, according to the literature [82] it corresponds to the quadrupole mode. A small absorption peak is observed at $\lambda_{\text{max}} = 413\text{nm}$, while absorption is negligible in the NIR. The silver nanocube exhibits four scattering peaks. Two small peaks are located at violet-blue wavelengths, an intense, distinct peak is observed at $\lambda_{\text{max}} = 570\text{nm}$ with a value of 6.9 and one broader peak is red-shifted at $\lambda = 700\text{nm}$ with a value of 6.2. The absorption has two smaller peaks in the visible range. The silver tetrahedron has an intense absorption peak at $\lambda_{\text{max}} = 710\text{nm}$, and a small scattering peak at $\lambda = 717\text{nm}$. Interband transitions are not observed in the silver spectra, since the threshold is located at shorter wavelengths ($\approx 320\text{nm}$) than those considered in these simulations.

Aluminum NSs have the most blue-shifted SPR wavelengths. Their SPR ranges from UV to visible wavelengths. Aluminum is also a strong scattering material. The aluminum nanosphere has three distinct scattering peaks at $\lambda = 458, 280, \text{ and } 216\text{nm}$, while absorption is negligible. The aluminum nanocube has two scattering peaks, one distinct scattering peak at $\lambda_{\text{max}} = 419\text{nm}$ with a value of 5.3 and one broader, red-shifted peak at $\lambda = 605\text{nm}$ with a value of 3.85. The absorption is very broad, almost negligible, and has two small humps in the visible and NIR range. The aluminum tetrahedron has overlapping absorption and scattering peaks, at $\lambda_{\text{max}} \approx 470\text{nm}$, with the scattering being more intense. Interband transitions, for aluminum occur in the wavelength range of $775\text{--}825\text{nm}$ ($\sim 1.5\text{--}1.6\text{eV}$) [207] which are slightly visible in the absorption spectra as small humps in the NIR wavelength range.

Nickel NSs exhibit the lower and broader plasmon resonances. The nickel nanosphere has a scattering peak at $\lambda_{\text{max}} = 527\text{nm}$, and a very broad absorption peak ranging across the spectrum. The nickel nanocube has one scattering peak, at $\lambda_{\text{max}} = 685\text{nm}$ with a value of 2.4 and a broad absorption peak, exhibiting two slightly distinguishable humps at visible and NIR wavelengths. Finally, the nickel tetrahedron has an absorption peak at $\lambda_{\text{max}} = 592\text{nm}$, while scattering is decreasing elsewhere. Interband transitions, for nickel occur at a wavelength of $\approx 270\text{nm}$ [207], and are not observed in the spectra, since the threshold is located at shorter wavelengths than those considered in these simulations.

From Table 5.2, and tables in Appendix E, it is observed that none of the simple metal NSs has the unique property required for a dual-mode NS, since they exhibited either absorption, or scattering or overlapping plasmon bands. A gold nanocube, having an edge length of $b = 120\text{nm}$, exhibits a good scattering value at the NIR range with less absorption, and also a small scattering value in red wavelength range. Given these properties, the gold nanocube can be considered as a potential NIR scattering building block of a dual-mode NS. To further examine the suitability of the gold nanocube, ratios of absorption to scattering efficiency factors (and vice versa) were estimated for the wavelengths of $\lambda = 635, \text{ and } 785\text{nm}$. The first ratio, $Q_{\text{abs}}/Q_{\text{sca}}$, indicates the amount of absorption over scattering (absorption ratio), and the second ratio, $Q_{\text{sca}}/Q_{\text{abs}}$, the amount of scattering over absorption (scattering ratio). For theranostic applications, it is required high ratios in the respective wavelength ranges. Table 5.3 presents the efficiency ratios of various metal nanocubes having an edge length of 120nm , while Table 5.4 presents the efficiency ratios of various gold NSs having a size parameter of 120nm , calculated at the two wavelengths of interest.

Table 5.2: Efficiency factors of various simple metal NSs having a constant size parameter of 120nm



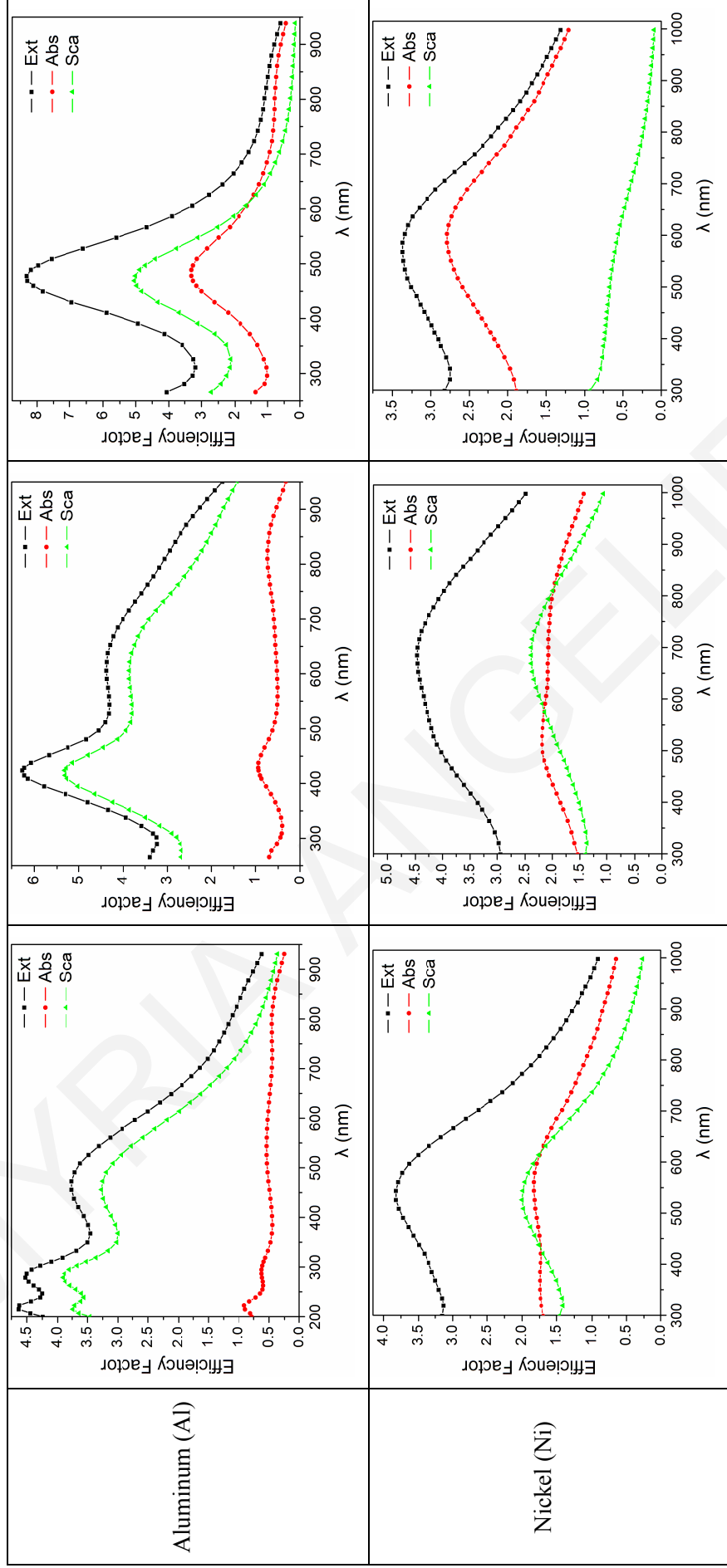


Table 5.3 clearly illustrates that the ratios depend on the material. The nickel nanocube has the best absorption ratio at $\lambda = 635\text{nm}$. However, it displays a low scattering ratio in the NIR, which means that both absorption and scattering occur which is not desirable. The silver nanocube has the best scattering ratio at $\lambda = 785\text{nm}$, but a low absorption value in visible, which means that the scattering is as significant as the absorption in the visible which, again, is not desirable. The gold nanocube appears to offer the best trade-off. It has a high scattering value in the NIR and a relatively good absorption value, compared to the other materials, at red wavelengths.

Table 5.3: Ratios of absorption to scattering efficiencies (and vice versa) for various metal nanocubes having $b = 120\text{nm}$, for the two wavelengths of interest

	$Q_{\text{abs}}/Q_{\text{sca}}$, at 635nm	$Q_{\text{sca}}/Q_{\text{abs}}$, at 785nm
Gold	0.733	14.32
Silver	0.093	17.95
Aluminum	0.147	3.52
Nickel	0.900	1.04

The efficiency ratios depend also on the shape, as shown in Table 5.4. The nanosphere has a low absorption ratio at $\lambda = 635\text{nm}$, and a good scattering ratio at $\lambda = 785\text{nm}$. The nanocube displays the best scattering ratio at $\lambda = 785\text{nm}$, and a value of 0.7 at $\lambda = 635\text{nm}$, meaning that scattering effects occur in the visible. The tetrahedron offers the best absorption ratio, while its scattering ratio is very low, meaning that absorption effects are dominant over scattering at the wavelength of 785nm. Again, the gold nanocube exhibits the best scattering ratio value and, even though its absorption value is relatively low, it can be considered as a scattering material for NIR imaging applications. If the gold nanocube is combined with a strong absorber, then the combined absorption and scattering plasmon bands can be located at different wavelengths, thus resulting in a dual-mode NS.

Table 5.4: Ratios of absorption to scattering efficiencies (and vice versa) for the three gold nanostructures having a size parameter of 120nm, for the two wavelengths of interest

	$Q_{\text{abs}}/Q_{\text{sca}}$, at 635nm	$Q_{\text{sca}}/Q_{\text{abs}}$, at 785nm
Nanosphere	0.265	4.32
Nanocube	0.733	14.32
Tetrahedron	5.09	0.434

5.2.2 Effect of size (edge length, b) on the nanocube properties

By varying the nanocube size, the ratio of absorption to scattering can also be varied. Figure 5.4 shows an example. The absorption, scattering, and extinction efficiency factors of a gold nanocube having three different edge lengths are displayed. As the size of the nanocube is increased, absorption becomes less pronounced, while scattering is enhanced significantly. Also, both absorption and scattering peaks broaden, and shift to longer wavelengths, with the scattering peak been red-shifted more than the absorption peak. Table 5.5 provides the ratios of absorption to scattering, and vice versa, for the two wavelengths of interest. It is observed that as the size of the nanocube increases, the $Q_{\text{abs}}/Q_{\text{sca}}$ ratio decreases while the $Q_{\text{sca}}/Q_{\text{abs}}$ ratio increases significantly.

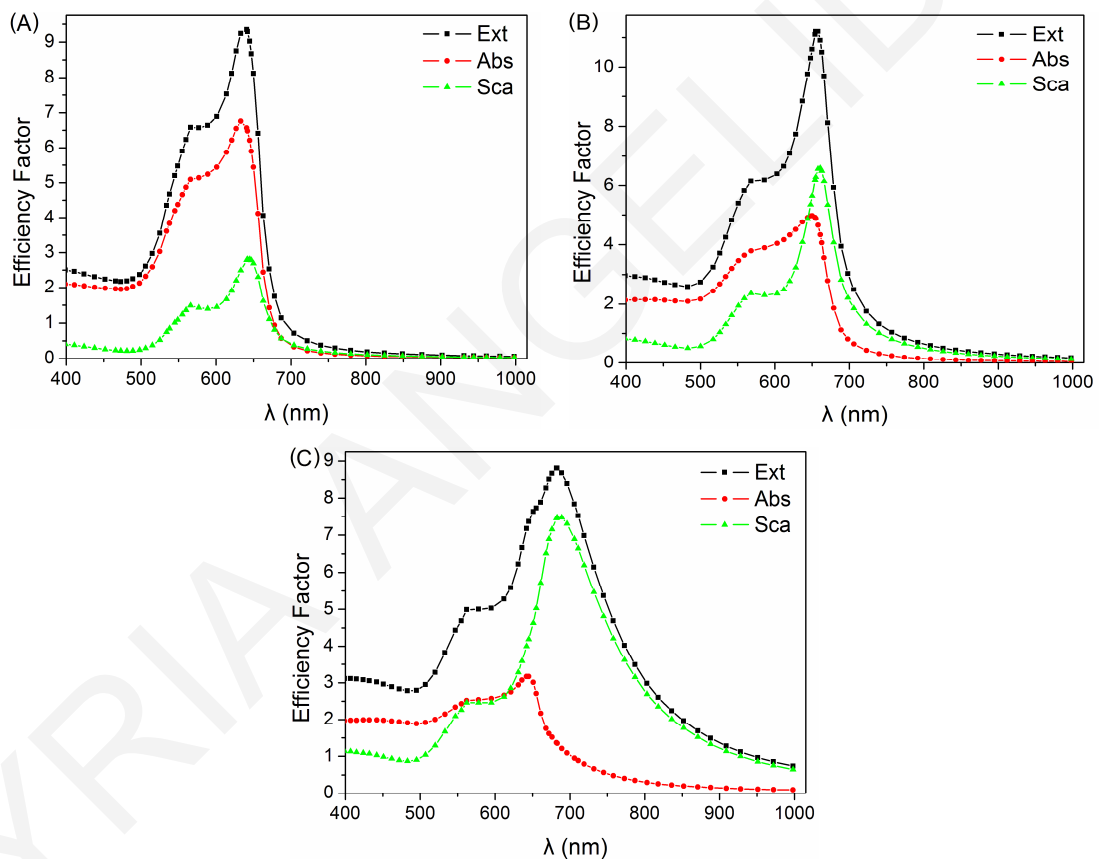


Figure 5.4: Efficiency factors of a gold nanocube with various edge lengths, b , of (A) 50nm, (B) 70nm, and (C) 100nm.

Table 5.5: Ratios of absorption to scattering efficiencies (and vice versa) for a gold nanocube having various edge lengths, b , for the two wavelengths of interest

	$Q_{\text{abs}}/Q_{\text{sca}}$, at 635nm	$Q_{\text{sca}}/Q_{\text{abs}}$, at 785nm
50nm	2.61	1.405
70nm	1.165	3.78
100nm	0.86	9.10
120nm	0.73	14.32
140nm	0.55	17.03

5.2.3 Discussion

It is clear from tables and figures that each simple metal NS displays different spectral characteristics and, by varying the shape and size parameters, the optical properties can be tuned from UV-vis to NIR wavelengths. However, the simple NSs exhibit either absorption, or scattering or overlapping plasmon bands. None of them was found to have distinct and separated absorption and scattering plasmon bands, so complex combinations of NSs must be considered further as dual-mode NSs. A gold nanocube with an edge length of $b = 120\text{nm}$, was chosen as the scattering building block, since it provides with the best ratios of scattering to absorption, and vice versa, at the two wavelengths of interest.

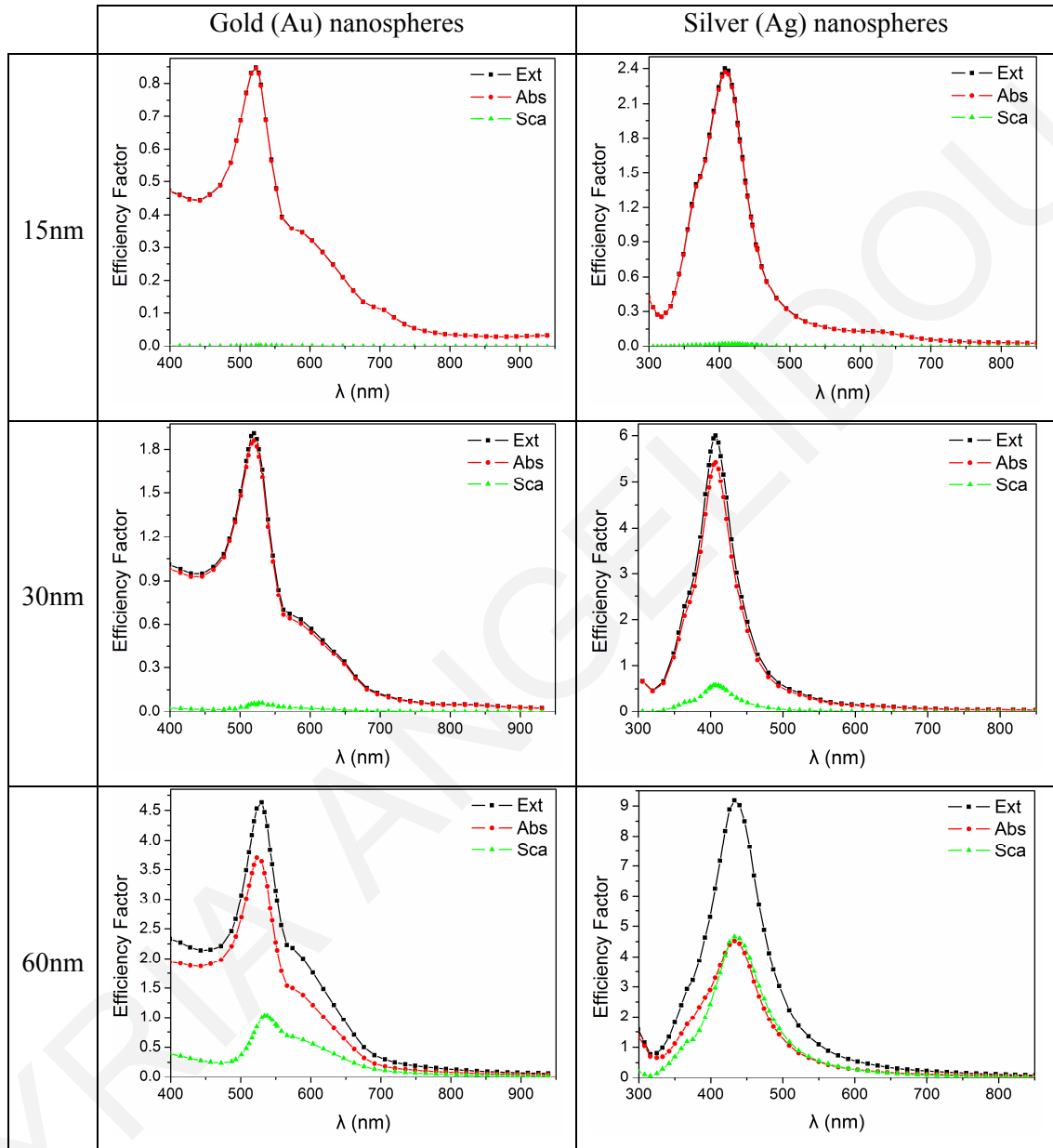
5.3 Small Nanospheres as Absorption Building Blocks

Before investigating complex NSs, the efficiency spectra of small gold and silver nanospheres, having sizes (diameters, d_m) of 15, 30, and 60nm, were calculated. The refractive index, of silver and gold, was taken from Palik [91]. The optical constants, for both metals, were modified to include the surface damping effect, as described in Chapter 2. The interdipole separation, d , was set to be 1.5nm. The effective radius, r_{eff} , was set to be equal to the small nanosphere radius.

Table 5.6 includes the figures of the efficiency factors of the various small nanospheres. For smaller nanospheres, the extinction spectrum, for both metals, is dominated by absorption, while scattering is negligible. With increasing the nanosphere diameter, the single peak is slightly red-shifted and scattering begins to increase for gold nanospheres. For silver nanospheres, scattering gradually becomes more pronounced, finally becoming identical with absorption. It is also important to note that silver nanospheres exhibit higher absorption amplitude values than gold nanospheres. Small nanospheres can be considered as potential therapeutic NPs since they provide adequate

absorption in the visible wavelength range, as also demonstrated previously [1, 88, 161, 208].

Table 5.6: Efficiency factors of small nanospheres having various diameters, dm



5.4 Complex Metal Nanostructures

To achieve the desired absorption and scattering properties of dual-mode NS, small nanospheres were combined with a gold (Au) nanocube ($b = 120\text{nm}$), creating a complex NS. The Au nanocube and small nanospheres were chosen due to their absorption and scattering properties. The small nanospheres were arranged as a layer on the cube facets. Parameters such as the number (n_{sph}), size (dm), and material (gold, Au, or silver, Ag) of the small nanospheres and, to a lesser extent, the overall size of the complex NS and

nanosphere arrangement relative to the incident wave propagation, were varied in order to find the complex NS with the optimum separation between absorption and scattering plasmon bands.

Figure 5.5 shows three examples of complex NSs. Figures 5.5(A), and (B) show a cube combined with 16 spheres, arranged as a 4×4 layer on the front face of the cube (perpendicular to the x axis), as viewed from the side, and front, respectively. The direction of incident light wave and polarization are also shown. Figure 5.5(C) show 16 spheres arranged on the side of the cube, (perpendicular to the z axis), while in Fig. 5.5(D) the spheres cover the entire cube surface. Both configurations are viewed from the front. All images of complex shapes can be found in Appendix F. Due to computational limitations, the interdipole separation, d , was chosen to have a value of 1.5nm for all simulations. Smaller values of d increased the memory requirements beyond the capabilities of the available computer hardware. The optical constants, for gold and silver, were obtained from Palik [91]. The small nanosphere refractive index was modified to include the surface damping effect. The effective radius, r_{eff} , was calculated as described in Chapter 3.

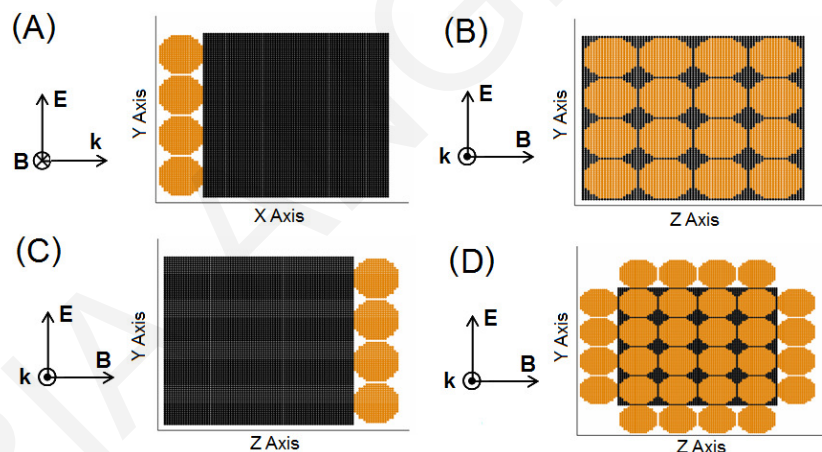


Figure 5.5: Examples of three complex NSs. First the small spheres were arranged on the front face of cube, as viewed from the (A) side (x - y plane), and (B) front (z - y plane). Then the nanospheres were (C) arranged on the side (viewed from the front), and, finally (D) covering the nanocube (viewed from the front). (Cube in black, spheres in orange.) The incident wave propagation direction is along the x axis, while the polarization is along the y axis.

5.4.1 Gold nanocube combined with various numbers (sizes) of small gold and silver nanospheres

The Au nanocube ($b = 120\text{nm}$), was combined with various small Au and Ag nanospheres. The nanospheres were arranged as a layer on the front face of the nanocube, perpendicular to the incident light propagation (x axis). The number of the nanospheres, n_{sph} , was set to 4

(2×2), 16 (4×4), or 64 (8×8). In order for the nanospheres to fit on the nanocube side, their size (diameter, dm) was adjacent accordingly. For $n_{\text{sph}} = 4, 16,$ and 64 , the diameters were $dm = 60, 30,$ and 15nm , respectively.

Table 5.7 presents the absorption, scattering, and extinction efficiency factors for the complex NSs for various small nanosphere combinations. The plasmon bands of gold and silver nanospheres combined with the nanocube,, differ only slightly. The plasmon bands, when silver nanospheres were used, appeared to be more distinct than those with a gold nanosphere layer. The absorption was more enhanced and broader, especially in the wavelength range of $550\text{--}650\text{nm}$ for the silver nanospheres. The gold nanospheres provided relatively increased scattering compared to the combination with silver nanospheres.

As the number of nanospheres, n_{sph} , increased, absorption dominated in the $400\text{--}655\text{nm}$ wavelength range, though it overlapped with small scattering peaks. In the NIR wavelength range, scattering was enhanced with its peaks being more pronounced as n_{sph} increased. Absorption had an unusual pattern, with a peak at $\lambda \approx 750\text{--}785\text{nm}$ of variable amplitude as a function of nanosphere number and size. The combination of the gold nanocube with 16 silver nanospheres exhibited the best separation between absorption and scattering, even though the plasmon bands overlapped to some degree.

The efficiency factors for the complex NS (cube with 16 spheres) were also calculated using the optical constants, n and k , obtained from Johnson and Christy [98]. The corresponding efficiencies are given in Table 5.7, as well. It is clear that the use of a different data set, for the material characterization, affects the results. The plasmon bands are similar to those obtained with the Palik [91] data set, however, the absorption band is narrower and blue-shifted in the visible range, while scattering is broader in the NIR range.

For better comparison between the various combinations, and in order to better evaluate the separation of absorption and scattering plasmon bands for each complex NS, the ratios $Q_{\text{abs}}/Q_{\text{sca}}$ and $Q_{\text{sca}}/Q_{\text{abs}}$ were calculated for the wavelengths of $635,$ and 785nm , respectively, and are given in Table 5.8. For dual-mode operation, high absorption in the visible and high scattering in the NIR range are required, so the highest possible value, for both ratios, is sought. From the table, the complex NS combination of a gold nanocube with 16 silver nanospheres provided the highest values compared to all other combinations. The ratios for the J&C efficiencies, are also given in Table 5.8. Although the ratio of $Q_{\text{abs}}/Q_{\text{sca}}$ appears to differ significantly, this is just a result of the blue-shift of the peak. At the peak wavelength of 594nm , both simulations (Palik, J&C) give similar and still high $Q_{\text{abs}}/Q_{\text{sca}}$ ratios.

Table 5.7: Efficiency factors of complex NSs having various numbers (sizes) of small gold and silver nanospheres

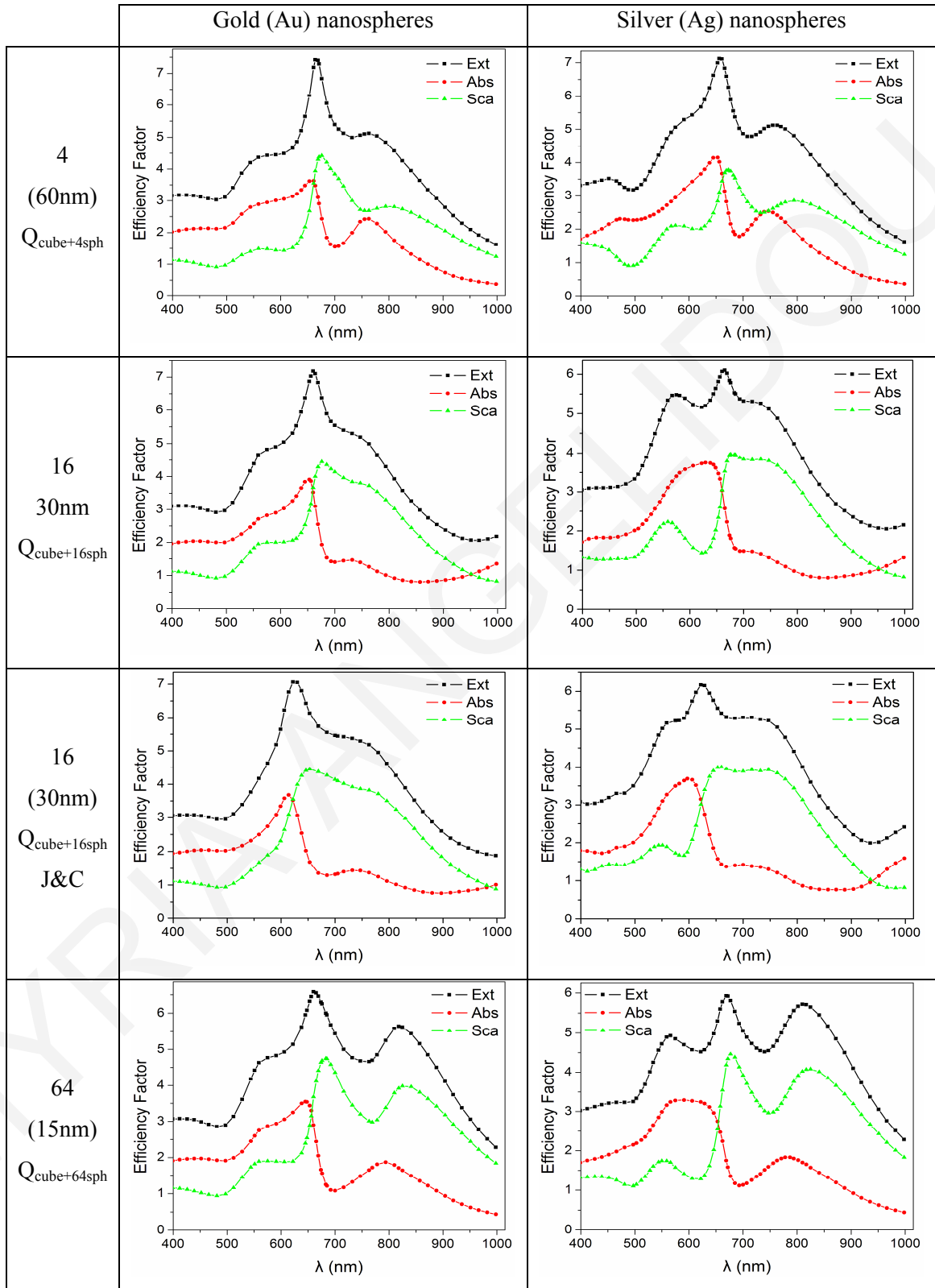


Table 5.8: Ratios of absorption to scattering efficiencies (and vice versa) for the two wavelengths of interest for the various complex NSs

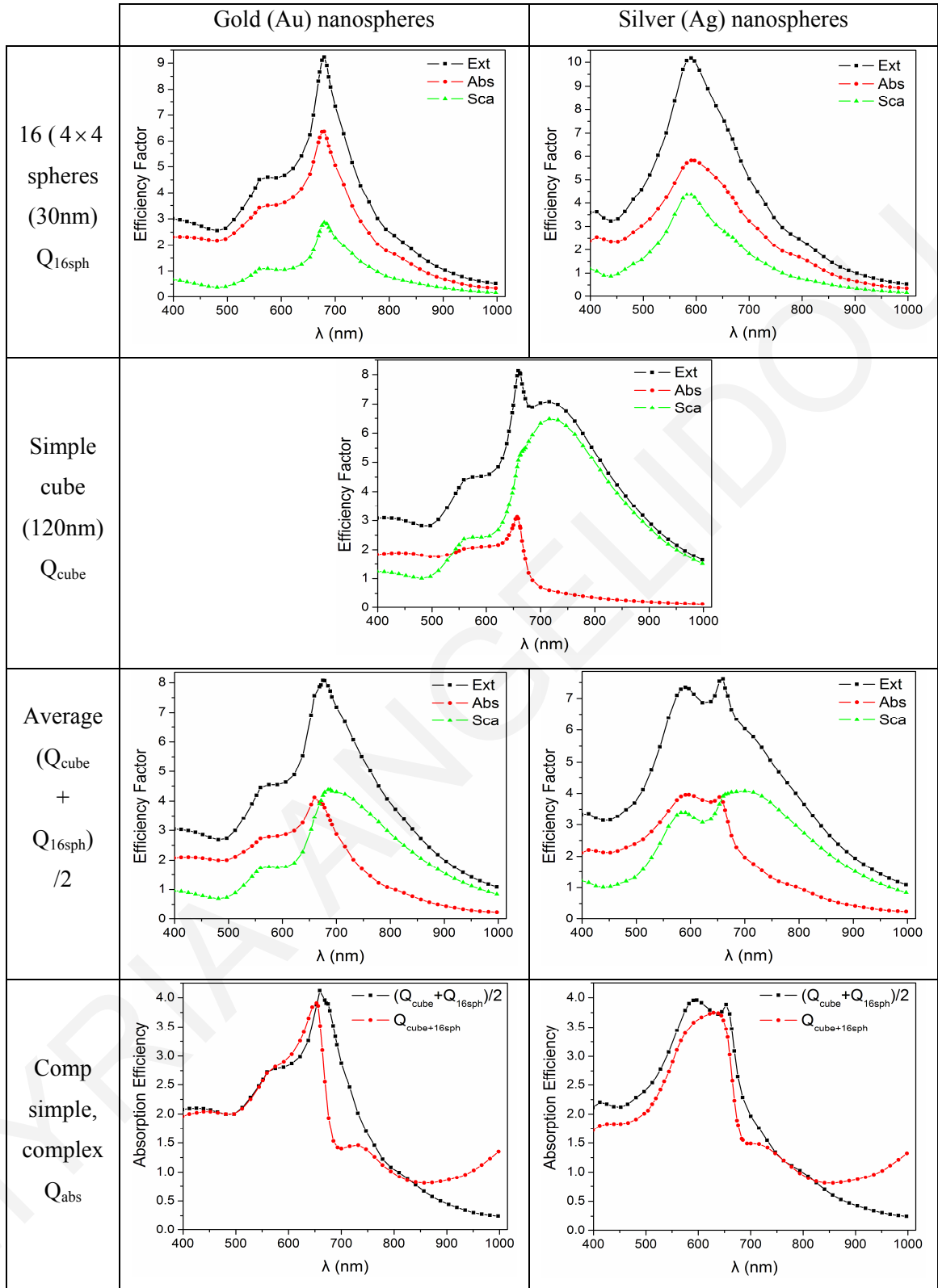
	$Q_{\text{abs}}/Q_{\text{sca}}$, at 635nm	$Q_{\text{sca}}/Q_{\text{abs}}$, at 785nm
4 Au (Palik) spheres	1.773	1.317
4 Ag (Palik) spheres	1.781	1.354
16 Au (Palik) spheres	1.583	3.242
16 Ag (Palik) spheres	2.366	3.233
16 Au (J&C) spheres	0.657	3.016
16 Ag (J&C) spheres	0.675	3.438
64 Au (Palik) spheres	1.647	1.729
64 Ag (Palik) spheres	1.992	1.947

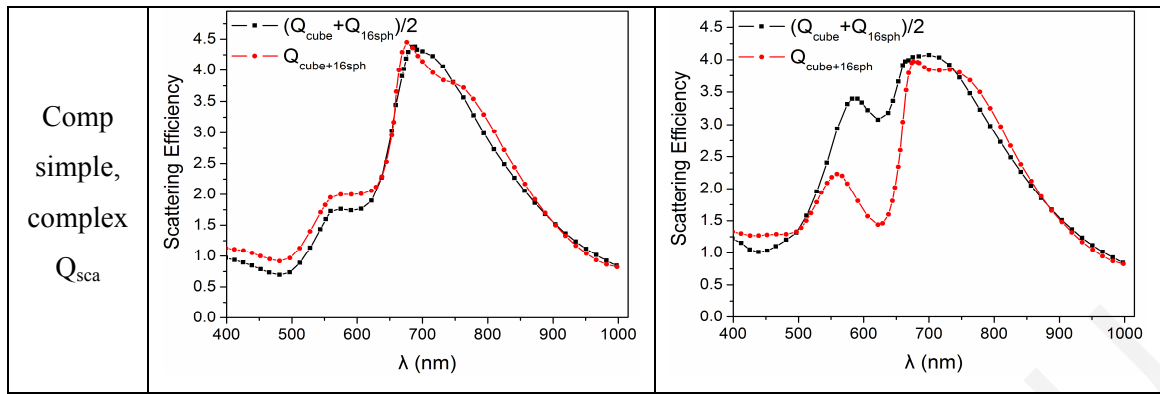
The separation between absorption and scattering plasmon bands depends strongly on the number, n_{sph} , and correspondingly the size, d_m , and material of the nanospheres. The best possible complex NS candidate for dual-mode operation is the combination of a gold nanocube ($b = 120\text{nm}$) combined with 16 (4×4 , $d_m = 30\text{nm}$) silver nanospheres, arranged on the front face of the nanocube.

5.4.2 Comparison spectra between individual and combined nanostructures

An obvious question is why combine the two simple NSs (cube and small spheres), and not used them simultaneously but individually in theranostics applications? The answer is that by combining them, the individual optical responses are modified favorably, due to the interactions occurring between the NSs. The efficiency factors of an individual layer of 16 (4×4 , 30nm) single nanospheres, $Q_{16\text{sph}}$, of a gold nanocube ($b = 120\text{nm}$), Q_{cube} , and the average efficiency values when the two are mixed, $(Q_{\text{cube}} + Q_{16\text{sph}})/2$, are all given in Table 5.9. The absorption and scattering of the average efficiencies, $(Q_{\text{cube}} + Q_{16\text{sph}})/2$, compared with the absorption and scattering efficiencies of the complex NS, $Q_{\text{cube}+16\text{sph}}$, exhibit few differences, with the exception of scattering. The scattering efficiencies of the individual NSs is increased in the visible range thus overlapping with the absorption at 635nm. This effect makes this option less desirable for theranostic applications.

Table 5.9: Comparison spectra between individual and combined NSs





5.4.3 Effect of the overall size and other nanosphere arrangements

So far, the effect of the number, n_{sph} , and correspondingly the size, d_m , of small nanospheres arranged on the front face of the nanocube (perpendicular to the propagation x axis) as well as the nanosphere material was explored. In this section, the effect of other parameters, such as the overall dimension of the complex NS, other arrangements of the layer of small nanospheres on the nanocube, and also the addition of another opposite nanosphere layer, is investigated. The simulations mainly focused on 16 Ag nanosphere combinations. The corresponding results for the 16 Au nanosphere combinations are given in Appendix G.

5.4.3.1 Overall complex nanostructure size variation

First, the overall size of the complex NS was varied. The previously described complex, dual-mode NS has dimensions of nanocube edge length, $b = 120\text{nm}$, and nanosphere diameter, $d_m = 30\text{nm}$, which results in an effective radius, $r_{\text{eff}} = 77.55\text{nm}$. The properties of two other complex NSs having smaller and larger overall size (effective radii) were also calculated. The nanocube edge length, b , and nanosphere diameter, d_m , both varied, while the number of nanospheres remained constant ($n_{\text{sph}} = 16$). For the smaller complex size, b was set to 100nm and d_m to 25nm , which resulted in $r_{\text{eff}} = 64.6\text{nm}$, while for the larger complex size, b was set to 140nm and d_m to 35nm , which resulted in $r_{\text{eff}} = 90.5\text{nm}$. Again, the nanospheres were arranged on the front face of the cube, perpendicular to the propagation axis.

Figures 5.6(A), and (B) show the results for the above structures. As the size became smaller (Fig. 5.6(A)) the absorption increased, while the scattering decreased. The more characteristic features were an absorption enhancement at $\lambda = 570$, and 700nm , a decreased scattering peak at $\lambda = 550\text{nm}$ decaying in the NIR. When the overall size became larger (Fig. 5.6(B)) the reverse changes were observed. Absorption decreased and

overlapped with scattering at visible wavelengths, while scattering increased and broadened to a longer NIR wavelength range. The property of distinct and separated absorption and scattering plasmon bands is less prominent and at different wavelength regions (e.g., in the visible for the smaller size NS).

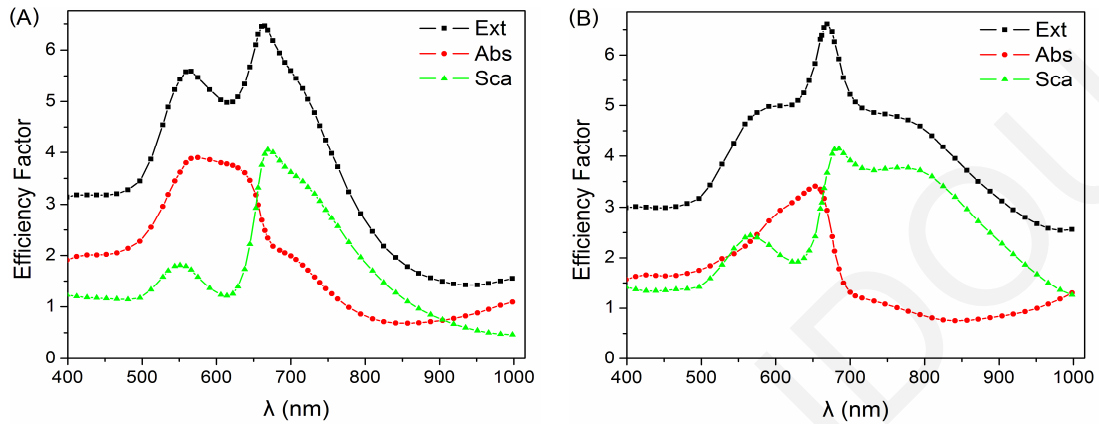


Figure 5.6: Efficiency factors of an Au nanocube combined with 16 Ag nanospheres having dimensions of (A) $b = 100\text{nm}$, $d_m = 25\text{nm}$, and (B) $b = 140\text{nm}$, $d_m = 35\text{nm}$.

5.4.3.2 Small nanosphere arrangement on nanocube

Other arrangements for the small Ag nanospheres, on various sides of the nanocube, were also explored, since the simulations described so far assumed that the small nanospheres were arranged on the front face (y - z plane) of the nanocube. The effect of the positioning of the nanospheres on the nanocube, in relation to the incident light propagation, on the optical response, and more particular the absorption and scattering plasmon bands, was investigated.

First, the 16 Ag nanospheres were arranged on the back of the nanocube. The efficiency factors are shown in Fig. 5.7(A). The overall extinction efficiency was identical to that of the nanospheres arranged on the front face of the nanocube, but the absorption and scattering efficiencies were totally different. The visible absorption peak at $\lambda = 615\text{nm}$ was gone, and almost flat absorption is observed. Scattering was the dominant effect in this case, ranging from 520nm to the NIR, with three peaks at $\lambda = 580, 660,$ and 735nm . The separation between absorption and scattering plasmon bands was lost. The different absorption and scattering plasmon bands observed when the nanospheres were arranged on the back instead on the front, were probably due to the fact that incident light first passed through the scattering nanocube and then interacted with the small nanosphere arrangement, therefore strong scattering initially occurred due to the large size of the nanocube followed by some absorption due to the nanospheres. The extinction plasmon

bands were identical due to the fact that overall size of the complex NS did not change and the incident light perceived the same complex NS shape.

Figure 5.7(B) shows the efficiency factors for the complex NS where the nanospheres were arranged on the side (x - y plane) of the nanocube, perpendicular to the z axis. (Note that the incident light propagates along the x axis.) The absorption and scattering plasmon bands changed significantly. The absorption had an almost flat efficiency spectrum with a small peak emerging at $\lambda = 652\text{nm}$. The scattering was more intense for most of the wavelength range. Three scattering peaks were observed, at $\lambda = 565, 700,$ and 845nm , with the second being the most intense. More importantly, the separation between the absorption and scattering plasmon bands was again, lost.

It is important to note that when the nanospheres are arranged on the side of the nanocube, the efficiencies are polarization dependent, as demonstrated in Fig. 5.7(C). The extinction spectra for an incident y polarization ($Q_{\text{polar},y}$) were compared with z ($Q_{\text{polar},z}$) and the average value, ($Q_{\text{avg}(yz)}$). The three extinction spectra were similar for two wavelength ranges ($400\text{--}465\text{nm}$ and $625\text{--}665\text{nm}$). Major differences were observed in the NIR range, where the value of $Q_{\text{polar},z}$ was significantly higher, with an extra peak observed at 855nm , probably due to the interaction between the nanocube and the nanospheres. In the visible wavelength range, there were only some small variations in the peak intensity. For nanospheres arranged above or below the cube, (perpendicular to the y axis) similar average efficiency factors but reverse polarization responses were obtained. When the nanospheres were arranged on the front or back of the nanocube, there was no polarization dependence of the results since the complex NS was symmetric along the y and z axis (Fig. 5.7 (B)).

These results imply that the optical response of the complex NS (nanocube plus nanospheres) depends on the arrangement of nanospheres on the nanocube in relation to the incident light direction and polarization.

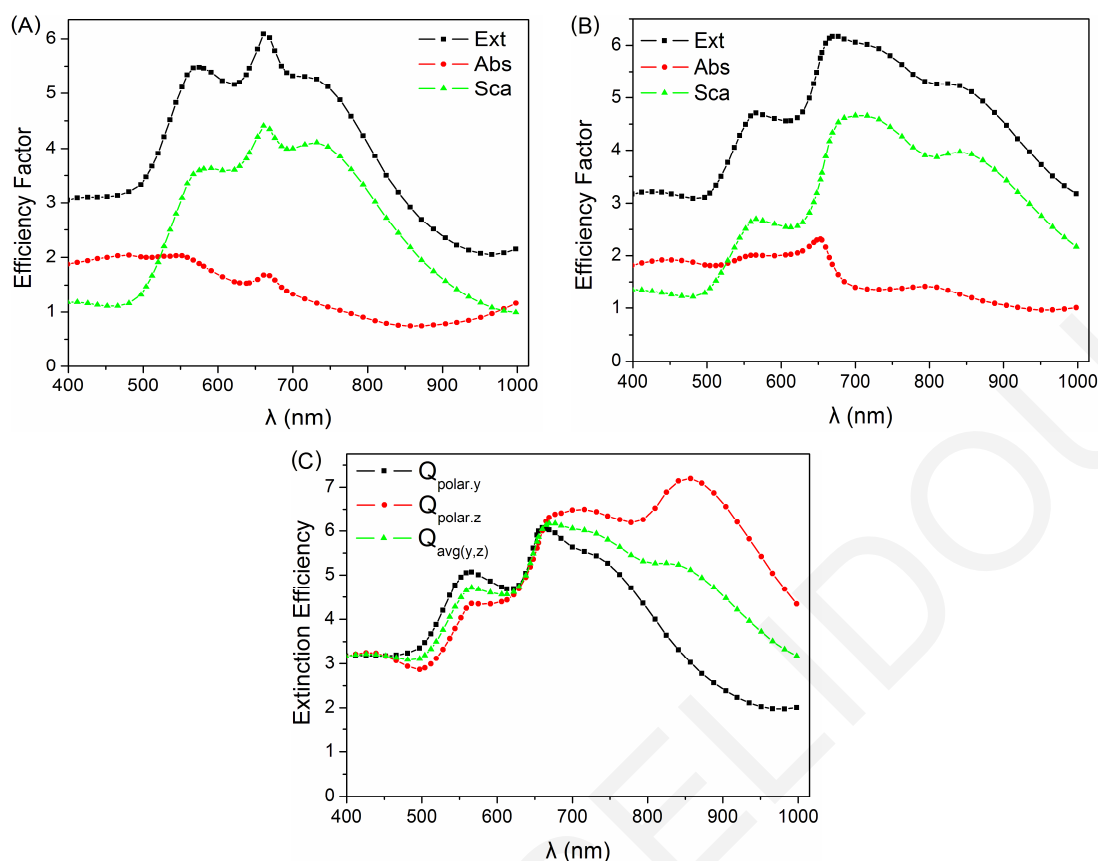


Figure 5.7: Efficiency factors of an Au nanocube combined with 16 Ag nanospheres arranged (A) on the back, and (B) on the side of the nanocube. (C) Extinction efficiency spectra showing the polarization dependence when the 16 Ag nanospheres were arranged on the side, perpendicular to the z axis.

5.4.3.3 Addition of a second layer of small nanosphere to the complex nanostructure

The effect of the addition of a second nanosphere layer, arranged at the opposite face from the first layer, were also investigated. Figure 5.8(A) shows the efficiency factors of a complex NS consisting of 2 layers, with 16 Ag nanospheres each, arranged on the front and back of the nanocube. The absorption and scattering plasmon bands, again, changed significantly. The absorption increased, with a peak emerging at $\lambda = 578\text{nm}$ and a shoulder observed at $\lambda = 635\text{nm}$. The scattering plasmon band had a peak at $\lambda = 567\text{nm}$, which overlapped with the absorption, and a second red-shifted peak at 750nm . For even longer wavelengths, in the NIR range, the absorption increased and dominated over scattering. The separation between absorption and scattering plasmon bands was lost.

Figure 5.8(B) show the efficiency factors for a complex NS were the two layers of nanospheres were arranged on opposite sides (x - y plane) of the nanocube, perpendicular to the z axis (i.e., left and right). In this case absorption had a flat plasmon band whereas the

scattering was more intense for most of the wavelength range. Three scattering broad peaks were observed, at $\lambda = 565, 715,$ and 910nm , with all having almost equal amplitudes.

Since the nanospheres were arranged on the sides, polarization dependent phenomena were also observed (Fig. 5.8(C)). The addition of a second nanosphere layer did affect the absorption and scattering plasmon bands and the optical response in general. The optical responses to the two polarization states were similar to those where only one layer was considered but with more pronounced effects in the NIR wavelength range.

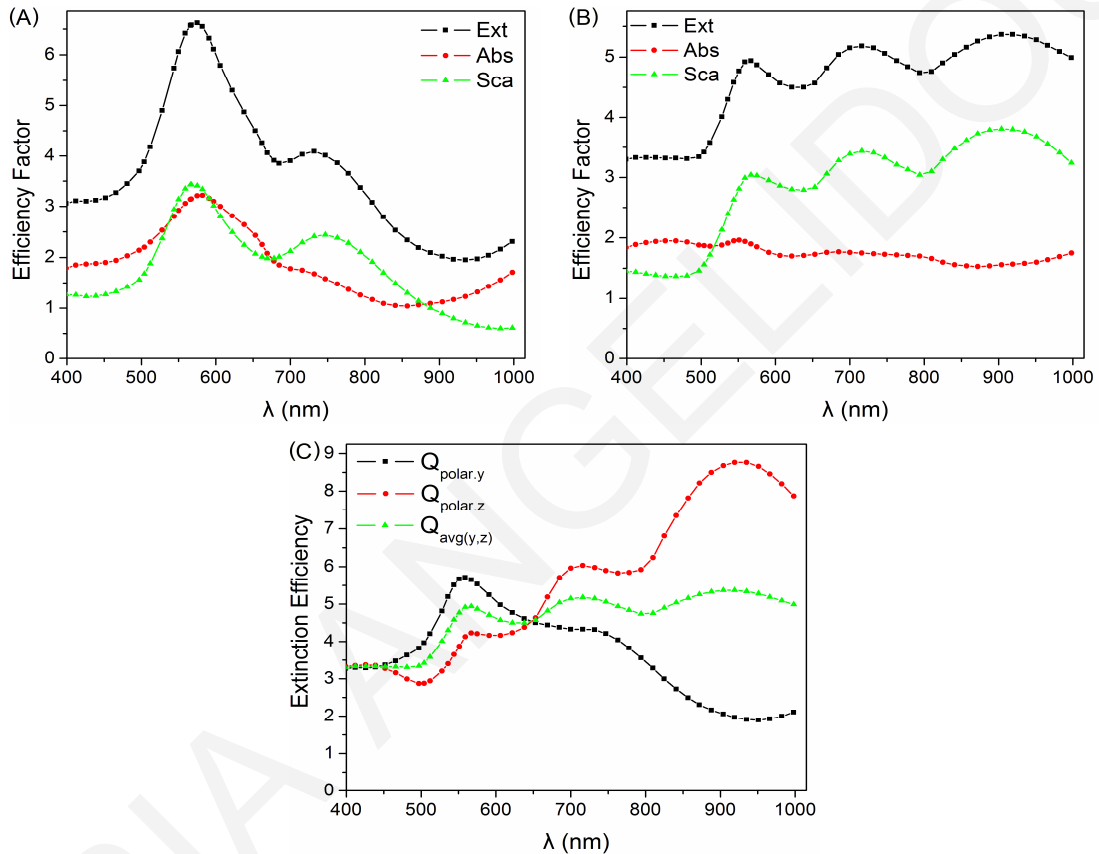


Figure 5.8: Efficiency factors of an Au nanocube combined with 2 layers of 16 Ag nanospheres arranged (A) on the front and back, and (B) on opposite sides of the nanocube. (C) Extinction efficiency spectra showing the polarization dependence when the 16 Ag nanospheres were arranged on opposite sides, perpendicular to the z axis.

5.4.4 Nanocube covered by small nanospheres

To complete the analysis of complex NSs, the small nanospheres were arranged on all the nanocube facets. The Au nanocube was covered either by 96 (6×16 , $dm = 30\text{nm}$), or by 384 (6×64 , $dm = 15\text{nm}$) Ag nanospheres. The efficiency factors for 24 (6×4 , $dm = 60\text{nm}$) Ag nanospheres were not calculated, since the large grid size required for the dipole array was impossible to implement due to computational limitations. Figure 5.9(A,B)

shows the results for these NSs. A broad, uniform, absorption over the entire wavelength range was observed for both configurations, which overlapped significantly with the scattering. Two distinct scattering peaks were observed, at $\lambda = 552$ and 863nm , for the 6×16 configuration, (Fig. 5.9(A)) while a small peak, at $\lambda = 542\text{nm}$, and a larger peak, at $\lambda = 958\text{nm}$, were present in the 6×64 configuration. The configuration of the Au nanocube covered by nanospheres did not provide the necessary separation between the plasmon bands, thus is not a good candidate for combined imaging and therapy applications.

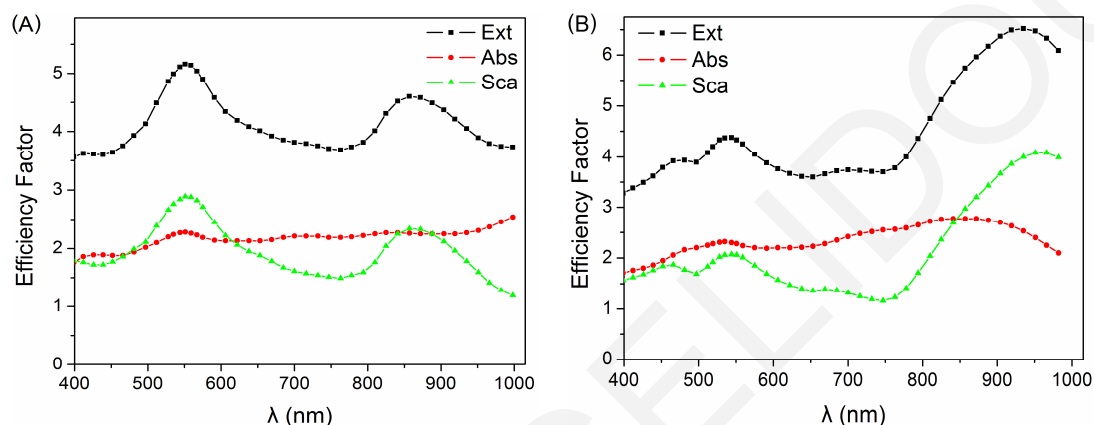


Figure 5.9: Efficiency factors of a nanocube combined with (A) 96 (30nm), and (B) 384 (15nm) Ag nanospheres. The small nanospheres cover all 6 nanocube facets.

5.5 Cubical Nanoshells

Since the gold nanocube provided the best ratios of scattering to absorption, and vice versa, at the two wavelengths of interest, a new shape, the cubical nanoshell, was also considered. The cubical nanoshell is similar to a classical nanoshell, which consists of a dielectric, silica core and a gold shell, but it has a cubical, instead of spherical shape. The plasmon bands of cubical nanoshell were calculated and compared with the classical nanoshells and simple nanocubes, to see whether and how the optical response was affected.

The cubical nanoshell was chosen to have an outer edge length of $b = 140\text{nm}$, which was considered to be constant for the simulations. The shell thickness was defined as $(b - b_{\text{core}})$, where b_{core} was the edge length of the core. The interdipole separation, d , was set to be 2nm , and the effective radius was set equal to 86.85nm , for all cubical nanoshell shapes. The value, r_{eff} , was derived from the cubical shape and the constant edge length, b .

Different efficiency factors were calculated by varying the parameters of:

- Shell material, (silver (Ag), and gold (Au)).
- The ratio, b_{core}/b , (≈ 0.57 and 0.86 , which corresponded to shell thicknesses of 30, and 10nm, respectively).
- The core material, (dielectric (SiO_2 , $m_{\text{core}} = 1.44 + i0$, at all wavelengths) and metallic (Ag, Au)).

Figures 5.10(A) and (B) show a section of the two cubical nanoshells considered here, with their parameters as marked. Another NS was also proposed, the nanobox, which was considered to be a metal nanocube having embedded a smaller dielectric nanocube [47, 48, 50]. One may consider that the cubical nanoshell to actually be a nanobox, but since metal cores are considered here, the nanoshell term seems more appropriate.

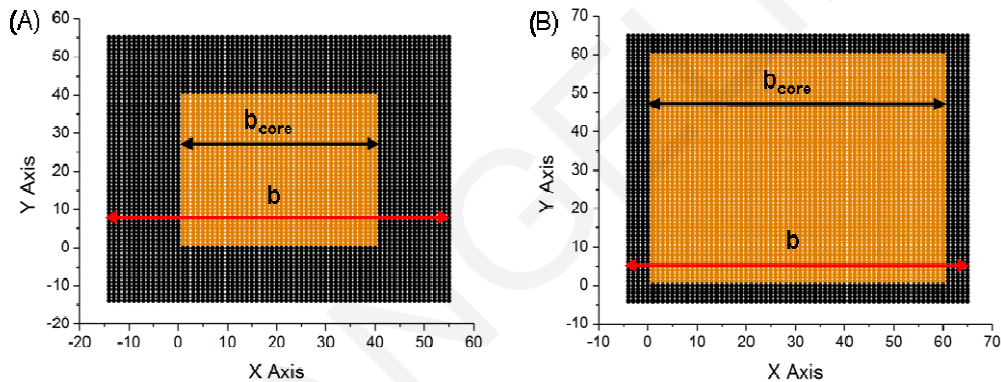
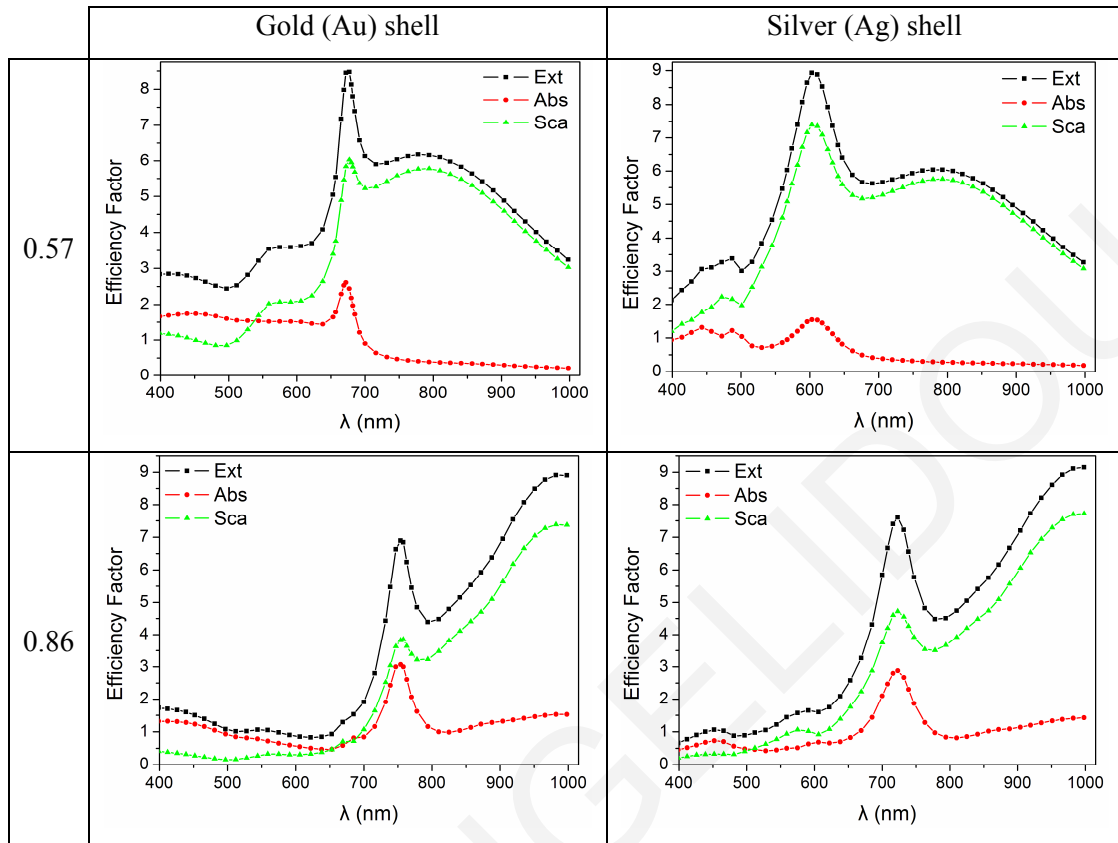


Figure 5.10: Sections of two cubical nanoshell, which have a constant edge length, $b = 140\text{nm}$, and ratios, b_{core}/b , of (A) 0.57, and (B) 0.86nm. (Core is in orange, and shell in black.)

5.5.1 Cubical nanoshells consisting of a silica core and various metal shells

First, the efficiency factors of cubical nanoshells consisting of a silica core, and metal shells, such as gold or silver, were calculated for the two ratios, b_{core}/b mentioned above. The bulk values of the optical constants, n and k , were used, and obtained from Palik [91]. Table 5.10 indicated that when the ratio is small and the shell thickness is large, scattering dominated the spectra. When the ratio was increased, the two scattering peaks observed, were shifted to longer, NIR, wavelengths. The small absorption peaks were also red-shifted and increased in intensity. For the larger ratios, ($b_{\text{core}}/b = 0.57$) the efficiency factors were vary similar for both metals considered.

Table 5.10: Efficiency factors of cubical nanoshells with silica, SiO₂, core and metal shell, for two ratios, b_{core}/b



5.5.2 Comparison with spherical nanoshells

Classical nanoshells consist of a dielectric spherical core, usually silica, and a metal shell. Gold [209], and silver [210] nanoshells have been extensively studied. For more accurate comparison, the efficiency factors of the cubical nanoshells were recalculated using modified optical constants, n and k , with the tabulated data set, for gold and silver, obtained from Johnson and Christy [98]. The value of the shell thickness, $(b - b_{\text{core}})$, was used for the size-dependent modification. The extinction efficiencies of the cubical nanoshells (silica core, metal shell) were then compared with those of spherical nanoshells.

Figures 5.11(A) and (B) show the results for gold and silver shells, respectively, for the ratios b_{core}/b . The cubical nanoshells exhibited red-shifted extinction efficiencies with more than one peaks and increased peak intensities, compared to the classical, spherical nanoshells. Also, the gold shells (Fig. 5.11(A)) exhibited peak efficiencies at longer wavelengths compared to the silver shells (Fig. 5.11(B)). For the cubical nanoshells as the ratio b_{core}/b increased, the peaks red-shifted all the way to infrared (IR) wavelengths, in the case of the gold-shell nanoshell. From Fig. 5.11 one can deduce that the cubical nanoshell should be the NS of choice when NIR wavelength is required for imaging (e.g., Optical Coherence Tomography (OCT) at 800 or 1300nm, or SERS at 785nm).

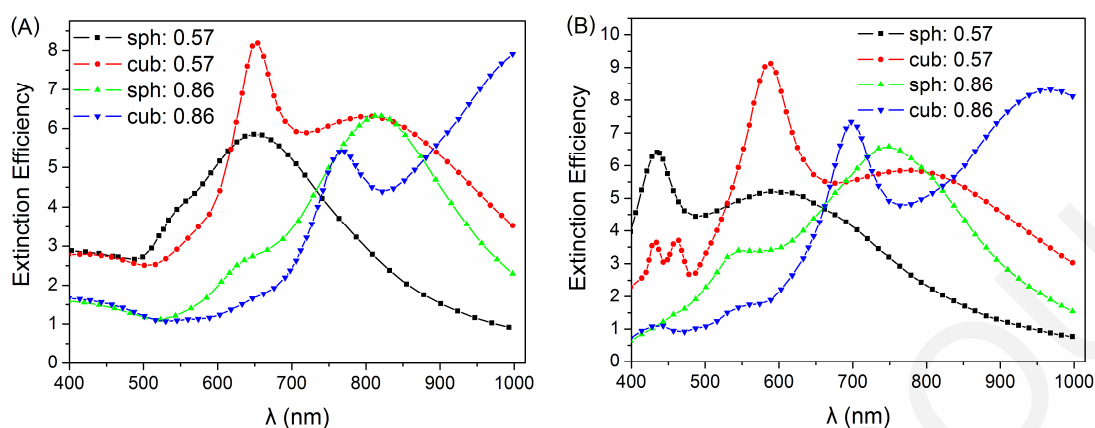


Figure 5.11: Comparison between extinction efficiency spectra of spherical and cubical nanoshells of silica core and (A) gold, or (B) silver shell.

5.5.3 Cubical nanoshells with metal cores

The efficiency factors of cubical nanoshells with metal core were also calculated for two ratios, b_{core}/b . The bulk values of the optical constants, n and k , were used, from the tabulated data of Palik [91]. Table 5.11 shows the results. The most important observation, from Table 5.11, is that for all four cubical nanoshells, scattering dominated the spectra. For the ratio of $b_{\text{core}}/b = 0.57$, the efficiency factors were similar to those of the cubical nanoshell with a silica core, implying that the observed extinction efficiency is little affected by the core due to the increased shell thickness.

It is also important to note that for the thick shell, where $b_{\text{core}}/b = 0.57$, the efficiency factors also looked similar to those of the corresponding gold and silver nanocubes. Figure 5.12(A,B) compares the metallic cubical nanoshells with the simple nanocubes. As the metal shell was increased, the cubical nanoshell extinction spectrum was shifted to the extinction spectrum of the corresponding simple nanocube. From Fig. 5.12, one can assume that for thick shells, such as 30nm, ($b_{\text{core}}/b = 0.57$), the material core does not contribute to the optical response of the core/shell NS. Similar observations were reported for spherical Ag/Au [160, 211], and Au/Ag [212, 213] core/shell NSs.

Table 5.11: Efficiency factors of cubical nanoshells with metal core for two ratios, b_{core}/b

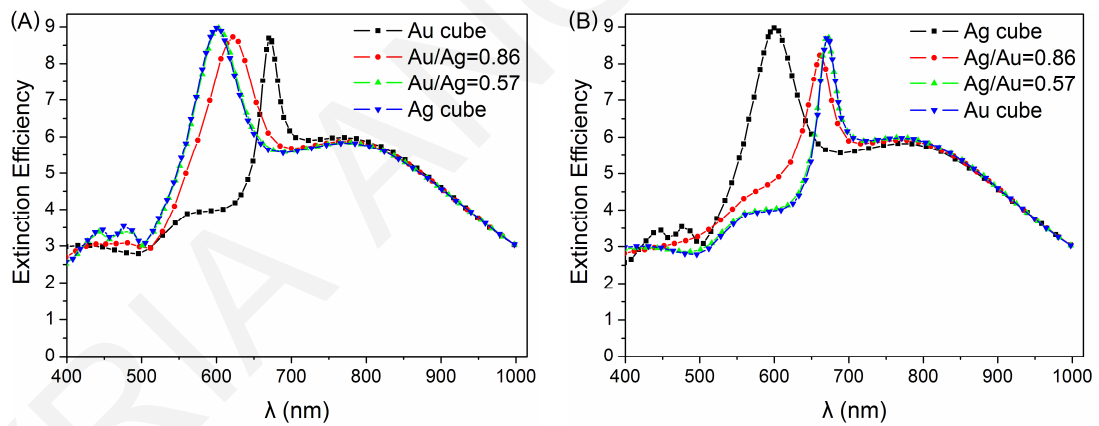
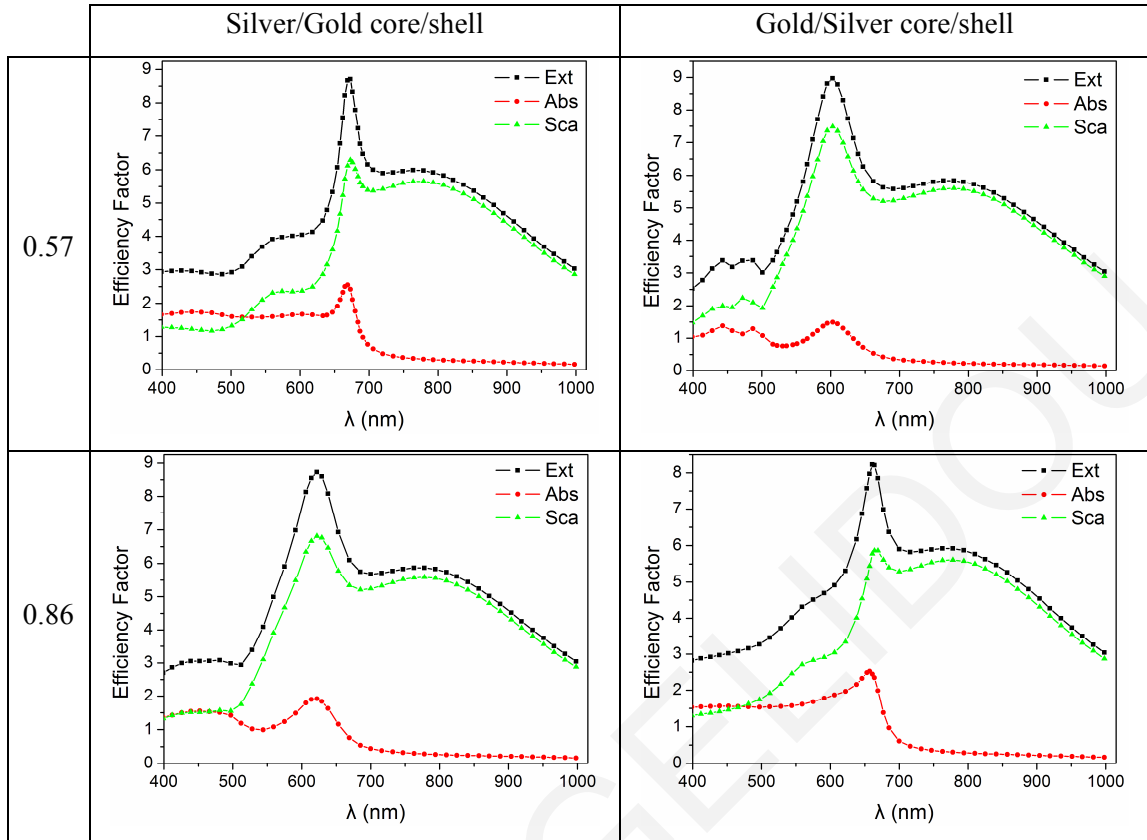


Figure 5.12: Comparison between extinction efficiency spectra of simple gold and silver nanocubes ($b = 140\text{nm}$) with cubical nanoshells, having (A) Au/Ag, and (B) Ag/Au, core/shell materials.

5.6 Summary

The purpose of this study was to theoretically investigate the design a new metal NS that could exhibit the unique property of distinct and separated absorption and scattering plasmon bands. The metal NS would, preferably, have an absorption band at $\lambda = 635\text{nm}$ and a scattering band at $\lambda = 785\text{nm}$, both in the “optical window” range for biological applications. This new, so-called “dual-mode” NS would have the potential to be used in

theranostic applications where the shorter wavelength (absorption) could be used for therapy and the longer wavelength (scattering) could be used for diagnosis (imaging or spectroscopy).

First, the efficiency factors of various simple metal NSs were calculated. The materials of silver, gold, aluminum, and nickel and the shapes of nanosphere, nanocube, and tetrahedron, for sizes ranging from 50 to 140nm, were explored. The absorption and scattering plasmon bands were found to overlap, to some degree, in the visible range, while, at NIR wavelengths, scattering was dominant. The optical properties of small gold and silver nanospheres were verified as well. None of the simple metal NSs was found to have separated plasmon bands at the desired wavelengths, leading the investigation to combinations which were considered next.,

A gold nanocube, having an edge length, b , of 120nm was chosen as the scattering building block and small nanospheres were chosen as the absorption NPs. The two NSs were combined to create a more complex NS. A detailed investigation was performed, where parameters such as the number (coupled with the diameter) and material (silver or gold) of small nanospheres were varied. Initially, the small nanospheres were arranged on the front face of the nanocube, perpendicular to the propagation axis. The ratios of $Q_{\text{abs}}/Q_{\text{sca}}$, and $Q_{\text{sca}}/Q_{\text{abs}}$, for the two wavelengths of interest, were calculated for better comparison between the complex combinations. A nanocube, combined with 16 silver nanospheres, exhibited the best efficiency ratios and most clear separation between the plasmon bands.

Further investigation proved that it is beneficial to use the combined NSs rather than individual NSs, for simultaneous imaging and therapy applications. Also, the effect of the overall size of the complex NS, the arrangement of the nanospheres on the nanocube, and the combination of a nanocube covered by nanospheres, were also considered. The optical response of the proposed complex NS appeared to be orientation dependent, relative to the incident propagation, and small nanosphere arrangement dependent. The plasmon bands were significantly different, with the separation between them lost.

New cubical nanoshells consisting of a silica or a metal core and a metal shell, were also explored. These nanoshells have a cubical rather than the classic spherical shape. It was shown that they mainly exhibited scattering plasmon bands. For a thick metal shell, such as 30nm, the cubical nanoshell exhibited the same optical response as the corresponding metal nanocube. However, they provide red-shifted and increased efficiencies compared to the spherical nanoshells. Making the ideal as diagnostic contrast agents in the IR range.

6. Synthesis and Experimental Verification of Monolayer Shell Aggregates

6.1 Introduction

The thorough theoretical analysis of the novel shell aggregates was followed by the synthesis and experimental confirmation of their optical properties. The “shell aggregate”, described in Chapter 4, is a gold (Au) nanostructure (NS) resulting from small nanospheres aggregating and creating a monolayer shell. Figure 6.1(A) show an image of the monolayer shell aggregate, and in Fig. 6.1(B) a quarter is removed to better visualize the shell aggregate structure. For the purposes of this chapter, a shell aggregate is considered to consist of small Au nanospheres which aggregate on the surface of a larger dielectric particle. The material of the dielectric particle can have any refractive index (real part n , zero k), since it does not affect the optical response of the shell aggregate. The bilayer shell aggregates were not experimentally explored, since were found to provide similar optical properties to the monolayers.

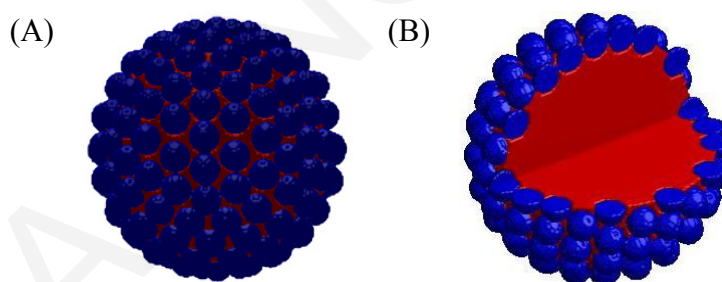


Figure 6.1: Image of a whole monolayer shell aggregate. (B) A quarter of the shell aggregate was removed for better visualization. (Gold nanospheres (shell) are in blue, and core material in red.)

There are no reports in the literature describing the synthesis of shell aggregates. A shape of layered gold nanospheres was reported by Song et al. [214] and was described as a sub-100nm, hollow, spherical, gold, nanoparticle superstructure. Their method is quite complex, since it involved peptide conjugation and esterification for nanosphere aggregation. Synthetic protocols were reported by various authors where small Au nanospheres can be either directly formed on a core template or aggregate on its surface. The core material was either a liposome [215-218], or a silica [24, 219-222], or a polystyrene [223-228] sphere.

Liposomes are mainly used as drug carriers. They are also ideal for delivering Au nanoparticles (NPs) to target sites in vivo [215, 216]. Three types of complexes of Au NPs with liposomes were reported. The first is a liposome containing Au NPs in the inner phase, the second in the lipid membrane, and the third a liposome modified with Au NPs on its surface [217, 218]. The third complex could be considered for the formation of shell aggregates. However, the Au NPs cannot be made to cover enough of the liposome surface, which implies that no intersphere coupling interactions can exist and the optical properties of the NS will resemble more those of a single nanosphere. Silica NPs were used as aggregation substrates [219, 220], or as core templates [24, 221, 222] for composite NPs or nanoshell formation. However, the silica surface required functionalization with amine or methyl groups for the Au nanospheres to be deposited. However, simpler methods, using unmodified substrates made of other materials exist. For example, polystyrene (PS) spheres have been used either in the formation of gold nanoshells [223-225], or as carriers [226] or SERS substrates [227, 228]. Synthetic protocols involving unmodified [223, 227, 228], or modified [224-226] PS surfaces for Au deposition were explored. For the purpose of the shell aggregate synthesis, PS spheres were chosen as cores since they are readily available and can even be easily removed later, if hollow shell aggregates are required.

Gold nanoparticle-coated polystyrene (AuNP-coated PS), by directly formatting small Au nanospheres on the surface of uncoated, unmodified, and micro-size PS, has been reported [227], resulting in “raspberry-like” morphologies. For the purposes of the synthesis of the shell aggregate, the protocol parameters were modified accordingly to account for the fact that a nanometer (rather than micrometer) scale core was used. In addition, the synthesis of shell aggregates requires more precise reaction control in order to result in an assembly of nanospheres rather than a fused “raspberry-like” formation. The synthesized NS was called as composite

6.2 Materials – Equipment

The materials required for the synthesis were:

- Polybead polystyrene (PS) microspheres, which were purchased from Polysciences, Inc. The PS spheres have a diameter of $0.1139 \pm 0.0017 \mu\text{m}$. The latex suspension had a 2.59% (w/v) concentration.
- A chemical compound of gold (Au), such as hydrogen tetrachloroaurate(III) hydrate ($\text{HAuCl}_4 \cdot x\text{H}_2\text{O}$, MM = 339.8g/mol), which was purchased from Aldrich.

- Trisodium citrate 2-hydrate ($C_6H_5Na_3O_7 \cdot 2H_2O$, or $Na_3Citrate$, MM = 294.1g/mol) which was purchased from Panreac Quimica S.L.U. The $Na_3Citrate$ acts both as a reducing, and as a stabilizing agent.
- Deionized water, which was used at every stage of reaction and washing.

The experimental equipment and supplies used during the synthesis process were:

- Electronic balance, AE Adam, model PW 124, which was used to measure the exact amount of gold and $Na_3Citrate$, in order to create the corresponding aqueous solutions and to obtain the desired molar concentration.
- Hotplate/stirrer, Stuart, model SB 162, which was used to boil and stir the solutions.
- Sigma laboratory refrigerated 3K30 centrifuge, which was used to redisperse the final solution. Two fixed-angle rotors were used in the centrifugation process:
 - Rotor no. 12111H (max speed: 26000/min, max centrifugal field: 57440g, centrifuge tubes 10mL).
 - Rotor no. 12158H (max speed: 26200/min, max centrifugal field: 60630g, centrifuge tubes 30mL).

Other supplies and consumables included flasks, pipettes, laboratory tubes, and a timer.

The experimental equipment and supplies used for the characterization of the synthesized NSs were:

- UV-vis spectrophotometer, Jasco model V-650, which was used to measure absorbance spectra for the various final and redispersed.
- Scanning electron microscope (SEM), a VegaII LSU model, which was used to obtain morphological images of the synthesized composite NSs.

Pipettes, cuvettes and SEM specimen mounts were also used.

6.3 Experimental Procedures

6.3.1 Basic protocol for AuNP-coated PS synthesis

Li et al. [227] proposed a one-step heterocoagulation strategy, to fabricate “raspberry-like” AuNP-coated PS composite particles. A heteroagulation strategy is based on the colloid steric stabilization theory in order to prepare host/guest composite particles, whereby small guest particles, are located at the host surface [229, 230]. Li et al. [227] showed that the Au

NPs acted as stabilizers, and in the presence of PS microspheres they generate and adhere onto the PS surface.

The method where trisodium citrate ($\text{Na}_3\text{Citrate}$) is used as a reductant [227], was chosen to create the monolayer shell aggregates. Briefly, 16.4mL HAuCl_4 ($3 \times 10^{-3} \text{M}$) aqueous solution was added to 84mL deionized water, and the solution was heated up to boiling under magnetic stirring. Then, 2mL PS emulsion (2.5 μm size, 0.2g, 10% (w/v) concentration) and $\text{Na}_3\text{Citrate}$ solution (e.g., 0.42–2mL, $80 \times 10^{-3} \text{M}$) were added simultaneously to the boiling solution and the above mixture was stirred for another 15min. The solution from yellowish (gold) turned into lavender, and then ruby red due to the formation of free Au NPs. The resulting composite particles were separated by centrifugation/redispersion cycles to remove free Au NPs. The authors also noted that the composite particles remained stable, since no morphological changes were induced during the centrifugation process.

Other reducing agents were also explored, and it was found that Au NPs were successfully attached to the PS surface regardless of the reductant. However, the method chosen requires less time and readily available materials. The amount of $\text{Na}_3\text{Citrate}$ plays a significant role in the final size of gold nanospheres. Adding 2mL of reductant resulted in 15nm size, while adding 0.42mL resulted in larger 55nm size nanospheres. The $\text{Na}_3\text{Citrate}$ also acted as a stabilizer in the formation of nanospheres [227] preventing further aggregation [231].

6.3.2 Experimental considerations

Before performing any experimental procedures, the various parameters of the procedures were determined, the materials were prepared, and the various procedures calibrated. Let's note that the composite particles generated by the experimental procedure are named as composite Au@PS (gold-at-polystyrene) NSs

6.3.2.1 Aqueous solutions preparation

The HAuCl_4 (gold salt) and $\text{Na}_3\text{Citrate}$ were available as solids (crystal form). The molar concentrations for the aqueous solutions, based on [227], were set to $3 \times 10^{-3} \text{M}$ for HAuCl_4 , and $80 \times 10^{-3} \text{M}$ for $\text{Na}_3\text{Citrate}$. To obtain the desired molar concentration, given the molar mass (MM) of each material, 20mg of HAuCl_4 were diluted in 20mL water and 235mg of $\text{Na}_3\text{Citrate}$ diluted in 10mL water. (Chemical formulas are given in Appendix

A.4.) The gold and citrate aqueous solutions were then stored in the refrigerator, at 4°C. It is important to note that after a time period of approximately three months from its preparation Na₃Citrate was no longer effective in reducing HAuCl₄, most likely due to oxidation.

6.3.2.2 Estimation of the amount of PS to be used

The appropriate amount of PS suspension to create a 10% (w/v) solution was calculated, to account for the smaller PS (0.114µm) spheres used in these experiment compared to the basic protocol. Li et al. [227] used 0.2g of 2.5µm PS spheres. This corresponded to 0.009g of PS. The polybead PS suspension purchased has a 2.59% concentration, which means that every 100mL of latex suspension contains 2.59g PS spheres. For 0.009g of PS spheres, 0.35mL of the latex suspension is required.

6.3.2.3 Centrifugation of the final solutions

Centrifugation of the solutions was performed after the synthesis. All relevant parameters such as speed (rpm), centrifugal field (rcf), time, and temperature were set on the centrifuge. (More information regarding rpm and rcf can be found in Appendix A.5.) The same settings were used in all experimental procedures, to separate free unbounded Au nanospheres from the composite Au@PS NSs. The centrifuge was set to rcf = 1500g (speed: 4121) for 5min, at a temperature of 5°C to cool down. Then, two centrifugation/redispersion cycles were performed. First, 8mL of the final solution was centrifuged at 5000g (speed: 7524) for 10min and then at 7000g (speed: 8902) for 5min to obtain a pellet. At these speeds, both free and composite Au@PS NSs were collected at the bottom of the centrifuge tube [232]. The supernatant (≈ 7mL) was removed, and the same amount of water (≈ 7mL) was added to the pellet to redisperse. Then, a second centrifugation was performed, at lower speeds, so that only the heaviest, composite Au@PS NSs gathered at the pellet. The redispersed, 8mL, solution was centrifuged at 2000g (speed: 4758) for 5min, and then at 1000g (speed: 3364) for 5min. Again, the supernatant (≈ 7mL) was removed, 2mL of water were added to the centrifuge tube, and the pellet was again redispersed. Both centrifugation processes were performed at 5°C temperature.

6.3.2.4 UV-vis spectrophotometry

After the conclusion of the synthesis, UV-vis absorbance (A) spectra were collected over the wavelength range of 400 to 900nm, at room temperature. All samples were dispersed in water and loaded into a quartz cuvette of 1cm optical path length (L). Parameters, such as the band width of the incident beam, initial and final wavelength, the data pitch (which determines the number of data points taken during collection), and scan speed, were specified. (More information regarding UV-vis spectrophotometry is given in Appendix A.6.)

For the measurements described in this chapter, the band width was set to 2nm, the data pitch to 0.2nm, and the scan speed to 400nm/min. Continuous mode was used for all data collection. Also, three absorbance spectra of plain water samples were measured and the average water spectrum was later subtracted from each measured absorbance spectrum.

6.3.2.5 SEM imaging

The SEM instrument was operating at an acceleration voltage of 30kV with magnification between $2,000\times$ and $22,000\times$. A drop of the final, dilute solution was deposited on a carbon coated pin stub specimen mount and left to dry under sunlight before inserted into the vacuum chambers of the electron microscope. Sometimes in order to enhance a signal, the sample is sputter coated with gold prior to SEM imaging. In the case of the composite Au@PS NSs there was no need, since they already consist of gold. (More information regarding SEM is given in Appendix A.7.)

6.3.3 Experiments

After the preparation of the aqueous solutions, the basic protocol was verified. Then, a reverse method was followed, meaning that the water was first boiled, then the PS and $\text{Na}_3\text{Citrate}$ solutions were added simultaneously, and then the 16.4mL HAuCl_4 solution was added too. The same color changes were observed in both cases (see colors below).

Next, three different experimental procedures were performed, using the reverse method, but with different amounts of gold added, at different time points. The experimental procedure was stopped sooner before single Au nanospheres were formed. The synthesis stopped when the final solution had a bluish to lavender color, which corresponded to the composite Au@PS NSs. For all experiments, 0.84mL $\text{Na}_3\text{Citrate}$ was used to obtain 25nm sized Au nanospheres, which could be compared with the monolayer shell aggregate model with dimensions of $R = 70\text{nm}$, $r = 25\text{nm}$, and various

edge-to-edge distances, ds . The amount of gold salt and time scale between drops was different for each experiment. Figure 6.2 displays the three experimental procedure charts, which are explained below.

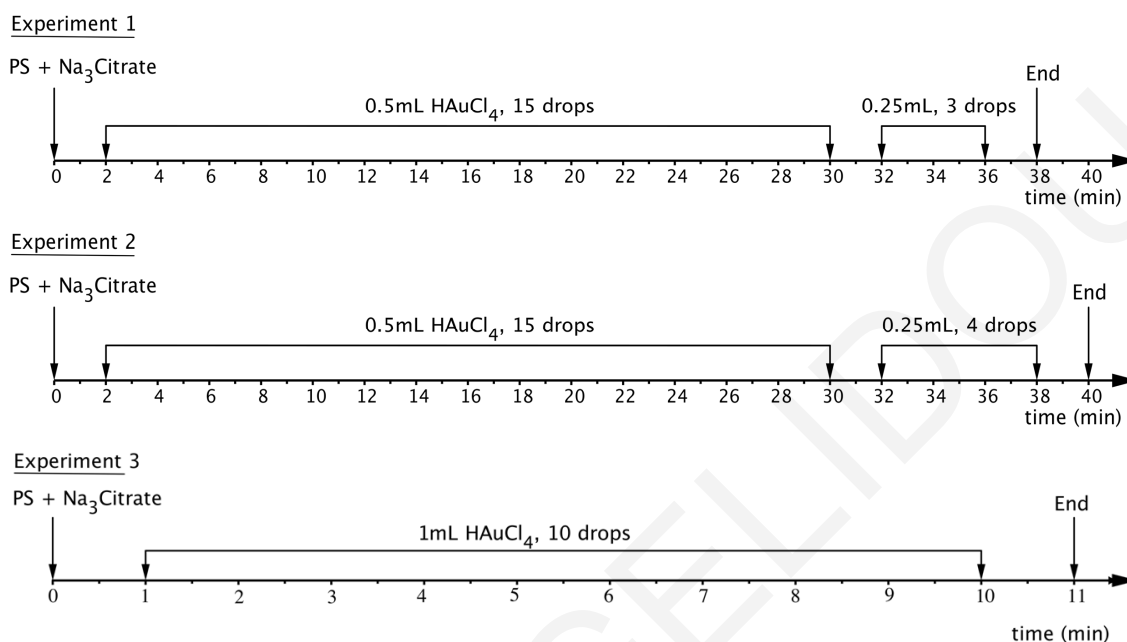


Figure 6.2: Charts showing the time scale and gold drops for each experimental procedure.

6.3.3.1 Experiment 1

Initially, 84mL deionized water was heated to boiling (100°C) under magnetic stirring (indicator 2). Then, 0.35mL of PS and 0.84mL of Na₃Citrate were added. Simultaneously, the timer started to count the duration of the experimental procedure, while the solution was continuously boiled and stirred. After 2min, a drop of 0.5mL of gold salt was added to the initial PS+Citrate solution. Then, 0.5mL of gold salt was added every 2min. After 30min of boiling and adding drops, color changes were observed. Then, 0.25mL of gold was added, again every 2min. The final drop was added at 36min, at which point the solution had a royal blue color. The procedure ended at 38min, the hotplate turned off, and the final solution was removed from heat at 39min. Half of the final solution was left to cool down at room temperature (25°C) (experiment 1(a)), and the other half was left to cool in ice (0°C) (experiment 1(b)). Overall 15 drops of 0.5mL and 3 drops of 0.25mL of gold solution were added to the initial PS+Citrate solution. The absorbance spectra, A , were then collected using a spectrophotometer.

The centrifugation process was performed the next day (day 2nd of experiment), for both final solutions (the cooled-on-ice solution and the cooled-at-room-temperature solution) in order to remove any free Au nanospheres. Then, absorbance spectra of both

final and redispersed were measured. The centrifugation process was repeated after seven days (day 8th of experiment). Again, all spectra (final and redispersed solutions) were collected using a spectrophotometer.

It is important to note that after the synthesis process, measurements, and centrifugation, all solutions were stored, in the refrigerator, at 4°C.

6.3.3.2 Experiment 2

Experiment 2 was similar to experiment 1, with the only difference being an extra 0.25mL gold drop added to the solution. Briefly, 0.5mL HAuCl₄ drops were added to the initial PS+Citrate solution, every 2min. After 30min, 0.25mL of HAuCl₄ were added, with the final 0.25mL drop added at 38min. The procedure stopped at 40min and the final solution was removed from the heat at 41min. For this experiment, all the final solutions were cooled on ice. Overall 15 drops of 0.5mL and 4 drops of 0.25mL of gold solution were added to the initial PS+Citrate solution. Then, the absorbance spectrum of the final solution was measured, using the spectrophotometer.

The centrifugation process and measurements were performed on the 2nd day, and were repeated again on the 8th day of the experiment. After the synthesis, centrifugation, and measurements, all solutions were stored, in the refrigerator, at 4°C.

6.3.3.3 Experiment 3

Experiment 3 was different than the previous procedures. Here, larger HAuCl₄ drops at a shorter time points, were added to the solution. Again, 84mL of deionized water was heated to boiling (100°C) under magnetic stirring (at indicator 2). Then, 0.35mL of PS, and 0.84mL of Na₃Citrate were added. Simultaneously, the timer was started to count the duration of the experimental procedure, while the solution was continuously boiled and stirred. After 1min, and at every 1min, a drop of 1mL of HAuCl₄ was added. The final drop was added at 10min and the final solution was removed from heat at 11min and cooled on ice. Overall 10 drops of 1mL gold solution were added to the initial PS+Citrate solution. Then, the absorbance spectrum of the final solution was measured, using the spectrophotometer.

The centrifugation process and measurements were performed on the 8th day of the experiment and were repeated again on the 15th and 22nd days. The reason why the centrifugation process was performed on the 8th day of synthesis is due to the fact that there was no peak observed in the absorbance spectrum of the final solution on the day of

the synthesis (Table 6.4). The reason why there was no peak initially is probably because the reaction was too slow, as the reductant used was over 3 months old. Later, SEM images were obtained for both final and redispersed solutions. Again, all solutions, after synthesis, centrifugation, and measurements, were stored, in the refrigerator, at 4°C.

6.4 Analysis

To verify the synthesis of the composite Au@PS NSs, the measured absorbances were compared with the calculated extinctions efficiencies. For a colloidal solution containing N particles per unit volume, the absorbance, A , is given by

$$A = 0.434 \times N C_{\text{ext}} L = 0.434 \times \pi r_{\text{eff}}^2 N Q_{\text{ext}} L, \quad (6.1)$$

where C_{ext} , and Q_{ext} are the extinction cross section and efficiency factor, respectively. The number 0.434 results from $\log(e)$ [90, 233, 234]. Since the absorbance and extinction factor wavelength dependence is equivalent, it can be assumed that they exhibit similar spectral profiles which can be correlated through constant Additive and multiplicative factors.

Initially, water spectrum (average over three measurements) was subtracted from all measured A spectra. Then, the calculated extinctions efficiencies, Q_{ext} , and the new absorbance, A' , were interpolated, to have the same wavelength sampling step, and normalized, to have amplitude of 0 to 1 values. The resulting absorbance was fitted using a linear combination of scaled extinction efficiency curves from a variety of NPs and NSs.

The fitting constants estimate, approximately, the contribution of each nanoparticle–nanostructure (NP–NS) to the spectrum obtained from each solution. The extinction efficiencies, used for the fitting process included those of:

- Single Au nanospheres, with a 25nm diameter.
- Monolayer shell aggregates with $R = 70\text{nm}$, $r \approx 12,5\text{nm}$, $ds = 2, 1$, and 0nm . (These shell aggregates correspond to structures T4H, T6E, and T6F, as described in Chapter 4.)
- Nanoshells with a PS core and an Au shell, ($R_c = 57\text{nm}$, various shell thicknesses ranging from 10 to 35nm). (Efficiency factors are given in Appendix H.)

6.4.1 Step 1: Water subtraction

Three absorbance measurements were performed for plain water samples. The average water spectrum was then calculated (Fig. 6.3(A)). As expected the signal was very low,

since water molecules begin to significantly absorb above 900nm [73, 74]. Small peaks and spikes observed can be either caused by the spectrophotometer itself or the cuvette. In Fig. 6.3(B), and (C), an absorbance spectrum of the composite Au@PS NS is shown before and after water subtraction.

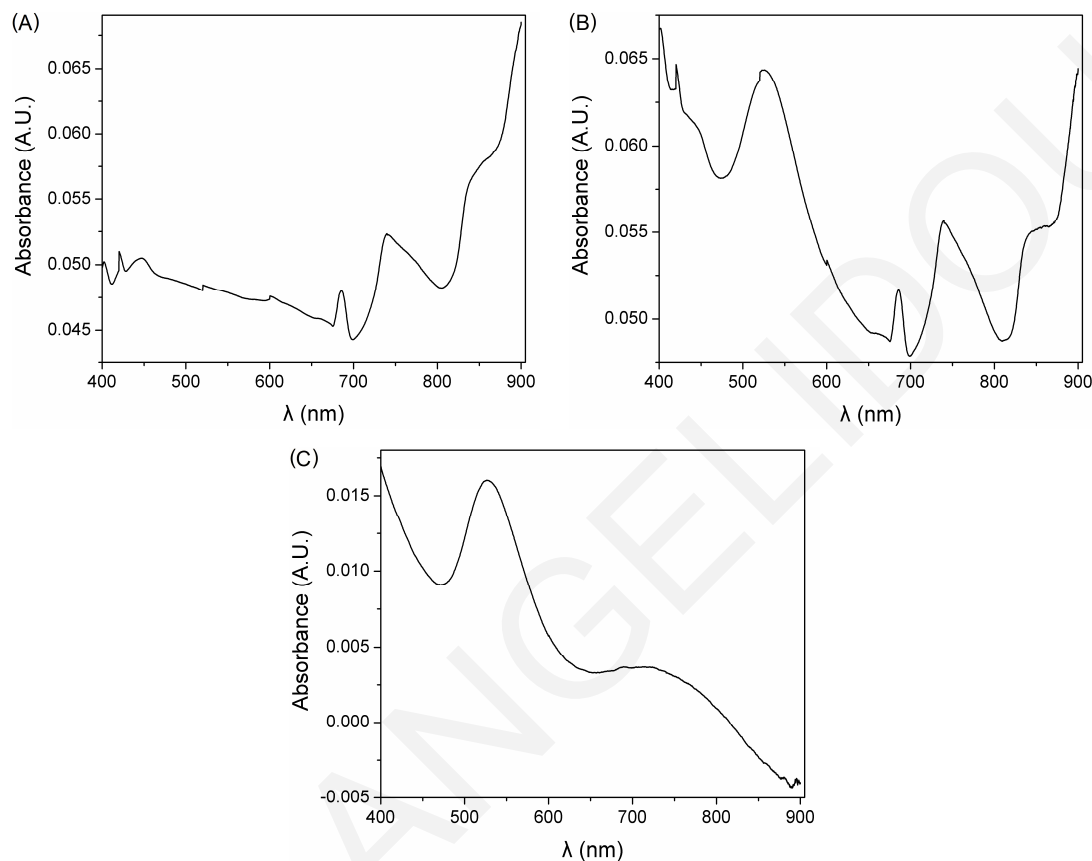


Figure 6.3: (A) Average water spectrum, (B) Measured absorbance, A , of a redispersed solution, and (C) Measured absorbance, A' with water spectrum subtracted.

It is clear that the NIR peak, of the composite Au@PS NS, is masked by the water spectrum peaks, which this means that water subtraction was necessary. Thereby, before any spectral analysis performed, the averaged water spectrum was subtracted from all the measured absorbance, A , spectra.

6.4.2 Step 2: Data interpolation

All spectra, calculated (Q_{ext}) and measured (A'), were interpolated to correspond the same wavelength, λ , values. By applying interpolation, there was no spectral distortion. Two examples are given below. The first example is a water spectrum, where peaks and small spikes contribute to the absorbance. As shown (Fig. 6.4(A)) the two profiles (measured, A ,

and interpolated, A_{new}) are essentially identical. A similar result is observed in Fig. 6.4(B), for spectra (A' compared to A'_{new}) of a composite Au@PS NS.

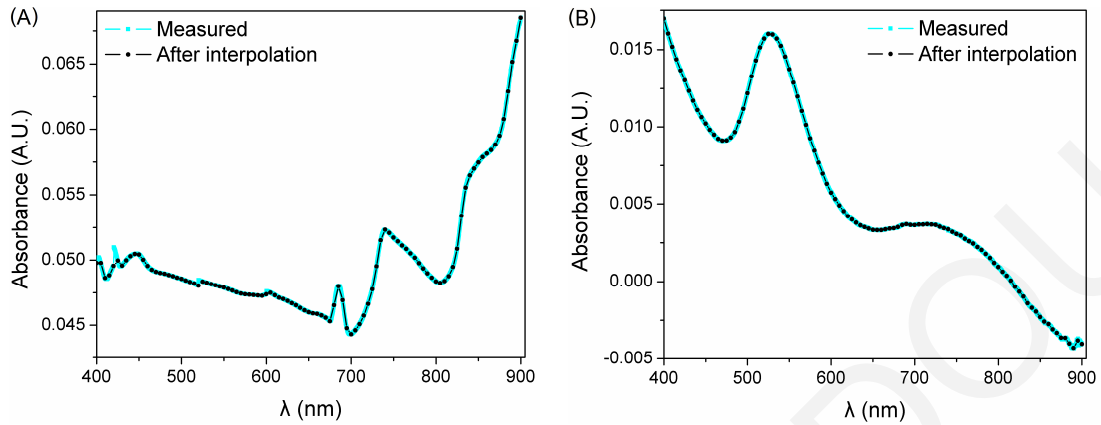


Figure 6.4: Comparison between measured and interpolated data for (A) the average water spectrum and (B) a redispersed solution spectrum.

6.4.3 Step 3: Data normalization

Next, all interpolated data was normalized to obtained values ranging from 0 (min) to 1 (max). Equation (6.2) was used to calculate the normalized “ y_{new} ” spectra. The constant 0.001 was added to avoid zero values in the denominator.

$$y_{\text{norm}} = \frac{y_{\text{new}} - \text{MIN}(y_{\text{new}}) + 0.001}{\text{MAX}(y_{\text{new}}) - \text{MIN}(y_{\text{new}}) + 0.001} \quad (6.2)$$

Normalization was performed, since the measured absorbance spectra had varying amplitudes, and after subtracting the spectrum, even had values below zero (Fig. 6.5(A)). By applying normalization, the spectrum profile (Fig. 6.5(B)) remained unchanged but the values became comparable between solutions.

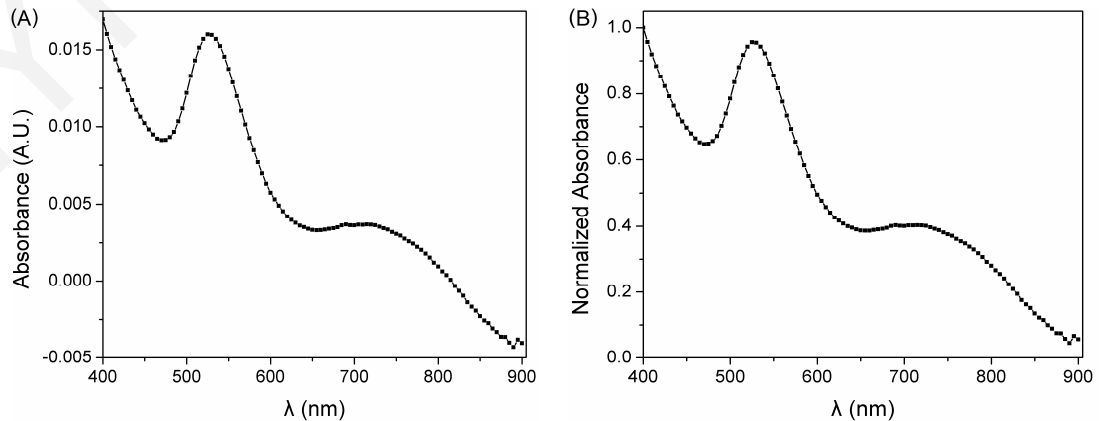


Figure 6.5: (A) Absorbance of a redispersed solution, A'_{new} , and the corresponding (B) normalized spectrum, A'_{norm} .

6.4.4 Step 4: Data fitting and comparison

The resampled and normalized absorbance spectra were fitted using the calculated extinction efficiencies to extract information regarding the morphology of the composite NSs synthesized by the experiments. First, eq. (6.3) was applied to estimate a fitted absorbance, A_{fit} , for each λ_{new} using the calculated $Q_{\text{ext, norm}}$ from the various NP–NS contributions, such as PS spheres, single nanospheres, shell aggregates, and nanoshells. The error was estimated using eq. (6.4), where the normalized measured absorbance, A'_{norm} , was compared to the fitted absorbance, A_{fit} , and finally the mean error (eq. (6.5)) was also estimated.

$$A_{\text{fit}} = \left(a_1 Q_{\text{PS, norm}} + a_2 Q_{\text{sph, norm}} + a_3 Q_{\text{ds=2nm, norm}} + a_4 Q_{\text{ds=1nm, norm}} + a_5 Q_{\text{ds=0nm, norm}} + a_6 Q_{\text{sh=15nm, norm}} + a_7 Q_{\text{sh=25nm, norm}} \right) * a_8 + a_9, \quad (6.3)$$

$$\text{error} = \text{ABS} \left[\frac{A'_{\text{norm}} - A_{\text{fit}}}{A'_{\text{norm}}} \right], \quad (6.4)$$

$$\text{mean_error} = \text{AVERAGE}(\text{error}). \quad (6.5)$$

Parameters a_f , where $f = 1, \dots, 9$, are fitting constants. Q_{PS} is the extinction efficiency factor of the PS spheres, which is characterized by the Rayleigh scattering equation, $Q_{\text{PS}} = \alpha + \beta(1/\lambda^4)$, since PS is a non-absorbing material, where α , and β are Rayleigh coefficients [84, 235]. Q_{sph} is the extinction of single Au nanospheres, while $Q_{\text{ds=2,1,or0nm}}$ are the extinction efficiencies of monolayer shell aggregates, and $Q_{\text{sh=15,or,25nm}}$ are the extinction efficiencies of nanoshells.

The Solver function of Microsoft Office Excel was used to find an optimal solution and estimate the parameters a_f by minimizing the mean error. To begin, an initial value, of 0.7 was assigned to a_f , α , and β . The only constraint set was that the fitting constants a_1 to a_7 should be positive or zero. Figure 6.6 shows an example of the fitted, A_{fit} , spectrum compared to the measured, A'_{norm} , spectrum. The fitted data overlaps well with the measured data although there are some small differences in certain spectral ranges.

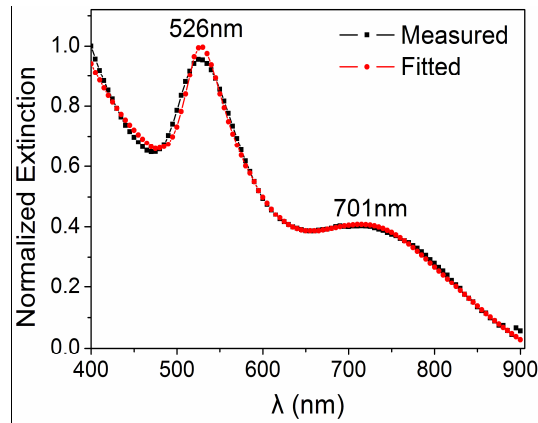


Figure 6.6: Comparison between the measured, A'_{norm} , with the fitted, A_{fit} , absorbances.

6.4.5 Step 5: Fitting constant normalization

The values of the fitting constants, a_1 to a_7 , as given by the fitting process, were normalized using eq. (6.6), so that their total sum be equal to unity. This was done to obtain a relative “percentage” of the contribution of each NP–NS extinction efficiency to the measured absorbance.

$$a'_f = \frac{a_f}{\text{SUM}(a_1 + \dots + a_7)} \quad (f = 1, \dots, 7). \quad (6.6)$$

6.5 Results

6.5.1 Synthesis of composite Au@PS NSs – Color variations

The duration of the experimental procedure was determined by the color changes of the aqueous solutions. An example of the process is shown below (Fig. 6.7(A)–(D)). First, the PS suspension and $\text{Na}_3\text{Citrate}$ solution were added simultaneously to the boiling water, which gave the solution a white color (Fig. 6.7(A)). The experimental procedure was stopped when the solution, after the addition of HAuCl_4 , reached a bluish to lavender color, (Fig. 6.7(B)) indicating the formation of composite Au@PS NSs. The progression of the synthesis was followed from the color changes of the solution. Figure 6.7(C) shows a series of images, during the synthesis, where the milky white initial PS+Citrate solution turned to the bluish final solution after several drops of HAuCl_4 were added. Finally, when the reaction was stopped by removing the final solution from heat, it was left to cool either at room temperature or on ice. Again, this affected the synthesis, and hence the color, since cooling the solution on ice stopped the reaction instantly while cooling at room temperature allowed the reaction to continue, resulting in a red-wine final solution (Fig. 6.7(D)). The red-wine color indicates the formation of free Au nanospheres [227]. After

several days, the color of the final cooled-on-ice solution also turned red-wine, meaning that the reaction continued, even though it was stored in the refrigerator. Further on, the color of both solutions remained stable for days, though a significant amount of sediment was generated at the bottom of the tubes.

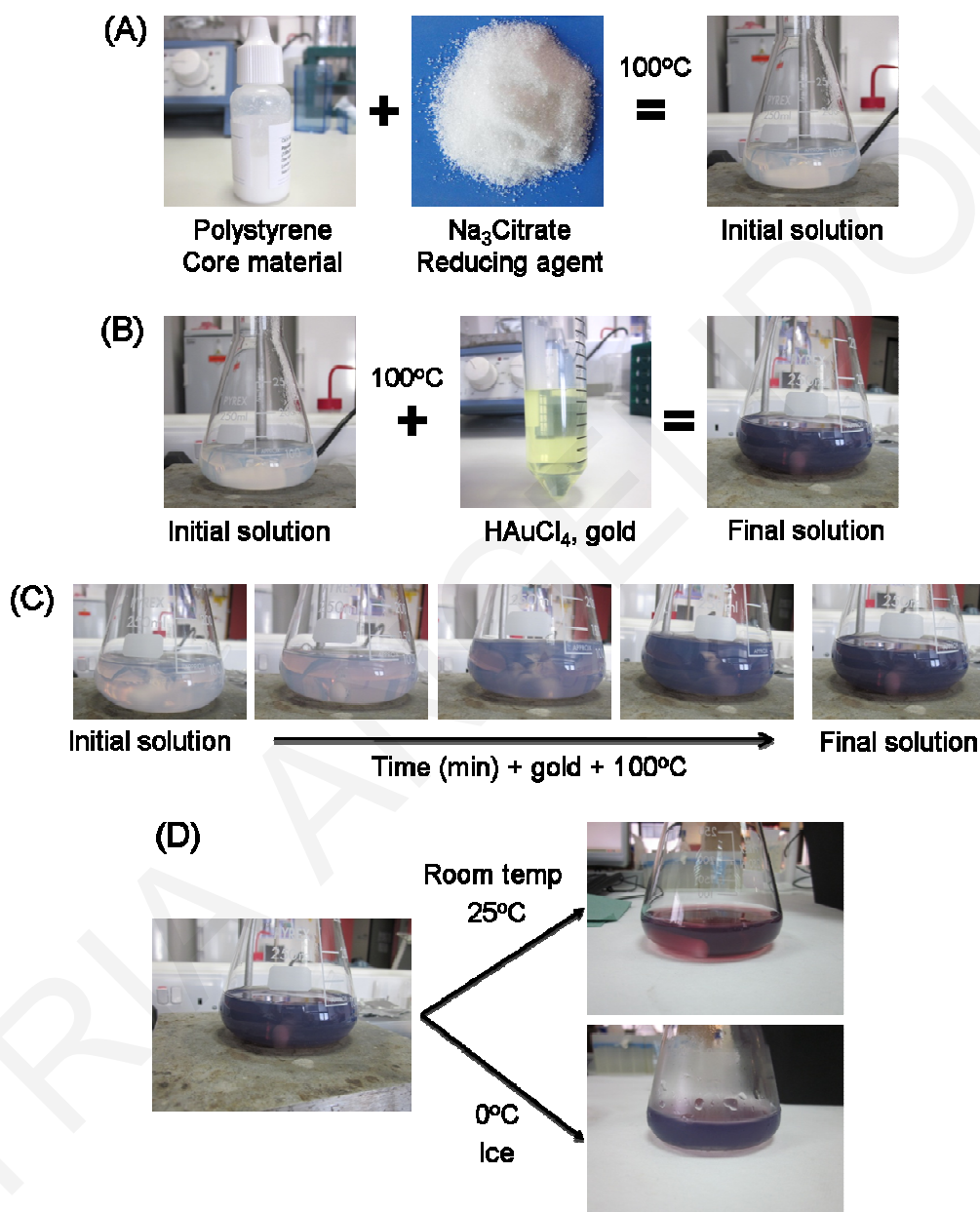


Figure 6.7: Step-by-step images of the experimental procedure for the formation of composite Au@PS NSs. (A) Initial solution, where PS and Na₃Citrate are added. (B) Bluish final solution, where gold is added. (C) Color changes as the synthesis was progressing with the addition of gold drops. (D) Different final solution colors after cooling at room temperature or on ice.

6.5.2 Composite Au@PS NSs characterization – SEM imaging

To verify the synthesis of composite Au@PS NSs, SEM images were taken from final and redispersed solutions of experiment 3. Images of the final solution were so blurred, due to the concentration of the solution, that there was no clear discrimination between particles (image not shown). Images of the redispersed solutions were clearer, as is shown in Fig. 6.8. Raspberry-like morphologies are observed, but with a significant aggregation between them.

There were some significant limitations to the SEM images. First, the image magnification of the system at $22,000\times$, resulted in a resolution of $0.5\mu\text{m}$. This resolution is not adequate to discriminate the NS's features but could not be further improved on the available instrument. As shown in the inset images of Fig. 6.8, however, the diameter can be roughly approximated to be 180nm not far from the theoretical value. Even the composite Au@PS NSs were too small to observe individually.

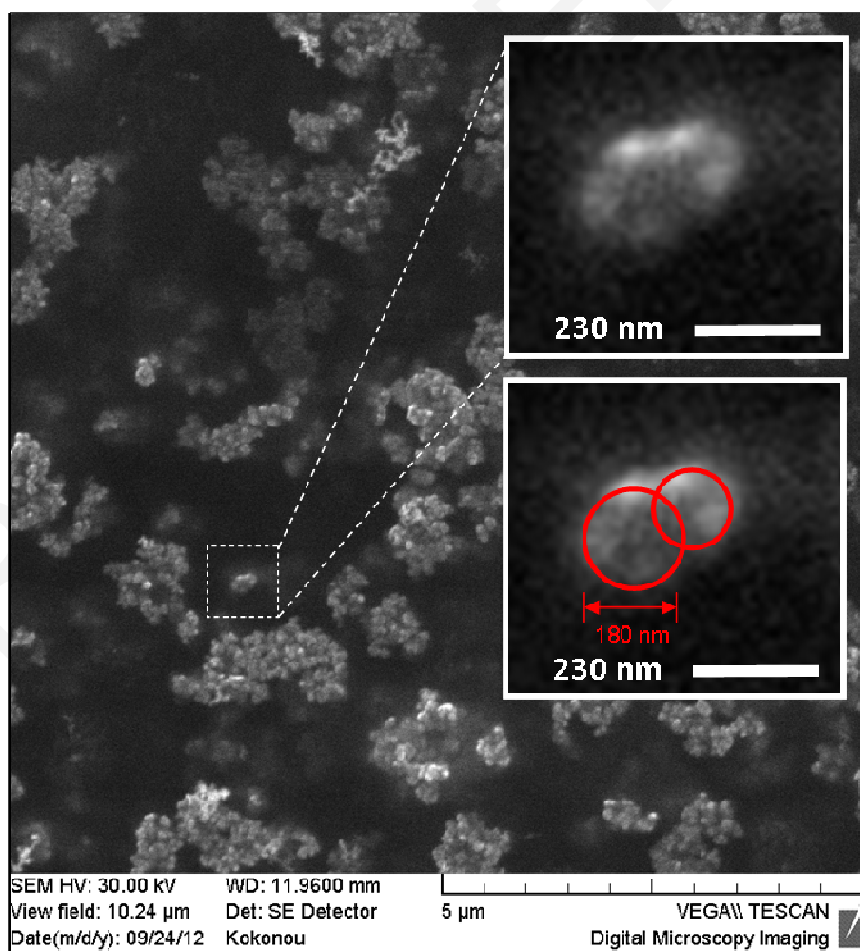


Figure 6.8: SEM image of a redispersed solution prepared using experiment 3.

Another limitation of the SEM imaging was the significant aggregation which was prominent, since the composite particles created larger and irregularly shaped formations. The reason why the composite Au@PS NSs aggregated was due to the drying process, since the sample under examination was dried under sunlight, due to limited time allotted for using the SEM. Composite Au@PS NSs were stored in the refrigerator, introducing them to sunlight to dry, at approximately 37°C. However, dispersed particles in a liquid may “pile up” or agglomerate after drying [236236]. Nevertheless, single composite NSs could still be distinguished, with the gold nanospheres giving a brighter signal than PS spheres, as shown in the Fig. 6.8 insets.

6.5.3 Measurements – Calculations

The normalized absorbances, A'_{norm} , for experiments 1(a,b) to 3, and the corresponding fitted absorbances, A_{fit} , are presented in Tables 6.1 to 6.4, respectively. The A_{fit} was calculated only for the redispersed solutions. In Table 6.5 the normalized fitting parameters, a'_f , are given with the corresponding mean errors for each fit. The unnormalized fitting constants, a_f ($f = 1, \dots, 9$), and Rayleigh coefficients, α , and β , can be found in Appendix I.

For each experiment, the final solution absorbances were measured when synthesized, and after some days. All final solutions have a single peak in the absorbance spectrum, at the wavelength close to that of single Au nanospheres. The corresponding absorbances of the redispersed solutions, which resulted after two centrifugation/redispersion cycles, are given as well. The spectra of the redispersed solutions reveal additional peaks in the absorbance spectra. The figures of redispersed solution spectra are labeled with letters and numbers, which correspond to a certain experiment and measurement. All notations can be found at Table 6.5.

Experiment 1(a) (Table 6.1), where 8.25mL of gold solution was added to the initial PS+Citrate solution, with the resulted final solution cooled at room temperature, can be an indicative example. Here, the absorbance of the final solution was measured on the day of synthesis. Then, on the 2nd day, the absorbance of the final solution was again measured. After two centrifugation/redispersion cycles, the redispersed solution spectrum was measured. The figure representing the redispersed solution of day 2 was labeled as **A0**. The measurements were repeated on the day 8th of the experiment. The final solution was again measured. After two centrifugation/redispersion cycles, the redispersed solution spectrum of the 8th day was measured and labeled **B0**. Finally, the solution redispersed on

day 2, was again measured on the 8th day and the spectrum was labeled C0. All other experiments were performed in a similar fashion, except of experiment 3 (Table 6.4), where the measurements were performed on the 8th, 15th, and 22nd day, since the reaction was significantly slower.

It is important to note that the reaction of the gold ions with the citrate, continued even though the solutions were removed from the heat and stored in the refrigerator. When the final solution was cooled at room temperature, the reaction appeared to be finished on the same day, since the color remained unchanged and the absorbance of the final solution also remained unchanged on the 2nd day. However, when the solutions were cooled on ice, their absorbance spectra, measured on the 2nd and 8th day, showed significant changes, implying that the reaction continued, even though they were stored in the refrigerator. This phenomenon appeared to be less significant for the redispersed solutions, probably because most of the reactants were washed off during the redispersion process. The experimental results are further explored in section 6.6.

6.5.4 Fitting results

The mean errors of the fitting procedures were in the range of 3.1% to 9.4%, as shown in Table 6.5. However, even though the mean error was always below 10%, the fitting was not always optimal. and the main issue with the fitting process was the inaccurate matching of the second, red-shifted, peak. The best fittings are those of the spectra B3, C3, E3, and A3 which demonstrated the lowest mean error, 3.07%, with the second peak perfectly matched. On the other hand, the spectra A1, C1, D3, F3, and C0 were sub-optimally fitted with the second, red-shifted, peak not well matched. An example of each is given in Fig. 6.9(A,B). The errors in the fitting of the absorbances induced a level of uncertainty in the interpretation of experimental results.

One reason for the sub-optimal fitting could be the fact that it was performed using a finite number of calculated extinction efficiency spectra, representing PS, single 25nm nanospheres, monolayer shell aggregates, and nanoshells. Additional structures could be required for the fitting model, such as, for example, monolayer shell aggregates having distances, d_s , of 0.5, and 1.5nm. However, calculations of those spectra was not feasible, due to computational limitations.

Table 6.1: Experiment 1(a): Gold-polystyrene solution (8.25mL HAuCl₄ + 0.35mL PS) cooled at room temp (25°C), then stored at 4°C

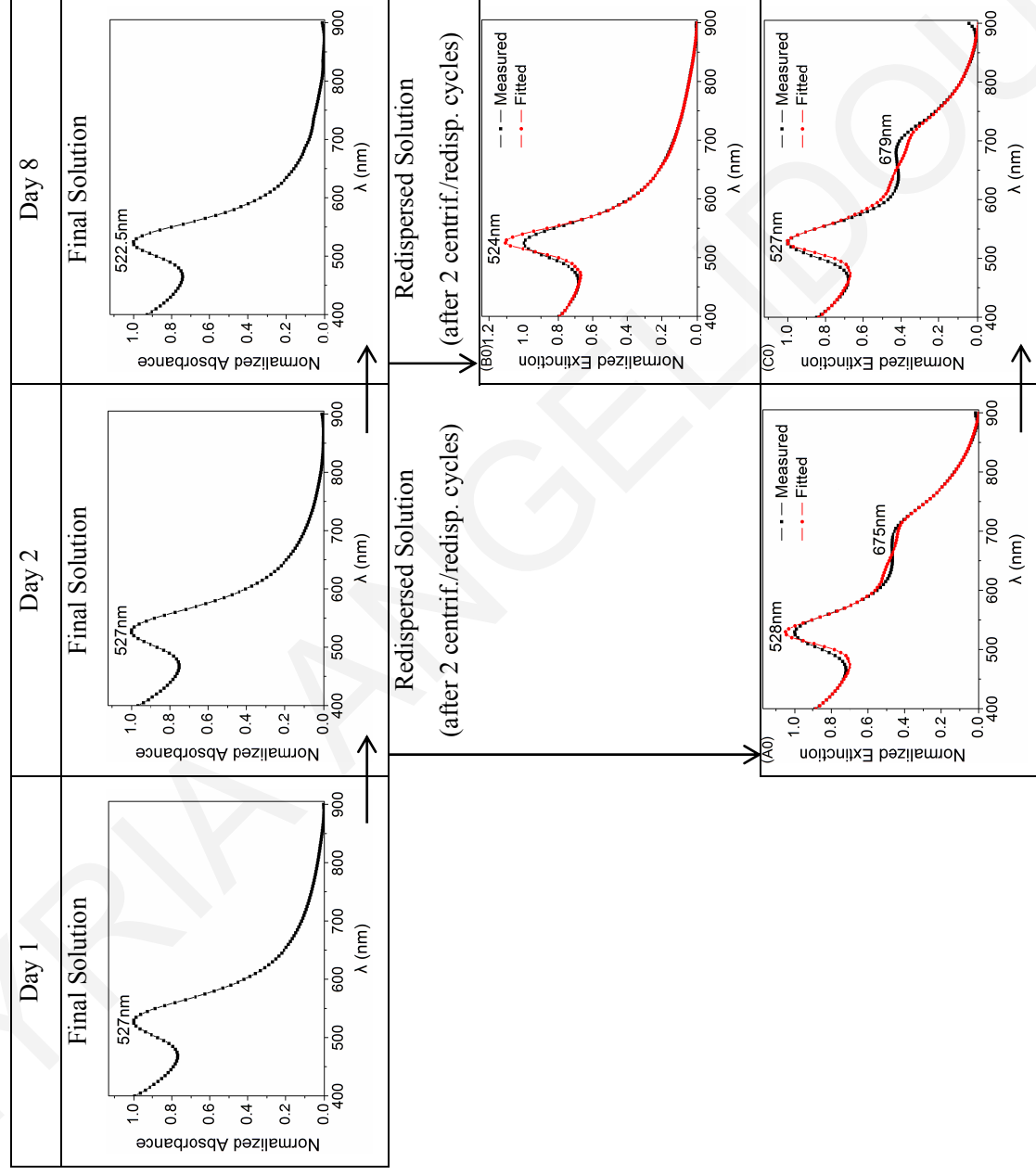


Table 6.2: Experiment 1(b): Gold-polystyrene solution (8.25mL HAuCl₄ + 0.35mL PS), cooled on ice (0°C), then stored at 4°C

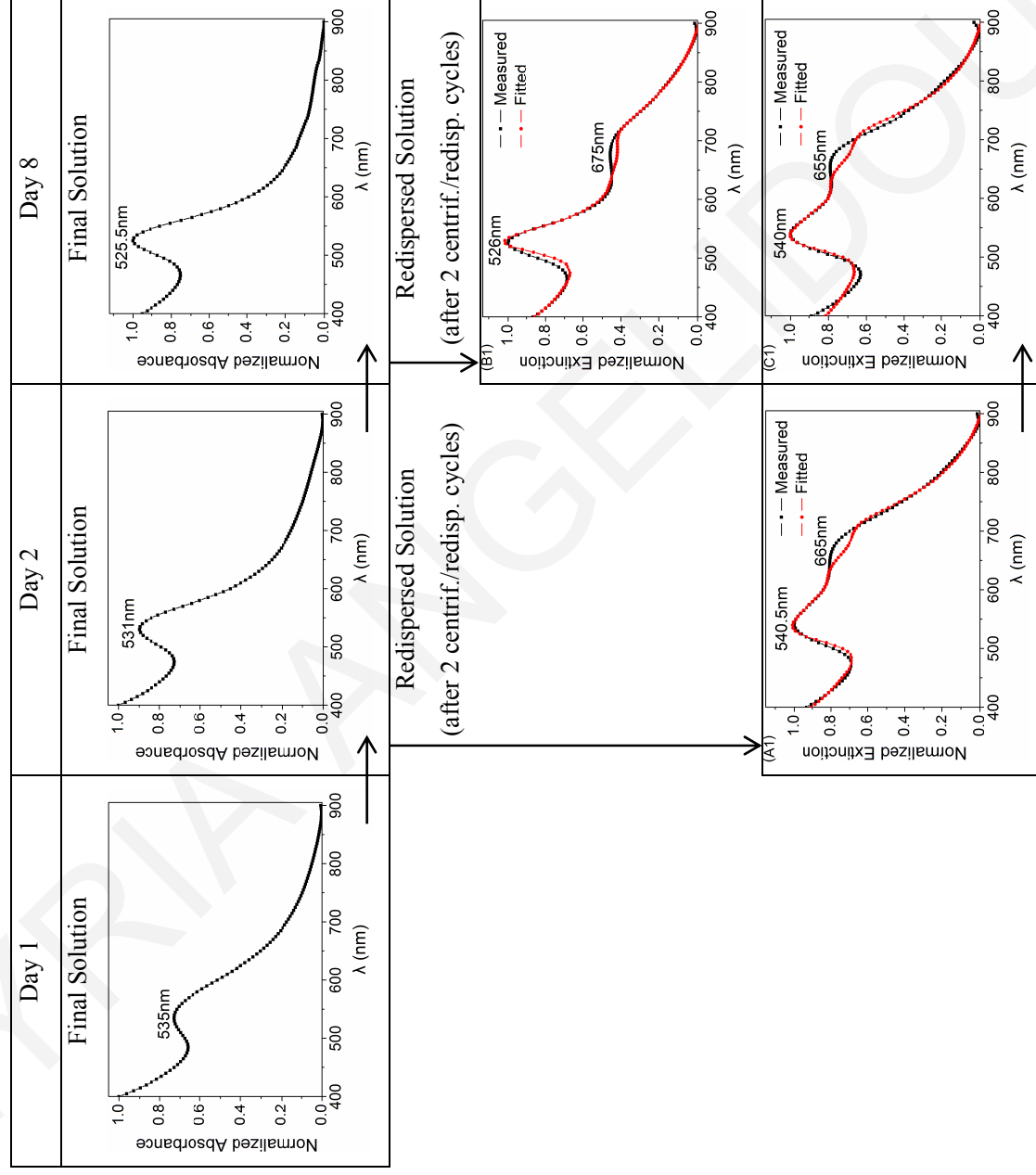


Table 6.3: Experiment 2: Gold-polystyrene solution (8.5mL HAuCl₄ + 0.35mL PS) cooled on ice (0°C), then stored at 4°C

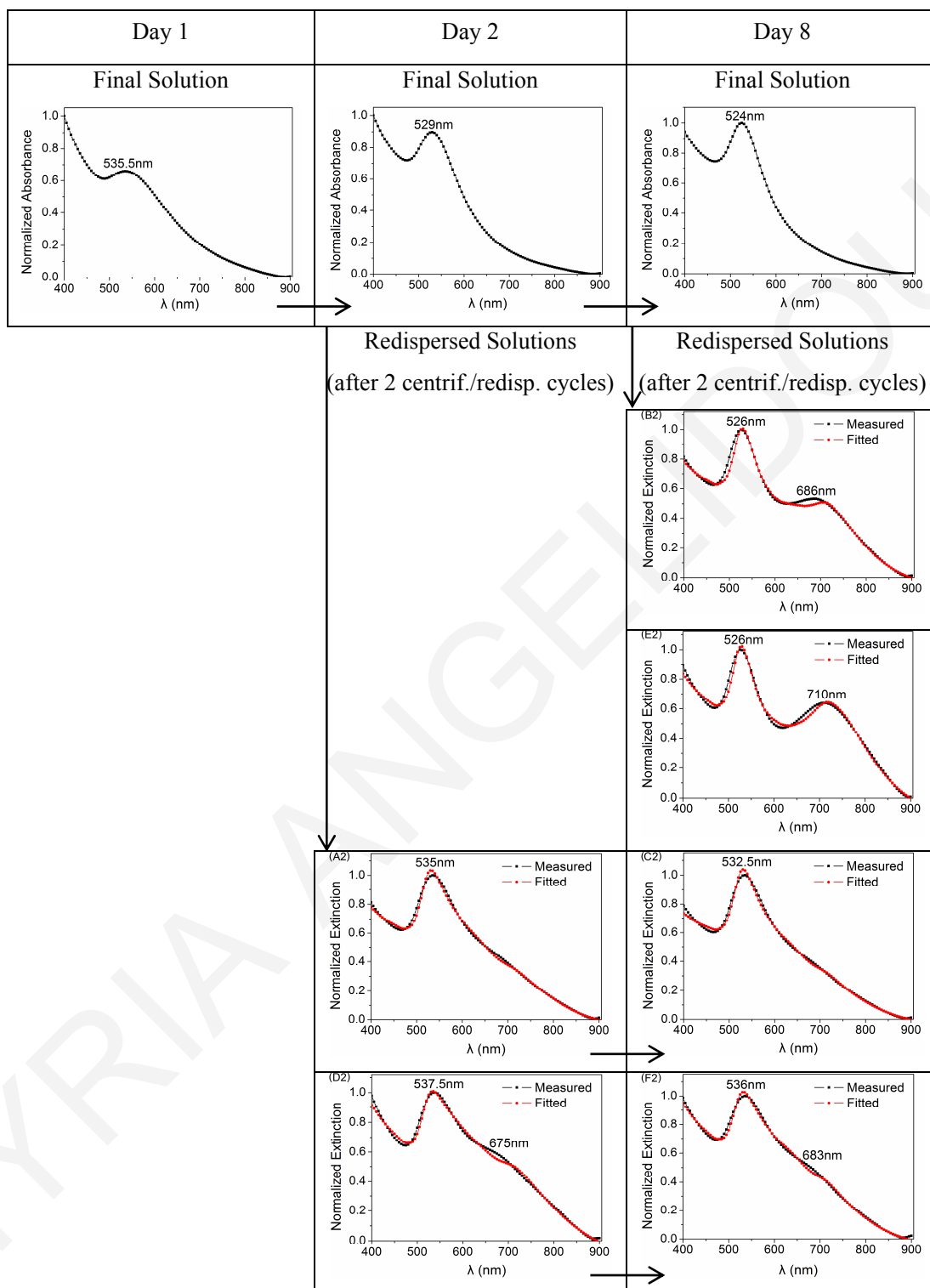


Table 6.4: Experiment 3: Gold-polystyrene solution (10mL HAuCl₄ + 0.35mL PS) cooled on ice (0°C), then stored at 4°C

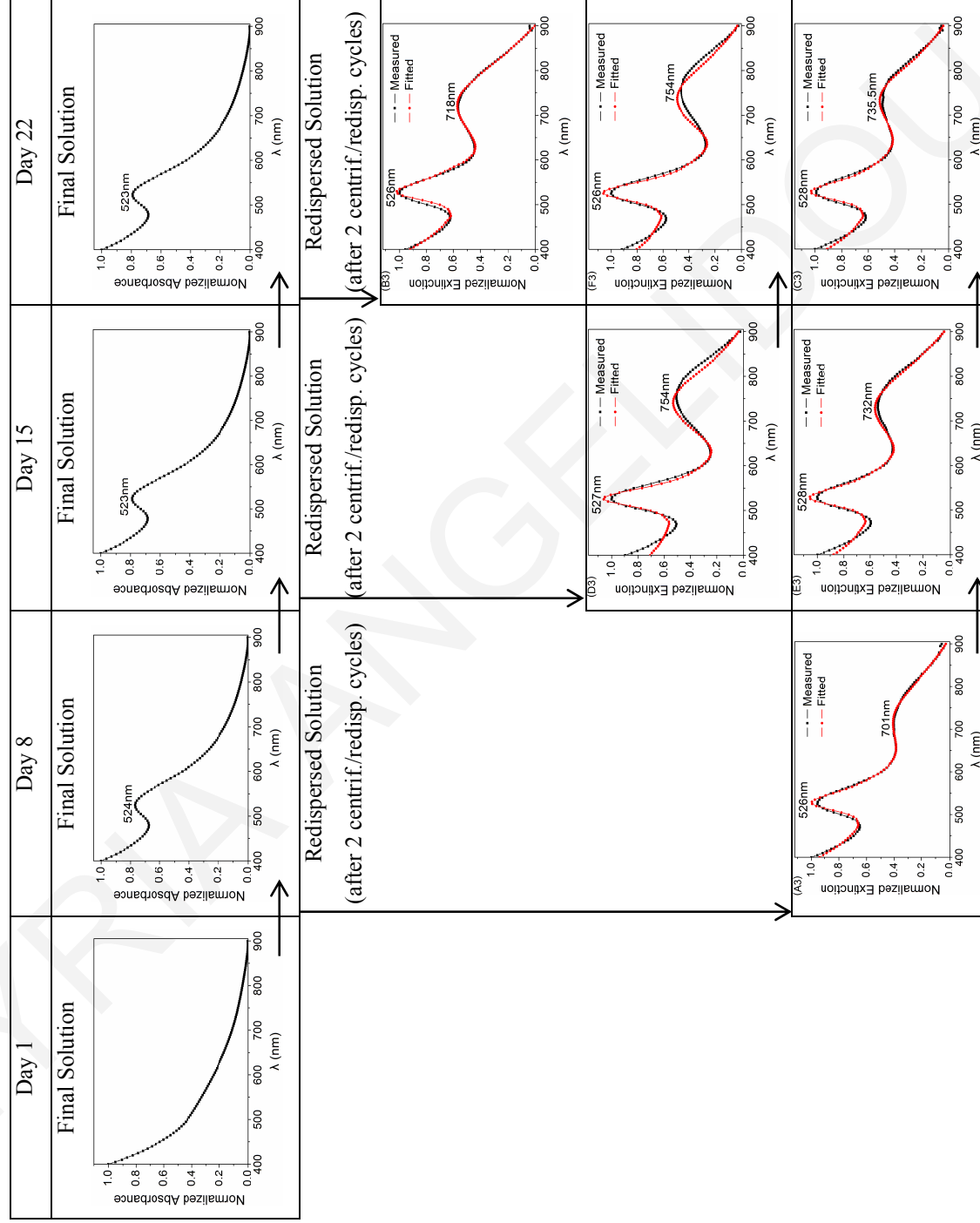


Table 6.5: Normalized fitting constants, a'_f , for the various fitted absorbances

Experiment	Polystyrene dm = 114nm	Single sphere dm = 25nm	Shell aggregate R = 70nm, ds = 2nm	Shell aggregate R = 70nm, ds = 1 nm	Shell aggregate R = 70nm, ds = 0nm	Nanoshell R = 70nm, shell = 15nm	Nanoshell R = 70nm, shell = 25nm	mean error	
	a'_1	a'_2	a'_3	a'_4	a'_5	a'_6	a'_7		
1(a)	A0	0.01274	0.57556	0.35994	0.00000	0.00000	0.05176	0.00000	0.062430
	B0	0.21793	0.64757	0.01940	0.00000	0.11510	0.00000	0.00000	0.05277
	C0	0.03482	0.61251	0.35268	0.00000	0.00000	0.00000	0.00000	0.09426
1(b)	A1	0.04753	0.24041	0.50696	0.00000	0.14768	0.05721	0.00020	0.07862
	B1	0.00365	0.54138	0.31714	0.00000	0.00005	0.13770	0.00008	0.06782
	C1	0.00263	0.29068	0.63027	0.00000	0.06786	0.00856	0.00000	0.08807
2	A2	0.17953	0.39851	0.11284	0.00000	0.26402	0.04510	0.00000	0.05140
	B2	0.13835	0.45231	0.25273	0.00000	0.00000	0.15660	0.00000	0.05830
	C2	0.05294	0.50883	0.14977	0.00000	0.25998	0.02847	0.00000	0.05509
	D2	0.02307	0.37225	0.18504	0.02675	0.26545	0.11087	0.01658	0.06576
	E2	0.14286	0.41770	0.16989	0.00000	0.00000	0.25694	0.01261	0.05865
	F2	0.02236	0.43154	0.23115	0.00000	0.26780	0.04716	0.00000	0.06936
3	A3	0.02333	0.56908	0.00000	0.02650	0.12382	0.11917	0.13810	0.03068
	B3	0.02158	0.54084	0.00033	0.00000	0.05683	0.09314	0.28729	0.03710
	C3	0.02773	0.53128	0.00000	0.00004	0.11494	0.20981	0.11621	0.04175
	D3	0.00142	0.62831	0.00000	0.00335	0.00006	0.27832	0.08853	0.08363
	E3	0.03694	0.53930	0.00000	0.03506	0.06253	0.18102	0.14515	0.03410
	F3	0.05957	0.59022	0.00000	0.04987	0.00001	0.25276	0.04758	0.07752

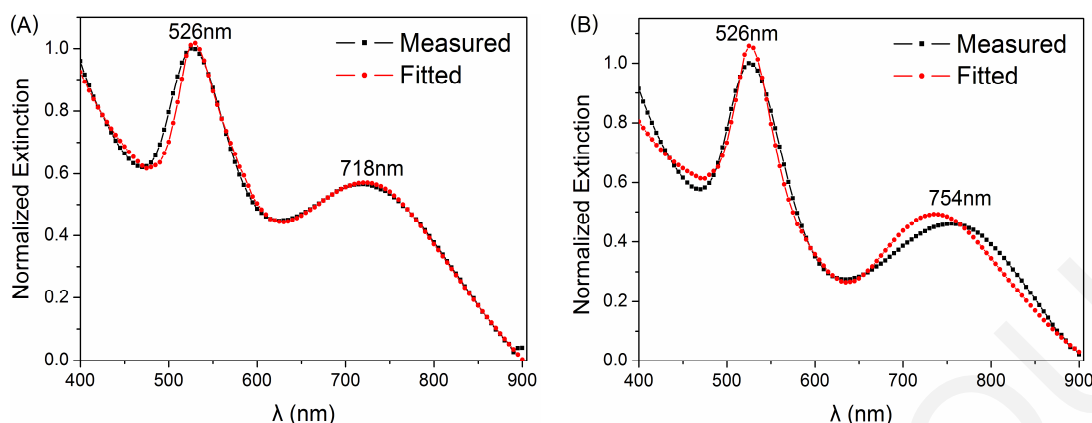


Figure 6.9: Example of a (A) good fit (B3), and (B) a sub-optimal fit (F3) for experiment 3.

6.6 Discussion

Tables 6.1–6.4 show the measured and fitted absorbances at each experimental stage of the synthesis of composite Au@PS NSs. The contribution of each NP–NS to the fitted absorbance, A_{fit} , is given by the normalized fitting constants a'_f (Table 6.5).

Figures 6.10(A)–(H) show plots of the values of a'_f corresponding to the NP–NS contributions to each experiment. In general, the solutions redispersed on day 8 (B curves), exhibited more shell aggregates with $d_s = 0\text{nm}$, and nanoshell like structures, compared to the solutions redispersed on day 2 (A curves), which implies that the reaction continued and the shell aggregates having an edge-to-edge nanosphere distance $d_s > 0\text{nm}$, transformed into shell aggregates, with $d_s = 0\text{nm}$, and even nanoshells. This is further supported by the fact that, when measured again on day 8, the solution redispersed on day 2 (C curves) exhibited similar contributions of NPs–NSs to the synthesized composite Au@PS NSs. Another important conclusion is that when synthesis was fast, such as in experiment 1(a), the composite Au@PS NSs mainly resembled shell aggregate like structures, while when the synthesis was slow, such as in experiment 3, the final composite Au@PS NSs mainly resembled nanoshells. This implies that the speed of the reaction affects the features of the shape. It appears that when the speed is slow the nanospheres do not stabilize and continue to form into nanoshell-like structures instead of shell aggregates.

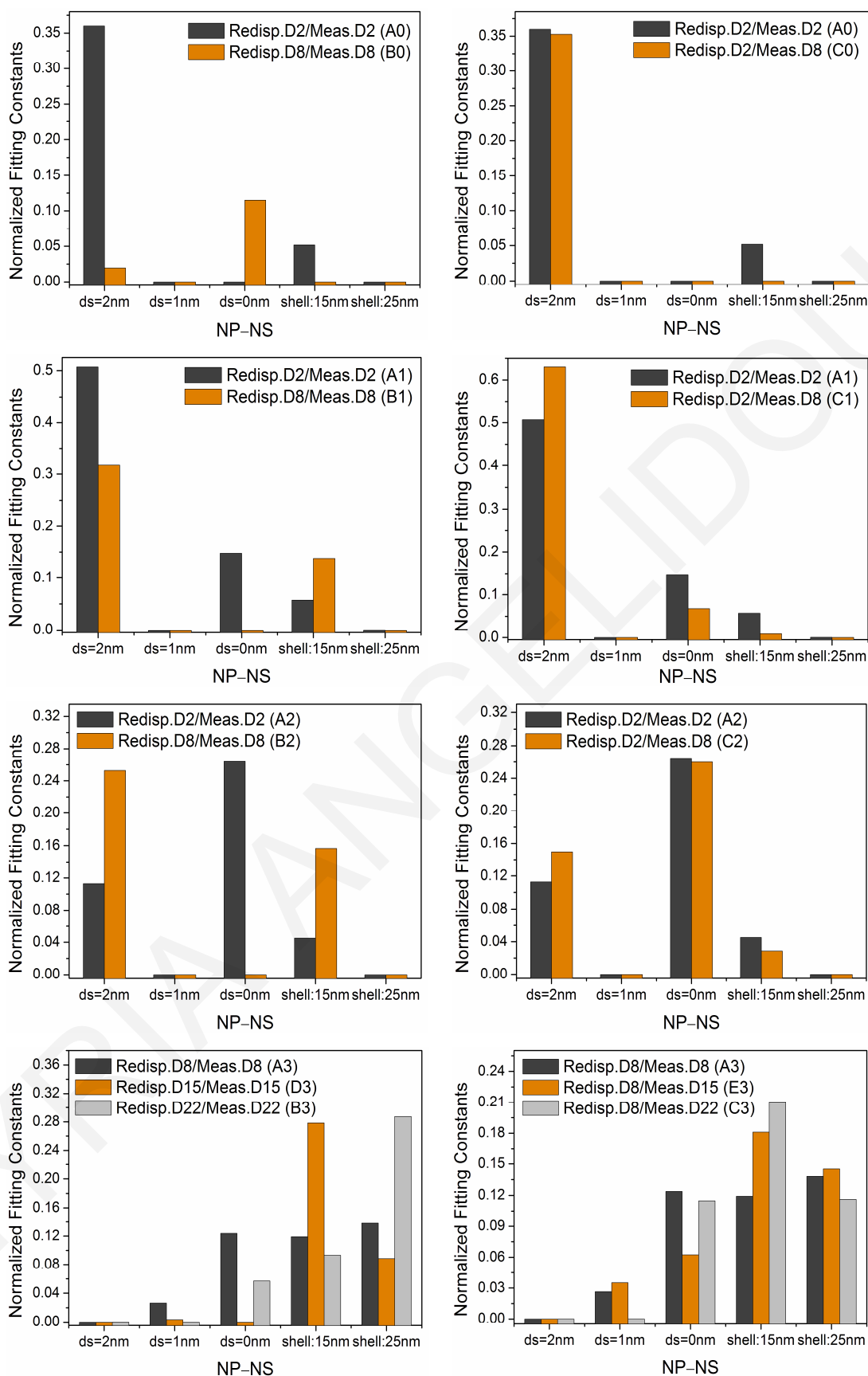


Figure 6.10: Nanoparticle–Nanostructure (NP–NS) contributions to each synthesized composite Au@PS NSs resulting from (A)–(B) experiment 1(a), (C)–(D) experiment 1(b), (E)–(F) experiment 2, and (G)–(H) experiment 3.

6.6.1 Effect of cooling the final solution

The termination of the reaction appears to play a very important role in the formation of the shell aggregates. When the reaction was terminated at lower temperatures (i.e. the solution was cooled immediately on ice), the reaction terminated more effectively and the sample stabilized. This is illustrated in Fig. 6.11(A,B) (bars A1 and B1) where the shell aggregates ($d_s = 2\text{nm}$) in the solution cooled to 0°C appear to still be present even after the final solution was kept refrigerated for one week. On the contrary, the shell aggregates ($d_s = 2\text{nm}$), in the solution where the reaction was allowed to terminate gradually at room temperature (Fig. 6.11(A,B), bars A0 and B0), almost completely disappeared after the final solution was refrigerated for one week, being replaced mostly by shell aggregates with $d_s = 0\text{nm}$. In both cases, however, the reaction did progress as is evident by the fact that there were more nanoshells in the solutions at the later stage. This is further evident by the fact that the solutions redispersed on day 2 and re-measured on day 8 (Fig. 6.11(C)) did not exhibit many changes compared to day 2 (Fig. 6.11(A)), a finding expected since the redispersion process washes off most of the reactants. However, one might also note that the figures are not exactly the same. The differences are probably a result of the repeatability issue explained in section 6.6.3.

6.6.2 Effect of the total amount of HAuCl_4

A careful examination of the results, from experiments where different amounts of gold salt were added, indicates that the total amount of HAuCl_4 affects the rate of the reaction. In experiments 1 & 2, 8.25mL and 8.5mL of HAuCl_4 were added respectively. On day 2 (Fig. 6.11(A)), the two final solutions are markedly different. The final solution in experiment 2, seems to have progressed further since more shell aggregates with $d_s = 0\text{nm}$ and nanoshells are present. However, when kept refrigerated for one week, the reaction of experiment 1 progresses enough to reach the same endpoint as the reaction of experiment 2 (Fig. 6.12(B)). As in other cases, the solution redispersed on day 2 and re-measured on day 8 (Fig. 6.12(C)), does not show any signs of reaction progression as both bars (C0 and C1) are almost identical.

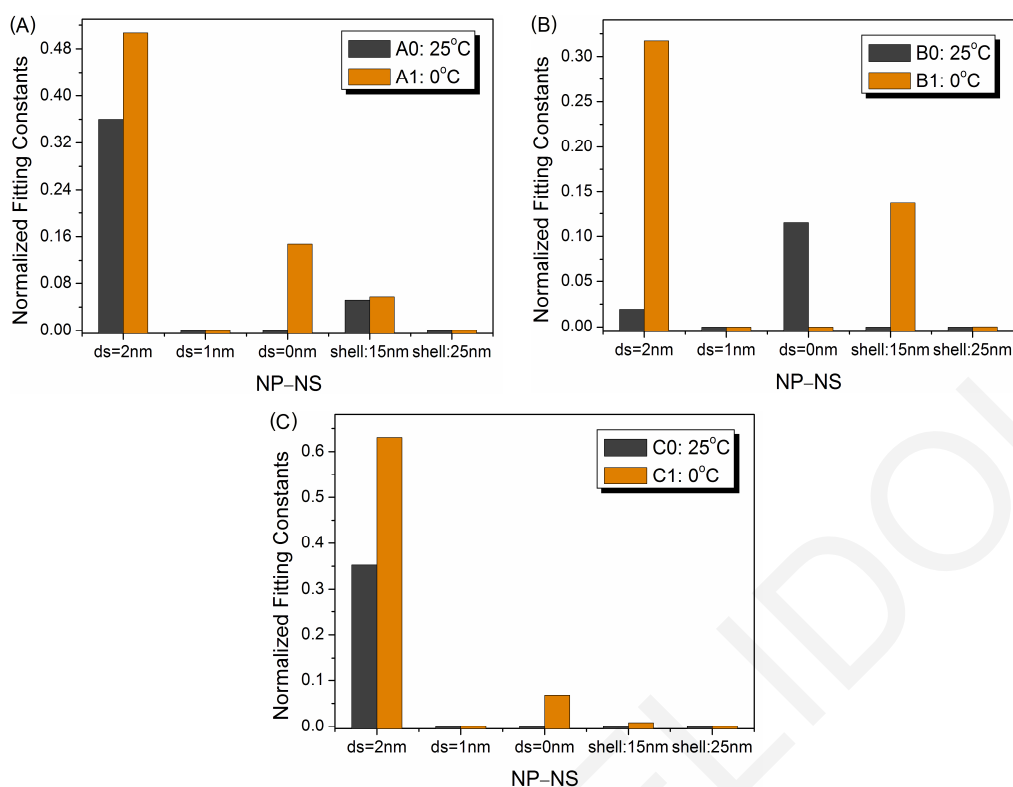


Figure 6.11: Composite Au@PS NSs synthesized in experiment 1, and cooled down at two different temperatures. The normalized fitting constants are given for the redispersed solutions of (A) day 2, (B) day 8, and (C) day 2 measured on day 8.

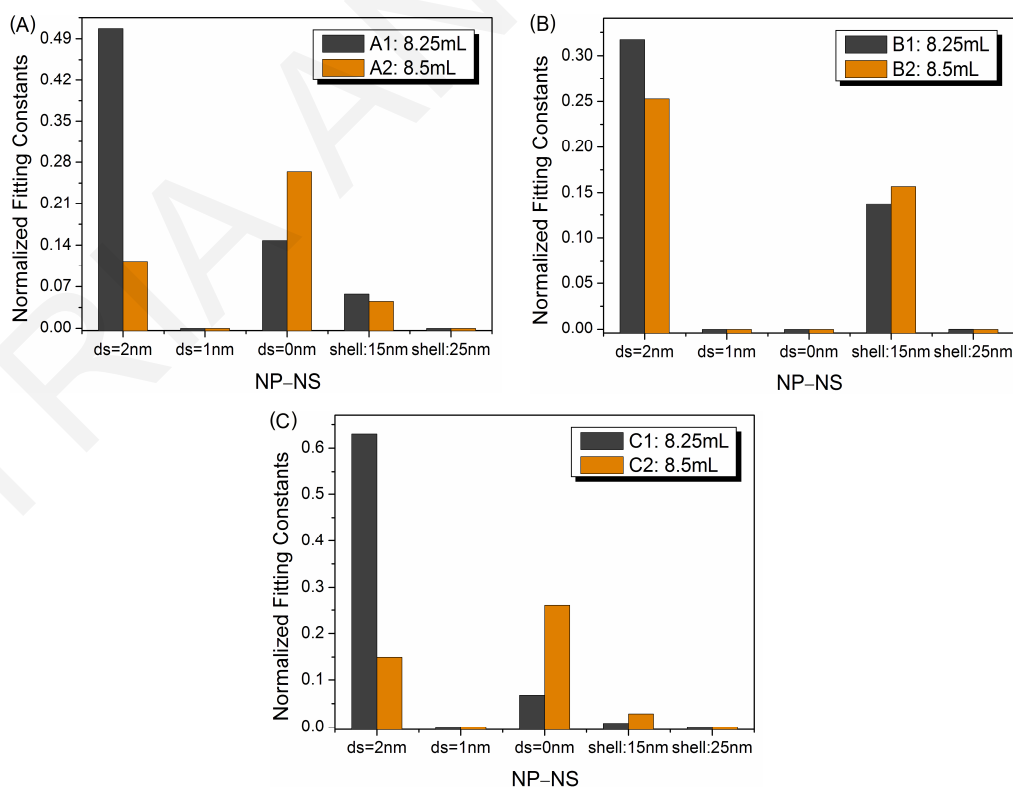


Figure 6.12: Composite Au@PS NSs synthesized using two different total amounts of gold solution. The normalized fitting constants are given for the redispersed solutions of (A) day 2, (B) day 8, and (C) day 2 measured on day 8.

6.6.3 Experimental repeatability

Figure 6.13 addresses issues regarding the assessment of the repeatability of the experiments and analysis described in this chapter. Figures 6.13(A) and (B) show the results for two portions of the same final solution which were redispersed and fitted separately on day 2 and day 8 of the experiment, respectively. The bar charts should be exactly the same given that exactly the same procedures were applied to two portions of the same solution. However, there are some differences which in certain cases are up to 30%. In addition, Fig. 6.13(C) shows the results from the same solution as in Fig. 6.13(A), measured on two separate days (redispersed on day 2 and measured on days 2 and 8). Although similar, Fig. 6.13(A) and (C) are not identical. The conclusion, from the above observations, is that the procedure is not 100% repeatable. The reasons for this reduced repeatability probably include:

- Centrifugation and redispersion process induce error: Although exactly the same process and settings were used every time, there was some variability in the pellet formations.
- Fitting process error: This issue has already been discussed.
- Sedimentation and aggregation of the solutions: Visual observations of the same solutions indicate that the solutions seem to aggregate and settle variably. Although the solutions were stirred, that could not guarantee complete repeatability.

The repeatability of the technique could probably be improved if:

- The experimental techniques were extended to include a stabilization process where the reaction is terminated and the NSs are prevented from aggregating and settling (e.g. with the use of some surfactant).
- The process of centrifugation is further optimized to more effectively separate the different NSs and lessen the probability of error in the redispersion process.
- The fitting process is implemented either with the introduction of an analytical model (one does not exist at this time) or with the inclusion of calculated extinction efficiencies from even more structures (after significantly increasing the computational resources used.)

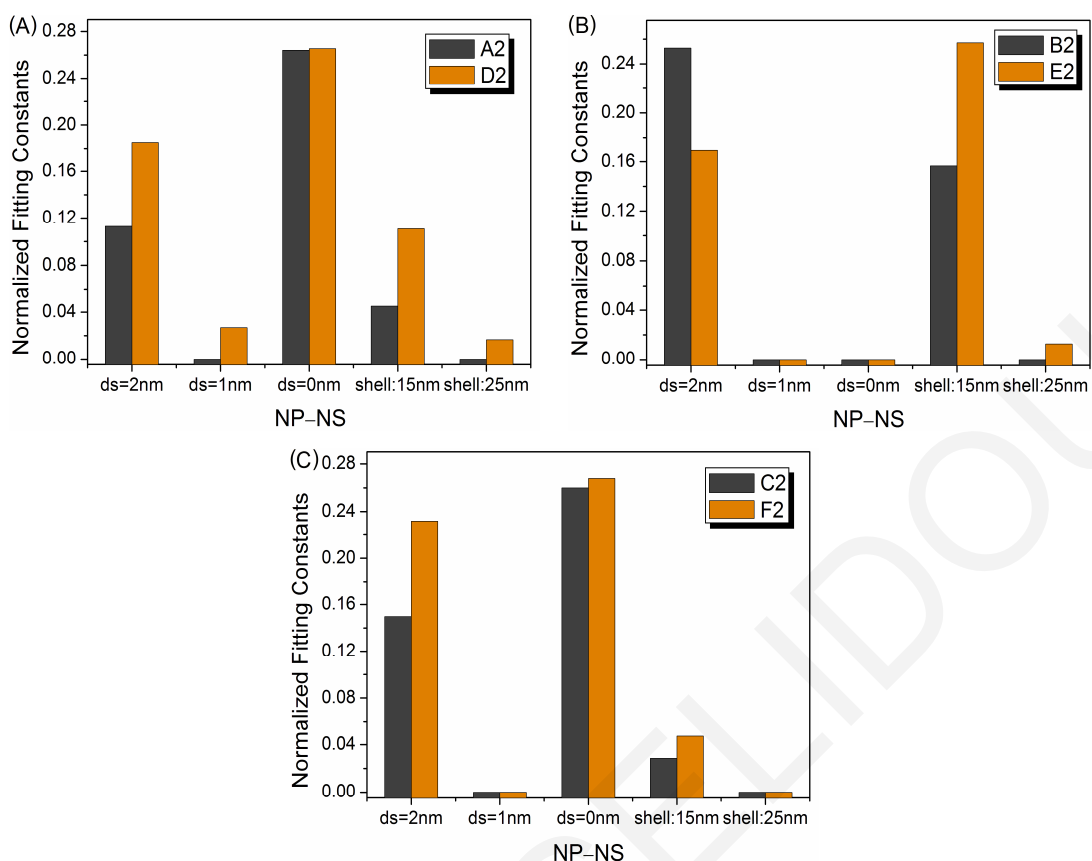


Figure 6.13: Composite Au@PS NSs synthesized in experiment 2. Two redispersed solutions were produced from the same final solution, with the same centrifugation parameters on the same day. The normalized fitting constants are given for the two redispersed solutions of (A) day 2, (B) day 8, and (C) day 2 measured on day 8.

6.7 Summary

The goal of this study was to synthesize and experimentally verify optical properties of the monolayer shell aggregates. The monolayer shell aggregates consist of a layer of small gold nanospheres which aggregate around a dielectric core.

The core was chosen to be polystyrene (PS) spheres. Composite Au@PS NSs were generated using the trisodium citrate ($\text{Na}_3\text{Citrate}$) as a reductant. The small gold Au nanospheres directly formed on the PS surface. Three experiments were performed, each having different parameters. In experiment 1, 8.25mL of gold solution was added to the boiling PS+Citrate solution, with half of the solution cooled at room temperature (25°C) and half on ice (0°C). In experiment 2, 8.5mL of gold solution was added to the boiling PS+Citrate solution and then cooled on ice. In experiment 3, 10mL of gold solution was added to the boiling PS+Citrate solution and then cooled on ice. Each experimental procedure stopped when the solution obtained a bluish color, indicating the formation of composite Au@PS NSs. The structure morphologies were imaged using a SEM.

Absorbance spectra were measured using a UV-vis spectrophotometer. Then, the measurements were fitted with combinations of the extinction efficiencies of polystyrene spheres, single nanospheres (25nm diameter), shell aggregates ($R = 7\text{nm}$, $r \approx 12.5\text{nm}$, $ds = 2, 1, 0\text{nm}$) and nanoshells (PS core, $R_c = 57\text{nm}$, shell 15, 25nm). From this curve fitting, the relative contribution of each NP–NS to the synthesized composite Au@PS NSs, was extracted.

The interpretation of the experimental results depends on the accuracy of the experimental procedure and the analysis method. The composite Au@PS NSs were approximated well using the citrate reduction method, despite the variety of structures created using this experimental procedure. However, the experiments were not perfectly repeatable thus introducing some uncertainty in the interpretation of the results. Another contribution to the experimental interpretation uncertainty was the inaccuracies of the fitting model applied. Computational limitations precluded the use of more extinction spectra calculated for even more NSs thus leading to some fitting inaccuracies.

To conclude, the monolayer shell aggregates can be synthesized using relatively simple techniques. In the experiments performed, the formation of gold nanospheres on PS spheres was demonstrated, and the synthesis was stopped when composite Au@PS NSs exhibited shell aggregate structures. To obtain only shell aggregates, the synthesis must be performed fast, so that the gold ions form and stabilize into nanospheres on the PS surface, and not continued to grow into a uniform shell. The reactants must also be thoroughly be washed away from the solution since the reaction continuous to progress even at low temperatures. For the synthesis method to be repeatable, some experimental improvements are required, so as to create fewer structure variability and better controlled Au@PS NSs properties.

7. Conclusions and Future Work

7.1 Conclusions

Metal nanoparticles (NPs) have been extensively explored, theoretically and experimentally, over the years. Novel metal NPs, which have enhanced and unique optical properties not available by any other metal NPs, are necessary for biological and biomedical applications. For example, in the diagnosis and therapy of a disease. By understanding the surface plasmon resonance (SPR) phenomenon, the electron plasmon excitations can be tuned to match the laser wavelengths used at a specific application. This tuning can be achieved by varying the size, shape or structure, and material of the NP, the material of the surrounding medium and even the coupling interactions between NPs.

In this dissertation, two novel types of metal nanostructures (NSs) are presented, the “shell aggregate”, and the “dual-mode” nanostructure (NS). Their optical properties have been extensively investigated to optimum design them for various biological and biomedical applications.

The newly NS called “shell aggregate” consists of small gold nanospheres which aggregate around a dielectric core, creating a monolayer or a bilayer shell. A detailed investigation of its optical properties was presented for the visible to the NIR wavelengths. The parameters of small nanosphere radius, r , outer radius of the shell aggregate, R , the edge-to-edge distance between the small nanospheres, d_s , and even the material of small nanospheres, dielectric core and external medium were studied.

The extinction spectra, of monolayer shell aggregates, appeared to depend mostly on the distance between the small nanospheres, which make up the shell. At small edge-to-edge distances, d_s , for example 0, and 1nm, coupling interactions between the nanospheres, are observed, which resulted in a red-shift and the appearance of two and even three peaks in the extinction spectrum. As the distance, d_s , increased, the interaction between nanospheres is reduced and this resulted in a blue-shift and merge of the peaks into a single one. By increasing the outer radius, R , the peak of the extinction spectrum increased in amplitude, and red-shifted from the visible to the NIR. Also, for d_s of 1nm, as R increased, two and even three peaks emerge.

It was shown that two monolayer shell aggregates have satisfactory $Q_{\text{abs}}/Q_{\text{sca}}$ and $Q_{\text{sca}}/Q_{\text{abs}}$ ratios, at the two wavelengths of 635 and 785nm, making them suitable for surface-enhanced Raman spectroscopy (SERS) applications. In addition, the monolayer

shell aggregates exhibited more than one distinct peaks with broader widths and more shifted to the NIR compared to nanospheres, aggregates, and nanoshells. Also, it was shown that the addition of a second layer, located behind of the first layer, did not contribute significant to the optical properties of shell aggregates, due to the “shadowing” effects. Also, the optical properties of monolayer shell aggregates were mainly attributed to absorption, as demonstrated by the efficiency factor spectra, suggesting that the monolayer shell aggregates can be potential photoacoustic imaging (PAI) contrast agents, where high absorption is required.

These results suggest that the gold monolayer shell aggregate is a good candidate for uses in biological and biomedical applications, such as in spectroscopy, in imaging, and photothermal therapy, since it provides a reasonably tunable plasmon resonance wavelength, and strong absorption, while the small size of its components can be exploited for intracellular distribution.

A novel metal NS, called “dual-mode” NS, having the unique property of distinct and separated absorption and scattering plasmon bands was investigated. This metal NP is design to have an absorption band at $\lambda = 635\text{nm}$, and a scattering band at $\lambda = 785\text{nm}$, both in the range of the “optical window” for biological applications. Initially, the optical properties, and more specific the efficiency factors of various simple metal NSs were calculated for the wavelengths ranging from the UV-vis to the NIR. The parameters of material, shape and size were studied. It was found that the simple metal NPs exhibited overlapping absorption and scattering plasmon bands in the visible range, while, for NIR wavelengths, scattering was dominant. None of the simple metal NSs was found to have distinct and separated spectra, so combinations were considered next.

A gold nanocube, having an edge length of 120nm was chosen as the scattering building block of the dual-mode NS and small nanospheres, of gold and silver were chosen as the absorption building blocks. A complex metal NS was created by combining these two NSs. Initially, the small nanospheres were arranged as a layer on the front face of the gold nanocube. A detailed investigation was performed, where parameters such as the number (diameter), and material (silver and gold) of small nanospheres were varied. Also, the overall size of the complex NS, the arrangement of the nanospheres on the nanocube relative to the incident propagation, and the combination of a nanocube covered by nanospheres, were explored as well. From the results (figures, ratios of $Q_{\text{abs}}/Q_{\text{sca}}$ and $Q_{\text{sca}}/Q_{\text{abs}}$), the complex NS of a gold nanocube combined with 16 silver nanospheres, having a 30nm diameter, arranged on the front face of the nanocube, perpendicular to the propagation direction, exhibited the best distinct and separated plasmon bands. However,

this complex NS appeared to be orientation and small nanosphere arrangement dependent, due to the results obtained when the nanospheres were arranged on the back or one of the sides of the nanocube, or even when a second, opposite layer was added. Even though its limitation this complex metal NS can be considered as a “dual-mode” NS and can be used as a substrate in both imaging (NIR wavelengths) and therapy (visible wavelengths) applications.

The new cubical nanoshells were also investigated and compared with the simple nanocubes and classical nanoshells. These NSs exhibited mainly scattering plasmon bands, ranging from the visible to the NIR making them perfect for imaging applications, such as in optical coherence tomography (OCT) as contrast agents.

The monolayer shell aggregates were also designed experimentally. A simple method was chosen to synthesize the shell aggregates, where gold nanospheres were directly formatted on the surface of a polystyrene (PS)_core, using the citrate method. The total amount of gold solution added, the time between gold drops, and the cooling down temperature are the parameters which were explored. Bluish to lavender final solutions were reported. Even though high aggregation was induced, raspberry-like morphologies were observed using scanning electron microscopy (SEM). From the experimental analysis and comparison with the extinction spectra of various gold NPs–NSs, it was found that the synthesized composite Au@PS NSs exhibited both shell aggregate and nanoshell like structures. To obtain specifically shell aggregates the synthesis must be performed fast, so that nanospheres to be formed and stabilized onto the PS surface, and not continue to grow into a shell like structures. Moreover, improvements are required on the centrifugation process and the fitting model applied to estimate a new absorbance out of the calculated extinctions.

To finalize, we have successfully design two novel metal NSs. The gold monolayer “shell aggregate”, which by varying its parameters the SPRs can be tuned to NIR wavelengths, valuable for biological sensing, and imaging applications, and the complex metal “dual-mode” NS, which exhibits the unique property of distinct and separated absorption and scattering plasmon bands, not yet seen in other metal NPs. This complex metal NS could be a potential theranostic agent, where simultaneous imaging and therapy can be applied into a single NS. Also, an initial experimental effort to synthesize the shell aggregates was successfully performed, were the composite Au@PS NSs exhibited raspberry-like morphologies, and monolayer shell aggregate extinction spectra.

7.2 Future Work

In the future, more advanced synthetic methods for the monolayer shell aggregates generation, will be investigated. Currently, the synthesis was performed using a simple method, PS core template, and in aqueous solutions, were bluish solutions and raspberry-like composite Au NSs were demonstrated. As mentioned in Chapter 4, the shell aggregates idea comes from the fact that small modified gold nanospheres, enter the cell, escape the endosomal vesicles, and distribute into the cytoplasm. Then, the small nanospheres will aggregate around a cellular organelle or vesicle, creating a shell around it, so that the overall NS would be large enough exhibiting intersphere coupling interactions, in order to provide an efficient SERS signal as well as tunable NIR plasmon resonances. Therefore, the next step is to examine an in vitro synthesis and then internalization of the shell aggregates into cells. Later, one can explore the various surface modifications for the small nanospheres, then the entry and distribution of the modified nanospheres into the cytoplasm, and finally the aggregation of small nanospheres on a nanometer size cell vesicle. Much research must be done to satisfy these criteria.

Another potential investigation is to further study the optical properties of the complex, dual-mode NS, and find a way to be independent on the orientation in relation to the incident wave propagation. Also, the synthesis of the complex, dual-mode NSs can be explored. There are known synthetic methods for single metal nanospheres, and nanocubes. Then, these two structures are required to be combined, the nanospheres creating a layer on one face of the nanocube, so various surface modifications and aggregation parameters will be investigated. Since the dual-mode NS has the potential to be explored as a theranostic agent, it is important to examine how the complex NS will be attached to the sample under examination, and if is going to be used as a substrate or it will be internalized into the tissue or cells. Lots of work is to be done, since only the theoretical part was performed in this dissertation.

Bibliography

- [1] N. G. Khlebtsov and L. A. Dykman, "Optical properties and biomedical applications of plasmonic nanoparticles," *Journal of Quantitative Spectroscopy & Radiative Transfer*, vol. 111, pp. 1-35, 2010.
- [2] K. L. Kelly, E. Coronado, L. L. Zhao, and G. C. Schatz, "The optical properties of metal nanoparticles: the influence of size, shape, and dielectric environment," *The Journal of Physical Chemistry B*, vol. 107, pp. 668-677, 2003.
- [3] P. K. Jain, X. H. Huang, I. H. El-Sayed, and M. A. El-Sayad, "Review of some interesting surface plasmon resonance-enhanced properties of noble metal nanoparticles and their applications to biosystems," *Plasmonics*, vol. 2, pp. 107-118, 2007.
- [4] N. G. Khlebtsov, "Optics and biophotonics of nanoparticles with a plasmon resonance," *Quantum Electronics*, vol. 38, pp. 504-529, 2008.
- [5] N. K. Grady, N. J. Halas, and P. Nordlander, "Influence of dielectric function properties on the optical response of plasmon resonant metallic nanoparticles," *Chemical Physics Letters*, vol. 399, pp. 167-171, 2004.
- [6] V. Myroshnychenko, J. Rodriguez-Fernandez, I. Pastoriza-Santos, A. M. Funston, C. Novo, P. Mulvaney, *et al.*, "Modelling the optical response of gold nanoparticles," *Chemical Society Reviews*, vol. 37, pp. 1792-1805, 2008.
- [7] B. J. Wiley, S. H. Im, Z.-Y. Li, J. McLellan, A. Siekkinen, and Y. Xia, "Maneuvering the surface plasmon resonance of silver nanostructures through shape-controlled synthesis," *The Journal of Physical Chemistry B*, vol. 110, pp. 15666-15675, 2006.
- [8] M. Kerker, "The optics of colloidal silver: something old and something new," *Journal of Colloid and Interface Science*, vol. 105, pp. 297-314, 1985.
- [9] S. Eustis and M. A. El-Sayed, "Why gold nanoparticles are more precious than pretty gold: noble metal surface plasmon resonance and its enhancement of the radiative and nonradiative properties of nanocrystals of different shapes," *Chemical Society Reviews*, vol. 35, pp. 209-217, 2006.
- [10] M. Faraday, "The Bakerian lecture: experimental relations of gold (and other metals) to light," *Philosophical Transactions of the Royal Society of London*, pp. 145-181, 1857.
- [11] M.-C. Daniel and D. Astruc, "Gold nanoparticles: assembly, supramolecular chemistry, quantum-size-related properties, and applications toward biology, catalysis, and nanotechnology," *Chemical Reviews*, vol. 104, pp. 293-346, 2004.
- [12] M. Pelton and G. W. Bryant, *Introduction to Metal-Nanoparticle Plasmonics* vol. 5: John Wiley & Sons, 2013.
- [13] S. Horikoshi and N. Serpone, "Introduction to nanoparticles," in *Microwaves in Nanoparticle Synthesis*, ed: Wiley-VCH Verlag, 2013, pp. 1-24.
- [14] *The Lycurgus Cup*. Available:
https://www.britishmuseum.org/explore/highlights/highlight_objects/pe_mla/t/the_lycurgus_cup.aspx
- [15] I. Freestone, N. Meeks, M. Sax, and C. Higgitt, "The Lycurgus cup - A roman nanotechnology," *Gold Bulletin*, vol. 40, pp. 270-277, 2007.

- [16] G. Mie, "Beiträge zur Optik trüber Medien, speziell kolloidaler Metallösungen," *Annalen der Physik*, vol. 330, pp. 377-445, 1908.
- [17] D. L. Fedlheim and C. A. Foss, "Overview," in *Metal nanoparticles: Synthesis, Characterization, and Applications*, D. L. Fedlheim and C. A. Foss, Eds., 1st ed: CRC Press, 2001, pp. 1-16.
- [18] J. Turkevich, P. C. Stevenson, and J. Hillier, "A study of the nucleation and growth processes in the synthesis of colloidal gold," *Discussions of the Faraday Society*, vol. 11, pp. 55-75, 1951.
- [19] P. C. Lee and D. Meisel, "Adsorption and surface-enhanced Raman of dyes on silver and gold sols," *The Journal of Physical Chemistry*, vol. 86, pp. 3391-3395, 1982.
- [20] K. Song, S. Lee, T. Park, and B. Lee, "Preparation of colloidal silver nanoparticles by chemical reduction method," *Korean Journal of Chemical Engineering*, vol. 26, pp. 153-155, 2009/01/01 2009.
- [21] A. A. Lazarides and G. C. Schatz, "DNA-linked metal nanosphere materials: structural basis for the optical properties," *The Journal of Physical Chemistry B*, vol. 104, pp. 460-467, 2000.
- [22] T. J. Norman Jr, C. D. Grant, D. Magana, J. Z. Zhang, J. Liu, D. Cao, *et al.*, "Near infrared optical absorption of gold nanoparticle aggregates," *The Journal of Physical Chemistry B*, vol. 106, pp. 7005-7012, 2002.
- [23] N. G. Khlebtsov, A. Melnikov, L. Dykman, and V. Bogatyrev, "Optical properties and biomedical applications of nanostructures based on gold and silver bioconjugates," in *Photopolarimetry in Remote Sensing*, Y. Y. Vidden G., Mishchenko M., Ed., ed Netherlands: Springer, 2005, pp. 265-308.
- [24] S. J. Oldenburg, R. D. Averitt, S. L. Westcott, and N. J. Halas, "Nanoengineering of optical resonances," *Chemical Physics Letters*, vol. 288, pp. 243-247, 1998.
- [25] E. Hao, G. C. Schatz, and J. T. Hupp, "Synthesis and optical properties of anisotropic metal nanoparticles," *Journal of Fluorescence*, vol. 14, pp. 331-341, 2004.
- [26] S. Kalele, S. W. Gosavi, J. Urban, and S. K. Kulkarni, "Nanoshell particles: synthesis, properties and applications," *Current Science*, vol. 91, pp. 1038-1052, 2006.
- [27] X. C. Jiang, A. Brioude, and M. P. Pileni, "Gold nanorods: limitations on their synthesis and optical properties," *Colloids and Surfaces A: Physicochemical and Engineering Aspects*, vol. 277, pp. 201-206, 2006.
- [28] A. Brioude, X. C. Jiang, and M. P. Pileni, "Optical properties of gold nanorods: DDA simulations supported by experiments," *The Journal of Physical Chemistry B*, vol. 109, pp. 13138-13142, 2005.
- [29] E. S. Kooij and B. Poelsema, "Shape and size effects in the optical properties of metallic nanorods," *Physical Chemistry Chemical Physics*, vol. 8, pp. 3349-3357, 2006.
- [30] B. Wiley, Y. G. Sun, J. Y. Chen, H. Cang, Z. Y. Li, X. D. Li, *et al.*, "Shape-controlled synthesis of silver and gold nanostructures," *MRS Bulletin*, vol. 30, pp. 356-361, 2005.
- [31] E. Ringe, J. M. McMahon, K. Sohn, C. Cobley, Y. N. Xia, J. X. Huang, *et al.*, "Unraveling the effects of size, composition, and substrate on the localized surface plasmon resonance frequencies of gold and silver nanocubes: a systematic single-

- particle approach," *The Journal of Physical Chemistry C*, vol. 114, pp. 12511-12516, 2010.
- [32] F. Kim, S. Connor, H. Song, T. Kuykendall, and P. D. Yang, "Platonic gold nanocrystals," *Angewandte Chemie-International Edition*, vol. 43, pp. 3673-3677, 2004.
- [33] D. Seo, C. I. Yoo, I. S. Chung, S. M. Park, S. Ryu, and H. Song, "Shape adjustment between multiply twinned and single-crystalline polyhedral gold nanocrystals: decahedra, icosahedra, and truncated tetrahedra," *The Journal of Physical Chemistry C*, vol. 112, pp. 2469-2475, 2008.
- [34] S. E. Skrabalak, J. Chen, Y. Sun, X. Lu, L. Au, C. M. Cobley, *et al.*, "Gold nanocages: synthesis, properties, and applications," *Accounts of Chemical Research*, vol. 41, pp. 1587-1595, 2008.
- [35] J. Chen, B. Wiley, Z. Y. Li, D. Campbell, F. Saeki, H. Cang, *et al.*, "Gold nanocages: engineering their structure for biomedical applications," *Advanced Materials*, vol. 17, pp. 2255-2261, 2005.
- [36] C. G. Khoury and T. Vo-Dinh, "Gold nanostars for surface-enhanced Raman scattering: synthesis, characterization and optimization," *The Journal of Physical Chemistry C*, vol. 112, pp. 18849-18859, 2008.
- [37] S. Barbosa, A. Agrawal, L. Rodriguez-Lorenzo, I. Pastoriza-Santos, R. A. Alvarez-Puebla, A. Kornowski, *et al.*, "Tuning size and sensing properties in colloidal gold nanostars," *Langmuir*, vol. 26, pp. 14943-14950, 2010.
- [38] H. Wang, D. W. Brandl, F. Le, P. Nordlander, and N. J. Halas, "Nanorice: a hybrid plasmonic nanostructure," *Nano Letters*, vol. 6, pp. 827-832, 2006.
- [39] B. J. Wiley, Y. C. Chen, J. M. McLellan, Y. J. Xiong, Z. Y. Li, D. Ginger, *et al.*, "Synthesis and optical properties of silver nanobars and nanorice," *Nano Letters*, vol. 7, pp. 1032-1036, 2007.
- [40] C. J. Huang, P. H. Chiu, Y. H. Wang, W. R. Chen, T. H. Meen, and C. F. Yang, "Preparation and characterization of gold nanodumbbells," *Nanotechnology*, vol. 17, pp. 5355-5362, 2006.
- [41] M. F. Cardinal, B. Rodriguez-Gonzalez, R. A. Alvarez-Puebla, J. Perez-Juste, and L. M. Liz-Marzan, "Modulation of localized surface plasmons and SERS response in gold dumbbells through silver coating," *The Journal of Physical Chemistry C*, vol. 114, pp. 10417-10423, 2010.
- [42] J. Lee, W. Hasan, C. L. Stender, and T. W. Odom, "Pyramids: a platform for designing multifunctional plasmonic particles," *Accounts of Chemical Research*, vol. 41, pp. 1762-1771, 2008.
- [43] K. A. Stoerzinger, W. Hasan, J. Y. Lin, A. Robles, and T. W. Odom, "Screening nanopyramid assemblies to optimize surface enhanced Raman scattering," *The Journal of Physical Chemistry Letters*, vol. 1, pp. 1046-1050, 2010.
- [44] A. M. Schwartzberg, T. Y. Olson, C. E. Talley, and J. Z. Zhang, "Synthesis, characterization, and tunable optical properties of hollow gold nanospheres," *The Journal of Physical Chemistry B*, vol. 110, pp. 19935-19944, 2006.
- [45] T. Y. Olson, A. M. Schwartzberg, C. A. Orme, C. E. Talley, B. O'Connell, and J. Z. Zhang, "Hollow gold-silver double-shell nanospheres: structure, optical absorption, and surface-enhanced Raman scattering," *The Journal of Physical Chemistry C*, vol. 112, pp. 6319-6329, 2008.

- [46] M. Chandra, A.-M. Dowgiallo, and K. L. Knappenberger Jr, "Controlled plasmon resonance properties of hollow gold nanosphere aggregates," *Journal of the American Chemical Society*, vol. 132, pp. 15782-15789, 2010.
- [47] M. Hu, H. Petrova, A. R. Sekkinen, J. Y. Chen, J. M. McLellan, Z. Y. Li, *et al.*, "Optical properties of Au-Ag nanoboxes studied by single nanoparticle spectroscopy," *The Journal of Physical Chemistry B*, vol. 110, pp. 19923-19928, 2006.
- [48] M. Cao, M. Wang, and N. Gu, "Optimized surface plasmon resonance sensitivity of gold nanoboxes for sensing applications," *The Journal of Physical Chemistry C*, vol. 113, pp. 1217-1221, 2009.
- [49] L. Au, Y. C. Chen, F. Zhou, P. H. C. Camargo, B. Lim, Z. Y. Li, *et al.*, "Synthesis and optical properties of cubic gold nanoframes," *Nano Research*, vol. 1, pp. 441-449, 2008.
- [50] M. A. Mahmoud, B. Snyder, and M. A. El-Sayed, "Surface plasmon fields and coupling in the hollow gold nanoparticles and surface-enhanced Raman spectroscopy: theory and experiment," *The Journal of Physical Chemistry C*, vol. 114, pp. 7436-7443, 2010.
- [51] P. K. Jain, X. H. Huang, I. H. El-Sayed, and M. A. El-Sayed, "Noble metals on the nanoscale: optical and photothermal properties and some applications in imaging, sensing, biology, and medicine," *Accounts of Chemical Research*, vol. 41, pp. 1578-1586, 2008.
- [52] K. A. Willets and R. P. Van Duyne, "Localized surface plasmon resonance spectroscopy and sensing," *Annual Review of Physical Chemistry*, vol. 58, pp. 267-297, 2007.
- [53] J. Z. Zhang and C. Noguez, "Plasmonic optical properties and applications of metal nanostructures," *Plasmonics*, vol. 3, pp. 127-150, 2008.
- [54] K. S. Lee and M. A. El-Sayed, "Gold and silver nanoparticles in sensing and imaging: sensitivity of plasmon response to size, shape, and metal composition," *The Journal of Physical Chemistry B*, vol. 110, pp. 19220-19225, 2006.
- [55] M. Lismont and L. Dreesen, "Comparative study of Ag and Au nanoparticles biosensors based on surface plasmon resonance phenomenon," *Materials Science & Engineering C-Materials for Biological Applications*, vol. 32, pp. 1437-1442, 2012.
- [56] S. Kumar, N. Harrison, R. Richards-Kortum, and K. Sokolov, "Plasmonic nanosensors for imaging intracellular biomarkers in live cells," *Nano Letters*, vol. 7, pp. 1338-1343, 2007.
- [57] K. M. Mayer and J. H. Hafner, "Localized surface plasmon resonance sensors," *Chemical Reviews*, vol. 111, pp. 3828-3857, 2011.
- [58] K. Kneipp, R. R. Dasari, and Y. Wang, "Near-infrared surface-enhanced Raman-scattering (NIR SERS) on colloidal silver and gold," *Applied Spectroscopy*, vol. 48, pp. 951-957, 1994.
- [59] R. F. Aroca, R. A. Alvarez-Puebla, N. Pieczonka, S. Sanchez-Cortez, and J. V. Garcia-Ramos, "Surface-enhanced Raman scattering on colloidal nanostructures," *Advances in Colloid and Interface Science*, vol. 116, pp. 45-61, 2005.
- [60] C. W. Huang, Y. W. Hao, J. Nyagilo, D. P. Dave, L. F. Xu, and X. K. Sun, "Porous hollow gold nanoparticles for cancer SERS imaging," *Journal of Nano Research*, vol. 10, pp. 137-148, 2010.
- [61] A. Agrawal, S. Huang, A. W. H. Lin, M. H. Lee, J. K. Barton, R. A. Drezek, *et al.*, "Quantitative evaluation of optical coherence tomography signal enhancement with

- gold nanoshells," *Journal of Biomedical Optics*, vol. 11, pp. 0411211-0411218, 2006.
- [62] J. K. Barton, N. J. Halas, J. L. West, and R. A. Drezek, "Nanoshells as an optical coherence tomography contrast agent," 2004, pp. 99-106.
- [63] M. Y. Kirillin, P. D. Agrba, M. A. Sirotkina, M. V. Shiryamova, E. V. Zagainova, and V. A. Kamensky, "Nanoparticles as contrast-enhancing agents in optical coherence tomography imaging of the structural components of skin: quantitative evaluation," *Quantum Electronics*, vol. 40, pp. 525-530, 2010.
- [64] J. A. Copland, M. Eghtedari, V. L. Popov, N. Kotov, N. Mamedova, M. Motamedi, *et al.*, "Bioconjugated gold nanoparticles as a molecular based contrast agent: implications for imaging of deep tumors using optoacoustic tomography," *Molecular Imaging and Biology*, vol. 6, pp. 341-349, 2004.
- [65] C. Kim, E. C. Cho, J. Chen, K. H. Song, L. Au, C. Favazza, *et al.*, "In vivo molecular photoacoustic tomography of melanomas targeted by bioconjugated gold nanocages," *ACS nano*, vol. 4, pp. 4559-4564, 2010.
- [66] W. Lu, Q. Huang, K. B. Geng, X. X. Wen, M. Zhou, D. Guzatov, *et al.*, "Photoacoustic imaging of living mouse brain vasculature using hollow gold nanospheres," *Biomaterials*, vol. 31, pp. 2617-2626, 2010.
- [67] X. Huang, W. Qian, I. H. El - Sayed, and M. A. El - Sayed, "The potential use of the enhanced nonlinear properties of gold nanospheres in photothermal cancer therapy," *Lasers in Surgery and Medicine*, vol. 39, pp. 747-753, 2007.
- [68] X. H. Huang, P. K. Jain, I. H. El-Sayed, and M. A. El-Sayed, "Plasmonic photothermal therapy (PPTT) using gold nanoparticles," *Lasers in Medical Science*, vol. 23, pp. 217-228, 2008.
- [69] J. Nam, N. Won, H. Jin, H. Chung, and S. Kim, "pH-induced aggregation of gold nanoparticles for photothermal cancer therapy," *Journal of the American Chemical Society*, vol. 131, pp. 13639-13645, 2009.
- [70] J. Xie, S. Lee, and X. Y. Chen, "Nanoparticle-based theranostic agents," *Advanced Drug Delivery Reviews*, vol. 62, pp. 1064-1079, 2010.
- [71] X. Wu, T. Ming, X. Wang, P. N. Wang, J. F. Wang, and J. Y. Chen, "High-photoluminescence-yield gold nanocubes: for cell imaging and photothermal therapy," *ACS Nano*, vol. 4, pp. 113-120, 2010.
- [72] J. K. Young, E. R. Figueroa, and R. A. Drezek, "Tunable nanostructures as photothermal theranostic agents," *Annals of Biomedical Engineering*, vol. 40, pp. 438-459, 2012.
- [73] R. Weissleder, "A clearer vision for in vivo imaging," *Nature Biotechnology*, vol. 19, pp. 316-317, 2001.
- [74] P. Debbage and W. Jaschke, "Molecular imaging with nanoparticles: giant roles for dwarf actors," *Histochemistry and Cell Biology*, vol. 130, pp. 845-875, 2008.
- [75] T. Itoh, A. Sujith, and Y. Ozaki, "Surface-enhanced Raman scattering spectroscopy," in *Frontiers of Molecular Spectroscopy*, J. Laane, Ed., ed: Elsevier Science, 2011, pp. 289-320.
- [76] K. Kneipp, A. S. Haka, H. Kneipp, K. Badizadegan, N. Yoshizawa, C. Boone, *et al.*, "Surface-enhanced Raman spectroscopy in single living cells using gold nanoparticles," *Applied Spectroscopy*, vol. 56, pp. 150-154, 2002.

- [77] X. M. Qian, X. H. Peng, D. O. Ansari, Q. Yin-Goen, G. Z. Chen, D. M. Shin, *et al.*, "In vivo tumor targeting and spectroscopic detection with surface-enhanced Raman nanoparticle tags," *Nature Biotechnology*, vol. 26, pp. 83-90, 2008.
- [78] T. A. Erickson and J. W. Tunnell, "Gold nanoshells in biomedical applications," in *Nanotechnologies for the Life Sciences*. vol. 3, S. S. R. K. Challa, Ed., ed: Wiley-VCH Verlag, 2009, pp. 1-44.
- [79] X. H. Huang, S. Neretina, and M. A. El-Sayed, "Gold nanorods: from synthesis and properties to biological and biomedical applications," *Advanced Materials*, vol. 21, pp. 4880-4910, 2009.
- [80] C. Noguez, "Surface plasmons on metal nanoparticles: the influence of shape and physical environment," *The Journal of Physical Chemistry C*, vol. 111, pp. 3806-3819, 2007.
- [81] U. Kreibig and M. Vollmer, *Optical Properties of Metal Clusters*. Berlin: Springer, 1995.
- [82] E. S. Kooij, W. Ahmed, H. J. W. Zandvliet, and B. Poelsema, "Localized plasmons in noble metal nanospheroids," *The Journal of Physical Chemistry C*, vol. 115, pp. 10321-10332, 2011.
- [83] C. Noguez, "Optical properties of isolated and supported metal nanoparticles," *Optical Materials*, vol. 27, pp. 1204-1211, 2005.
- [84] C. F. Bohren and D. R. Huffman, *Absorption and Scattering of Light by Small Particles*. New York: John Wiley & Sons, 1998.
- [85] S. Link and M. A. El-Sayed, "Spectral properties and relaxation dynamics of surface plasmon electronic oscillations in gold and silver nanodots and nanorods," *The Journal of Physical Chemistry B*, vol. 103, pp. 8410-8426, 1999.
- [86] P. K. Jain and M. A. El-Sayed, "Plasmonic coupling in noble metal nanostructures," *Chemical Physics Letters*, vol. 487, pp. 153-164, 2010.
- [87] E. Hao and G. C. Schatz, "Electromagnetic fields around silver nanoparticles and dimers," *The Journal of Chemical Physics*, vol. 120, pp. 357-366, 2004.
- [88] P. K. Jain, K. S. Lee, I. H. El-Sayed, and M. A. El-Sayed, "Calculated absorption and scattering properties of gold nanoparticles of different size, shape, and composition: applications in biological imaging and biomedicine," *The Journal of Physical Chemistry B*, vol. 110, pp. 7238-7248, 2006.
- [89] I. O. Sosa, C. Noguez, and R. G. Barrera, "Optical properties of metal nanoparticles with arbitrary shapes," *The Journal of Physical Chemistry B*, vol. 107, pp. 6269-6275, 2003.
- [90] S. K. Ghosh and T. Pal, "Interparticle coupling effect on the surface plasmon resonance of gold nanoparticles: from theory to applications," *Chemical Reviews*, vol. 107, pp. 4797-4862, 2007.
- [91] E. D. Palik, *Handbook of Optical Constants of Solids* vol. 1. Orlando: Academic Press, 1985.
- [92] R. Fuchs, "Theory of the optical properties of ionic crystal cubes," *Physical Review B*, vol. 11, pp. 1732-1740, 02/15/ 1975.
- [93] A. L. González and C. Noguez, "Optical properties of silver nanoparticles," *Physica Status Solidi (c)*, vol. 4, pp. 4118-4126, 2007.
- [94] F. Zhou, Z.-Y. Li, Y. Liu, and Y. Xia, "Quantitative analysis of dipole and quadrupole excitation in the surface plasmon resonance of metal nanoparticles," *The Journal of Physical Chemistry C*, vol. 112, pp. 20233-20240, 2008.

- [95] A. J. Haes, C. L. Haynes, A. D. McFarland, G. C. Schatz, R. P. Van Duyne, and S. Zou, "Plasmonic materials for surface-enhanced sensing and spectroscopy," *MRS Bulletin*, vol. 30, pp. 368-375, 2005.
- [96] L. B. Scaffardi, N. Pellegrini, O. De Sanctis, and J. O. Tocho, "Sizing gold nanoparticles by optical extinction spectroscopy," *Nanotechnology*, vol. 16, pp. 158-163, 2004.
- [97] T. Larson, K. Travis, P. Joshi, and K. Sokolov, "Nanoparticles for targeted therapeutics and diagnostics," in *Handbook of Biomedical Optics*. vol. 1, D. A. Boas, C. Pitris, and N. Ramanujam, Eds., ed: CRC Press, 2012, pp. 697-721.
- [98] P. B. Johnson and R. W. Christy, "Optical constants of the noble metals," *Physical Review B*, vol. 6, pp. 4370-4379, 1972.
- [99] P. B. Johnson and R. W. Christy, "Optical constants of transition metals: Ti, V, Cr, Mn, Fe, Co, Ni, and Pd," *Physical Review B*, vol. 9, pp. 5056-5070, 1974.
- [100] H. J. Hagemann, W. Gudat, and C. Kunz, "Optical-constants from far infrared to X-ray region - Mg, Al, Cu, Ag, Au, Bi, C, and Al₂O₃," *Journal of the Optical Society of America*, vol. 65, pp. 742-744, 1975.
- [101] S. Link and M. A. El-Sayed, "Shape and size dependence of radiative, non-radiative and photothermal properties of gold nanocrystals," *International Reviews in Physical Chemistry*, vol. 19, pp. 409-453, 2000.
- [102] S. O. Pillai, "Electrical properties of metals," in *Solid State Physics*, 6th ed New Delhi: New Age International, 2005, pp. 179-333.
- [103] J. R. Hook and H. E. Hall, "Free electrons in metals," in *Solid State Physics*, 2nd ed Chichester: John Wiley & Sons, 1991, pp. 76-99.
- [104] H. Hovel, S. Fritz, A. Hilger, U. Kreibig, and M. Vollmer, "Width of cluster plasmon resonances - bulk dielectric functions and chemical interface damping," *Physical Review B*, vol. 48, pp. 18178-18188, 1993.
- [105] E. A. Coronado and G. C. Schatz, "Surface plasmon broadening for arbitrary shape nanoparticles: a geometrical probability approach," *The Journal of Chemical Physics*, vol. 119, pp. 3926-3934, 2003.
- [106] T. Okamoto, "Near-field spectral analysis of metallic beads," in *Near-Field Optics and Surface Plasmon Polaritons*, S. Kawata, Ed., ed Berlin: Springer, 2001, pp. 97-123.
- [107] M. M. Alvarez, J. T. Khoury, T. G. Schaaff, M. N. Shafiqullin, I. Vezmar, and R. L. Whetten, "Optical absorption spectra of nanocrystal gold molecules," *The Journal of Physical Chemistry B*, vol. 101, pp. 3706-3712, 1997.
- [108] L. B. Scaffardi and J. O. Tocho, "Size dependence of refractive index of gold nanoparticles," *Nanotechnology*, vol. 17, pp. 1309-1315, 2006.
- [109] C. G. Granqvist and O. Hunderi, "Optical-absorption of ultrafine metal spheres with dielectric cores," *Zeitschrift Fur Physik B-Condensed Matter*, vol. 30, pp. 47-51, 1978.
- [110] S. Schelm and G. B. Smith, "Internal electric field densities of metal nanoshells," *The Journal of Physical Chemistry B*, vol. 109, pp. 1689-1694, 2005.
- [111] B. Khlebtsov and N. G. Khlebtsov, "Ultrasharp light-scattering resonances of structured nanospheres: effects of size-dependent dielectric functions," *Journal of Biomedical Optics*, vol. 11, pp. 0440021-0440025, 2006.
- [112] R. D. Averitt, D. Sarkar, and N. J. Halas, "Plasmon resonance shifts of Au-coated Au₂S nanoshells: insight into multicomponent nanoparticle growth," *Physical Review Letters*, vol. 78, pp. 4217-4220, 1997.

- [113] R. D. Averitt, S. L. Westcott, and N. J. Halas, "Linear optical properties of gold nanoshells," *Journal of the Optical Society of America B-Optical Physics*, vol. 16, pp. 1824-1832, 1999.
- [114] C. G. Granqvist and O. Hunderi, "Optical-properties of ultrafine gold particles," *Physical Review B*, vol. 16, pp. 3513-3534, 1977.
- [115] N. Felidj, J. Aubard, and G. Levi, "Discrete dipole approximation for ultraviolet-visible extinction spectra simulation of silver and gold colloids," *The Journal of Chemical Physics*, vol. 111, pp. 1195-1208, 1999.
- [116] E. J. Zeman and G. C. Schatz, "An accurate electromagnetic theory study of surface enhancement factors for silver, gold, copper, lithium, sodium, aluminum, gallium, indium, zinc, and cadmium," *The Journal of Physical Chemistry*, vol. 91, pp. 634-643, 1987.
- [117] S. P. Yuan and P. X. Jiang, "Thermal conductivity of small nickel particles," *International Journal of Thermophysics*, vol. 27, pp. 581-595, 2006.
- [118] K. L. Kelly, A. A. Lazarides, and G. C. Schatz, "Computational electromagnetics of metal nanoparticles and their aggregates," *Computing in Science & Engineering*, vol. 3, pp. 67-73, 2001.
- [119] G. Mie, "Contributions to the optics of turbid media, particularly of colloidal metal solutions," *Transl. into ENGLISH from Ann. Phys.(Leipzig)*, v. 25, no. 3, 1908 p 377-445, vol. 25, pp. 377-445, 1976.
- [120] M. A. Yurkin and A. G. Hoekstra, "The discrete dipole approximation: an overview and recent developments," *Journal of Quantitative Spectroscopy and Radiative Transfer*, vol. 106, pp. 558-589, 2007.
- [121] S. Tanev, V. V. Tuchin, and P. Paddon, "Finite-difference time-domain modeling of light scattering from biological cells containing gold nanoparticles," *Photon-based Nanoscience and Nanobiotechnology*, pp. 97-119, 2006.
- [122] J. Zhao, A. O. Pinchuk, J. M. McMahon, S. Z. Li, L. K. Ausman, A. L. Atkinson, *et al.*, "Methods for describing the electromagnetic properties of silver and gold nanoparticles," *Accounts of Chemical Research*, vol. 41, pp. 1710-1720, 2008.
- [123] M. I. Mishchenko, L. D. Travis, and A. A. Lacis, *Scattering, Absorption, and Emission of Light by Small Particles*. Cambridge: University Press, 2002.
- [124] T. Wriedt, "A review of elastic light scattering theories," *Particle & Particle Systems Characterization*, vol. 15, pp. 67-74, 1998.
- [125] E. M. Purcell and C. R. Pennypacker, "Scattering and absorption of light by nonspherical dielectric grains," *Astrophysical Journal*, vol. 186, pp. 705-714, 1973.
- [126] B. T. Draine, "The discrete-dipole approximation and its application to interstellar graphite grains," *Astrophysical Journal*, vol. 333, pp. 848-872, 1988.
- [127] J. J. Goodman, B. T. Draine, and P. J. Flatau, "Application of fast-Fourier-transform techniques to the discrete-dipole approximation," *Optics Letters*, vol. 16, pp. 1198-1200, 1991.
- [128] B. T. Draine and J. Goodman, "Beyond Clausius-Mossotti: wave propagation on a polarizable point lattice and the discrete dipole approximation," *Astrophysical Journal*, vol. 405, pp. 685-697, 1993.
- [129] B. T. Draine and P. J. Flatau, "Discrete-dipole approximation for scattering calculations," *Journal of the Optical Society of America A-Optics Image Science and Vision*, vol. 11, pp. 1491-1499, 1994.
- [130] M. J. Collinge and B. T. Draine, "Discrete-dipole approximation with polarizabilities that account for both finite wavelength and target geometry,"

- Journal of the Optical Society of America A-Optics Image Science and Vision* vol. 21, pp. 2023-2028, 2004.
- [131] D. Gutzkowicz-Krusin and B. T. Draine. (2004, Propagation of electromagnetic waves on a rectangular lattice of polarizable points. Available: <http://arxiv.org/abs/astro-ph/0403082>
- [132] B. T. Draine, "The discrete dipole approximation for light scattering by irregular targets," in *Light Scattering by Nonspherical Particles: Theory, Measurements, and Applications*. vol. 1, M. I. Mishchenko, J. W. Hovenier, and L. D. Travis, Eds., ed: Academic Press, 2000, pp. 131-144.
- [133] T. Jensen, L. Kelly, A. Lazarides, and G. C. Schatz, "Electrodynamics of noble metal nanoparticles and nanoparticle clusters," *Journal of Cluster Science*, vol. 10, pp. 295-317, Jun 1999.
- [134] W. H. Yang, G. C. Schatz, and R. P. Van Duyne, "Discrete dipole approximation for calculating extinction and Raman intensities for small particles with arbitrary shapes," *The Journal of Chemical Physics*, vol. 103, pp. 869-875, 1995.
- [135] B. T. Draine and P. J. Flatau. 2004, User guide for the discrete dipole approximation code DDSCAT6.1. Available: <http://arxiv.org/abs/astro-ph/0409262v2>
- [136] B. T. Draine and P. J. Flatau. 2008, User guide for the discrete dipole approximation code DDSCAT 7.0. Available: <http://arxiv.org/abs/0809.0337v4>
- [137] M2HTML. (2005). *Matlab Index*. Available: http://eeg.sourceforge.net/doc_m2html/index.html
- [138] W. Cai, T. Gao, H. Hong, and J. Sun, "Applications of gold nanoparticles in cancer nanotechnology," *Nanotechnology, Science and Applications*, vol. 1, pp. 17-32, 2008.
- [139] K. Hering, D. Cialla, K. Ackermann, T. Dörfer, R. Möller, H. Schneidewind, *et al.*, "SERS: a versatile tool in chemical and biochemical diagnostics," *Analytical and Bioanalytical Chemistry*, vol. 390, pp. 113-124, 2008.
- [140] E. B. Hanlon, R. Manoharan, T. W. Koo, K. E. Shafer, J. T. Motz, M. Fitzmaurice, *et al.*, "Prospects for in vivo Raman spectroscopy," *Physics in Medicine and Biology*, vol. 45, pp. R1-R59, 2000.
- [141] R. Petry, M. Schmitt, and J. Popp, "Raman spectroscopy -A prospective tool in the life sciences," *ChemPhysChem*, vol. 4, pp. 14-30, 2003.
- [142] G. C. Schatz and R. P. Van Duyne, "Electromagnetic mechanism of surface - enhanced spectroscopy," in *Handbook of Vibrational Spectroscopy*, J. M. Chalmers, Griffiths, P. R., Ed., ed Chichester: John Wiley & Sons, 2002.
- [143] M. Moskovits, "Surface-enhanced Raman spectroscopy: a brief retrospective," *Journal of Raman Spectroscopy*, vol. 36, pp. 485-496, 2005.
- [144] K. Kneipp, H. Kneipp, I. Itzkan, R. R. Dasari, and M. S. Feld, "Surface-enhanced Raman scattering and biophysics," *Journal of Physics: Condensed Matter*, vol. 14, pp. R597-R624, 2002.
- [145] R. M. Jarvis, N. Law, L. T. Shadi, P. O'Brien, J. R. Lloyd, and R. Goodacre, "Surface-enhanced Raman scattering from intracellular and extracellular bacterial locations," *Analytical Chemistry*, vol. 80, pp. 6741-6746, 2008.
- [146] K. Kneipp, H. Kneipp, and J. Kneipp, "Surface-enhanced Raman scattering in local optical fields of silver and gold nanoaggregates - From single-molecule Raman

- spectroscopy to ultrasensitive probing in live cells," *Accounts of Chemical Research*, vol. 39, pp. 443-450, 2006.
- [147] M. Ahamed, M. S. AlSalhi, and M. K. J. Siddiqui, "Silver nanoparticle applications and human health," *Clinica Chimica Acta*, vol. 411, pp. 1841-1848, 2010.
- [148] C. Marambio-Jones and E. V. Hoek, "A review of the antibacterial effects of silver nanomaterials and potential implications for human health and the environment," *Journal of Nanoparticle Research*, vol. 12, pp. 1531-1551, 2010.
- [149] J. Wu, F. Zhang, and H. Zhang, "Facile synthesis of carboxymethyl curdlan-capped silver nanoparticles and their application in SERS," *Carbohydrate Polymers*, vol. 90, pp. 261-269, 2012.
- [150] L. S. Nair and C. T. Laurencin, "Silver nanoparticles: synthesis and therapeutic applications," *Journal of Biomedical Nanotechnology*, vol. 3, pp. 301-316, 2007.
- [151] R. M. Jarvis and R. Goodacre, "Characterisation and identification of bacteria using SERS," *Chemical Society Reviews*, vol. 37, pp. 931-936, 2008.
- [152] A. Panáček, L. Kvítek, R. Prucek, M. Kolář, R. Večeřová, N. Pizúrová, *et al.*, "Silver colloid nanoparticles: synthesis, characterization, and their antibacterial activity," *The Journal of Physical Chemistry B*, vol. 110, pp. 16248-16253, 2006/08/01 2006.
- [153] E. E. Connor, J. Mwamuka, A. Gole, C. J. Murphy, and M. D. Wyatt, "Gold nanoparticles are taken up by human cells but do not cause acute cytotoxicity," *Small*, vol. 1, pp. 325-327, 2005.
- [154] J. A. Khan, B. Pillai, T. K. Das, Y. Singh, and S. Maiti, "Molecular effects of uptake of gold nanoparticles in HeLa cells," *ChemBioChem*, vol. 8, pp. 1237-1240, 2007.
- [155] Y. Pan, S. Neuss, A. Leifert, M. Fischler, F. Wen, U. Simon, *et al.*, "Size-dependent cytotoxicity of gold nanoparticles," *Small*, vol. 3, pp. 1941-1949, 2007.
- [156] R. Shukla, V. Bansal, M. Chaudhary, A. Basu, R. R. Bhonde, and M. Sastry, "Biocompatibility of gold nanoparticles and their endocytotic fate inside the cellular compartment: a microscopic overview," *Langmuir*, vol. 21, pp. 10644-10654, 2005.
- [157] J. Xiao, "Single-Molecule Imaging in Live Cells," in *Handbook of Single-Molecule Biophysics*, P. Hinterdorfer and A. van Oijen, Eds., ed: Springer, 2009, pp. 43-94.
- [158] Z. Zhong, S. Patskovskyy, P. Bouverette, J. H. Luong, and A. Gedanken, "The surface chemistry of Au colloids and their interactions with functional amino acids," *The Journal of Physical Chemistry B*, vol. 108, pp. 4046-4052, 2004.
- [159] M. Hu, J. Y. Chen, Z. Y. Li, L. Au, G. V. Hartland, X. D. Li, *et al.*, "Gold nanostructures: engineering their plasmonic properties for biomedical applications," *Chemical Society Reviews*, vol. 35, pp. 1084-1094, 2006.
- [160] T. Y. Olson and J. Z. Zhang, "Structural and optical properties and emerging applications of metal nanomaterials," *Journal of Materials Science & Technology*, vol. 24, pp. 433-446, 2008.
- [161] I. H. El-Sayed, X. Huang, and M. A. El-Sayed, "Surface plasmon resonance scattering and absorption of anti-EGFR antibody conjugated gold nanoparticles in cancer diagnostics: applications in oral cancer," *Nano Letters*, vol. 5, pp. 829-834, 2005.
- [162] B. Merchant, "Gold, the noble metal and the paradoxes of its toxicology," *Biologicals*, vol. 26, pp. 49-59, 1998.

- [163] J. Kneipp, H. Kneipp, M. McLaughlin, D. Brown, and K. Kneipp, "In vivo molecular probing of cellular compartments with gold nanoparticles and nanoaggregates," *Nano Letters*, vol. 6, pp. 2225-2231, 2006.
- [164] S. J. Oldenburg, S. L. Westcott, R. D. Averitt, and N. J. Halas, "Surface enhanced Raman scattering in the near infrared using metal nanoshell substrates," *The Journal of Chemical Physics*, vol. 111, pp. 4729-4735, 1999.
- [165] M. H. Chowdhury, C. J. Campbell, E. Theofanidou, S. J. Lee, A. Baldwin, G. Sing, *et al.*, "Surface enhanced Raman spectroscopy (SERS) for the detection of intracellular constituents using gold nanoshells," 2006, pp. 6099051-6099058.
- [166] G. Von Maltzahn, A. Centrone, J. H. Park, R. Ramanathan, M. J. Sailor, T. A. Hatton, *et al.*, "SERS-coded gold nanorods as a multifunctional platform for densely multiplexed near-infrared imaging and photothermal heating," *Advanced Materials*, vol. 21, pp. 3175-3180, 2009.
- [167] V. Cunningham and H. Lamela, "Optical and optoacoustic measurements of the absorption properties of spherical gold nanoparticles within a highly scattering medium," *Optics & Laser Technology*, vol. 42, pp. 769-774, 2010.
- [168] Y. Wang, X. Xie, X. Wang, G. Ku, K. L. Gill, D. P. O'Neal, *et al.*, "Photoacoustic tomography of a nanoshell contrast agent in the in vivo rat brain," *Nano Letters*, vol. 4, pp. 1689-1692, 2004.
- [169] M. Eghtedari, A. Oraevsky, J. A. Copland, N. A. Kotov, A. Conjusteau, and M. Motamedi, "High sensitivity of in vivo detection of gold nanorods using a laser optoacoustic imaging system," *Nano Letters*, vol. 7, pp. 1914-1918, Jul 2007.
- [170] J. T. Krug, G. D. Wang, S. R. Emory, and S. Nie, "Efficient Raman enhancement and intermittent light emission observed in single gold nanocrystals," *Journal of the American Chemical Society*, vol. 121, pp. 9208-9214, 1999.
- [171] A. Wei, B. Kim, B. Sadtler, and S. L. Tripp, "Tunable surface-enhanced Raman scattering from large gold nanoparticle arrays," *ChemPhysChem*, vol. 2, pp. 743-745, 2001.
- [172] B. D. Chithrani, A. A. Ghazani, and W. C. W. Chan, "Determining the size and shape dependence of gold nanoparticle uptake into mammalian cells," *Nano Letters*, vol. 6, pp. 662-668, 2006.
- [173] Anshup, J. S. Venkataraman, C. Subramaniam, R. R. Kumar, S. Priya, T. R. S. Kumar, *et al.*, "Growth of gold nanoparticles in human cells," *Langmuir*, vol. 21, pp. 11562-11567, 2005.
- [174] A. Shamsaie, M. Jonczyk, J. Sturgis, J. P. Robinson, and J. Irudayaraj, "Intracellularly grown gold nanoparticles as potential surface-enhanced Raman scattering probes," *Journal of Biomedical Optics*, vol. 12, pp. 0205021-0205023, 2007.
- [175] N. G. Khlebtsov, L. A. Dykman, Y. M. Krasnov, and A. G. Melnikov, "Light absorption by the clusters of colloidal gold and silver particles formed during slow and fast aggregation," *Colloid Journal*, vol. 62, pp. 765-779, 2000.
- [176] M. Yang, G. Chen, Y. Zhao, G. Silber, Y. Wang, S. Xing, *et al.*, "Mechanistic investigation into the spontaneous linear assembly of gold nanospheres," *Physical Chemistry Chemical Physics*, vol. 12, pp. 11850-11860, 2010.
- [177] M. H. Chowdhury, C. J. Campbell, E. Theofanidou, S. J. Lee, A. Baldwin, G. Sing, *et al.*, "Surface enhanced Raman spectroscopy (SERS) for the detection of intracellular constituents using gold nanoshells," in *Biomedical Optics 2006*, 2006, pp. 609905-609905-8.

- [178] T. Niidome, M. Yamagata, Y. Okamoto, Y. Akiyama, H. Takahashi, T. Kawano, *et al.*, "PEG-modified gold nanorods with a stealth character for in vivo applications," *Journal of Controlled Release*, vol. 114, pp. 343-347, 2006.
- [179] P. N. Prasad, "Basics of Biology," in *Introduction to Biophotonics*, ed: John Wiley & Sons, 2004, pp. 50-91.
- [180] C. Ungureanu, R. G. Rayavarapu, S. Manohar, and T. G. van Leeuwen, "Discrete dipole approximation simulations of gold nanorod optical properties: choice of input parameters and comparison with experiment," *Journal of Applied Physics*, vol. 105, pp. 102032-102032-7, 2009.
- [181] S. W. Prescott and P. Mulvaney, "Gold nanorod extinction spectra," *Journal of Applied Physics*, vol. 99, pp. 123504-123504-7, 2006.
- [182] V. V. Tuchin, *Tissue Optics: Light Scattering Methods and Instruments for Medical Diagnosis*, 2nd ed. Washington: SPIE Press, 2007.
- [183] B. Khlebtsov, V. Zharov, A. Melnikov, V. Tuchin, and N. G. Khlebtsov, "Optical amplification of photothermal therapy with gold nanoparticles and nanoclusters," *Nanotechnology*, vol. 17, pp. 5167-5179, 2006.
- [184] E. R. Encina and E. A. Coronado, "Plasmon coupling in silver nanosphere pairs," *The Journal of Physical Chemistry C*, vol. 114, pp. 3918-3923, 2010.
- [185] P. K. Jain, W. Huang, and M. A. El-Sayed, "On the universal scaling behavior of the distance decay of plasmon coupling in metal nanoparticle pairs: a plasmon ruler equation," *Nano Letters*, vol. 7, pp. 2080-2088, 2007.
- [186] P. K. Jain and M. A. El-Sayed, "Universal scaling of plasmon coupling in metal nanostructures: extension from particle pairs to nanoshells," *Nano letters*, vol. 7, pp. 2854-2858, 2007.
- [187] P. K. Jain and M. A. El-Sayed, "Surface plasmon coupling and its universal size scaling in metal nanostructures of complex geometry: elongated particle pairs and nanosphere trimers," *The Journal of Physical Chemistry C*, vol. 112, pp. 4954-4960, 2008.
- [188] X. M. Yang, E. W. Stein, S. Ashkenazi, and L. H. V. Wang, "Nanoparticles for photoacoustic imaging," *Wiley Interdisciplinary Reviews-Nanomedicine and Nanobiotechnology*, vol. 1, pp. 360-368, 2009.
- [189] S. Mallidi, T. Larson, J. Aaron, K. Sokolov, and S. Emelianov, "Molecular specific optoacoustic imaging with plasmonic nanoparticles," *Optics Express*, vol. 15, pp. 6583-6588, 2007.
- [190] S. M. Janib, A. S. Moses, and J. A. MacKay, "Imaging and drug delivery using theranostic nanoparticles," *Advanced Drug Delivery Reviews*, vol. 62, pp. 1052-1063, 2010.
- [191] M. Olivo, S. S. Lucky, R. Bhuvanewari, and N. Dendukuri, "Nano-sensitizers for multi-modality optical diagnostic imaging and therapy of cancer," in *European Conferences on Biomedical Optics*, 2011, pp. 80870T-80870T-12.
- [192] C. Loo, A. Lin, L. Hirsch, M. H. Lee, J. Barton, N. J. Halas, *et al.*, "Nanoshell-enabled photonics-based imaging and therapy of cancer," *Technology in Cancer Research & Treatment*, vol. 3, pp. 33-40, 2004.
- [193] X. H. Huang, I. H. El-Sayed, W. Qian, and M. A. El-Sayed, "Cancer cell imaging and photothermal therapy in the near-infrared region by using gold nanorods," *Journal of the American Chemical Society*, vol. 128, pp. 2115-2120, 2006.

- [194] J. Y. Chen, M. X. Yang, Q. A. Zhang, E. C. Cho, C. M. Cobley, C. Kim, *et al.*, "Gold nanocages: a novel class of multifunctional nanomaterials for theranostic applications," *Advanced Functional Materials*, vol. 20, pp. 3684-3694, 2010.
- [195] P. K. Jain, I. H. El-Sayed, and M. A. El-Sayed, "Au nanoparticles target cancer," *Nano Today*, vol. 2, pp. 18-29, 2007.
- [196] C. Shen, C. Hui, T. Yang, C. Xiao, J. Tian, L. Bao, *et al.*, "Monodisperse noble-metal nanoparticles and their surface enhanced Raman scattering properties," *Chemistry of Materials*, vol. 20, pp. 6939-6944, 2008.
- [197] V. Amendola, O. M. Bakr, and F. Stellacci, "A study of the surface plasmon resonance of silver nanoparticles by the discrete dipole approximation method: effect of shape, size, structure, and assembly," *Plasmonics*, vol. 5, pp. 85-97, 2010.
- [198] M. A. van Dijk, A. L. Tchegotareva, M. Orrit, M. Lippitz, S. Berciaud, D. Lasne, *et al.*, "Absorption and scattering microscopy of single metal nanoparticles," *Physical Chemistry Chemical Physics*, vol. 8, pp. 3486-3495, 2006.
- [199] D. D. Evanoff and G. Chumanov, "Size-controlled synthesis of nanoparticles. 2. Measurement of extinction, scattering, and absorption cross sections," *The Journal of Physical Chemistry B*, vol. 108, pp. 13957-13962, 2004.
- [200] J. A. Creighton and D. G. Eadon, "Ultraviolet visible absorption-spectra of the colloidal metallic elements," *Journal of the Chemical Society-Faraday Transactions*, vol. 87, pp. 3881-3891, 1991.
- [201] K. S. Lee and M. A. El-Sayed, "Dependence of the enhanced optical scattering efficiency relative to that of absorption for gold metal nanorods on aspect ratio, size, end-cap shape, and medium refractive index," *The Journal of Physical Chemistry B*, vol. 109, pp. 20331-20338, 2005.
- [202] S. E. Skrabalak, J. Chen, L. Au, X. Lu, X. Li, and Y. N. Xia, "Gold nanocages for biomedical applications," *Advanced Materials*, vol. 19, pp. 3177-3184, 2007.
- [203] G. H. Chan, J. Zhao, G. C. Schatz, and R. P. V. Duyne, "Localized surface plasmon resonance spectroscopy of triangular aluminum nanoparticles," *The Journal of Physical Chemistry C*, vol. 112, pp. 13958-13963, 2008.
- [204] T. L. Temple and D. M. Bagnall, "Optical properties of gold and aluminium nanoparticles for silicon solar cell applications," *Journal of Applied Physics*, vol. 109, 2011.
- [205] B. G. Ershov, "Aqueous solutions of colloidal nickel: radiation-chemical preparation, absorption spectra, and properties," *Russian Chemical Bulletin*, vol. 49, pp. 1715-1721, 2000.
- [206] J. Chen, P. Albella, Z. Pirzadeh, P. Alonso - González, F. Huth, S. Bonetti, *et al.*, "Plasmonic nickel nanoantennas," *Small*, vol. 7, pp. 2341-2347, 2011.
- [207] T. Pakizeh, "Optical absorption of nanoparticles described by an electronic local interband transition," *Journal of Optics*, vol. 15, pp. 0250011-0250017, 2013.
- [208] I. H. El-Sayed, X. Huang, and M. A. El-Sayed, "Selective laser photo-thermal therapy of epithelial carcinoma using anti-EGFR antibody conjugated gold nanoparticles," *Cancer Letters*, vol. 239, pp. 129-135, 2006.
- [209] L. R. Hirsch, A. M. Gobin, A. R. Lowery, F. Tam, R. A. Drezek, N. J. Halas, *et al.*, "Metal nanoshells," *Annals of Biomedical Engineering*, vol. 34, pp. 15-22, 2006.
- [210] J. B. Jackson and N. J. Halas, "Silver nanoshells: variations in morphologies and optical properties," *The Journal of Physical Chemistry B*, vol. 105, pp. 2743-2746, 2001.

- [211] C. E. Román-Velázquez, C. Noguez, and J. Z. Zhang, "Theoretical study of surface plasmon resonances in hollow gold–silver double-shell nanostructures," *The Journal of Physical Chemistry A*, vol. 113, pp. 4068-4074, 2009.
- [212] J. H. Hodak, A. Henglein, M. Giersig, and G. V. Hartland, "Laser-induced interdiffusion in AuAg core-shell nanoparticles," *The Journal of Physical Chemistry B*, vol. 104, pp. 11708-11718, 2000.
- [213] A. Steinbrück, A. Csáki, G. Festag, and W. Fritzsche, "Preparation and optical characterization of core–shell bimetal nanoparticles," *Plasmonics*, vol. 1, pp. 79-85, 2006.
- [214] C. Song, G. Zhao, P. Zhang, and N. L. Rosi, "Expeditious synthesis and assembly of sub-100 nm hollow spherical gold nanoparticle superstructures," *Journal of the American Chemical Society*, vol. 132, pp. 14033-14035, 2010.
- [215] T. S. Troutman, J. K. Barton, and M. Romanowski, "Biodegradable plasmon resonant nanoshells," *Advanced Materials*, vol. 20, pp. 2604-2608, 2008.
- [216] R. Michel and M. Gradzielski, "Experimental aspects of colloidal interactions in mixed systems of liposome and inorganic nanoparticle and their applications," *International Journal of Molecular Sciences*, vol. 13, pp. 11610-11642, 2012.
- [217] T. K. Sau, A. S. Urban, S. K. Dondapati, M. Fedoruk, M. R. Horton, A. L. Rogach, *et al.*, "Controlling loading and optical properties of gold nanoparticles on liposome membranes," *Colloids and Surfaces A: Physicochemical and Engineering Aspects*, vol. 342, pp. 92-96, 2009.
- [218] C. Kojima, Y. Hirano, E. Yuba, A. Harada, and K. Kono, "Preparation and characterization of complexes of liposomes with gold nanoparticles," *Colloids and Surfaces B: Biointerfaces*, vol. 66, pp. 246-252, 2008.
- [219] S. L. Westcott, S. J. Oldenburg, T. R. Lee, and N. J. Halas, "Formation and adsorption of clusters of gold nanoparticles onto functionalized silica nanoparticle surfaces," *Langmuir*, vol. 14, pp. 5396-5401, 1998.
- [220] S. L. Westcott, S. J. Oldenburg, T. R. Lee, and N. J. Halas, "Construction of simple gold nanoparticle aggregates with controlled plasmon-plasmon interactions," *Chemical Physics Letters*, vol. 300, pp. 651-655, Feb 1999.
- [221] J. H. Zhang, J. B. Liu, S. Z. Wang, P. Zhan, Z. L. Wang, and N. B. Ming, "Facile methods to coat polystyrene and silica colloids with metal," *Advanced Functional Materials*, vol. 14, pp. 1089-1096, 2004.
- [222] Y. Kobayashi, Y. Tadaki, D. Nagao, and M. Konno, "Deposition of gold nanoparticles on silica spheres by electroless metal plating technique," *Journal of Colloid and Interface Science*, vol. 283, pp. 601-604, 2005.
- [223] K. E. Peceros, X. D. Xu, S. R. Bulcock, and M. B. Cortie, "Dipole-dipole plasmon interactions in gold-on-polystyrene composites," *The Journal of Physical Chemistry B*, vol. 109, pp. 21516-21520, 2005.
- [224] W. Shi, Y. Sahoo, M. T. Swihart, and P. Prasad, "Gold nanoshells on polystyrene cores for control of surface plasmon resonance," *Langmuir*, vol. 21, pp. 1610-1617, 2005.
- [225] K.-T. Yong, Y. Sahoo, M. T. Swihart, and P. N. Prasad, "Synthesis and plasmonic properties of silver and gold nanoshells on polystyrene cores of different size and of gold–silver core–shell nanostructures," *Colloids and Surfaces A: Physicochemical and Engineering Aspects*, vol. 290, pp. 89-105, 2006.

- [226] S. H. Li, Y. T. Xia, J. P. Zhang, J. H. Han, and L. Jiang, "Polystyrene spheres coated with gold nanoparticles for detection of DNA," *Electrophoresis*, vol. 31, pp. 3090-3096, 2010.
- [227] Y. X. Li, Y. F. Pan, L. L. Zhu, Z. Q. Wang, D. M. Su, and G. Xue, "Facile and controlled fabrication of functional gold nanoparticle-coated polystyrene composite particle," *Macromolecular Rapid Communications*, vol. 32, pp. 1741-1747, 2011.
- [228] J.-H. Lee, M. A. Mahmoud, V. B. Sitterle, J. J. Sitterle, and J. C. Meredith, "Highly scattering, surface-enhanced Raman scattering-active, metal nanoparticle-coated polymers prepared via combined swelling– heteroaggregation," *Chemistry of Materials*, vol. 21, pp. 5654-5663, 2009.
- [229] H. Li, J. Han, A. Panioukhine, and E. Kumacheva, "From heterocoagulated colloids to core–shell particles," *Journal of Colloid and Interface Science*, vol. 255, pp. 119-128, 2002.
- [230] Q. Wu, Z. Wang, X. Kong, X. Gu, and G. Xue, "A facile strategy for controlling the self-assembly of nanocomposite particles based on colloidal steric stabilization theory," *Langmuir*, vol. 24, pp. 7778-7784, 2008.
- [231] D. V. Goia and E. Matijevic, "Preparation of monodispersed metal particles," *New Journal of Chemistry*, vol. 22, pp. 1203-1215, 1998.
- [232] cYtodiagnosics. Gold nanoparticles storage & handling - tech note: #101. 2012(1st April 2012). Available: [http://www.cytodiagnosics.com/pdf/Handling%20and%20Storage%20\(gold%20NPs\)%20-%20TECH%20NOTE%20101.pdf](http://www.cytodiagnosics.com/pdf/Handling%20and%20Storage%20(gold%20NPs)%20-%20TECH%20NOTE%20101.pdf)
- [233] W. Haiss, N. T. Thanh, J. Aveyard, and D. G. Fernig, "Determination of size and concentration of gold nanoparticles from UV-vis spectra," *Analytical Chemistry*, vol. 79, pp. 4215-4221, 2007.
- [234] N. G. Khlebtsov, "Determination of size and concentration of gold nanoparticles from extinction spectra," *Analytical Chemistry*, vol. 80, pp. 6620-6625, 2008.
- [235] B. E. A. Saleh and M. C. Teich, *Fundamentals of Photonics*. New York: John Wiley & Sons, 1991.
- [236] K. Lu, *Nanoparticulate Materials: Synthesis, Characterization, and Processing*. New Jersey: John Wiley & Sons, 2012.

Appendix A – General Information

A.1 Equations of Energy, E, Versus Wavelength, λ

Photon energy:

$$E(\text{J}) = E(\text{eV}) \times 1.602 \times 10^{-19} \text{ J},$$

where $1\text{eV} = 1.602 \times 10^{-19} \text{ J}$.

Energy E(J):

$$E = \hbar\omega = \frac{hc}{\lambda},$$

where $h = 6.634 \times 10^{-34} \text{ J}\cdot\text{s}$, is the Planck constant, $\hbar = \frac{h}{2\pi}$, is the reduced Planck constant,

$\omega = 2\pi c/\lambda$, is the angular frequency (1/s), $c = 2.998 \times 10^8 \text{ m/s}$, is the speed of light, and λ is the wavelength of light.

Reference:

- B. E. A. Saleh and M. C. Teich, *Fundamentals of Photonics*. New York: John Wiley & Sons, 1991.

A.2 Electron Configurations of Various Metals

Aluminum (Al): $1s^2 2s^2 p^6 \mathbf{3s^2 p^1}$

Nickel (Ni): $1s^2 2s^2 p^6 \mathbf{3s^2 p^6 d^8 4s^2}$

Copper (Cu): $1s^2 2s^2 p^6 \mathbf{3s^2 p^6 d^{10} 4s^1}$

Silver (Ag): $1s^2 2s^2 p^6 \mathbf{3s^2 p^6 d^{10} 4s^2 p^6 d^{10} 5s^1}$

Gold (Au): $1s^2 2s^2 p^6 \mathbf{3s^2 p^6 d^{10} 4s^2 p^6 d^{10} f^{14} 5s^2 p^6 d^{10} 6s^1}$

Note: letters and numbers in bold, highlight the valence electrons of each metal

Reference:

- Γ. Μανουσάκης, *Γενική και Ανόργανη Χημεία*. Εκδόσεις Αδερφών Κυριακίδη, 1999.

A.3 Mathematical Equations for Various Objects

Equilateral Triangle Area: $A_{\text{tri}} = \frac{1}{4} \sqrt{3} t^2$, where t is the triangle side length.

Sphere Surface Area and Volume: $S_{\text{sph}} = 4\pi r^2$, $V_{\text{sph}} = \frac{4}{3} \pi r^3$, where r is the sphere radius.

Cube Volume: $V_{\text{cube}} = b^3$, where b is the cube edge length.

Regular Tetrahedron Volume: $V_{\text{tetrah}} = \frac{1}{12} \sqrt{2} t^3$, where t is the tetrahedron side length.

Note: All the faces of a regular tetrahedron are congruent to an equilateral triangle.

Reference:

- <http://mathworld.wolfram.com/RegularTetrahedron.html>
- <http://mathworld.wolfram.com/EquilateralTriangle.html>

A.4 Chemical Formulas

Molar mass (MM) refers to the mass of 1 mole of any substance,

$$MM = \frac{m}{n},$$

where n is the number of atoms or molecules in moles (1 mole = 6.023×10^{23} atoms), and m is the mass (in grams) of the substance. Unit: **g/mol**

Molar concentration, or Molarity (M) of a solution is defined as the amount of solute, expressed in moles, per unit volume of solution, expressed in liters. Unit: **mol/L**

$$\text{Molarity (M)} = \frac{\text{moles of solute}}{\text{liters of solution}} = \frac{n}{V} = \frac{m}{MM \times V}$$

Reference:

- J. Olmsted and G. M. Williams, *Chemistry: The Molecular Science*. Iowa: Wm. C. Brown, 1997, pp. 81-142.

A.5 Centrifuge Parameters

Speed is the angular velocity of the rotor and is given in **rpm** (revolution per minute).

Centrifugal field is given by **rcf** (relative centrifugal force) which is expressed as numbers of times relative to earth's gravitational acceleration, g, where $g = 9.807 \text{ m/s}^2$. The two terms are correlated by:

$$\text{rcf} = 1.118 \times 10^{-5} (\text{rpm})^2 r,$$

where r is the radial distance from the center of rotation (in cm).

Reference:

- R. O. Okotore, "Centrifugation," in *Basic Separation Techniques in Biochemistry*, ed New Delhi: New Age International, 1998, pp. 9-21.

A.6 UV-vis Spectrophotometer

The UV-vis spectrophotometer is an instrument which measures the plasmon absorption bands at the wavelengths of ultraviolet to visible. The V-650 model is a double-beam spectrophotometer with a photomultiplier tube detector. It measures the intensity of light passing through a sample (I), and compares it to the initial intensity of light (I_0). The ratio I/I_0 is called transmittance, T , and is usually expressed as a percentage ($\%T = T \times 100$). The absorbance, A , is based on the transmittance:

$$A = \log_{10}(100/T).$$

Reference:

- U. Kreibig and M. Vollmer, *Optical Properties of Metal Clusters*. Berlin: Springer, 1995.

A.7 Scanning Electron Microscope (SEM)

SEM is a valuable tool for morphological studies, since it provides with high resolution images. It is the most mature and widely used imaging technique for characterizing NP size, shape arrangement, and degree of agglomeration. In SEM, an electron beam (5–30kV acceleration) is focused on the sample and the reflected electrons (back scattered) or ejected electrons from the sample are collected for imaging. SEM serves as a quick and convenient technique for NP size, shape and arrangement analysis because of its widespread availability and ease of sample preparation. However, SEM can only be regarded as a quick but qualitative tool. Quantitative or statistical evaluation of NPs is generally not accurate.

Reference:

- K. Lu, *Nanoparticulate Materials: Synthesis, Characterization, and Processing*. New Jersey: John Wiley & Sons, 2012.

Appendix B – Parameter Files for DDSCAT Software

B.1 Parameter File for DDSCAT6.1

Example of an Au cube with $b = 120\text{nm}$ ($r_{\text{eff}} = 74.4\text{nm}$), $d = 2.5\text{nm}$ ($120/2.5 = 48$), error: 10^{-5} , ETASCA: 10, averaged polarization (IORTH = 2), and no orientation.

```
' ===== Parameter file ====='  
'**** PRELIMINARIES ****'  
'NOTORQ' = CMTORQ*6 (DOTORQ, NOTORQ) -- either do or skip torque calculations  
'PBCGST' = CMDSOL*6 (PBCGST, PETRKP) -- select solution method  
'GPFAFT' = CMETHD*6 (GPFAFT, FFTWJ, CONVEX)  
'LATDR' = CALPHA*6 (LATDR, SCLDR)  
'NOTBIN' = CBINFLAG (ALLBIN, ORIBIN, NOTBIN)  
'NOTCDF' = CNETFLAG (ALLCDF, ORICDF, NOTCDF)  
'RCTNGL' = CSHAPE*6 (FRMFIL, ELLIPS, CYLNDR, RCTNGL, HEXGON, TETRAH, UNICYL, UNIELL)  
48 48 48 = shape parameters PAR1, PAR2, PAR3  
1 = NCOMP = number of dielectric materials  
'TABLES' = CDIEL*6 (TABLES, H2OICE, H2OLIQ; if TABLES, then filenames  
follow...)  
'gold133.tab' = name of file containing dielectric function  
'**** CONJUGATE GRADIENT DEFINITIONS ****'  
0 = INIT (TO BEGIN WITH |X0> = 0)  
1.00e-5 = TOL = MAX ALLOWED (NORM OF |G>=AC|E>-ACA|X>)/(NORM OF AC|E>)  
'**** Angular resolution for calculation of <cos>, etc. ****'  
10 = ETASCA (number of angles is proportional to [(3+x)/ETASCA]^2 )  
'**** Wavelengths (micron) ****'  
0.300 0.750 38 'LIN' = wavelengths (first,last,how many,how=LIN,INV,LOG)  
'**** Effective Radii (micron) ****'  
0.0744 0.0744 1 'LIN' = eff. radii (first, last, how many, how=LIN,INV,LOG)  
'**** Define Incident Polarizations ****'  
(0,0) (1.,0.) (0.,0.) = Polarization state e01 (k along x axis)  
2 = IORTH (=1 to do only pol. state e01; =2 to also do orth. pol. state)  
0 = IWRKSC (=0 to suppress, =1 to write ".sca" file for each target orient.  
'**** Prescribe Target Rotations ****'  
0. 0. 1 = BETAMI, BETAMX, NBETA (beta=rotation around a1)  
0. 0. 1 = THETMI, THETMX, NTHETA (theta=angle between a1 and k)  
0. 0. 1 = PHIMIN, PHIMAX, NPHI (phi=rotation angle of a1 around k)  
'**** Specify first IWAV, IRAD, IORI (normally 0 0 0) ****'  
0 0 0 = first IWAV, first IRAD, first IORI (0 0 0 to begin fresh)  
'**** Select Elements of S_ij Matrix to Print ****'  
6 = NSMELTS = number of elements of S_ij to print (not more than 9)  
11 12 21 22 31 41 = indices ij of elements to print  
'**** Specify Scattered Directions ****'  
0. 0. 180. 10 = phi, thetan_min, thetan_max, dtheta (in degrees) for plane A  
90. 0. 180. 10 = phi, ... for plane B
```

B.2 Parameter File for DDSCAT7.0

Example of a complex nanostructure: Au cube combined with 16 Ag spheres (y - z plane).

```
' ===== Parameter file for v7.0.7 ====='  
'**** Preliminaries ****'  
'NOTORQ' = CMTORQ*6 (NOTORQ, DOTORQ) -- either do or skip torque calculations  
'PBCGS2' = CMDSOL*6 (PBCGS2, PBCGST, PETRKP) -- select solution method  
'GPFAFT' = CMDFFT*6 (GPFAFT, FFTMKL)  
'GKDLDR' = CALPHA*6 (GKDLDR, LATTDI)  
'NOTBIN' = CBINFLAG (NOTBIN, ORIBIN, ALLBIN)  
'**** Initial Memory Allocation ****'  
105 85 85 = dimensioning allowance for target generation  
'**** Target Geometry and Composition ****'  
'FROM_FILE' = CSHAPE*9 shape directive  
'shape.dat' = file containing dipoles  
2          = NCOMP = number of dielectric materials  
'gold133.tab' = file with refractive index 1  
'silver15nmPlkmed133.tab' = file with refractive index 2  
'**** Error Tolerance ****'  
1.00e-5 = TOL = MAX ALLOWED (NORM OF |G>=AC|E>-ACA|X>)/(NORM OF AC|E>)  
'**** Interaction cutoff parameter for PBC calculations ****'  
0 = GAMMA (1e-2 is normal, 3e-3 for greater accuracy)  
'**** Angular resolution for calculation of <cos>, etc. ****'  
10      = ETASCA (number of angles is proportional to [(3+x)/ETASCA]^2 )  
'**** Wavelengths (micron) ****'  
0.300 0.750 38 'LIN' = wavelengths (first,last,how many,how=LIN,INV,LOG)  
'**** Effective Radii (micron) **** '  
0.07756 0.07756 1 'LIN' = aeff (first,last,how many,how=LIN,INV,LOG)  
'**** Define Incident Polarizations ****'  
(0,0) (1.,0.) (0.,0.) = Polarization state e01 (k along x axis)  
2 = IORTH (=1 to do only pol. state e01; =2 to also do orth. pol. state)  
'**** Specify which output files to write ****'  
0 = IWRKSC (=0 to suppress, =1 to write ".sca" file for each target orient.  
0 = IWRPOL (=0 to suppress, =1 to write ".pol" file for each (BETA,THETA)  
'**** Prescribe Target Rotations ****'  
0.    0.    1 = BETAMI, BETAMX, NBETA (beta=rotation around a1)  
0.    0.    1 = THETMI, THETMX, NTHETA (theta=angle between a1 and k)  
0.    0.    1 = PHIMIN, PHIMAX, NPHI (phi=rotation angle of a1 around k)  
'**** Specify first IWAV, IRAD, IORI (normally 0 0 0) ****'  
0 0 0    = first IWAV, first IRAD, first IORI (0 0 0 to begin fresh)  
'**** Select Elements of S_ij Matrix to Print ****'  
4      = NSMELTS = number of elements of S_ij to print (not more than 9)  
11 12 21 22 = indices ij of elements to print  
'**** Specify Scattered Directions ****'  
'LFRAME' = CMDFRM (LFRAME, TFRAME for Lab Frame or Target Frame)  
1 = NPLANES = number of scattering planes  
0.    0. 180. 10 = phi, thetan_min, thetan_max, dtheta (in deg) for plane 1
```

Appendix C – Bilayer Shell Aggregate Results (J&C)

Table C.1: Shape parameters of bilayer shell aggregates ($R \approx 30, 50\text{nm}$) with various small nanosphere radii, r , edge-to-edge distances, ds , and $dl = 0\text{nm}$ ($R_{\text{inner}} = R_{\text{real}} - 2r_{\text{inner}} - dl$)

	R (nm)	r (nm)	R_{real} (nm)	r_{real} (nm)	ds (nm)	n_{sph}	R_{inner} (nm)	r_{inner} (nm)	ds (nm)	n_{sph}	
A	30	5 ($d = 1\text{nm}$)	29.09	4.88	0.0–0.82	66	17.61	5.74	0.0	18	
B		dense	5 ($d = 0.5\text{nm}$)	29.555	4.88	0.0–0.82	66	18.075	5.74	0.0	18
C	50	5	49.08	5.00	2.42–2.85	162	39.08	5.00	3.66–4.80	66	
D	50	5	51.02	6.21	0.0–0.43	162	37.36	6.83	0.0–1.145	66	
E		dense	7.5	50.02	8.19	0.0–1.375	66	30.12	9.95	0.0	18
F			10	50.17	10.93	0.0	42	34.86	7.65	0.0	18

Table C.2: Extinction peak characteristics and number of dipoles for bilayer shell aggregates with $R \approx 30\text{nm}$, and $R \approx 50\text{nm}$

	R (nm)	r (nm)	λ_{max} (nm)	Q'_{max}	N	N_{sph}	
A	30	5 ($d = 1\text{nm}$)	542.5	3.16	82259	45900	
B		dense	5 ($d = 0.5\text{nm}$)	541	3.14	660411	370218
C	50	5	554	6.05	425951	119216	
D	50	5	575	5.07	467079	247818	
E		dense	7.5	560	5.37	391801	224916
F			10	569	5.75	394253	263256

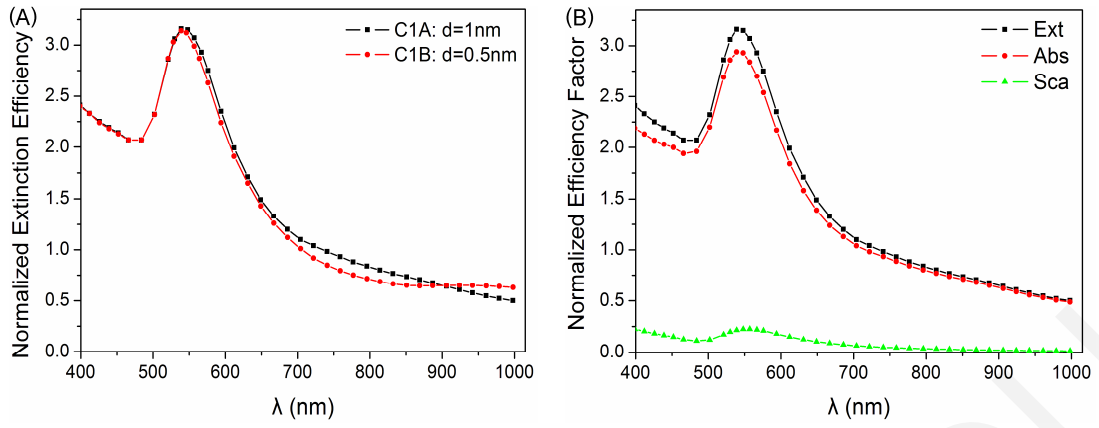


Figure C.1: (A) Normalized extinction spectra of densely-packed bilayer shell aggregates having $R \approx 30\text{nm}$, $r \approx 5\text{nm}$, and various interdipole separations, d . (B) Normalized efficiency factors of bilayer shell aggregate with $R \approx 30\text{nm}$, $r \approx 5\text{nm}$, and $d = 1\text{nm}$ (C1A).

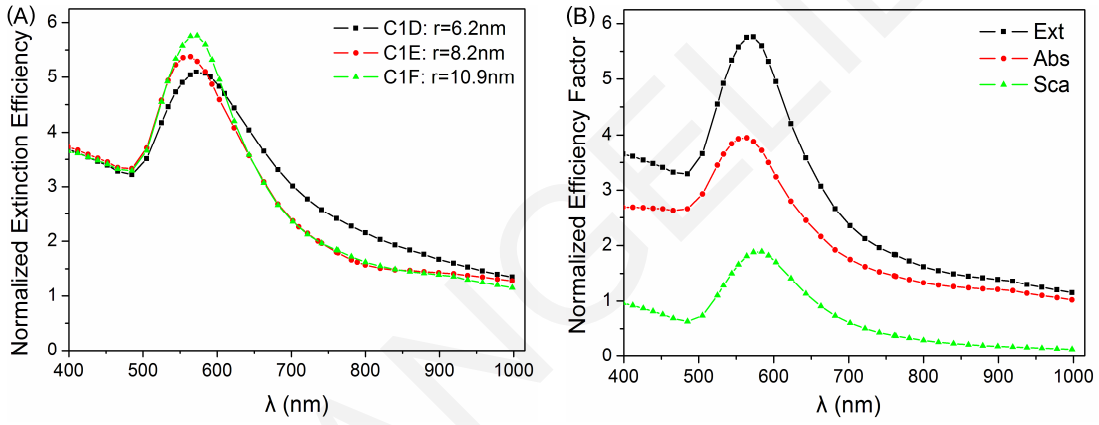


Figure C.2: (A) Normalized extinction spectra of densely-packed bilayer shell aggregates having $R \approx 50\text{nm}$, $d = 1\text{nm}$, and various radii, r . (B) Normalized efficiency factors of bilayer shell aggregate with $R \approx 50\text{nm}$ and $r = 8.2\text{nm}$ (C1E).

Table C.3: Shape parameters of bilayer shell aggregates ($R \approx 70\text{nm}$) with various small nanosphere radii, r , and edge-to-edge distances, ds ($R_{\text{inner}} = R_{\text{real}} - 2r_{\text{inner}} - dl$)

	R (nm)	r (nm)	R_{real} (nm)	r_{real} (nm)	ds (nm)	n_{sph}	R_{inner} (nm)	r_{inner} (nm)	ds (nm)	dl (nm)	n_{sph}
A	70 dense	5	71.03	6.37	0.0–4.74	258	60.25	5.39	0.0–4.01	0	258
B		7.5	70.06	8.55	0.0–0.59	162	52.12	8.97	0.0–1.505		66
C		12.5	72.12	15.58	0.0	42	48.39	11.86	0.0		18
D		12.5	72.01	15.08	1.0, $dl = 0\text{nm}$	42	49.29	11.36	1.0	0	18
E		12.5	72.01	15.08	1.0, $dl = 1\text{nm}$	42	49.05	10.98	1.0	1	18

Table C.4: Extinction peak characteristics and number of dipoles for bilayer shell aggregates with $R \approx 70\text{nm}$

	R (nm)	r (nm)	λ_{max} (nm)	Q'_{max}	N	N_{sph}
A	70 dense	5	583	6.82	1294275	440664
B		7.5	596	6.44	1221881	624642
C		12.5	595	6.155	1142249	790578
D		12.5	584, 691	6.38, 5.81	1106981	714210
E		12.5	584, 686	6.46, 5.70	1106981	702792

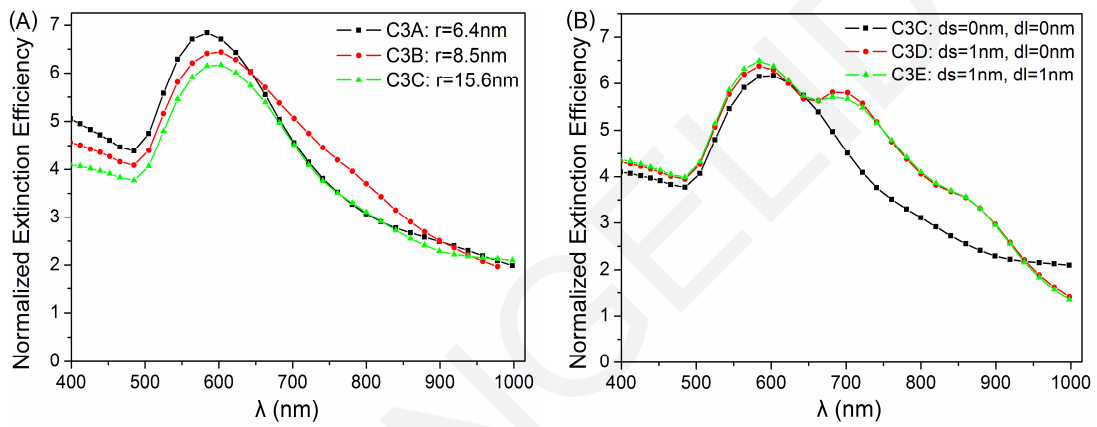


Figure C.3: Normalized extinction spectra of densely-packed bilayer shell aggregates having $R \approx 70\text{nm}$, $d = 1\text{nm}$, and various (A) radii, r , and (B) distances, ds .

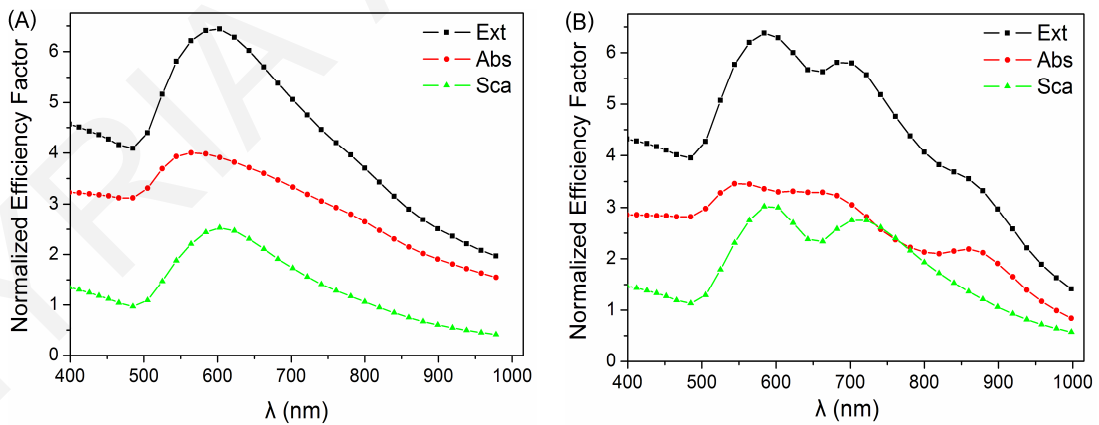


Figure C.4: Normalized efficiency factors of bilayer shell aggregates having $R \approx 70\text{nm}$, (A) $r = 8.5\text{nm}$ (C3B), and (B) $r \approx 15\text{nm}$, $ds = 1\text{nm}$, and $dl = 0\text{nm}$ (C3D).

Appendix D – Efficiency Factors of Various Classical Nanoparticles (J&C)

D.1 Nanoshells

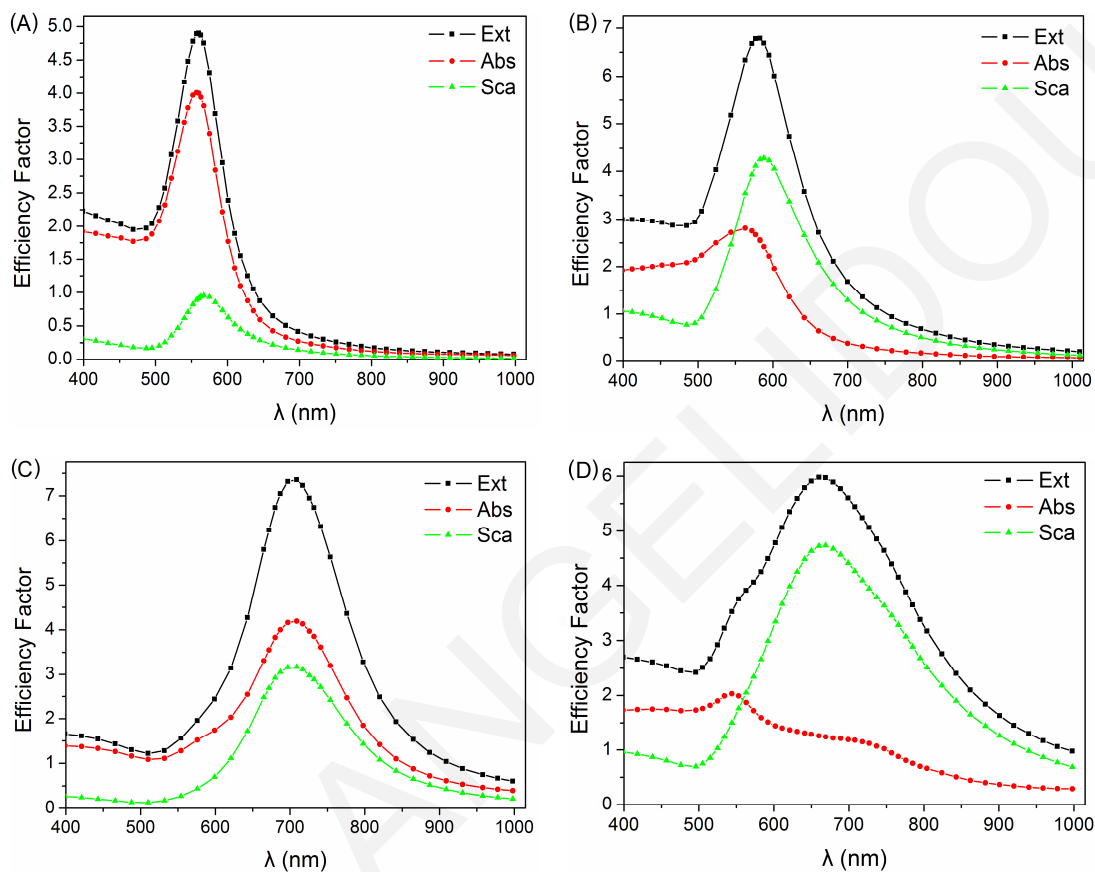
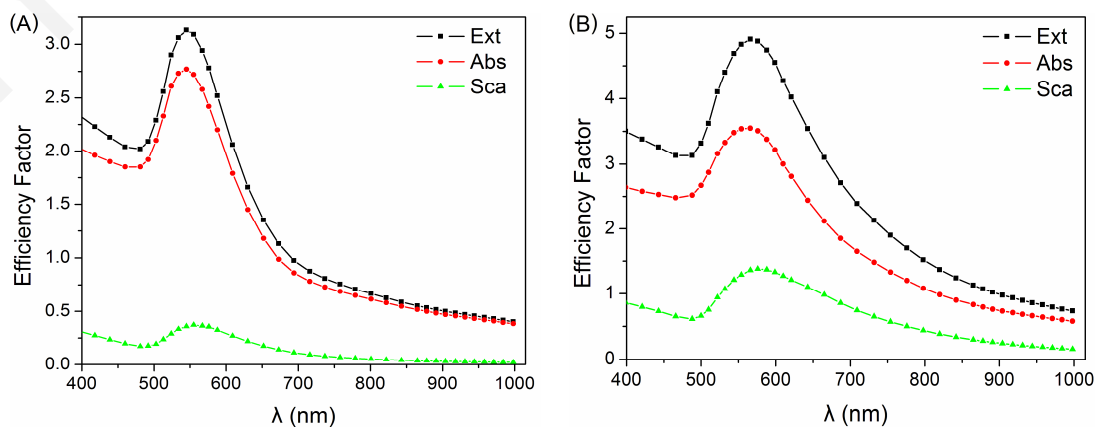


Figure D.1: Efficiency factors of nanoshells having (A) $R = 30\text{nm}$, shell = 15nm , ($R_c/R = 0.5$), (B) $R = 50\text{nm}$, shell = 30nm , ($R_c/R = 0.40$), (C) $R = 50\text{nm}$, shell = 10nm , ($R_c/R = 0.8$), and (D) $R = 70\text{nm}$, shell = 25nm , ($R_c/R \approx 0.64$).

D.2 Spherical Aggregates



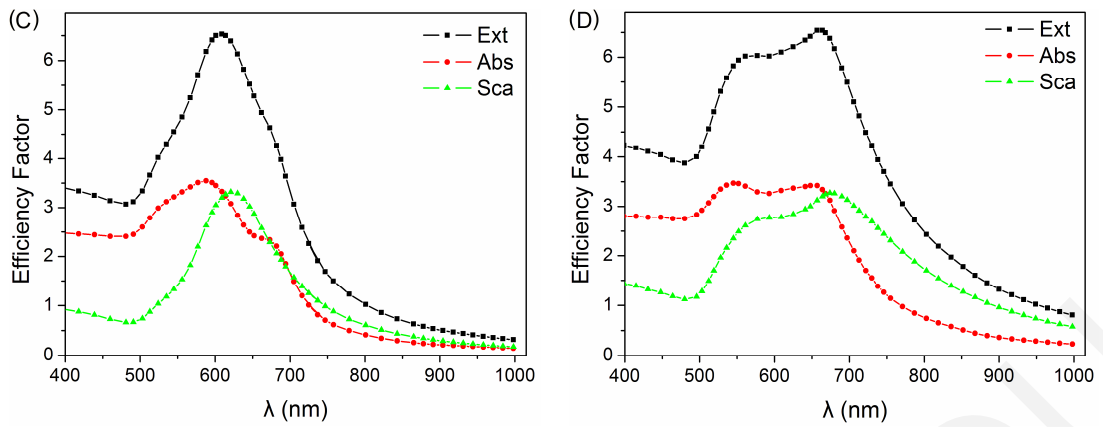


Figure D.2: Efficiency factors of spherical aggregates having (A) $R \approx 30\text{nm}$, $r = 5\text{nm}$, (T1A), (B) $R \approx 50\text{nm}$, $r = 5\text{nm}$, (T1C), (C) $R \approx 50\text{ nm}$, $r = 15\text{nm}$, (T1G), and (D) $R \approx 70\text{nm}$, $r = 12.5\text{nm}$, (T1I).

D.3 Monolayer Shell Aggregates of Various Cores/Spheres

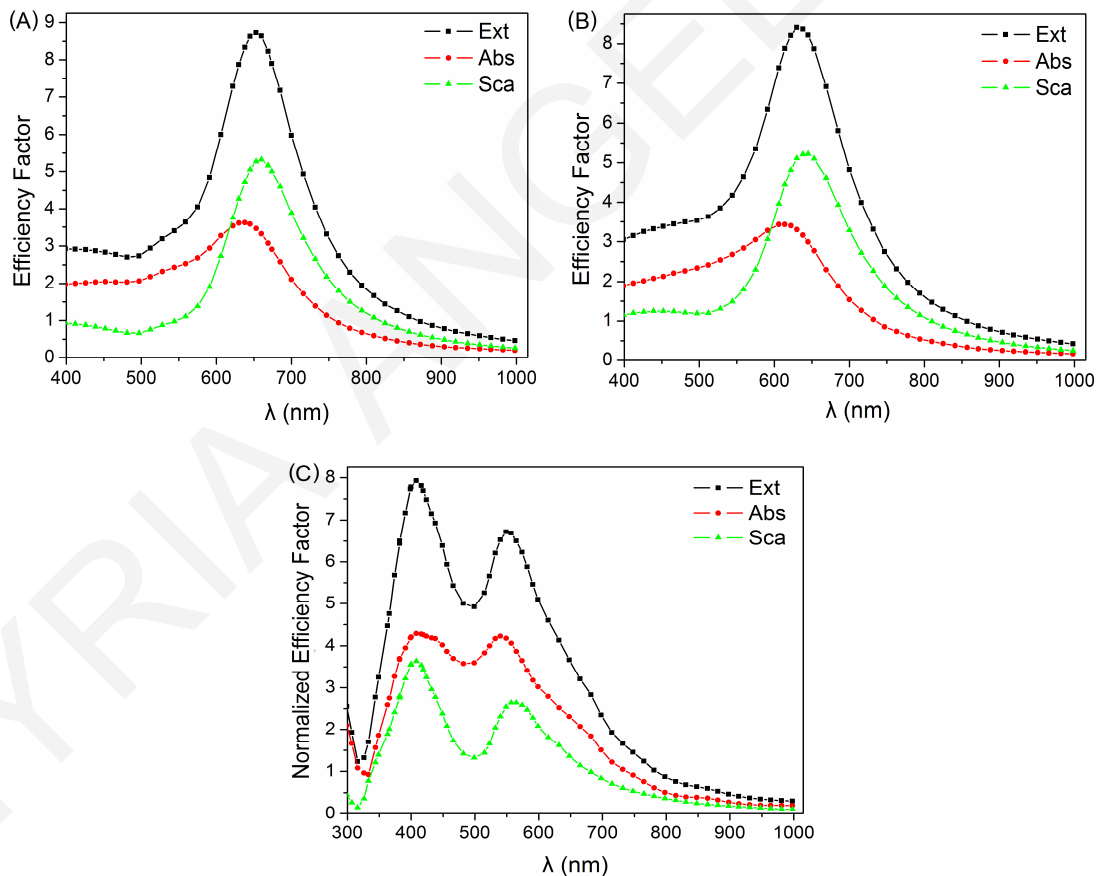


Figure D.3: Efficiency factors of monolayer shell aggregate ($R \approx 50\text{nm}$, $r = 12.5\text{nm}$ and $ds = 1\text{nm}$) of (A) gold/gold, (B) silver/gold, and (C) water/silver – core/spheres.

Appendix E – Efficiency Factors of Various Simple Nanostructures (Palik)

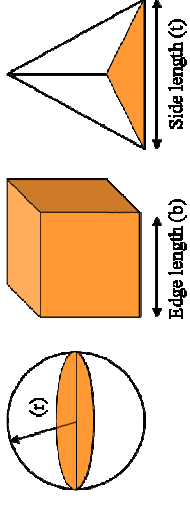
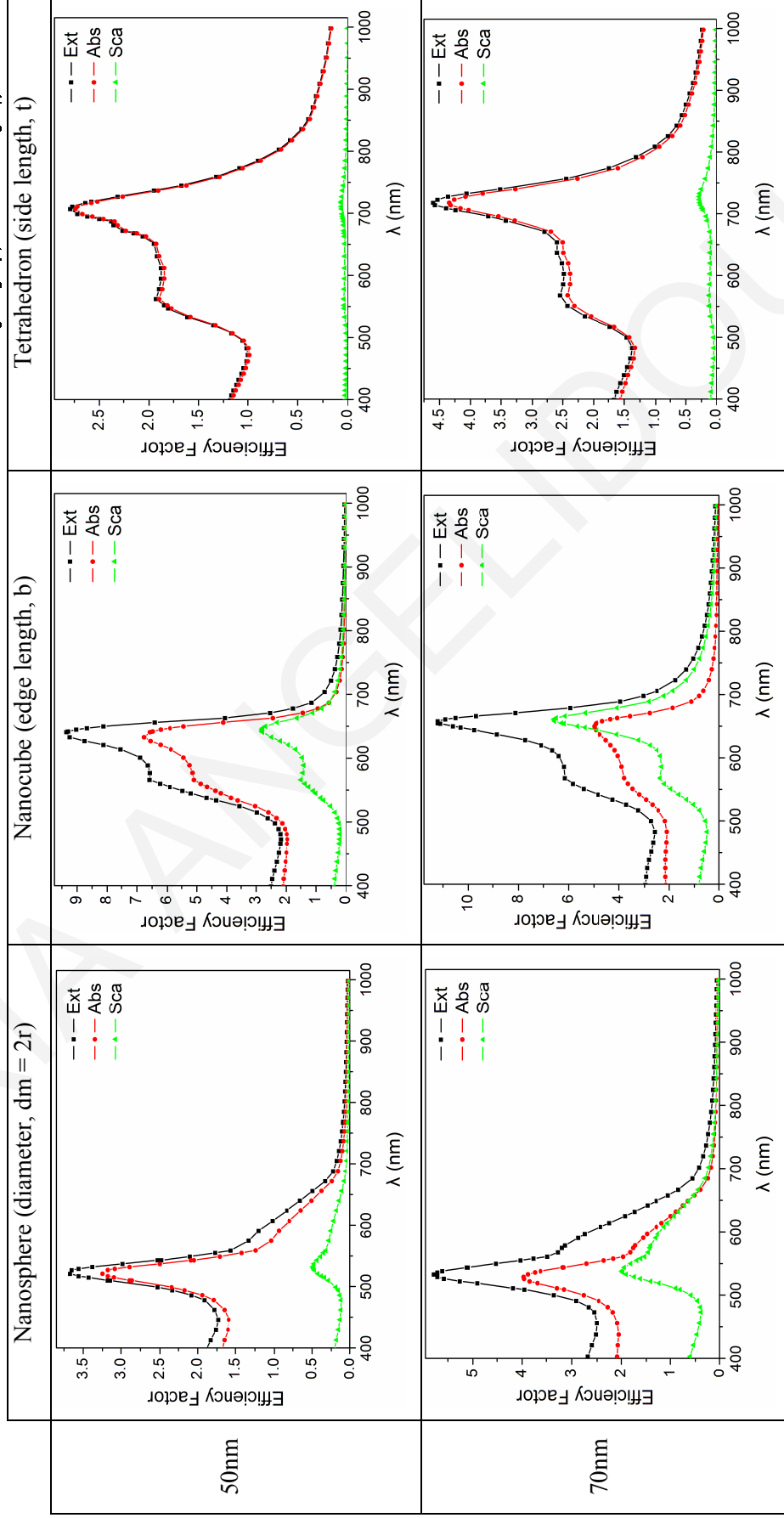
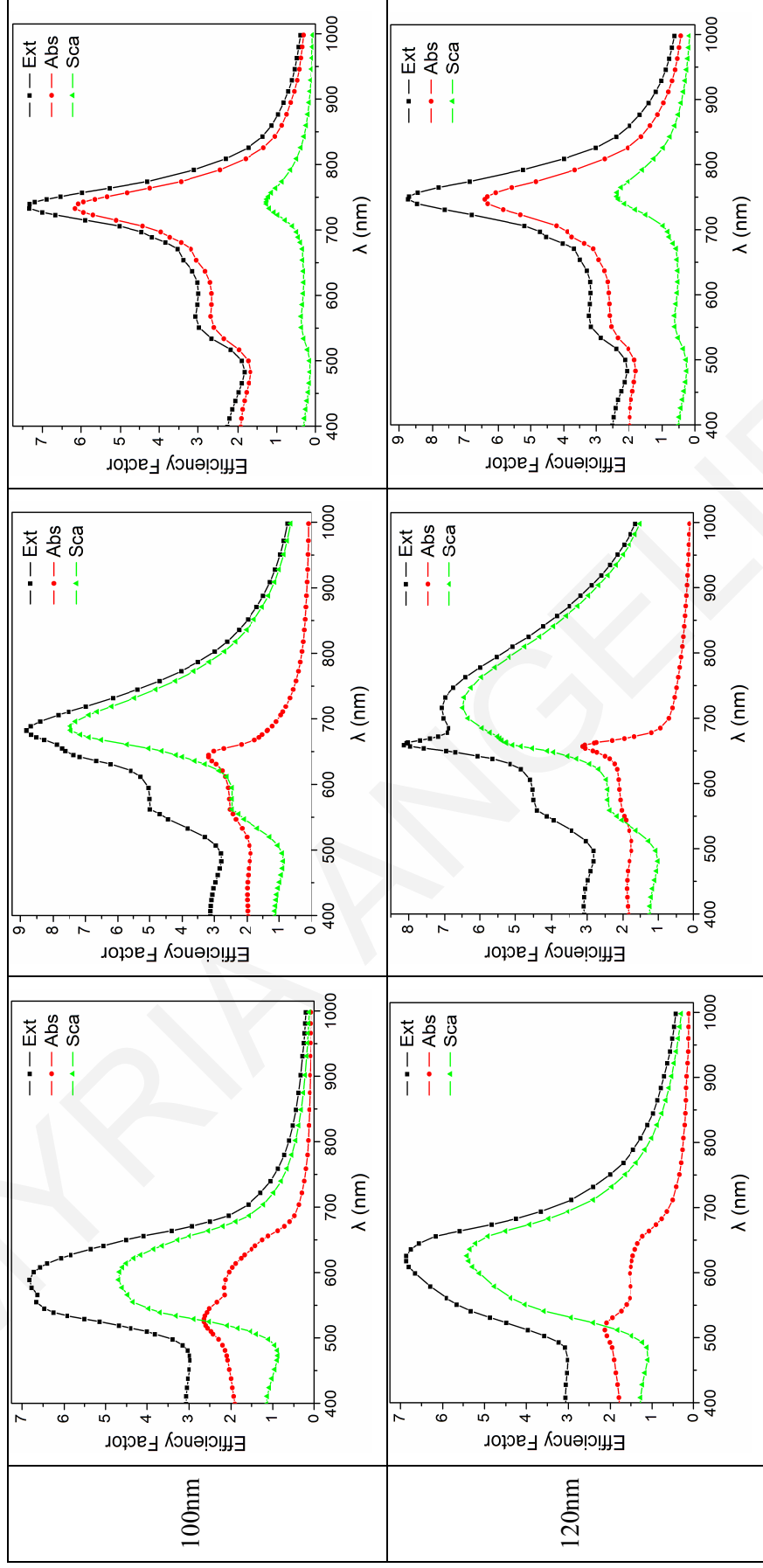


Table E.1: Gold (Au) Nanostructures





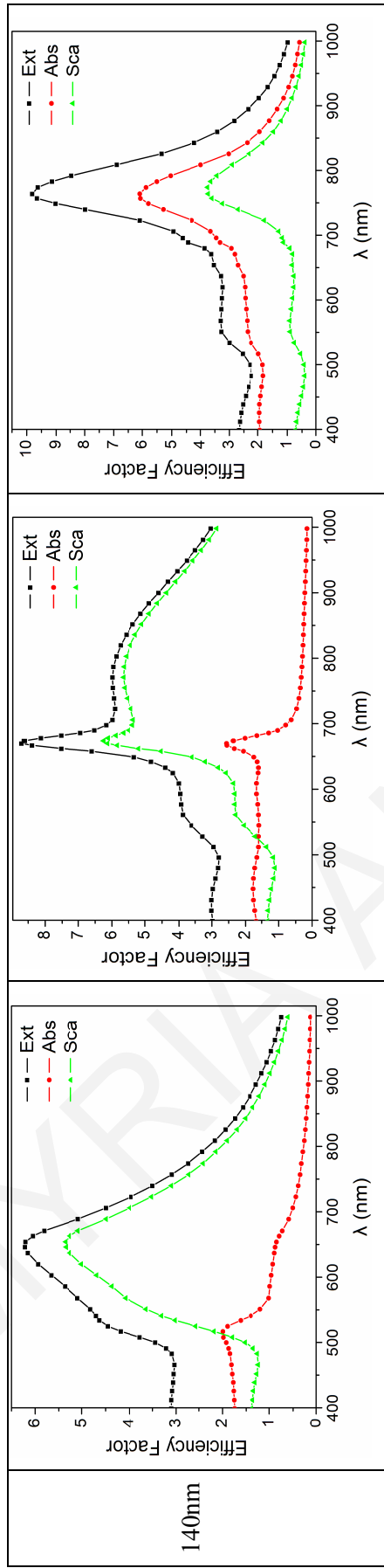
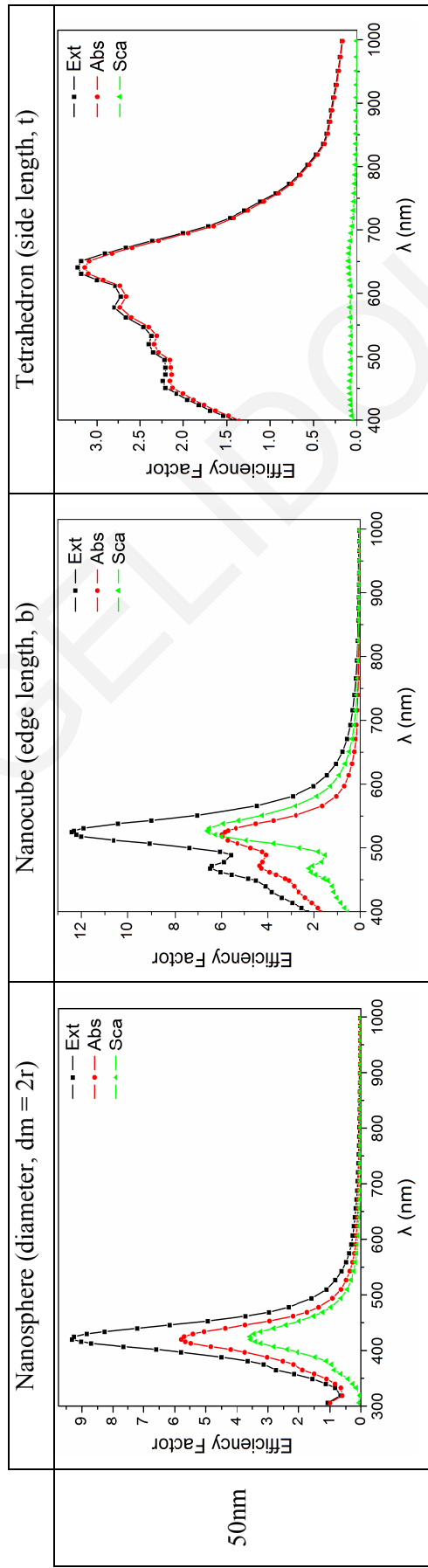
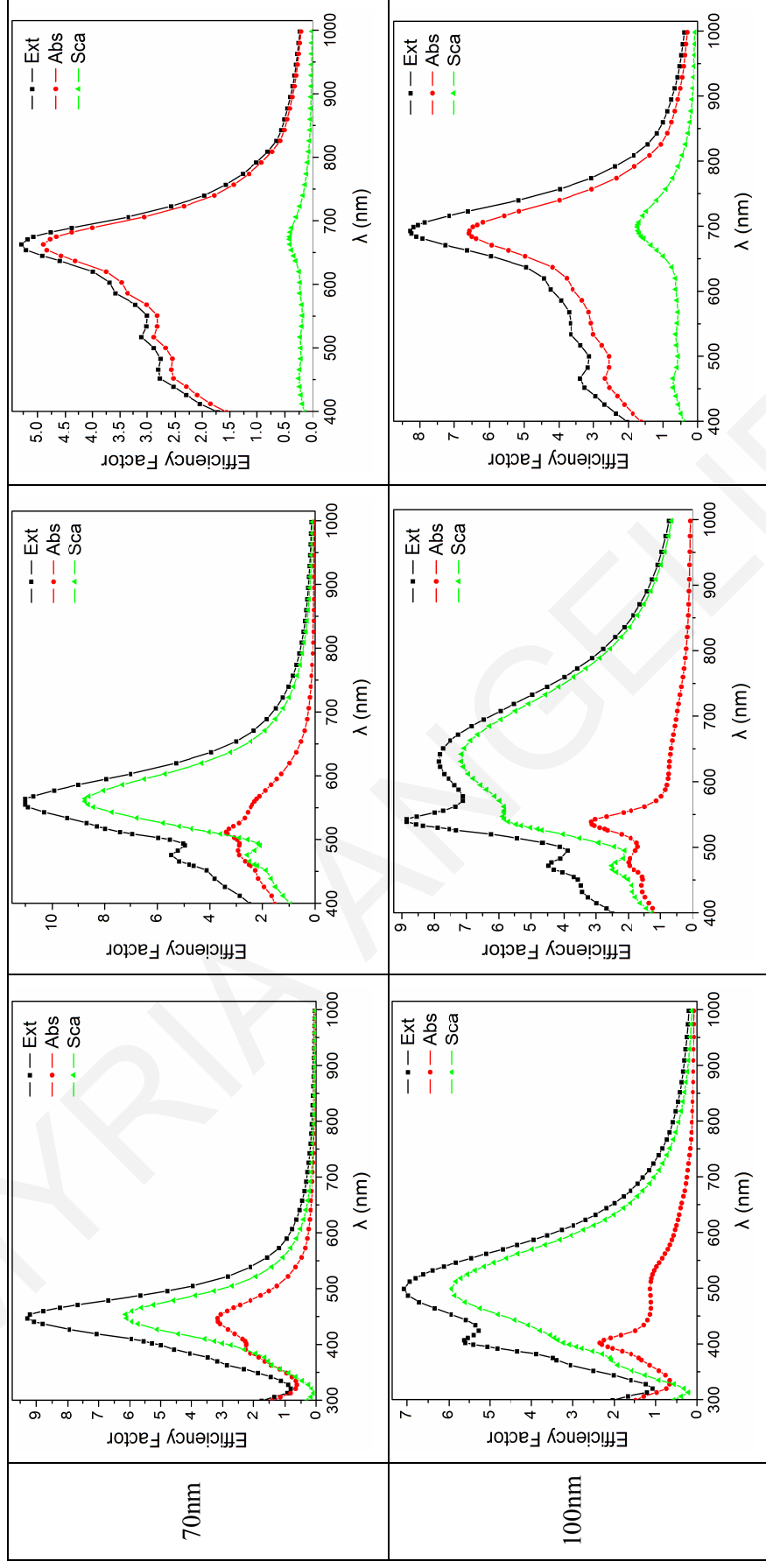


Table E.2: Silver (Ag) Nanostructures





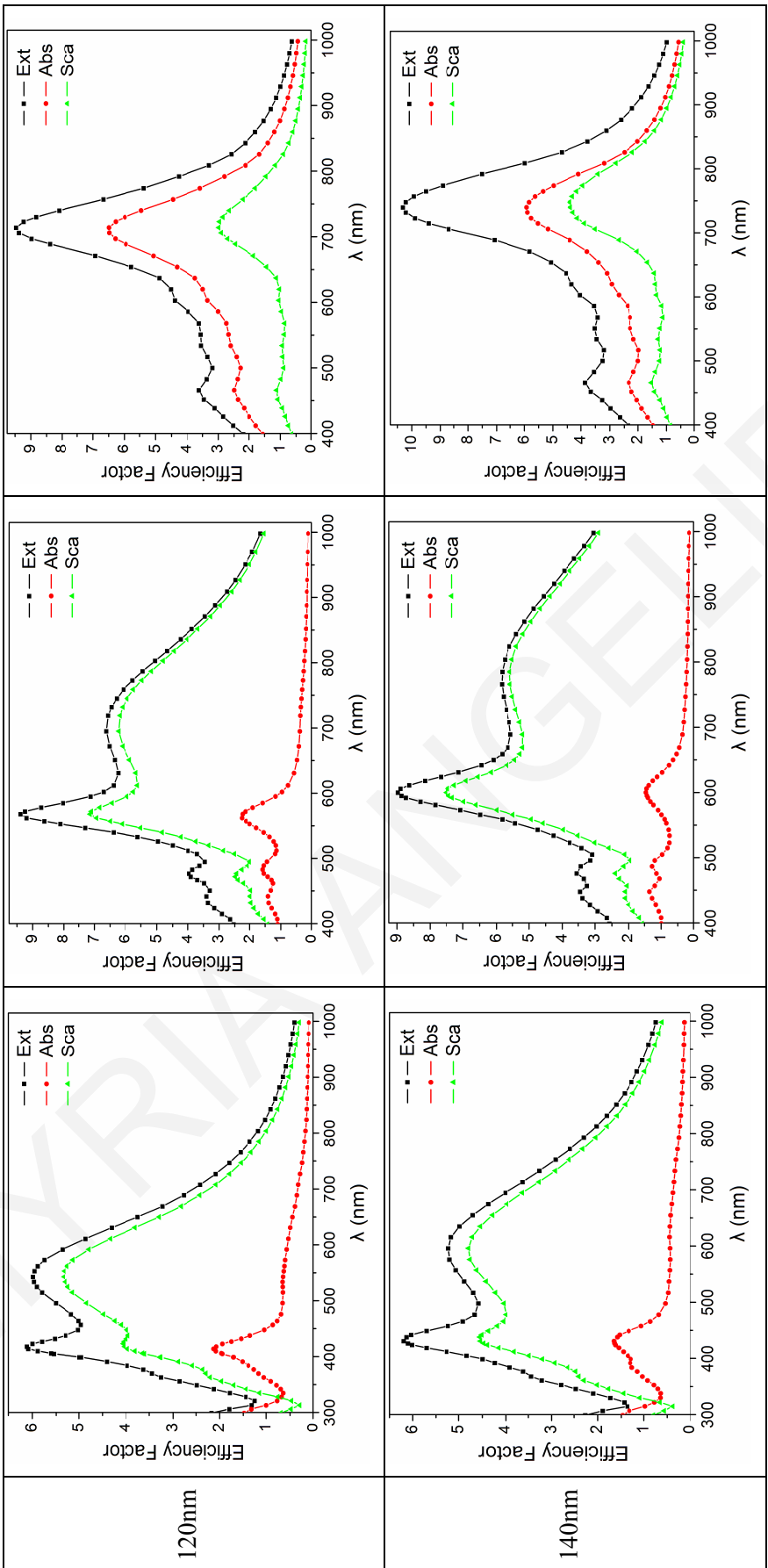
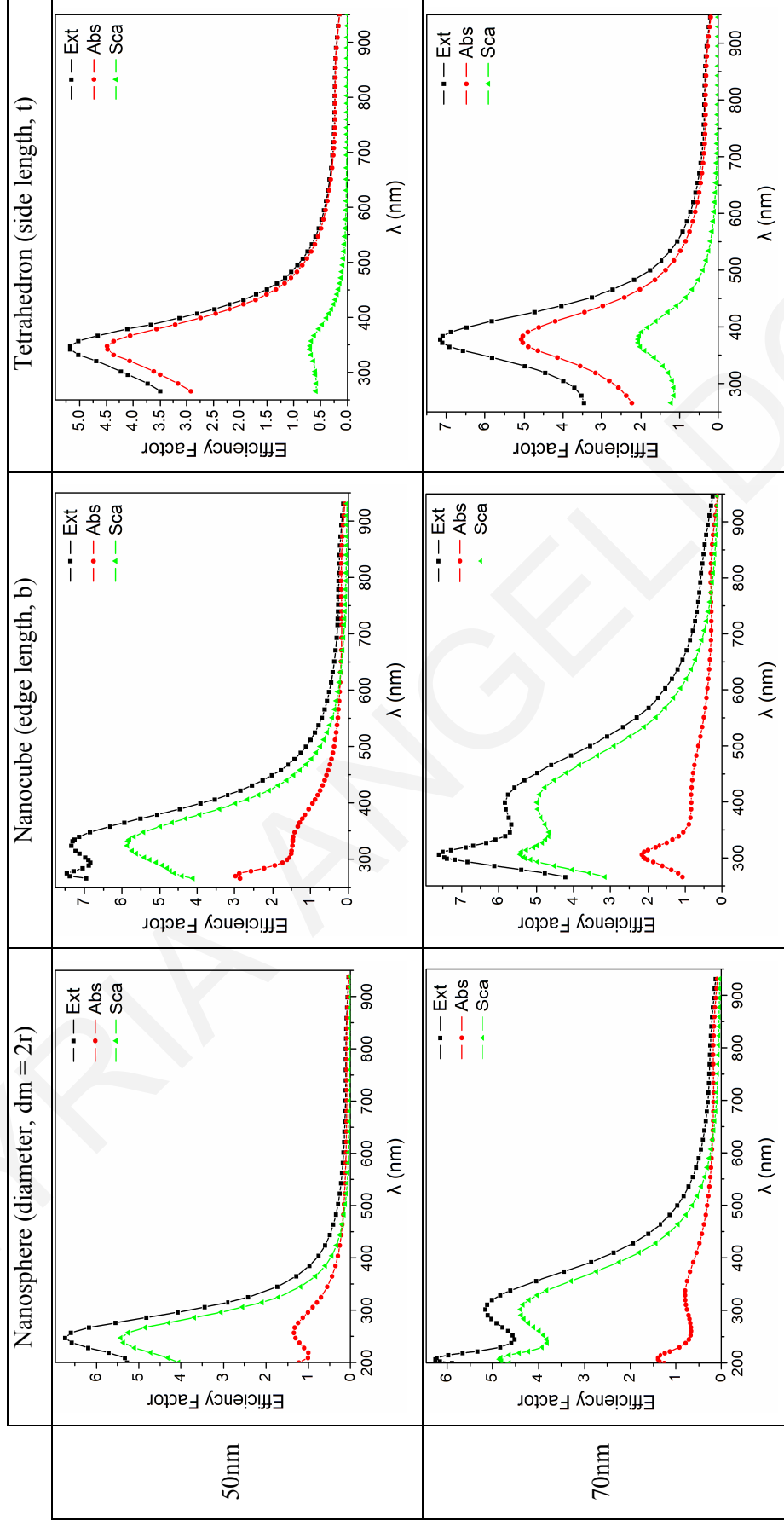
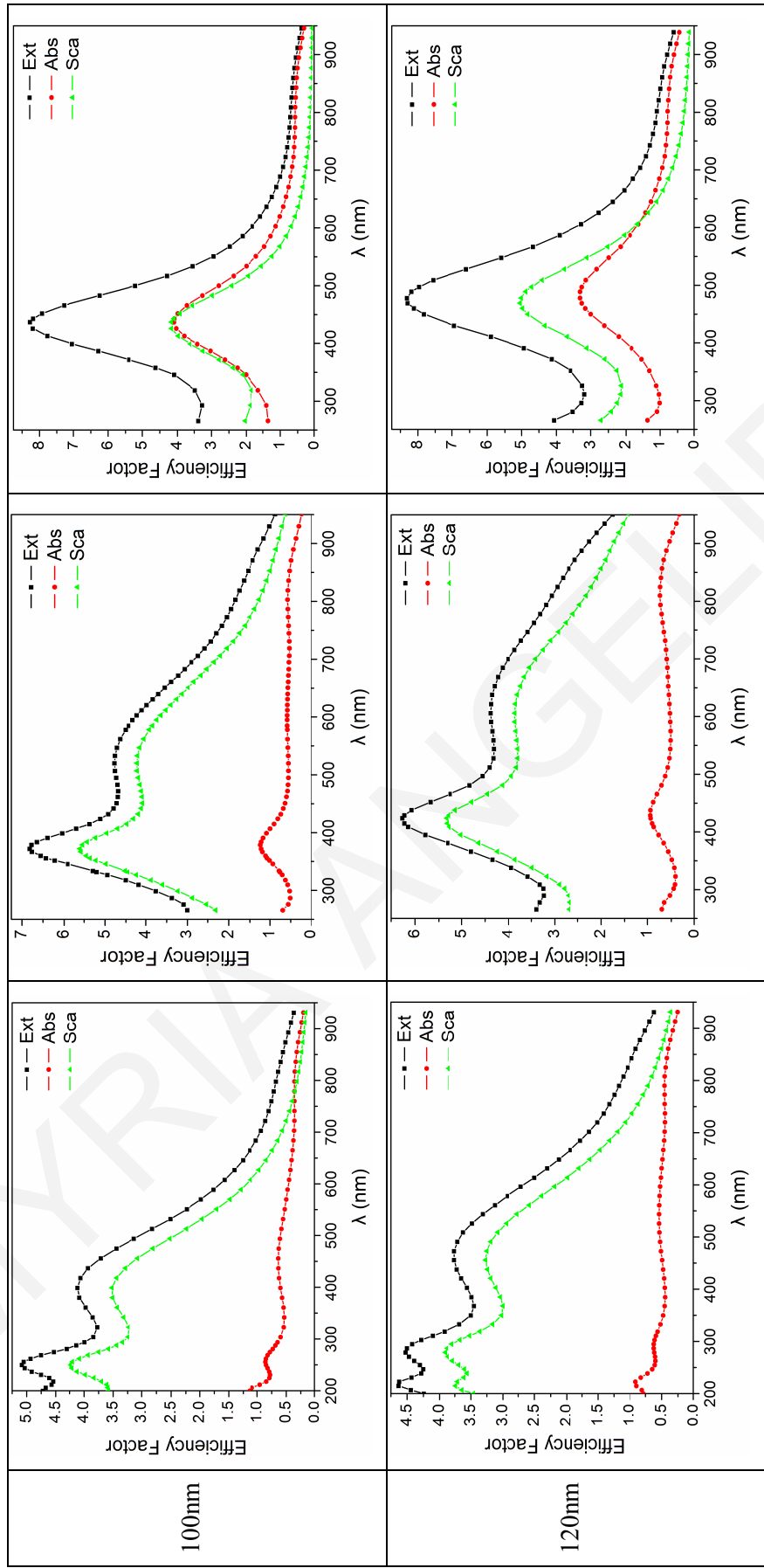


Table E.3: Aluminum (Al) Nanostructures





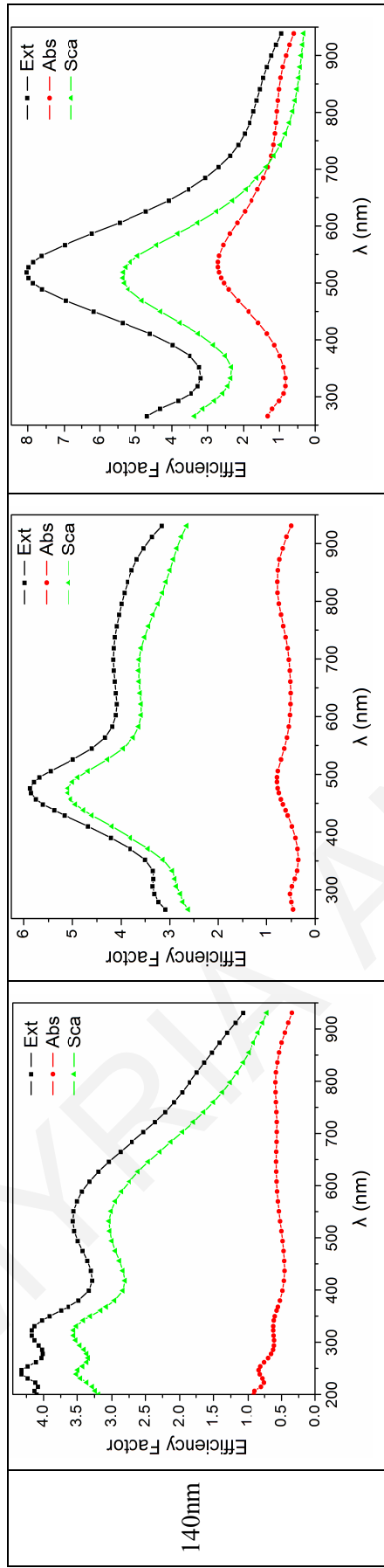
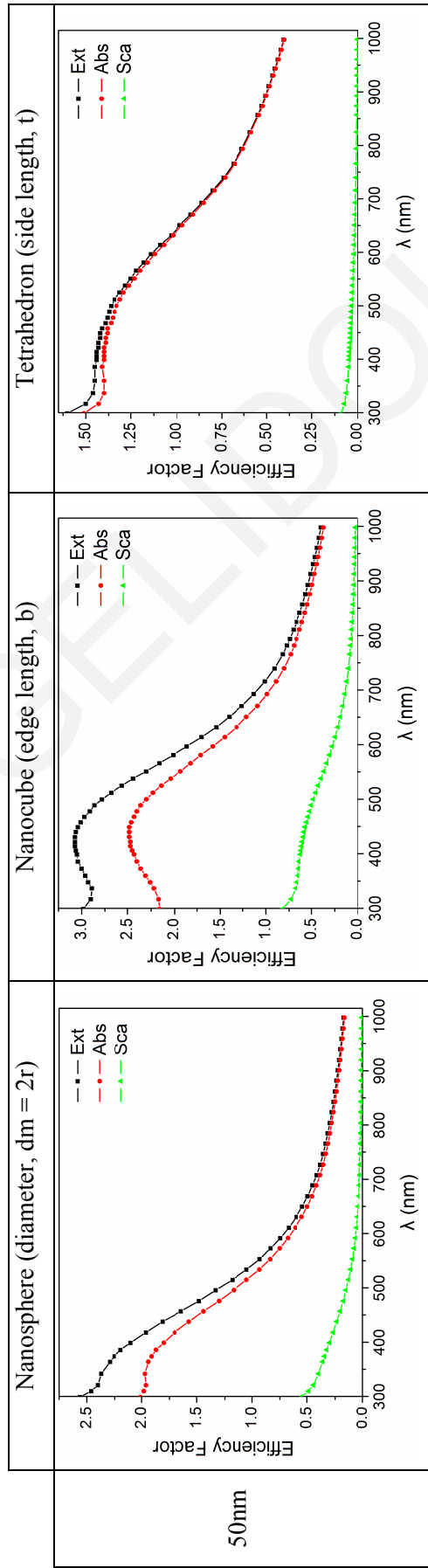
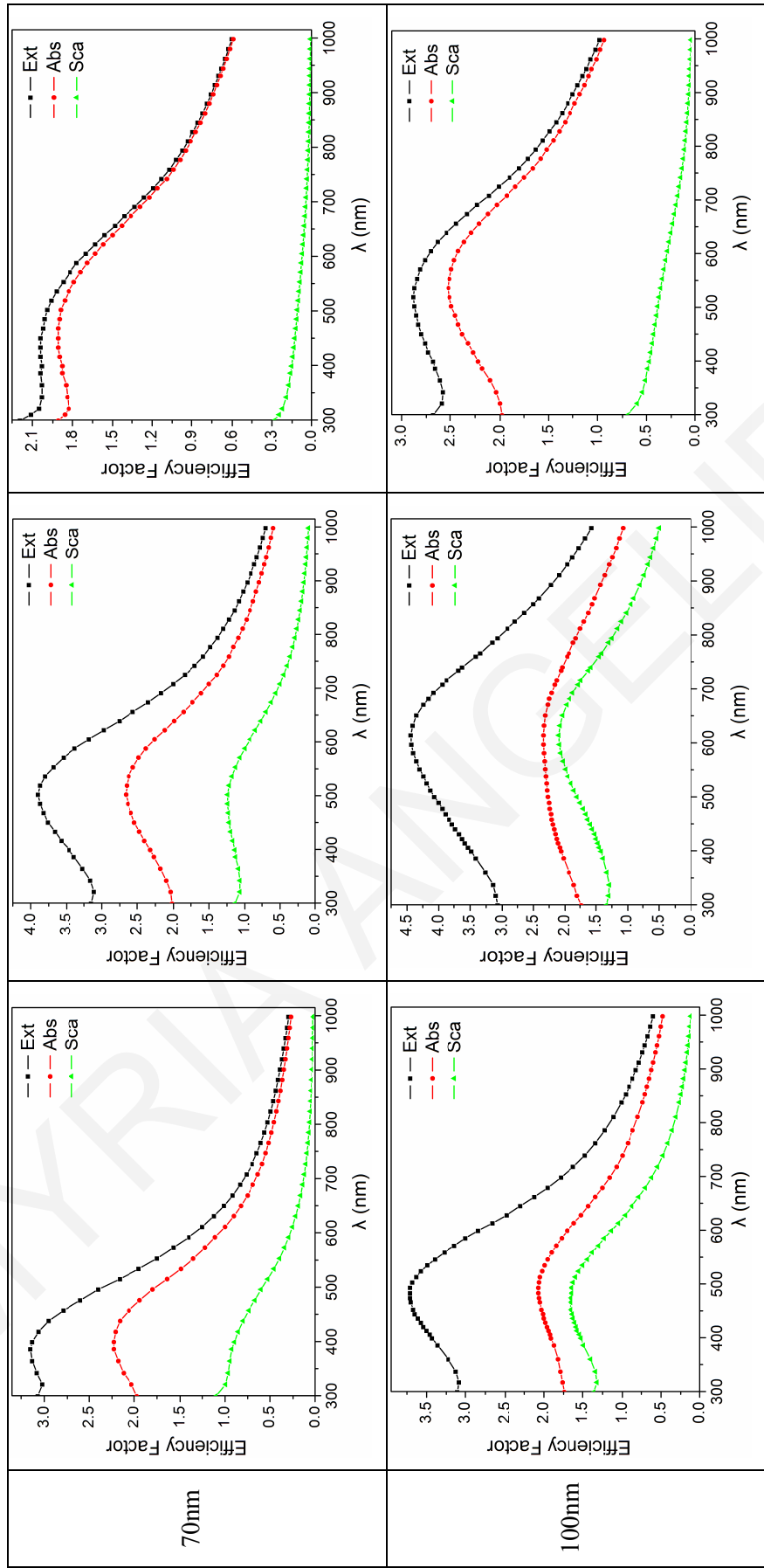


Table E.4: Nickel (Ni) Nanostructures





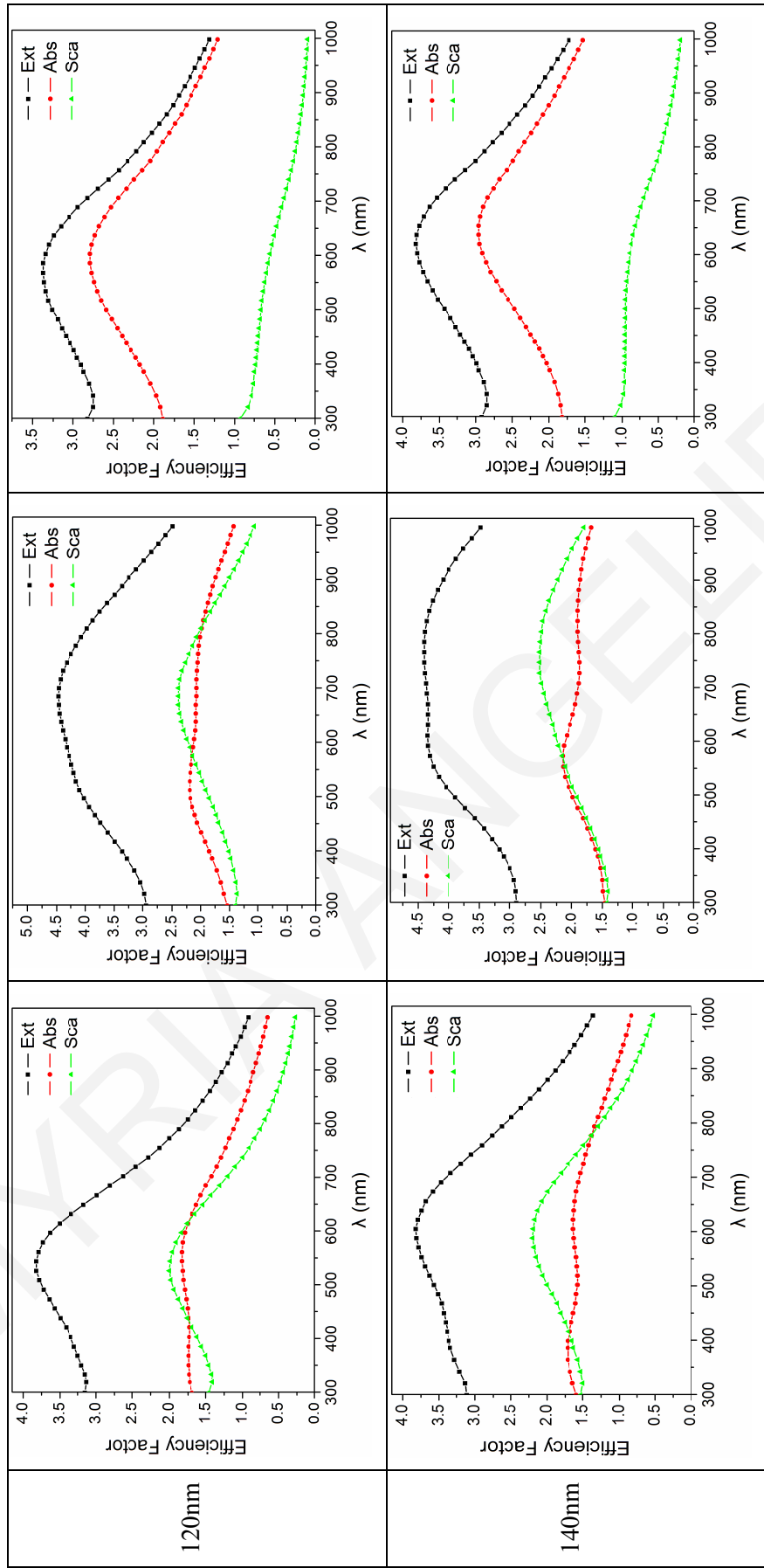
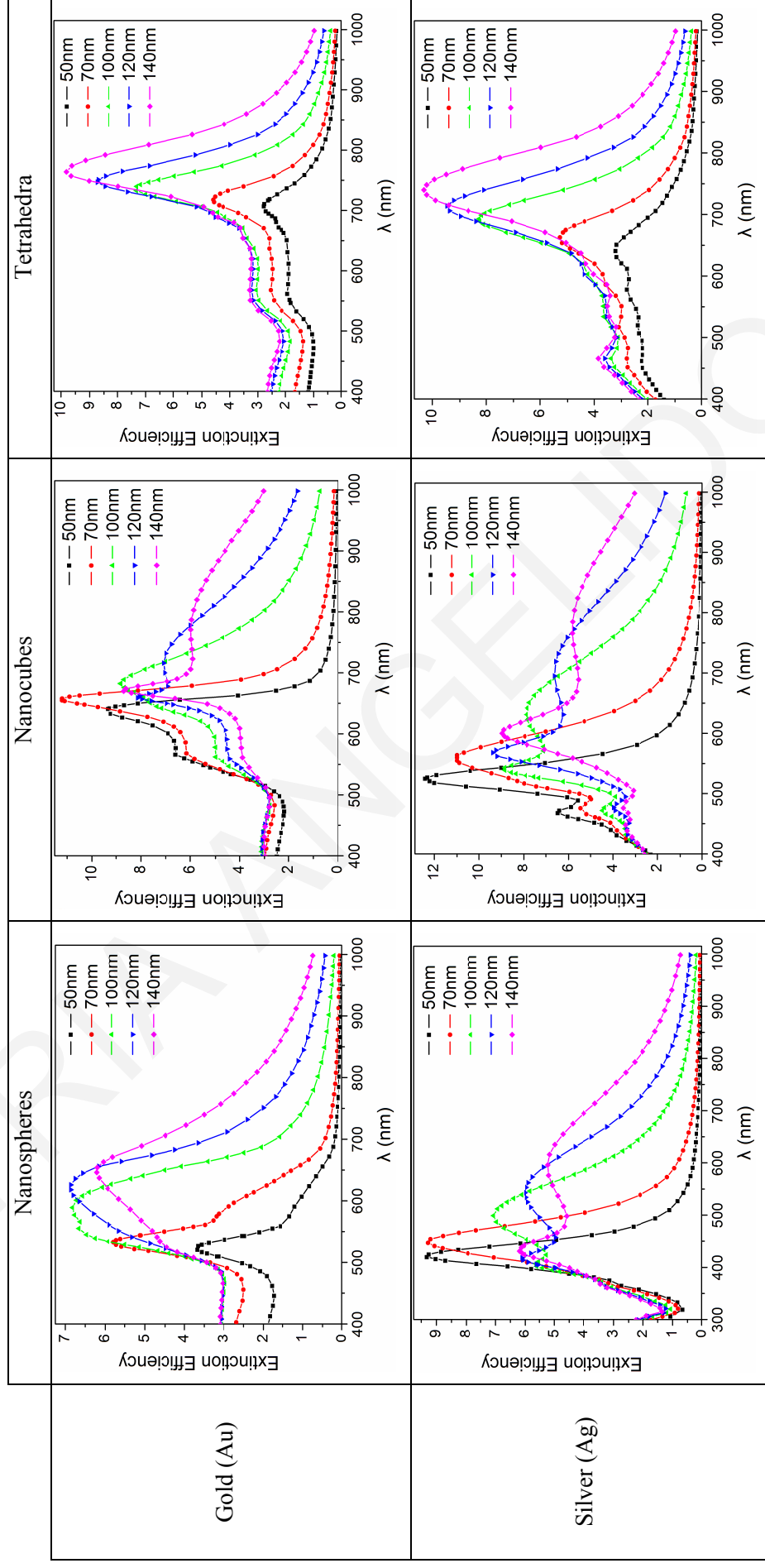
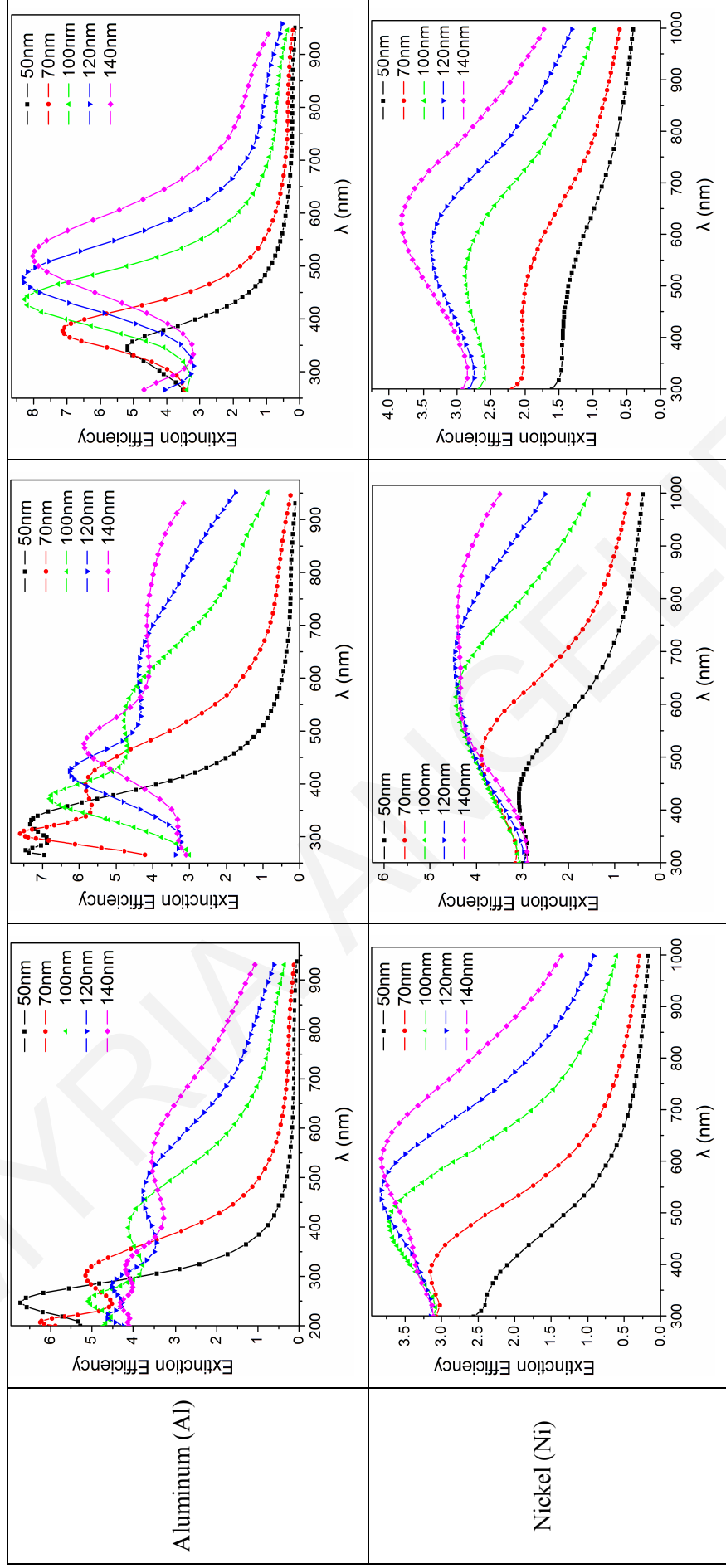


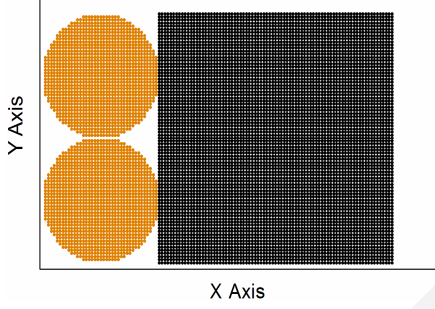
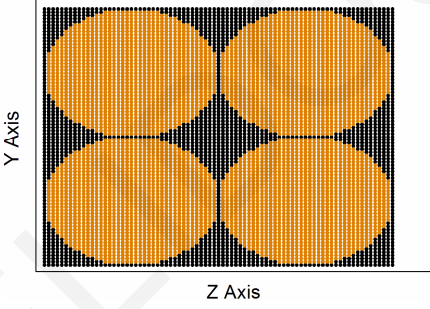
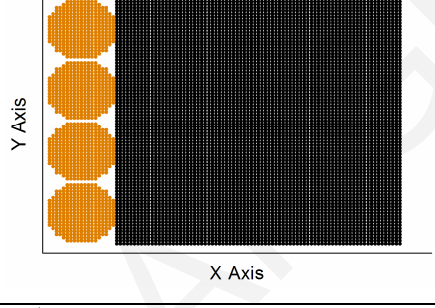
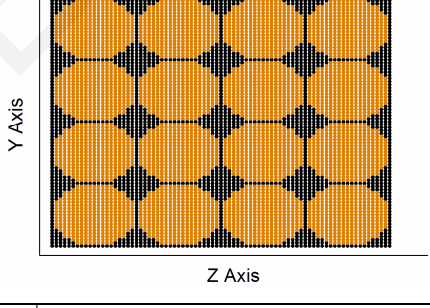
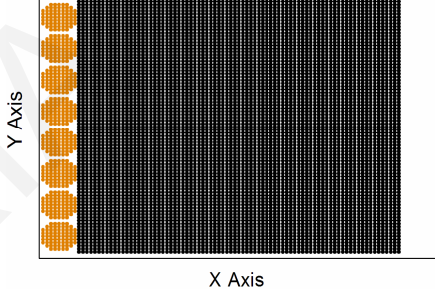
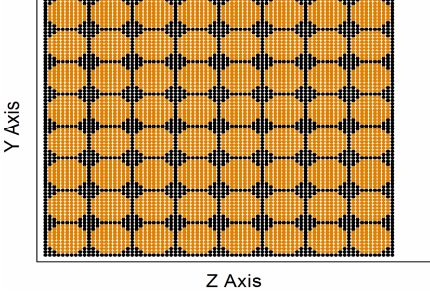
Table E.5: Comparison between extinction efficiency spectra for various nanostructure sizes, shapes, and materials





Appendix F – Shapes of Various Complex Nanostructures (Gold Nanocube Combined with Various Small Nanospheres)

Table F: Various numbers, n_{sph} , (diameters, d_m) of small nanospheres arranged on the front face of nanocube, perpendicular to the incident light propagation (x axis) (Cube in black, spheres in orange.)

	Viewed from the side (x - y plane)	Viewed from the front (y - z plane)
Cube plus 4 spheres (2×2 , 60nm)		
Cube plus 16 spheres (4×4 , 30nm)		
Cube plus 64 spheres (8×8 , 15nm)		

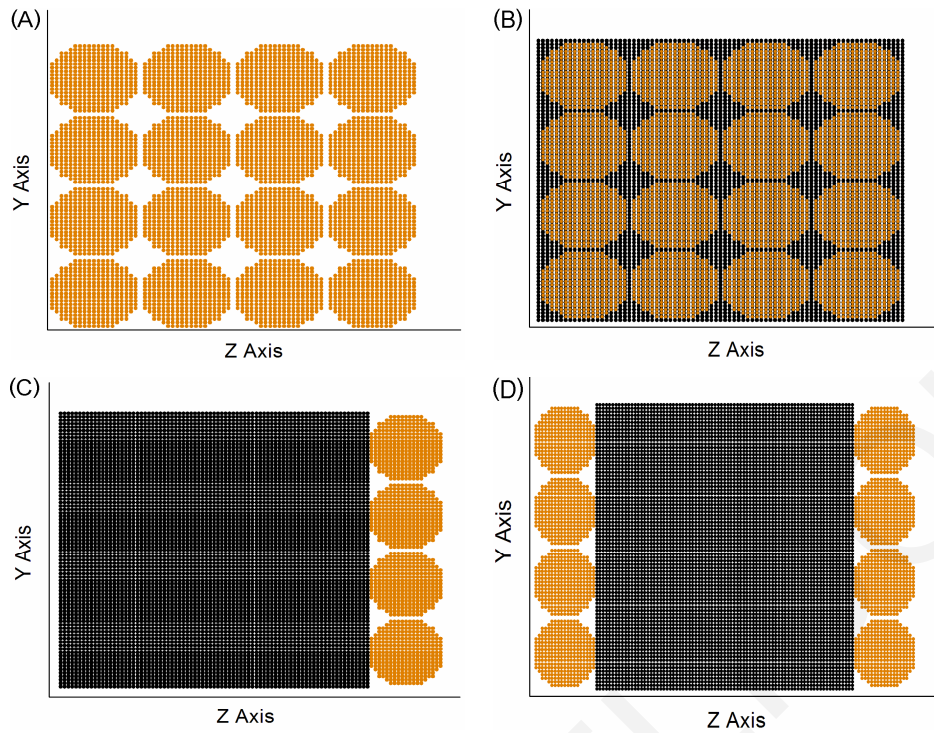


Figure F.1: Various other arrangements of small, 30nm, nanospheres. (A) 16 single nanospheres (no cube), arranged perpendicular to x axis, (B) 16 nanospheres arranged behind cube, (C) 16 nanospheres arranged on the side, and (D) 2 layers of 16 nanospheres arranged on opposite sides. All viewed from the front (y - z plane). Incident light propagation is along x axis, and polarization is along y or z axis. (Cube in black, spheres in orange.)

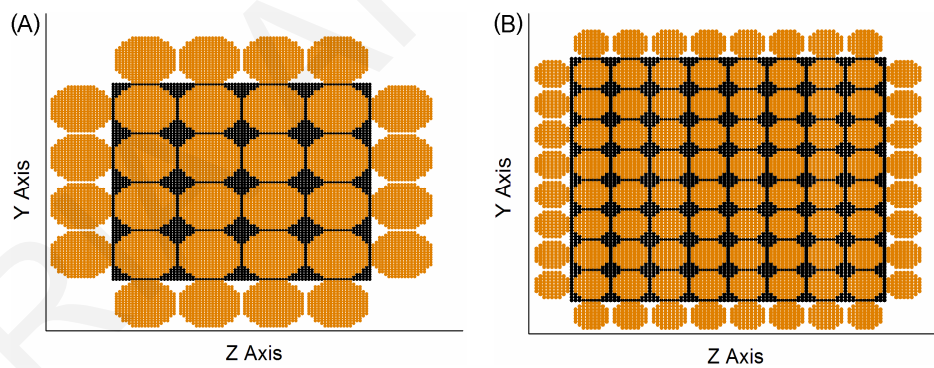


Figure F.2: Complex shapes of a nanocube covered with (A) 96 (30nm), and (B) 384 (15nm) small nanospheres. Both viewed from the front (y - z plane). Incident light propagation is along x axis, and polarization is along y or z axis. (Cube in black, spheres in orange.)

Appendix G – Other Results of Complex Nanostructures (Gold Nanocube Combined with Small Gold (Au) Nanospheres) (Palik)

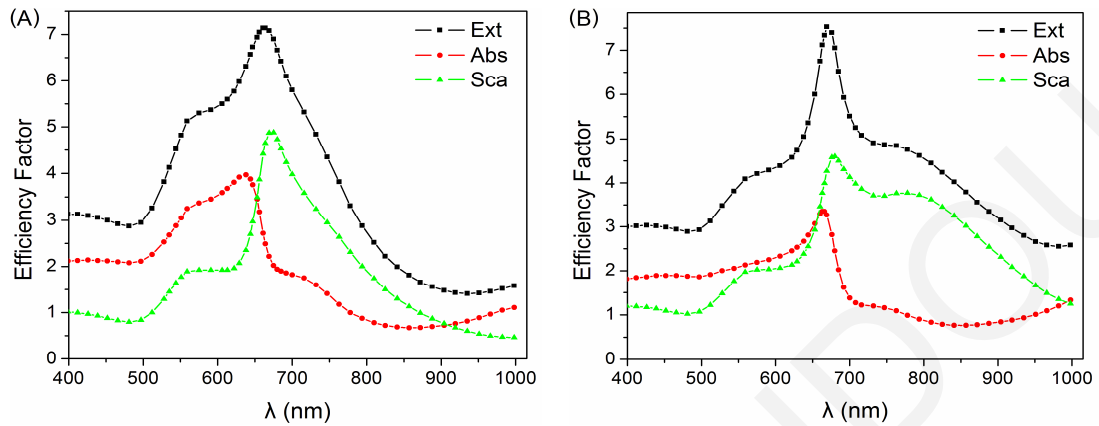


Figure G.1: Efficiency factors of a nanocube combined with 16 Au nanospheres having dimensions of (A) $b = 100\text{nm}$, $d_m = 25\text{nm}$, and (B) $b = 140\text{nm}$, $d_m = 35\text{nm}$.

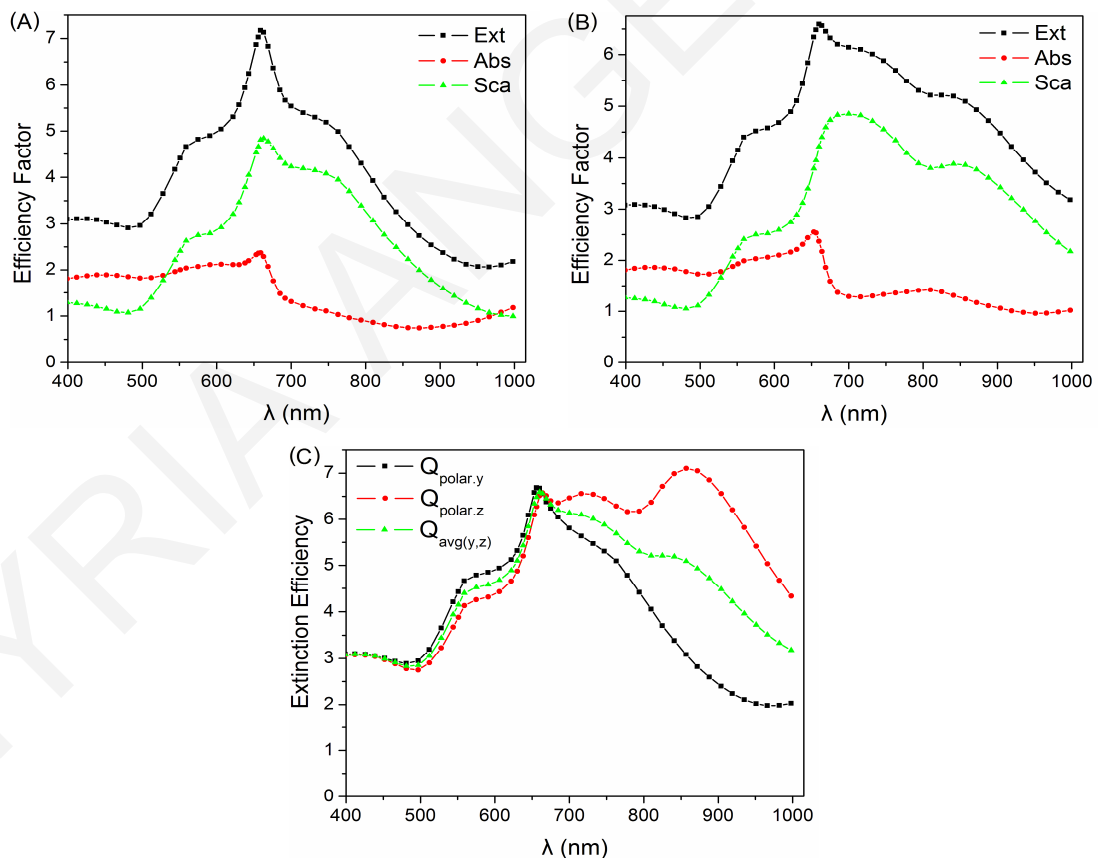


Figure G.2: Efficiency factors of a nanocube combined with 16 Au nanospheres arranged (A) on the back, and (B) on the side of the nanocube. (C) Extinction efficiency spectra showing the polarization dependence when the 16 Au nanospheres were arranged on the side, perpendicular to the z axis.

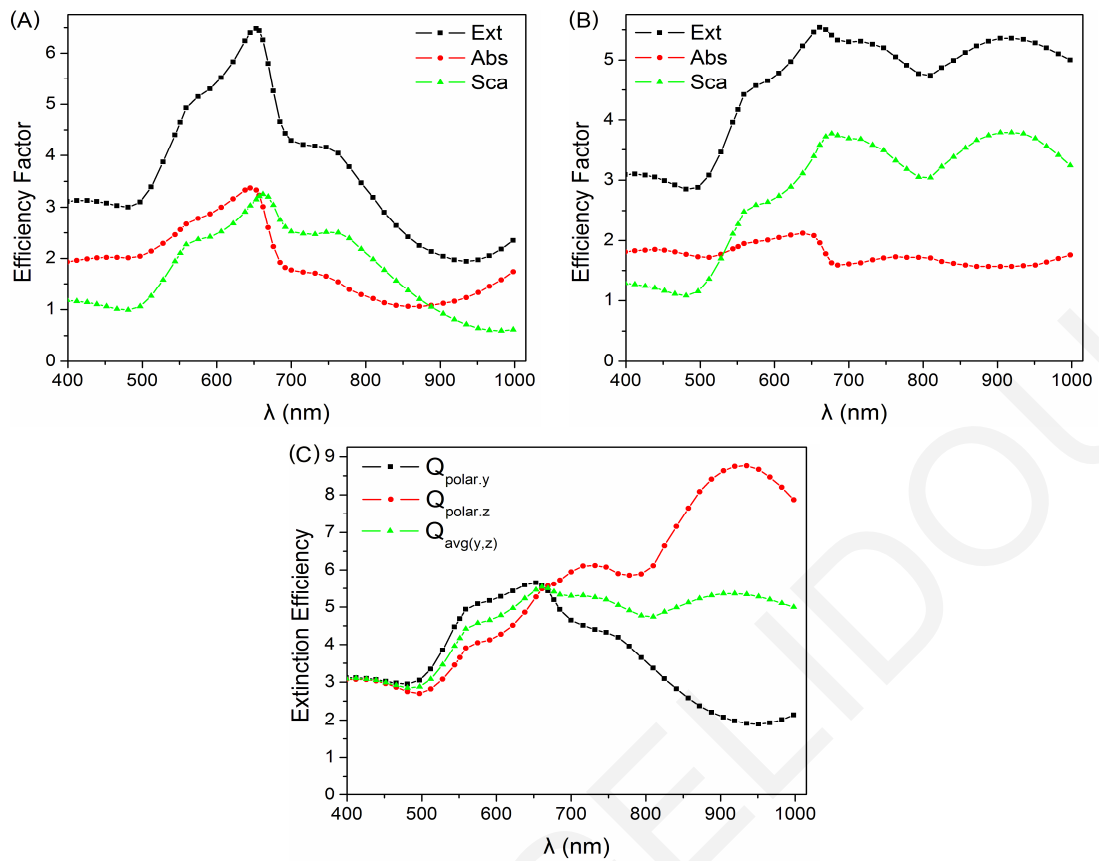


Figure G.3: Efficiency factors of an Au nanocube combined with 2 layers of 16 Au nanospheres arranged (A) on the front and back, and (B) on opposite sides of the nanocube. (C) Extinction efficiency spectra showing the polarization dependence when the 16 Au nanospheres were arranged on opposite sides, perpendicular to the z axis.

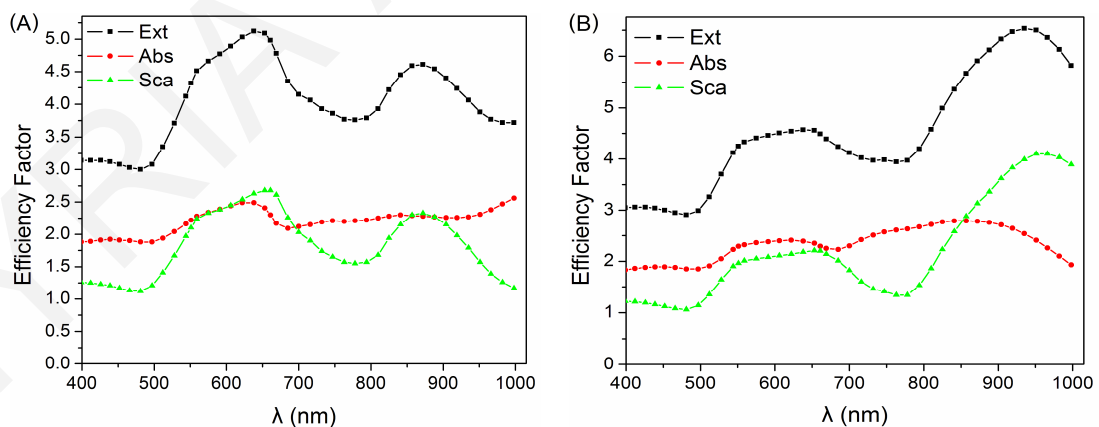


Figure G.4: Efficiency factors of a nanocube combined with (A) 96 (30nm), and (B) 384 (15nm) Au nanospheres. The nanospheres cover all 6 nanocube facets.

Appendix H – Efficiency Factors of Nanoshells Comprised of a Constant Polystyrene Core and Various Gold Shell Thicknesses

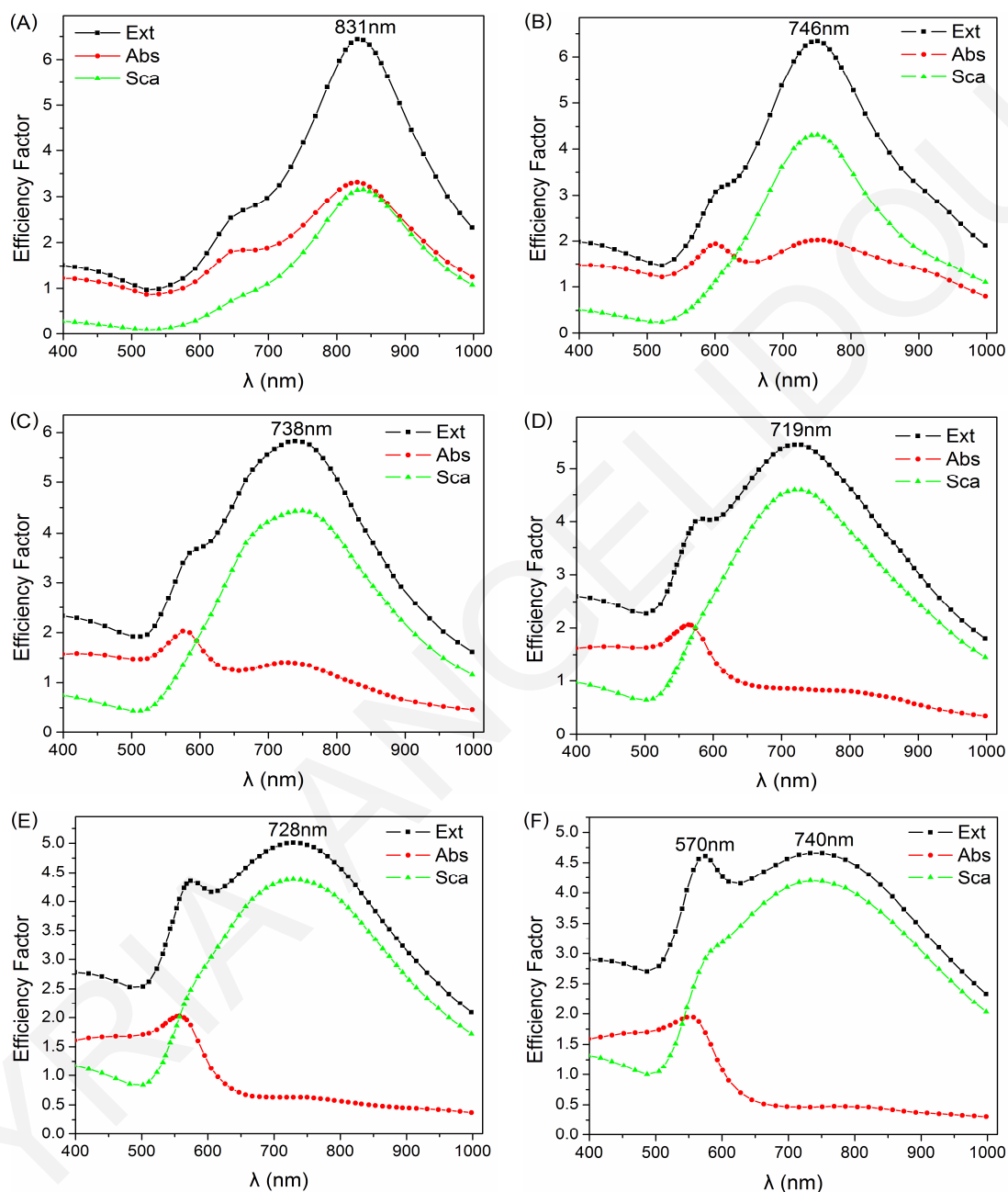


Figure H: Calculated efficiency factors of nanoshells having a constant polystyrene, PS, core ($R_c = 57\text{nm}$, $m_{\text{core}} = 1.586 + i0$) and various gold, Au, shell thicknesses of (A) 10nm, (B) 15nm, (C) 20nm, (D) 25nm, (E) 30nm, and (F) 35nm, with water as the external medium. (J&C)

Appendix I – Fitting Constants and Rayleigh Coefficient for Calculated New Absorbances A_{fit}

Table I.1: Rayleigh coefficients and other constants for fitting equation

Experiment			Rayleigh scattering coefficients		Fitting constants	
			α	β	a_8	a_9
1(a)	A0	room temp	0.21110	0.41165	0.41015	-0.03838
	B0		0.63650	0.01023	0.52938	-0.20825
	C0		1.00401	0.15408	0.34523	-0.05280
1(b)	A1		0.67011	0.10238	0.58063	-0.30126
	B1		1.30067	1.30161	0.64667	-0.19035
	C1		1.19985	1.19972	0.60364	-0.17853
2	A2	ice	0.08026	0.01271	0.35841	-0.05559
	B2		0.03035	0.01824	0.49098	-0.10745
	C2		0.04682	0.02870	0.61063	-0.02197
	D2		0.68651	0.27181	0.28378	-0.09944
	E2		0.22567	0.02055	0.80728	-0.27744
	F2		0.06249	0.33392	0.27147	-0.04441
3	A3		0.33883	0.32132	0.48009	-0.10553
	B3		0.29589	0.27242	0.59151	-0.20710
	C3		0.19041	0.18366	0.59911	-0.16161
	D3		0.62661	0.89736	0.63754	-0.20064
	E3		0.19868	0.11123	0.45838	-0.15724
	F3		1.50223	0.04727	0.51384	-0.32984

Table I.2: Unnormalized fitting constants, a_i , for calculating new absorbances, A_{fit}

Experiment	Polystyrene dm = 114nm		Single sphere dm = 25nm	R = 70nm, ds = 2nm	R = 70nm, ds = 1nm	R = 70nm, ds = 0nm	R = 70nm, shell = 15nm	R = 70nm, shell = 25nm	mean error
	a_1	a_2	a_3	a_4	a_5	a_6	a_7		
1(a)	A0	0.01274	0.57556	0.35994	0.00000	0.00000	0.05176	0.00000	0.62430
	B0	0.21793	0.64757	0.01940	0.00000	0.11510	0.00000	0.00000	0.05277
	C0	0.03482	0.61251	0.35268	0.00000	0.00000	0.00000	0.00000	0.09426
1(b)	A1	0.04753	0.24041	0.50696	0.00000	0.14768	0.05721	0.00020	0.07862
	B1	0.00365	0.54138	0.31714	0.00000	0.00005	0.13770	0.00008	0.06782
	C1	0.00263	0.29068	0.63027	0.00000	0.06786	0.00856	0.00000	0.08807
2	A2	0.17953	0.39851	0.11284	0.00000	0.26402	0.04510	0.00000	0.05140
	B2	0.13835	0.45231	0.25273	0.00000	0.00000	0.15660	0.00000	0.05830
	C2	0.05294	0.50883	0.14977	0.00000	0.25998	0.02847	0.00000	0.05509
	D2	0.02307	0.37225	0.18504	0.02675	0.26545	0.11087	0.01658	0.06576
	E2	0.14286	0.41770	0.16989	0.00000	0.00000	0.25694	0.01261	0.05865
	F2	0.02236	0.43154	0.23115	0.00000	0.26780	0.04716	0.00000	0.06936
3	A3	0.02333	0.56908	0.00000	0.02650	0.12382	0.11917	0.13810	0.03068
	B3	0.02158	0.54084	0.00033	0.00000	0.05683	0.09314	0.28729	0.03710
	C3	0.02773	0.53128	0.00000	0.00004	0.11494	0.20981	0.11621	0.04175
	D3	0.00142	0.62831	0.00000	0.00335	0.00006	0.27832	0.08853	0.08363
	E3	0.03694	0.53930	0.00000	0.03506	0.06253	0.18102	0.14515	0.03410
	F3	0.05957	0.59022	0.00000	0.04987	0.00001	0.25276	0.04758	0.07752